THEORETICAL AND EXPERIMENTAL INVESTIGATIONS OF INCOMPRESSIBLE LAMINAR BOUNDARY LAYERS WITH AND WITHOUT SUCTION

PROEFSCHRIFT

TER VERKRIJGING VAN DE GRAAD VAN DOCTOR IN DE TECHNISCHE WETENSCHAPPEN AAN DE TECHNISCHE HOGESCHOOL TE DELFT, OP GEZAG VAN DE RECTOR MAGNIFICUS IR. H. J. DE WIJS, HOOGLERAAR IN DE AFDELING DER MIJNBOUWKUNDE, VOOR EEN COMMISSIE UIT DE SENAAT TE VERDEDIGEN OP WOENSDAG 13 OKTOBER 1965, DES NAMIDDAGS TE 4 UUR

door

JAN LEENDERT VAN INGEN

vliegtuigbouwkundig ingenieur
geboren te Puttershoek

Dit proefschrift is goedgekeurd door de promotoren
prof. dr. ir. J. A. Steketee
en
prof. dr. ir. H. J. van der Maas

Aan mijn ouders
Aan mijn vrouw

5755

ERRATA

page 2	line 20 should read: "the laminar boundary layer is only 4°/o of that for the turbulent case."
page 9	in equation (2.1) and (2.2) the terms $-\frac{1}{\rho}\frac{p}{x}$ and $-\frac{1}{\rho}\frac{p}{y}$ should read $-\frac{1}{\rho}\frac{\partial p}{\partial x}$ and $-\frac{1}{\rho}\frac{\partial p}{\partial y}$ respectively.
page 35	the left hand side of equation (5.14) should read "Λ_2".
page 42	line 5: "fig. 5.8" should be replaced by "fig. 5.7".
page 72	line 10 below equation (7.68): "for N = 5 to 10" should be replaced by "for N = 5 to 9".
page 81	the first line below equation (7.96) should read "and for p odd and $\geqslant$ 1".
page 86	the first line below equation (7.102) should read "The parameters δ^*, Θ and ε as ......".
page 89	in line 11 from the bottom the first "a_o" should read "$\sqrt{a_o}$"
page 109	line 6: "(8.61)" should be replaced by "(8.50)".
page 115	line 4 should read "$\frac{c_r}{U}$ and $\frac{c_i}{U}$ are replaced by $\frac{\beta_r \nu}{U^2}$ and ....".
page 163	the last line should read "laminar separation point and the predicted transition position becomes".
page 168	in line 18 and 19 delete the words "where also the measured transition position is indicated".
table 11.2	the title of this table should read "position of pressure orifices in the suction model".
fig. 8.25	the curve —— - —— is missing; a corrected version of this figure appears on the next page.
fig. 8.26	in the lower right hand corner "$\longrightarrow \bar{x}$" should be replaced by "$\longrightarrow \sqrt{\bar{x}}$".
fig. 8.28	in the title of this figure the word "multimoment" should be replaced by "momentum".
fig. 11.55	the number 3.7 in this figure should be replaced by 3.37.

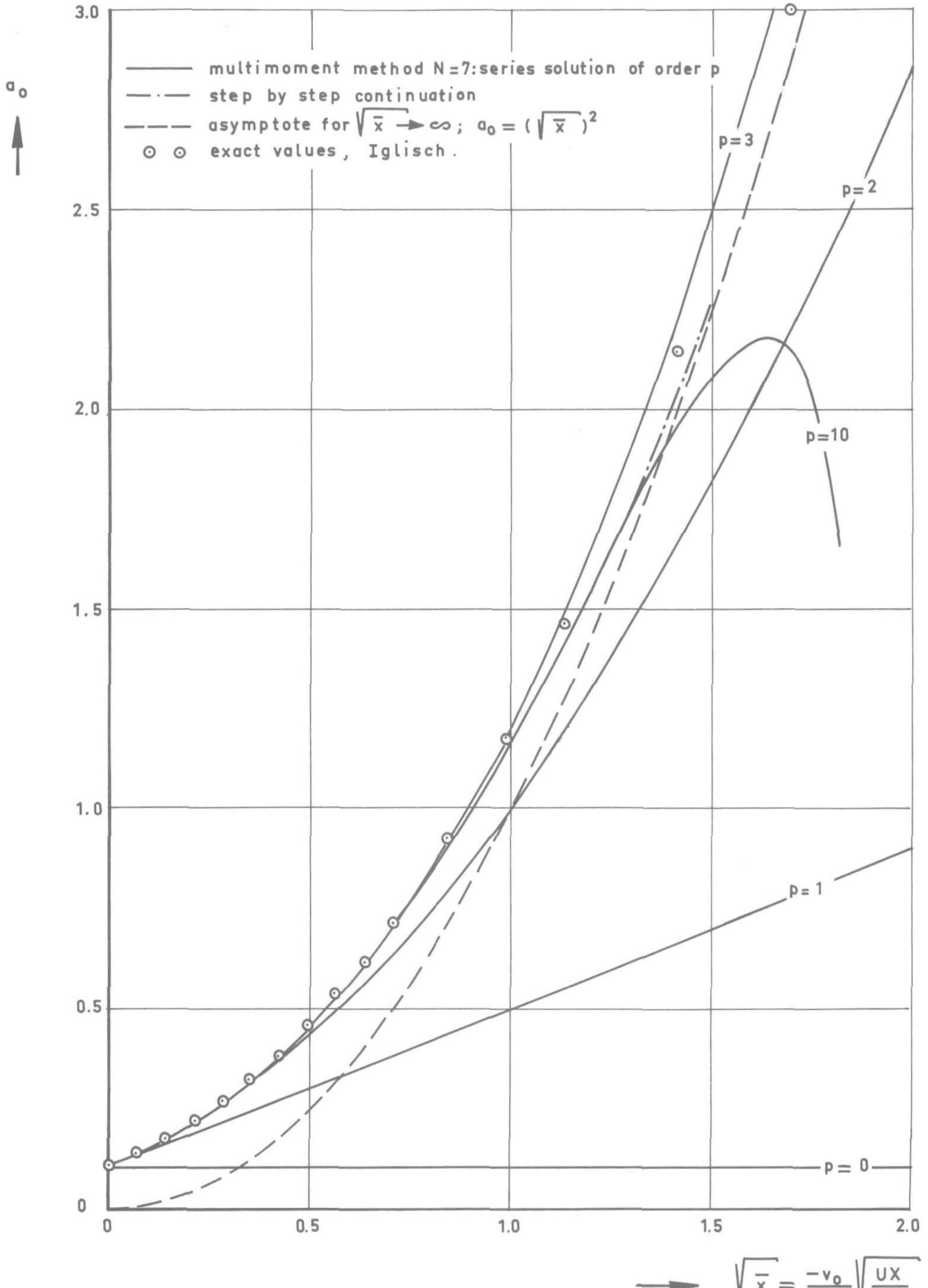

FIG. 8.25: SOME RESULTS OF THE MULTIMOMENT METHOD WITH $N = 7$ FOR THE FLAT PLATE WITH CONSTANT SUCTION VELOCITY.

Summary.

In this dissertation the results are presented of some theoretical and experimental investigations of two-dimensional laminar boundary layers with and without suction. Throughout the work the velocities involved are assumed to be of such a small magnitude that the effects of compressibility can be neglected. The investigations were undertaken with the purpose to clarify some points concerned with maintaining laminar flow in a boundary layer by means of suction through a porous surface. In the course of this work several results were obtained which also may be of interest for laminar boundary layers without suction.
A first investigation is concerned with the calculation of laminar boundary layers by means of approximate methods of the type introduced by Pohlhausen. A new method is described which, by a special choice of the velocity profile, is capable of providing accurate results in those cases where the suction velocity is not too large.
The second theoretical investigation deals with a "phase plane" description of the laminar boundary layer flow between non-parallel plane walls. Here shear τ is plotted versus the velocity component u parallel to the wall.
This is analogous to the use of the phase plane method in the theory of non-linear oscillations with one degree of freedom where speed is plotted versus displacement. In the latter theory singular points in the phase-plane correspond to equilibrium positions of the oscillation. For the flow between non-parallel plane walls the singularities in the "phase plane" are shown to correspond to the edge of a boundary layer. It is shown that the occurrence of boundary layer type solutions depends on the character of the singularity which is determined by the amount of suction.
For the case of inflow between converging walls without suction τ^2 can be expressed as a polynomial in u. From this observation a new calculation method for laminar boundary layers evolves which is described in detail. The method assumes for τ^2 a polynomial expression in u with coefficients depending on the streamwise coordinate x. These coefficients are determined from compatibility conditions and from moments of a modified form of Crocco's boundary layer equation. In contrast to existing

approximate methods the new approach allows the degree N of the polynomial to be increased without unduly complicating the method. For increasing N the results of the approximate method seem to converge to the exact solution.

The experimental part of the work consists of measurements on two airfoil sections in a low speed wind tunnel. The first model is a 28 °/o thick laminar flow airfoil section with an impermeable surface and a chord length of 1 meter. A detailed survey of the velocity profiles in the laminar boundary layer was made with hot wires; the measurements were extended so far downstream as to include the laminar separation point. Results of the measurements and a comparison with laminar boundary layer theory are presented.

The second model is a 15 °/o thick, 1.35 meter chord, laminar flow wing section with porous upper- and lower surfaces between the 30 °/o and 90 °/o chord positions. The inside of the model is divided into 40 different compartments each with its own suction line, flow-regulating valve and -measuring device. Hence the chordwise suction distribution could be varied between wide limits. Wake drag and transition position were measured for several suction distributions; for some of these detailed boundary layer surveys were made. In one case the suction distribution was chosen in such a way that a separating laminar boundary layer was obtained.

From the transition measurements on the porous model a semi-empirical method is derived which permits the determination of the transition position for two-dimensional incompressible laminar boundary layers with arbitrary pressure- and suction distributions. This method is an extension of an existing method which was shown to be valid for the no-suction case both by Smith and Gamberoni [1,2] and the present author [3,4,5].

The boundary layer calculation methods and the transition criterion provide the means for a rational design of the suction distribution needed to maintain laminar flow for a given pressure distribution. For instance a suction distribution may be determined for which the total drag coefficient is as small as possible.

Contents page

page

page

page

List of symbols.

Symbols which are used only locally are defined in the text; other symbols are listed below.

a	coefficient in eq. (4.1)
a	scaling factor for y; in chapter 5 only; numerical value 1.3
a_1	constant in equations (4.13) and (5.39)
a_n	coefficient in polynomial expression (7.29)
a_o	$\left(\frac{\tau_o x}{\mu U}\right)^2 \left(\frac{Ux}{\nu}\right)^{-1} = \bar{\tau}_o^{\,2}$
$a_{n,p}$	coefficients in series expansion (7.92) for a_n
Δa_n	increment of a_n; equation (7.70)
δa_n	increment of a_n; section 7.8
$\bar{a}_n$	starting value for a_n in sections 7.7 and 7.8
a_n^*	defined by equation (8.1)
A	integration constant in chapter 6
A_{ij}	elements of inverse matrix in chapter 7
b	coefficient in equation (4.1)
b	scaling factor for y; in chapter 5 only; numerical value 0.3
b	spanwise extent of porous surface in chapter 11 (0.805 m)
b_1	constant in equations (4.13) and (5.39)
c	coefficient in equation (4.1)
c	reference length, equal to chord length for airfoil sections
$\bar{c}$	$c_r + i\, c_i = \frac{\bar{\beta}}{\bar{\alpha}} = \frac{\beta_r}{\bar{\alpha}} + i\,\frac{\beta_i}{\bar{\alpha}}$; equation (9.6)
c_{d_f}	friction drag coefficient of flat plate defined by equation (3.18)
c_{d_s}	suction drag coefficient
c_{d_t}	total drag coefficient
c_{d_w}	wake drag coefficient
c_p	pressure loss coefficient $\frac{\Delta p}{\frac{1}{2}\rho U_\infty^2}$

c_q	suction flow coefficient $\frac{Q}{U_\infty c}$
c_{q_i}	suction flow coefficient for compartment number i in chapter 11
c_{q_u}	suction flow coefficient for the upper surface
c_{q_ℓ}	suction flow coefficient for the lower surface
d	coefficient in equation (4.1)
d	length scale in Lin's formulae (9.19) and (9.20)
D	dissipation integral defined by equation (2.23)
$2D^*$	$2\int_0^\infty \left(\frac{\partial u/U}{\partial y/\Theta}\right)^2 d\,\frac{y}{\Theta}$; nondimensional dissipation integral
e_{i_n}	$\frac{\partial E_i}{\partial a_n}$ defined by equation (7.76)
E_i	defined by equation (7.74)
$\overline{E}_i$	starting value for E_i in section (7.8)
f	number denoting value of reduced frequency $\frac{\beta_r \nu}{U^2}$ in table 9.4
f	exponent in equation (7.79); used in chapter 7 and 8 only
$f(\eta)$	nondimensional streamfunction: for chapter 3 defined by eq. (3.6)
$f(\eta)$	nondimensional streamfunction: for chapter 6 defined by eq. (6.8)
$f_1(\eta)$, $f_2(\eta)$, $f_3(\eta)$	defined by equations 5.6-5.9 in chapter 5
$f_1, f_3, f_5 \ldots$	defined by equation (3.25)
$F_{2n+1}(\eta)$	defined by eq. (3.24)
$F(\xi,\eta)$	nondimensional streamfunction in Görtler's series method; defined by eq. (3.29)
$F_o, F_{\frac{1}{2}}, F_1, \ldots$	Görtler's universal functions in section 3.2.4.
$F(\eta)$	defined by eq. (4.9) in chapter 4
$F(\Lambda_1)$	Pohlhausen's universal function defined by equation (4.12) in chapter 4

$F_1(\eta)$	
$F_2(\eta)$	defined by equations 5.3-5.9 in chapter 5
$F_3(\eta)$	
$G(\eta)$	defined by equation (4.10) in chapter 4
H	$\frac{\delta^*}{\Theta}$
$\bar{H}$	$\frac{\varepsilon}{\Theta}$
$j_{k,n}$	defined by eq. (7.55)
J_k	defined by eq. (7.52)
$J_{k,p}$	defined by eq. (7.98) and (7.99)
k	0,1,2,...K
K	N-5 in chapter 7
K	shape factor in chapter 5
K_1, K_2	constants in equation (9.25)
ℓ	$\left(\frac{\partial u/U}{\partial y/\Theta}\right)_o = \frac{\tau_o \Theta}{\mu U}$
ℓ_1	$\frac{\sigma^2}{\nu}\frac{dU}{dx} = \bar{\sigma}^2 \frac{d\bar{U}}{d\bar{x}}$
ℓ_2	$\frac{-v_o \sigma}{\nu} = \bar{v}_o \bar{\sigma}$
L	shape factor in chapter 5
m	$\left(\frac{\partial^2 u/U}{\partial (y/\Theta)^2}\right)_o$
m_1	constant in equation 3.1
M	$2\ell - 2(2+H)\Lambda_1 - 2\Lambda_2$
M_k	defined by equation (7.51)
$M_{k,p}$	defined by equation (7.98)-(7.99)
N	degree of polynomial expression (7.29)
p	static pressure in chapter 2 and 9
p	order of series expansion in chapter 7 and 8
p'	fluctuation of static pressure in chapter 9
p^*	p + p' in chapter 9

p_t	free stream total pressure in chapters 10 and 11
$p_1, p_2, .. p_9$	coefficients in eq. (5.10)-(5.12)
p_x	static pressure on body surface at distance x from the stagnation point
$p_{k,n}$	defined by equation (7.55)
P_k	defined by equation (7.53)
$P_{k,p}$	defined by eqns. (7.98)-(7.99)
p_{w+} p_{w-}	static pressures at side wall of wind tunnel (see fig.11.1)
Q	suction flow per unit span $m^3 sec^{-1} m^{-1}$
$q_{k,\ell,n}$	defined by equation (7.55)
Q_k	defined by equation (7.54)
$Q_{k,p}$	defined by equation (7.98)-(7.99)
r_p	defined by equations (7.94) and (7.96)
R	radius of cylinder in section 8.9
R_{δ^*}	$\frac{U\delta^*}{\nu}$
R_θ	$\frac{U\theta}{\nu}$
R_c	$\frac{U_\infty c}{\nu}$
S	$\bar{\tau}^2$
s	distance along contour of airfoil section, measured from leading edge (chapter 11 only)
$\bar{s}$	s/c
t	time
t_n	δa_n in section 7.8.
T	amplification rate of unstable disturbances defined by equation (9.17)
T_o	constant in eq. (9.25)
u	velocity component parallel to wall
u'	fluctuation of u
u^*	u+u' in chapter 9
$\bar{u}$	u/U in general; u/ $\|U\|$ in chapter 6

$\bar{u}_p$	velocity measured by surface tubes; chapter 10
U	velocity component parallel to wall at edge of boundary layer
$\bar{U}$	U/U_∞
U_∞	reference speed, equal to free stream speed in chapters 10 and 11
v	velocity component normal to wall
v'	fluctuation of v in chapter 9
v^*	$v+v'$ in chapter 9
v_o	normal velocity at surface; negative for suction
$\bar{v}_o$	$\frac{-v_o}{U_\infty}\sqrt{\frac{U_\infty c}{\nu}}$
V	wind speed in section 8.9
x	distance along wall measured from stagnation point, (fig. 2.1)
x_p	distance along chord of airfoil section (fig. 2.1)
$\bar{x}$	x/c
y	distance normal to wall
y_p	ordinate of airfoil section
y_r	distance from reference position outside boundary layer (chapter 10)
$\bar{y}$	$\frac{y}{\delta} = \frac{y}{x}\sqrt{\frac{Ux}{\nu}}$
z	new variable, defined by eq. (7.79)
z_p	spanwise coordinate, chapter 10
α	angle of attack of airfoil section
α_1	$\bar{U}\,\bar{\delta}^2$ in chapter 7
$\bar{\alpha}$	$\frac{2\pi}{\lambda}$ in chapter 9 only
β	Hartree parameter defined by eq. (3.4)
$\beta_1, \beta_2, \beta_3, ..$	defined by eq. (7.68)
$\beta(\xi)$	Görtler's function defined by eq. (3.31)
$\bar{\beta}$	$\beta_r + i\beta_i$ in section 9.2.2.

β_o	$\frac{2m_1}{m_1+1}$ (eq. 3.36)
γ	$1-3\lambda_1$
δ	measure for boundary layer thickness in general
δ	defined by $\frac{\delta}{x}\sqrt{\frac{Ux}{\nu}}=1$ in chapter 7 and further
$\bar{\delta}$	$\frac{\delta}{c}\sqrt{\frac{U_\infty c}{\nu}}$
δ^*	displacement thickness $\int_0^\infty (1-\bar{u})dy$
$\overline{\delta^*}$	$\frac{\delta^*}{c}\sqrt{\frac{U_\infty c}{\nu}}$
δ_{k+2}	defined by eq. (2.26)
ε	energy loss thickness $\int_0^\infty \bar{u}(1-\bar{u}^2)dy$
η	$y\sqrt{\frac{m_1+1}{2}\ \frac{U}{\nu x}}$ in section 3.12
η	$y\sqrt{\frac{u_1}{\nu c}}$ in section 3.2.2.
η	defined by eq. (3.28) in section (3.2.4)
η	$\frac{y}{\delta}$ in chapter 4
η	$\frac{y}{\sigma}$ in chapter 5
η	$\frac{y}{x}\sqrt{\frac{\lvert u_1\rvert}{\nu}} = \frac{y}{x}\sqrt{\frac{\lvert U\rvert x}{\nu}}$ in chapter 6
η_1	$-\lambda\eta$ in chapter 6
θ	momentum loss thickness $\int_0^\infty \bar{u}(1-\bar{u})dy$
$\bar{\theta}$	$\frac{\theta}{c}\sqrt{\frac{U_\infty c}{\nu}}$
λ	$\frac{v_o x}{\sqrt{\nu \lvert u_1\rvert}}$ in chapter 6
λ	$\frac{\delta^2}{\nu}\ \frac{dU}{dx}$ in chapter 4
λ	wave length of disturbance in chapter 9
λ_1	$\frac{x}{U}\ \frac{dU}{dx} = \frac{\bar{x}}{\bar{U}}\ \frac{d\bar{U}}{d\bar{x}} = \bar{\delta}^2\ \frac{d\bar{U}}{d\bar{x}}$

λ_2	$\frac{-v_o}{U}\sqrt{\frac{Ux}{\nu}} = \bar{v}_o . \bar{\delta} = \frac{-v_o \delta}{\nu}$
$\lambda_{1,p}$	coefficients in eq. (7.80)
$\lambda_{2,p}$	coefficients in eq. (7.81)
Λ_1	$\frac{\theta^2}{\nu}\frac{dU}{dx} = \bar{\theta}^2 \frac{d\bar{U}}{d\bar{x}} = \ell_1 (\frac{\theta}{\sigma})^2$
Λ_2	$\frac{-v_o \theta}{\nu} = \bar{v}_o \, \bar{\theta} = \ell_2 \frac{\theta}{\sigma}$
μ	coefficient of dynamic viscosity
ν	$\frac{\mu}{\rho}$ coefficient of kinematic viscosity
ξ	Görtler's variable defined by equation (3.27)
ρ	density
σ	measure for boundary layer thickness in chapter 5
$\bar{\sigma}$	$\frac{\sigma}{c}\sqrt{\frac{U_\infty c}{\nu}}$
σ_a	amplification factor defined by eq. (9.16)
$(\sigma_a)_{max}$	maximum value of σ_a at a certain position
σ_p	defined by equations (7.96) and (7.97)
τ	$\mu \frac{\partial u}{\partial y}$ shear stress
$\bar{\tau}$	$\frac{d\bar{u}}{d\eta}$ in chapter 6
$\bar{\tau}$	$\frac{\partial \bar{u}}{\partial \bar{y}} = \frac{\tau\delta}{\mu U}$ in chapter 7 and 8
τ_o	wall shear stress
$\bar{\tau}_o$	$\frac{\tau_o \delta}{\mu U} = \sqrt{a_o}$ in chapter 7 and further
$\varphi(y)$	$\varphi_r + i\varphi_i$, amplitude function in equation (9.4)
ψ	stream function in chapter 3 and 6
ψ	$\psi_r + i\psi_i$ stream function of disturbance defined by equation (9.4)

subscripts

i	at the instability point
o	at the surface
sep	at the separation point
st	at the stagnation point
tr	at transition
te	at trailing edge
le	at leading edge

primes denote differentiation with respect to η in chapter 3 and 6 and to $\overline{u}$ in chapter 7. They denote fluctuation components in chapter 9.

1. Introduction and outline of thesis.

1.1. Introduction.

During the development of the airplane to its present form a continuous reduction of aerodynamic drag has been achieved. This drag reduction was made possible by the practical application of wing theory beginning around 1918 and the introduction of streamlined shapes beginning after 1929. The year 1929 is marked by Mellvil Jones' well-known paper "The streamline aeroplane" [6] in which he indicated the improvements in performance to be obtained from streamlining.

Streamlining has been realised by the introduction of the cantilever monoplane, the retractable undercarriage, improved flow around the engines, better construction methods leading to a smoother surface etc. Finally the use of jet engines - being smaller than piston engines of the same power - led to a cleaner aeroplane with less drag than its predecessors.

The situation now is such that for big airliners the major part of the non-induced drag is due to skin-friction. Values of the non-induced drag found in practice for this type of airplane are about 25 °/o higher than the friction drag calculated for a turbulent boundary layer over the aircrafts wetted surface.

In view of this it is clear that a further important reduction of the non-induced drag can only be obtained by a further decrease in friction drag. This can be achieved naturally by a reduction of the wetted surface of the airplane. However, only a limited reduction in drag will be possible in this way since the minimum extent of the wetted surface is dictated by the requirement that sufficient volume should be provided for payload, fuel etc. Hence, for a further drag reduction the intensity of skin friction itself has to be decreased. It is well known that the skin friction is much higher for a turbulent boundary layer than for a laminar one. As an example fig. 1.1.a shows the friction drag coefficient of a flat plate for both laminar and turbulent flow as a function of the Reynolds number $\frac{Ux}{\nu}$ using the familiar logarithmic presentation. Here U is the windspeed, ν the coefficient of kinematic viscosity and x the length of the plate. The curve in fig. 1.1a for the laminar boundary layer follows from Blasius' theory to be discussed in chapter 3. The friction drag for the turbulent flow is given by a formula due to Schlichting ([7], chapter 21) which correlates a number of different experiments. The experimental results indicated in the figure for both laminar and turbulent flow are taken from unpublished measurements in the low speed wind tunnel of the Department of Aeronautical Engineering at Delft Technological University. The experimental observations show that for the smooth plate above a certain Reynoldsnumber there is a gradual change from laminar to turbulent flow. Fig. 1.1.b shows the same results given in fig. 1.1.a but now using a linear scale for c_{d_f} which indicates more clearly the difference in skin friction for laminar and turbulent flow. The situation for an aircraft wing or fuselage is approximately similar to a flat plate and fig. 1.1 can be used to get an idea about the differences in friction drag, which can exist for an airplane with laminar or turbulent boundary layers. For instance for a typical jet airliner in cruising flight the Reynoldsnumber based on wing chord is about 2.5×10^7. Hence, if fig. 1.1 is considered to be applicable to the wing, it follows that the skin friction drag for a laminar boundary layer is only $10^o/o$ of the value obtained for a turbulent flow. For the fuselage the Reynolds number based on length is about 2.5×10^8 and hence the friction drag for the laminar boundary layer is only $10^o/o$ of that for the turbulent case. It is clear therefore that a considerable advance in drag reduction can be made by maintaining laminar flow in the boundary layer along an airplane. A necessary requirement for the occurrence of laminar flow in the boundary layer is that the body surface be smooth. This requirement is not sufficient however since even on a smooth body the boundary layer may become turbulent due to instability against small disturbances. As an example fig. 1.1 shows that for the smooth flat plate the boundary layer becomes turbulent for stations on the plate where the Reynoldsnumber $\frac{Ux}{\nu}$ is higher than about 3×10^6.

It is found (chapter 9) that instability and transition are strongly influenced by a streamwise pressure gradient. When the static pressure increases in the downstream direction the instability and hence the danger of transition to turbulence become very marked. Such an "adverse" pressure gradient is found for instance downstream of the maximum

thickness of an airplane wing in cruising flight.
In order to increase the extent of the region with laminar flow on a smooth wing the position of maximum thickness has to be moved rearwards. Airfoil sections designed with this objective in mind are the "laminar flow airfoil sections" which have been in use since about 1940.
Another method to stabilise the laminar boundary layer is to make the surface impervious in order to suck away a very small amount of air from the boundary layer. This method has been proposed first, as far as the author knows, by Griffith and Meredith in 1936 [8].
In fig. 1.1 the drag of a flat plate with a sufficient amount of suction to stabilise the boundary layer is shown (see section 9.8). Due to suction the skin friction rises above the value for the Blasius boundary layer but it remains much smaller than the value for the turbulent flow occurring without suction. The power needed to drive the suction pump can be converted to an equivalent "suction drag coefficient" to be added to the wake drag (see appendix 1). For the flat plate the total drag coefficient including the suction drag is also shown in fig. 1.1.
For complete airplanes the nett reduction in power required which would result from laminarisation by suction is substantial (see for instance Lachmann [10]). For a present-day modern jet airliner for instance, skin friction on the wing alone amounts to about 25°/o of the total drag in subsonic cruising flight. Laminarisation of the wing would lead to about 75°/o reduction in its non-induced drag even when allowance is made for the suction power. Hence the total drag in cruising flight would be reduced by about 20°/o if the boundary layer on the wing could be kept laminar. Lachmann states [10] that by laminarisation of the wing and tailplanes and optimisation of the airplane design for the application of suction the lift to drag ratio would be doubled as compared with the optimised conventional airplane.
The potential improvement in aircraft performance indicated above has stimulated so many investigations in the field of laminarisation that a large part of a recent two-volume work on "Boundary layer and flow control" [9] is devoted to this problem. In these books a detailed account of the historical development of the subject may be found. In what follows only

a few of these investigations will be mentioned to place the present work in the proper perspective.

Early wind tunnel investigations have been made by Holstein [11], Pfenniger [12] and Kay [13]. Holstein and Pfenniger tested airfoil sections with suction through a number of slots; Kay applied suction to a porous flat plate. Later experiments were made in flight by Head [14] using a small aircraft to carry an airfoil section model with a porous surface. The geometry of the test airfoil was chosen in such a way that in the suction region the pressure distribution for a flat plate was simulated. The amount of suction needed to keep the boundary layer laminar corresponded approximately to the theoretical predictions of Ulrich based on stability theory (see chapter 9). Subsequent experiments in high speed flight by Head and Johnson [15] and Pfenniger [16,17] showed that also at chord-Reynoldsnumbers of the order of 30×10^6 laminarisation could be achieved by suction.
As suction through a porous surface consisting of very fine pores may present practical difficulties a number of experimental investigations have been made in England with perforated surfaces obtained by drilling small holes in the skin [18]. It appears that these perforated surfaces can be useful for unswept wings but that it will be very difficult if not impossible to design a suitable perforation pattern for a swept wing. Pfenniger's experiments both in the wind tunnel and in free flight have been made with suction through a large number of narrow spanwise slits. A full scale flight experiment using Pfenniger's slot suction scheme is being made by the Northropp Co in the U.S.A. [20,21].

Theoretical investigations have been mainly concerned with porous surfaces because suction through discrete holes or slots is much more difficult to treat theoretically. In calculating the suction flow required to prevent transition most investigators choose the suction distribution in such a way that the laminar boundary layer remains neutrally stable all the way to the trailing edge of the body. Since it is well-known that instability of the boundary layer does not imply that turbulence will immediately appear (see chapter 9) it is clear that this procedure leads to a conservative estimate of the suction flow. As transition can not yet be predicted theoretically it is much more difficult to indicate the - less intense - suction distribution which is sufficient to prevent transition.

One of the aims of the present work was to improve upon this situation by designing a method which allows the calculation of the transition point for arbitrary pressure- and suction-distributions. Such a method for the no-suction case had already been given independently of each other by Smith and Gamberoni [1,2] and the present author [3,4,5]. The method for the case of suction is a straightforward extension of the earlier version.

In this method the amplification of unstable disturbances in the boundary layer is calculated using linear stability theory. It is shown that for different experiments actual transition occurs at nearly the same value of a calculated "amplification factor".

To extend this method to the case of suction it was necessary to obtain experimental results on transition of boundary layers with suction. For this purpose an airfoil section model with a porous surface between the $30^{\circ}/o$ and $90^{\circ}/o$ chord positions was tested in the low speed wind tunnel of the Department of Aeronautical Engineering at Delft.

In connection with this work a study was made of available methods for the calculation of laminar boundary layers. A new method of the Pohlhausen type was designed with application to suction problems in mind (chapter 5).

The accuracy of methods of this type is normally assessed by comparison with exact solutions of the boundary layer equations. One of the available exact solutions is due to Pohlhausen [22] and concerns the inflow between non-parallel plane walls without suction. This flow had been studied already in 1916 by Jeffery [23] and Hamel [24] using the Navier-Stokes equations. From a consideration of this flow it appeared that a clear picture could be obtained by studying the solutions of the equations in a plane where shear stress τ is plotted versus the velocity component u parallel to the wall. Also the effects of suction and blowing can easily be shown in this way (chapter 6).

This procedure is analogous to the use of the phase plane in the study of

non-linear oscillations of autonomous systems with one degree of freedom where speed is plotted versus displacement. In the mechanical problem the oscillation can be described by an ordinary differential equation of the first order. Singular points of this equation correspond to equilibrium positions of the oscillation while the type of stability of the motion is determined by the character of the singularity. In the flow problem the singular points are shown to correspond to the edge of a boundary layer. The equation only allows solutions of the boundary layer type - for which the velocity becomes practically constant at large distances from the wall - when the singularity is a saddle point or a stable node. In the phase plane study, referred to above, it was found that for inflow between impervious walls the boundary layer equations give a solution for which τ^2 is a simple polynomial in u. This observation has been put to advantage for the design of a practical calculation method for boundary layers. In this method τ^2 is assumed to be a polynomial in u with coefficients depending on the streamwise coordinate x (chapter 7).
The boundary layer equation is written in a form where x and u are used as the independent variables and τ^2 as the dependent variable. The coefficients of the polynomial expression for τ^2 are determined from moments and compatibility conditions of this equation.
Essentially the new approach consists of the application of the well known von Kármán-Pohlhausen technique to a slightly changed form of Crocco's boundary layer equation. The moments have been designed in such a way that the degree N of the polynomial can easily be increased without complicating the method too much. For increasing values of N the results of the method seem to converge to the exact solution. For special suction- and pressure distributions the method allows a power series solution.
Results of accurate experimental investigations of laminar boundary layers which might be compared with results of boundary layers theory are very rare. Except for the flat plate - which has been considered by several investigators - the only accurate experiments known to the author are provided by Schubauer's investigation of the boundary layer on an elliptic cylinder [25]. Since the publication of [25] nearly all newly designed calculation methods have been applied to Schubauer's measured

pressure distribution. Some controversy has existed about these data because some calculation methods did not predict separation of the laminar boundary layer while the experiment had clearly shown that separation was present. It appears that the difficulty arises from the sensitivity of the boundary layer calculation to small changes in the pressure distribution near separation. According to Hartree [26] a very small change of the experimentally determined pressure distribution is sufficient to obtain separation.

As Schubauer's investigation has been made with a small chord model (11.78 inches) at the very low chord Reynoldsnumber of 72000 it was thought worth while to undertake an independent investigation on a larger scale. Therefore measurements were performed on a 28 °/o thick laminar flow airfoil section with a chord of 1 meter. A detailed survey of the velocity profiles in the laminar boundary layer was made using hot wires and pitot tubes. Special attention was given to the laminar separation point (chapter 10). For the case of suction through a porous surface with a streamwise pressure gradient no results of accurate boundary layer measurements were known to the author. Therefore measurements were made on the model with the porous surface - already referred to - for such a suction distribution that laminar separation occurred in the suction region. Also pressure distributions and wake drag coefficients were measured for this model (chapter 11).

1.2. Outline of thesis.

Chapter 2 reviews the basic equations of two-dimensional incompressible laminar boundary layer flows. Included are Prandtl's boundary layer equations, the von Kármán-Pohlhausen momentum equation, the kinetic energy equation and compatibility conditions of the boundary layer equations. Chapter 3 is concerned with known methods for the solution of the boundary layer equations. Similar solutions and series expansion methods are discussed; finite difference methods are only briefly mentioned. Chapter 4 reviews some existing approximate methods using the von Kármán-Pohlhausen technique. Chapters 2,3 and 4 do not contain new results and therefore readers acqainted with boundary layer theory

can omit this part of the present work.
In chapter 5 the new method of the Pohlhausen type is presented together with some applications. The "phase plane" representation of the boundary layer flow between non-parallel plane walls with and without suction is given in chapter 6. The new calculation method which evolved from this study is described in chapter 7; some applications of both new methods are presented in chapter 8. The following chapter first reviews the subject of transition and linear stability theory and then describes the semi-empirical method for the calculation of the transition region.
Chapters 10 and 11 are devoted to the experimental investigations of the laminar boundary layer on the impervious and the porous airfoil section respectively. Where possible, results of the experiments have been compared with boundary layer theory.
Conclusions about the results of the investigations are mentioned in chapter 12. An important result of the present work is that it has become possible to calculate the characteristics of the laminar boundary layer including the transition position for arbitrary chordwise pressure - and suction distributions. This provides, for the first time, the means for a rational design of the most economic suction distribution needed to maintain laminar flow for a given pressure distribution.

2. The equations for two-dimensional laminar boundary layer flows.

2.1. The Navier-Stokes equations.

Two-dimensional flows of an incompressible viscous fluid are governed by the Navier-Stokes equations and the continuity equation. Omitting body forces the equations may be written in cartesian coordinates as follows (see [7], chapter 3).

$$\frac{\partial u}{\partial t} + u\frac{\partial u}{\partial x} + v\frac{\partial u}{\partial y} = -\frac{1}{\rho}\frac{\partial p}{\partial x} + \nu\left(\frac{\partial^2 u}{\partial x^2} + \frac{\partial^2 u}{\partial y^2}\right) \tag{2.1}$$

$$\frac{\partial v}{\partial t} + u\frac{\partial v}{\partial x} + v\frac{\partial \cancel{y}^{\,v}}{\partial y} = -\frac{1}{\rho}\frac{\partial p}{\partial y} + \nu\left(\frac{\partial^2 v}{\partial x^2} + \frac{\partial^2 v}{\partial y^2}\right) \tag{2.2}$$

$$\frac{\partial u}{\partial x} + \frac{\partial v}{\partial y} = 0 \tag{2.3}$$

Equations (2.1) and (2.2) are the equations of motion in x and y direction respectively; (2.3) is the continuity equation. The notation is as usual: u and v are the velocity components in x and y direction, p is the pressure, ρ the density and ν the coefficient of kinematic viscosity. Throughout the present work ρ and ν are assumed to be constant. At the surface of a body placed in the flow the relative velocity vanishes. This leads to the usual boundary conditions that the normal and tangential components of the relative velocity vanish at the surface. In the present investigation problems with suction and blowing are considered so that a small normal component of the relative velocity at the surface will be allowed.

The Navier-Stokes equations are difficult to solve for flows around bodies of arbitrary shape. In a few cases where the geometry of the problem is very simple exact solutions show that for high values of the Reynoldsnumber $\frac{U_\infty c}{\nu}$ the effect of viscosity is confined to a narrow region near the surface called the boundary layer and a region behind the body called the wake. Within the boundary layer the relative velocity component tangential to the surface rises very fast from zero at the wall to a nearly constant value at a small distance from the wall.

This observation led Prandtl in 1904 [27] to his boundary layer theory which simplifies the Navier-Stokes equations by expressing the fact that there is a boundary layer of which the thickness is small compared to the body length.

2.2. Prandtl's boundary layer equations.

Prandtl's simplification of the Navier-Stokes equations leads to the following set of equations for the case of steady flow along a plane wall:

$$u \frac{\partial u}{\partial x} + v \frac{\partial u}{\partial y} = - \frac{1}{\rho} \frac{\partial p}{\partial x} + \nu \frac{\partial^2 u}{\partial y^2} \tag{2.4}$$

$$\frac{\partial u}{\partial x} + \frac{\partial v}{\partial y} = 0 \tag{2.5}$$

Here x and y are taken along and normal to the wall respectively. Eq.(2.4) is the boundary layer equation and results from (2.1). The equation of motion in y-direction (2.2) leads to the result that within the boundary layer $\frac{\partial p}{\partial y}$ can be neglected and hence for steady flow p only depends on x. The continuity equation (2.3) remains unchanged (2.5). A discussion of the boundary layer equations may be found in the books by Schlichting [7], Curle [28] and also in [29].

It can be shown that (2.4) and (2.5) are valid also for a two-dimensional curved body provided the radius of curvature is large compared to the boundary layer thickness and no rapid changes of curvature occur ([7], chapter 7). For curved bodies an orthogonal curvilinear coordinate system (x,y) should be used where x and y are measured parallel and normal to the wall respectively (fig. 2.1).

Outside the boundary layer the velocity gradient $\frac{\partial u}{\partial y}$ can be neglected and hence (2.4) reduces to:

$$U \frac{dU}{dx} = - \frac{1}{\rho} \frac{dp}{dx} \tag{2.6}$$

Using this, (2.4) may be written as

$$u \frac{\partial u}{\partial x} + v \frac{\partial u}{\partial y} = U \frac{dU}{dx} + \nu \frac{\partial^2 u}{\partial y^2} \tag{2.7}$$

Together with the continuity equation (2.5) this equation determines the development of the boundary layer flow downstream of an initial station $x = x_o$ when the velocity profile at $x = x_o$ is known. Solutions of (2.5) and (2.7) are subject to the following boundary conditions:

$$y = 0: \qquad u = 0, \quad v = v_o(x) \tag{2.8}$$

$$y \rightarrow \infty: \qquad u \longrightarrow U \tag{2.9}$$

In boundary layer theory the velocity U at the edge of the boundary layer is assumed to be known either from a calculation using potential flow theory or from measurements.

The boundary conditions (2.8) imply that no oblique suction or blowing is considered.

Although the boundary layer equations are much simpler than the full Navier-Stokes equations, they can only be solved exactly for special types of the functions $U(x)$ and $v_o(x)$. Some of the available exact solutions will be reviewed in chapters 3 and 8.

The application of finite difference methods to obtain accurate numerical solutions has been limited in the past due to the large amount of work required. However, due to the introduction of high speed digital computors this situation has changed, so that now a number of accurate solutions has been made available. Some of these solutions will be discussed in chapter 8. In what follows both the exact solutions and accurate finite difference solutions of the boundary layer equations will be denoted as "exact" solutions. Approximate methods of solution have found a wide application in the past due to the difficulty of obtaining "exact" solutions. An important approximate method was introduced by Pohlhausen in 1921 [22] (see also [7] chapter 4). In methods of this type the boundary layer equations are not satisfied from point to point but relations are sought which fulfil certain more simple formulae derived from (2.5) and (2.7). Some of these formulae will be described in the remaining sections of the present chapter.

It should be stated in advance that these equations do not provide information which goes beyond the boundary layer equations; they only give a part of the information contained in the boundary layer equations in a different form.

2.3. Compatibility conditions of the boundary layer equations.

If the boundary conditions at the wall (2.8) are substituted into the boundary layer equation (2.7) the following result is obtained

$$v_o \left(\frac{\partial u}{\partial y}\right)_o = U \frac{dU}{dx} + \nu \left(\frac{\partial^2 u}{\partial y^2}\right)_o \tag{2.10}$$

where the subscript O denotes values at the wall (y = O). Equation (2.10) is called the first compatibility condition at the wall; it relates the curvature of the velocity profile at the wall to the shear stress, pressure gradient and suction velocity. Compatibility conditions of higher order can be obtained by repeated differentiation of (2.7) with respect to y and using (2.5) and (2.8). The second compatibility condition thus obtained reads

$$v_o \left(\frac{\partial^2 u}{\partial y^2}\right)_o = \nu \left(\frac{\partial^3 u}{\partial y^3}\right)_o \tag{2.11}$$

and the third is found to be

$$\left(\frac{\partial u}{\partial y}\right)_o \frac{\partial}{\partial x} \left(\frac{\partial u}{\partial y}\right)_o + v_o \left(\frac{\partial^3 u}{\partial y^3}\right)_o = \nu \left(\frac{\partial^4 u}{\partial y^4}\right)_o \tag{2.12}$$

2.4. Moments of the boundary layer equations.

The boundary layer equation (2.7) can be written symbolically as

$$F(x,y) = O \tag{2.13}$$

It follows that solutions of the boundary layer equations satisfy equations of the type:

$$\int_o^\infty F(x,y)\, G(x,y)\,dy = O \tag{2.14}$$

Where G(x,y) may be any function subject to the condition that the integral (2.14) exists. Relations of the form (2.14) are called moments of the boundary layer equations. Since a wide class of functions G may be used many different moments can be obtained.

Von Kármán's momentum equation. With G(x,y) = 1 the well known von Kármán momentum equation is found ([7], chapter 8). This equation can be written in the forms

$$\frac{d}{dx}(U^2\Theta) = \frac{\tau_o}{\rho} + v_o\,U - U\delta^* \frac{dU}{dx} \tag{2.15}$$

and

$$\frac{U\Theta}{\nu}\frac{d\Theta}{dx} + (2+H)\frac{\Theta^2}{\nu}\frac{dU}{dx} - \frac{v_o\Theta}{\nu} = \frac{\tau_o\Theta}{\mu U} \tag{2.16}$$

with τ_o, δ^*, Θ and H denoting respectively

$$\tau_o = \mu\left(\frac{\partial u}{\partial y}\right)_o = \rho\nu\left(\frac{\partial u}{\partial y}\right)_o = \text{wall shear stress} \tag{2.17}$$

$$\delta^* = \int_o^\infty (1 - \frac{u}{U})dy = \text{displacement thickness} \tag{2.18}$$

$$\Theta = \int_o^\infty \frac{u}{U}(1 - \frac{u}{U})dy = \text{momentum loss thickness} \tag{2.19}$$

$$H = \frac{\delta^*}{\Theta} = \text{shape factor of the velocity profile} \tag{2.20}$$

Equation (2.15) was first obtained by von Kármán [30] as an equation expressing the momentum balance in the boundary layer. Later Pohlhausen [22] gave the derivation referred to above.

The kinetic-energy equation. With G(x,y) = u equation (2.14) leads to:

$$\frac{d}{dx}(U^3\mathcal{E}) = v_o\,U^2 + D \tag{2.21}$$

(see for instance [7], chapter 8 and 13). Equation (2.21) is called the kinetic energy equation, while $\mathcal{E}$ and D denote the energy-loss thickness and dissipation integral. They are defined by

$$\mathcal{E} = \int_o^\infty \frac{u}{U}\left[1 - (\frac{u}{U})^2\right] dy \tag{2.22}$$

and

$$D = 2\,\nu \int_o^\infty \left(\frac{\partial u}{\partial y}\right)^2 dy \tag{2.23}$$

Usually from $\mathcal{E}$ and Θ a second shape factor $\overline{H}$ is defined by

$$\overline{H} = \frac{\mathcal{E}}{\Theta} \tag{2.24}$$

The kinetic-energy equation expresses the balance between mechanical energy and heat developed through frictional forces; it was first given by Leibenson [31] and later by Wieghardt [32].

Other moment equations can be derived for instance by taking $G(x,y) = u^k$ with $k > 1$. The resulting expression becomes

$$\frac{d}{dx}\left[U^{k+2}\ \delta_{k+2}\right] = v_o U^{k+1} + (k+1)\ U \frac{dU}{dx} \int_o^\infty \frac{u}{U}\left[1 - \left(\frac{u}{U}\right)^{k-1}\right] dy$$
$$- \nu (k+1) \int_o^\infty u^k \frac{\partial^2 u}{\partial y^2}\ dy \tag{2.25}$$

in which

$$\delta_{k+2} = \int_o^\infty \frac{u}{U}\left[1 - \left(\frac{u}{U}\right)^{k+1}\right] dy \tag{2.26}$$

It can easily be shown that equation (2.25) reduces to the momentum equation (2.15) for $k = 0$ and to the kinetic energy equation (2.21) for $k = 1$.

3. Some known methods to obtain accurate solutions of the boundary layer equations.

3.1. Similar solutions.

3.1.1. General.

The partial differential equations (2.5) and (2.7) can be reduced to one ordinary differential equation for "similar" boundary layer flows. Here similarity means that the velocity profiles for all different stations x can be reduced to a single curve by rescaling the y and u variables with scaling factors depending on x. Well known examples are the flat plate boundary layer flow (Blasius, 1908, [33]) and the plane stagnation point (Hiemenz, 1921, [34]). A detailed discussion of the occurrence of similar boundary layers may be found in Goldstein [35], Mangler [36,37], Schlichting[7] (chapter 8) and [29] (chapter V).
It was found that similarity is only possible if the velocity U at the edge of the boundary layer is given by one of the following three expressions.

$$U = u_1\, x^{m_1} \tag{3.1}$$

$$U = u_1\, x^{-1} \tag{3.2}$$

$$U = u_1\, e^{u_2 x} \tag{3.3}$$

where u_1, u_2 and m_1 are constants.
Expression (3.1) corresponds to the potential flow in the neighbourhood of the vertex of a wedge with an angle $\pi\beta$ where

$$\beta = \frac{2\, m_1}{m_1+1} \tag{3.4}$$

The related boundary layer flows have been calculated by Hartree; they will be discussed further in section 3.1.2.
In potential flow, (3.2) corresponds to a line source or-sink and hence the related boundary layer flow is that between non-parallel plane walls. It will be discussed extensively in chapter 6.

Finally (3.3) describes the potential flow through a channel with curved walls (Goldstein [35], Mangler [36,37]); it will not be discussed further in the present work.

3.1.2. Hartree's boundary layer flows for $U = u_1 x^{m_1}$.

For the wedge-type similar flows $U = u_1 x^{m_1}$ the proper non-dimensional variables are η and $f(\eta)$ defined by

$$\eta = y \sqrt{\frac{m_1+1}{2} \frac{U}{\nu x}} \qquad (3.5)$$

and
$$\psi(x,y) = \sqrt{\frac{2\nu u_1}{m_1+1}}\; x^{\frac{m_1+1}{2}} f(\eta) \qquad (3.6)$$

In (3.6) ψ denotes the streamfunction which is related to the velocity components u and v by

$$u = +\frac{\partial \psi}{\partial y} \quad ; \quad v = -\frac{\partial \psi}{\partial x} \qquad (3.7)$$

From (3.5), (3.6) and (3.7) it follows that

$$u = U\, f'(\eta) \qquad (3.8)$$

and
$$v = -\sqrt{\frac{m_1+1}{2} \nu\, u_1\, x^{m_1-1}} \left[f + \frac{m_1-1}{m_1+1} \eta\, f' \right] \qquad (3.9)$$

where primes denote differentiation with respect to η.

With (3.7) the continuity equation (2.5) is already satisfied. The boundary layer equation (2.7) reduces to

$$f''' + f\, f'' + \beta(1 - f'^2) = 0 \qquad (3.10)$$

The boundary conditions (2.8) and (2.9) lead to

$$\eta = 0 : \quad f(o) = -v_o \sqrt{\frac{2}{m_1+1} \frac{x^{1-m_1}}{\nu\, u_1}} \quad ; \quad f'(o) = 0 \qquad (3.11)$$

$$\eta \to \infty : \quad f' \longrightarrow 1 \qquad (3.12)$$

Equation (3.10) was first given - in a slightly different form - by Falkner and Skan in 1930 [38] and is usually called after them. Special cases of (3.10) had been given earlier for the flat plate (β=0) by Blasius and for the stagnation point flow (β=1) by Hiemenz (see sections 3.1.3 and 3.1.4). Solutions of (3.10) for the no-suction case ($f(o) = 0$) were obtained by Hartree in 1937 [39] using a differential analyser.
He found that for $\beta \geqslant 0$ the boundary conditions (3.11) and (3.12) specify a unique solution of (3.10) whereas for $\beta < 0$ an infinity of solutions exists, all satisfying the boundary conditions. This is illustrated in fig. 3.1 where velocity profiles are sketched which correspond to solutions of (3.10) satisfying 3.11. It is seen from the figure that for $\beta \geqslant 0$ there is only one solution for which (3.12) is fulfilled; for $\beta < 0$ all solutions satisfy (3.12). For negative values of β Hartree selected as the relevant solution that one which satisfied the extra condition (see fig. 3.1):

" $f' = \frac{u}{U} \longrightarrow 1$ as fast as possible without making an overshoot"

With this choice the skin friction considered as a function of β becomes continuous at β=0. For $\beta = -0.198838$ the solution determined in this way gives $f''(o) = 0$ indicating that a boundary layer occurs which is on the verge of separation at all values of x.
Subsequent to Hartree's work many investigations have been made of the characteristic features of solutions of (3.10). An extensive review may be found in [29], chapter V.21. The extra condition at the edge of the boundary layer introduced by Hartree to obtain a unique solution has become known as the "Hartree condition". A mathematical justification for its use has been described recently by Goldstein [40].
It follows from (3.11) that in the case of suction similar solutions can be found if the suction distribution $v_o(x)$ is chosen in such a way that $f(o)$ is constant. The permissible suction distribution follows then from

$$-v_o(x) = \text{constant} \, . \, x^{\frac{m_1-1}{2}} \qquad (3.13)$$

Solutions of (3.10) for the case of suction have been obtained by various authors. A review of work in this field may be found in [29], chapter V.21.

3.1.3. Blasius' solution for the flat plate without suction.

For the flat plate $\frac{dU}{dx} = 0$ and hence $\beta=0$; this reduces the Falkner-Skan equation (3.10) to the well known Blasius equation

$$f''' + f\,f'' = 0 \qquad (3.14)$$

Boundary conditions for solutions of (3.14) in the no-suction case are

$$\eta = 0 : \quad f = f' = 0 \qquad (3.15)$$

$$\eta \to \infty : \quad f' \longrightarrow 1 \qquad (3.16)$$

The solution of (3.14) has been given already by Blasius in 1908 [33]. Improved solutions were given later by Töpfer, Hartree, Howarth, Smith and others. (see [29]).

Experimental observations of the flat plate boundary layer were made by Burgers and van der Hegge Zijnen in 1924 [41] and later by Hansen [42]. These investigations fully confirmed the validity of Blasius' solution at least for not too high values of the Reynolds number $\frac{Ux}{\nu}$. Fig. 3.2 shows the boundary layer velocity profile according to this theory as compared with results of a recent experimental investigation in the low speed wind tunnel of the Department of Aeronautical Engineering at Delft Technological University (unpublished).

According to the theory the shearing stress at the wall is given by

$$\frac{\tau_o}{\rho U^2} = 0.33206 \sqrt{\frac{\nu}{Ux}} \qquad (3.17)$$

Upon integration of (3.17) x = 0 to x = c the friction drag coefficient c_{d_f} of one side of a plate with unit span and length c is found to be

$$c_{d_f} = \frac{\int_o^c \tau_o \, dx}{\frac{1}{2}\rho U^2 c} = \frac{1.3282}{\sqrt{\frac{Uc}{\nu}}} \qquad (3.18)$$

Experimental results for the friction drag, taken from the measurements already referred to, are given as fig. 3.3.

It should be noted that for airfoil sections with unit span the drag coefficient is defined as the drag due to both the upper and the lower surface divided by $\frac{1}{2}\rho U^2 c$ where c is the chord length of the airfoil. Hence, if the flat plate is considered as an airfoil section with zero thickness the drag coefficient should be given twice the value following from (3.18).

3.1.4. The plane stagnation point without suction.

For a plane stagnation point U varies linearly with x as

$$U = u_1 x \tag{3.19}$$

and hence $\beta = 1$. In this case (3.10) reduces to

$$f''' + f f'' + 1 - f'^2 = 0 \tag{3.20}$$

with boundary conditions (3.15) and (3.16). This equation was obtained and solved in 1911 by Hiemenz [34]; later investigations were made by Hartree, Smith and many others (see section 3.1.2.). Results of these calculations will be given in chapter 8.

3.1.5. The asymptotic suction boundary layer.

A very special similar solution is given by the asymptotic suction boundary layer. Experimentally this layer is expected to occur far from the leading edge of a porous flat plate with constant suction velocity v_o (note that v_o is negative for suction).
Assuming $\frac{\partial}{\partial x} = 0$ *in (2.5) and (2.7) it is easily found that*

$$\frac{u}{U} = 1 - e^{\frac{v_o y}{\nu}} \tag{3.21}$$

The solution (3.2.1) is due to Griffith and Meredith [8]. The special feature of this boundary layer is that the velocity profiles at different values of x are not only similar but even identical. (see also section 8.11). From (3.21) it is easily found that for this case

$$\frac{-v_o \delta^*}{\nu} = 1 \ ; \quad \frac{-v_o \theta}{\nu} = 0.5 \ ; \ H = 2 \text{ and } \ell = \frac{\tau_o \theta}{\mu U} = 0.25$$

3.2. Solutions in series.

3.2.1. General.

In section 3.1 it was indicated that for a number of special functions $U(x)$ and $v_o(x)$ similar boundary layers are obtained for which the governing equations (2.5) and (2.7) are reduced to one ordinary differential equation. For more general functions $U(x)$ and $v_o(x)$ it is possible to obtain solutions of the boundary layer equations by solving a series of ordinary differential equations. In what follows some examples will be given.

3.2.2. Blasius' series.

For blunt-nosed bodies which are symmetrical with respect to the direction of the oncoming flow the velocity U at the edge of the boundary layer can be developed in a power series of the form

$$\overline{U} = u_1\overline{x} + u_3\,\overline{x}^3 + u_5\,\overline{x}^5 + \ldots\ldots = \sum_{n=0} u_{2n+1}\,\overline{x}^{\,2n+1} \qquad (3.22)$$

The coefficients u_{2n+1} depend on the shape of the body. In (3.22) $\overline{x} = x/c$ and $\overline{U} = U/U_\infty$ where c and U_∞ are a constant reference length and -speed respectively. Using a non-dimensional wall distance η defined by

$$\eta = y\sqrt{\frac{u_1}{\nu c}} \qquad (3.23)$$

the streamfunction ψ can be written in the form

$$\psi = (u_1 \nu c)^{\frac{1}{2}} \sum_{n=0} \overline{x}^{\,2n+1}\, F_{2n+1}(\eta) \qquad (3.24)$$

If, using (3.7) the expressions (3.22), (3.23) and (3.24) are introduced into the boundary layer equation (2.7) and the coefficients of the various powers of $\overline{x}$ are equated to zero a sequence of ordinary differential equations for the functions F_{2n+1} is obtained. These equations can be solved in succession giving F_1, F_3, ... etc. The procedure indicated above has been given by Blasius in 1908 [33].
The equation for F_1 is found to be non-linear and identical to equation

(3.20) given by Hiemenz for the plane stagnation point flow. Hence it follows that the boundary layer on any symmetrical blunt-nosed body starts at the leading-edge as the plane stagnation point flow discussed in section 3.1.4.

The functions F_{2n+1} for $n > 0$ are obtained from linear differential equations in which the coefficients are determined by the functions F_{2k+1} with $k < n$. Hiemenz showed [34] that the solution of the differential equations for F_1 and F_3 can be made independent of u_1 and u_3 by introducing new functions f_1 and f_3 defined by

$$F_1 = f_1$$
$$F_3 = 4 \frac{u_3}{u_1} f_3 \qquad (3.25)$$

Later Howarth showed that all the functions F_{2n+1} can be written as sums of universal functions which are independent of the u_{2n+1} and hence can be calculated once for all. Calculations were made by Howarth, Frössling, Ulrich and most recently by Tifford. At present the functions are available up to and including $n = 5$; hence six terms of the series (3.24) can be determined. References to the investigations mentioned above and abstracts of Tiffords tables may be found in Curle [28], chapter 2; (see also [7] and [29]).

A similar procedure can be used for the non-symmetrical case when also even powers of $\bar{x}$ occur in the power series development of U (Howarth, [43]). However, only very few of the universal functions have been calculated.

3.2.3. Series solution from a cusped leading-edge.

The procedure given by Blasius for bodies with a blunt leading-edge can be generalised to bodies with any wedge-shaped leading edge for which

$$U = u_1 \bar{x}^{m_1} \left[1 + a_1 \bar{x} + a_2 \bar{x}^2 + \ldots\ldots \right] \qquad (3.26)$$

In this case also it may be expected that the boundary layer calculation is reduced to the solution of a series of ordinary differential equations. The first of these equations then would be the Falkner-Skan equation (3.10) with β determined by m_1 according to (3.4). Hence, it may be assumed that the boundary layer on a body with a cusped leading-edge, for which $m_1 = \beta = 0$, would start like the Blasius flat plate boundary layer.

As far as the author knows, this case has not been worked out in as much generality and detail as the Blasius series. Only for the special case $\overline{U} = 1 - \overline{x}^j$ calculations have been made by Howarth [44] for j = 1 and by Tani [45] for j = 2, 4 and 8. Their results show indeed that the first differential equation of the series thus obtained is the Blasius equation (3.14); the remaining equations are linear. Results of the calculations by Howarth and Tani will be given in chapter 8.

3.2.4. Görtler's series method.

The most refined application of the series method available up till now is due to Görtler [46, 47, 48, 49] ; see also Schlichting [7], chapter 9. This method can be applied to any wedge-shaped leading-edge; it contains the blunt and cusped leading-edge as special cases.

Görtler introduces new variables ξ and η by

$$\xi = \frac{1}{\nu} \int_0^x U \, dx \tag{3.27}$$

$$\eta = yU \left(2 \nu \int_0^x U \, dx\right)^{-\frac{1}{2}} \tag{3.28}$$

The streamfunction ψ is written in the form

$$\psi(x,y) = \nu \sqrt{2\xi} \; F(\xi, \eta) \tag{3.29}$$

Introduction of (3.27) through (3.29) in the boundary layer equation (2.7) leads to the following differential equation for the non-dimensional streamfunction $F(\xi, \eta)$:

$$F_{\eta\eta\eta} + FF_{\eta\eta} + \beta(\xi) \left[1 - F_\eta^{\,2} \right] = 2\xi \left[F_\eta F_{\xi\eta} - F_\xi F_{\eta\eta} \right] \tag{3.30}$$

In this equation $\beta(\xi)$ depends on the given pressure distribution according to

$$\beta(\xi) = \frac{2 \frac{dU}{dx} \int_o^x U \, dx}{U^2} \qquad (3.31)$$

Boundary conditions for (3.30) in the no-suction case are:

$$\eta = 0 : \qquad F = 0 \quad ; \quad F_\eta = 0 \qquad (3.32)$$

$$\eta \rightarrow \infty : \qquad F_\eta \rightarrow 0 \qquad (3.33)$$

For the similar boundary layers corresponding to $U = u_1 x^{m_1}$ the function $\beta(\xi)$ becomes a constant; eq. (3.30) then reduces to the Falkner-Skan equation (3.10). For functions U(x) of the form

$$U = x^{m_1} \left[s_o + s_{\frac{1}{2}} x^{\frac{m_1+1}{2}} + s_1 x^{m_1+1} + s_{\frac{3}{2}} x^{\frac{3}{2}(m_1+1)} + \ldots\ldots \right] \qquad (3.34)$$

with $s_o \neq 0$, $m_1 \neq -1$ the function $\beta(\xi)$ is given by

$$\beta(\xi) = \beta_o + \beta_{\frac{1}{2}} \xi^{\frac{1}{2}} + \beta_1 \xi^1 + \beta_{\frac{3}{2}} \xi^{\frac{3}{2}} + \ldots\ldots \qquad (3.35)$$

The coefficients in the right-hand side of (3.35) follow from the coefficients of (3.34); especially β_o is given by

$$\beta_o = \frac{2 m_1}{m_1+1} \qquad (3.36)$$

Görtler assumes the following series for the streamfunction $F(\xi, \eta)$

$$F(\xi, \eta) = F_o(\eta) + F_{\frac{1}{2}}(\eta) \xi^{\frac{1}{2}} + F_1(\eta) \xi^1 + F_{\frac{3}{2}}(\eta) \xi^{\frac{3}{2}} + \ldots \qquad (3.37)$$

When this expression is substituted into (3.30) and the coefficients of various powers of ξ are equated to zero a series of differential equations is obtained. The first of these equations is non-linear and contains only F_o and β_o; it is identical to the Falkner-Skan equation (3.10) for $\beta = \beta_o$. Hence it follows that for bodies allowing an expansion

(3.34) for $U(x)$ the boundary layer at $x = 0$ starts as one of Hartree's boundary layers. The differential equations for the functions F of higher order are linear, the coefficients of the equations depend on the F's of lower order. It was shown by Görtler that the functions F can be split up into universal functions which depend only on β_o. Hence these functions can be tabulated once for all for each value of the leading-edge angle $\pi\,\beta_o$. For $\beta_o = 0$ and $\beta_o = 1$ the universal functions are available to calculate F_n for $n = 0, 1, \ldots, 5$; for $\beta_o = 1$ sufficient functions have been calculated to form F_n for $n = 0, \frac{1}{2}, 1, \ldots, 2$ [48]. With the aid of the tabulated functions boundary layer calculations can easily be made for $U(x)$ conforming to (3.34); however in general the results are not sufficiently accurate near a separation point (section 3.2.5).

The series method was extended by Görtler to the case of suction in [49]. For pressure distributions given by

$$U = x^{m_1} \left[s_o + s_1\, x^{m_1+1} + s_2\, x^{2(m_1+1)} + \ldots \right] \qquad (3.38)$$

the permissible suction distribution follows from

$$v_o = x^{\frac{m_1-1}{2}} \left[\sigma_o + \sigma_1\, x^{m_1+1} + \sigma_2\, x^{2(m_1+1)} + \ldots \right] \qquad (3.39)$$

The number of universal functions to be calculated is becoming very large in the case of suction and - for so far the author knows - these calculations have not yet been performed. Therefore this method will not be discussed further. Results of Görtler's method for some cases without suction will be mentioned in chapter 8 of the present work.

3.2.5. Disadvantages of the series methods.

For slender bodies like airfoil sections it is impossible to represent U by one of the series (3.22) or (3.34) with a resonable number of terms. Hence the series methods can not be used for practical boundary layer calculations. Of course they remain useful for small values of x to start the calculation near the leading-edge.

Another disadvantage is the following. Even if an expansion (3.22), (3.26) or (3.34) is possible with a small number of terms the number of differential equations to be solved is in principle infinitely large. The relatively small number of universal functions which is available, is in general sufficient for boundary layer calculations not too near separation. However, when separation is approached more functions are needed to obtain sufficient accuracy. Therefore in this region the available series methods have to be supplemented by different calculation methods.

3.3. Finite difference methods.

Various authors devised methods to solve the boundary layer equations with finite difference methods. A discussion of these methods is outside the scope of the present work however. Reviews of available methods may be found in [29]. Where they are available results obtained from these methods will be used in chapter 8 to test the accuracy of the new calculation methods.

4. Approximate boundary layer calculations using moment equations and compatibility conditions.

4.1. General.

For bodies with arbitrary pressure- and suction distributions the similarity and series solutions as discussed in chapter 3 can not be used. In this case only the finite-difference methods can be applied to provide accurate solutions of the boundary layer equations. In the past however use of these methods on a large scale has been prohibited by the large amount of work required. Therefore approximate methods have been used to a great extent and possibly they will continue to be used in the future for technical applications. An important class of these methods is based on the von Kármán-Pohlhausen technique. In these methods the requirement that the boundary layer equations should be satisfied for every fluid element within the boundary layer is abandoned. Instead a plausible form of the velocity profile is assumed. This expression contains a few parameters to be chosen in such a way as functions of x that certain moment equations and compatibility conditions are satisfied. This technique will be illustrated in section 4.2. for the well known Pohlhausen method. In later sections of this chapter some other methods will be mentioned.

4.2. Pohlhausen's method.

In 1921 Pohlhausen published a method [22] which allowed the approximate calculation of laminar boundary layers without suction using the momentum equation (2.16). This method was considerably simplified by Holstein and Bohlen in 1940 [50]; a description of the modified method may be found in chapter 12 of Schlichting's book [7]. In what follows the main characteristics of this method will briefly be discussed.

In the Pohlhausen method the boundary layer thickness δ is assumed to be finite. The velocity profile is approximated by the following quartic polynomial in $\eta = y/\delta$.

$$\bar{u} = u/U = a\,\eta + b\,\eta^2 + c\,\eta^3 + d\,\eta^4 \qquad 0 \leqslant \eta \leqslant 1 \qquad (4.1)$$

$$\bar{u} = 1 \qquad \eta \geqslant 1 \qquad (4.2)$$

The coefficients δ, a, b, c and d are functions of x to be determined from the following relations:

the momentum equation (2.16) for $v_o = 0$ (4.3)

the first compatibility condition (2.10) for $v_o = 0$ (4.4)

the boundary conditions

$$\eta = 0 : \quad \bar{u} = 0 \tag{4.5}$$

$$\eta = 1 : \quad \bar{u} = 1, \quad \frac{\partial \bar{u}}{\partial \eta} = \frac{\partial^2 \bar{u}}{\partial \eta^2} = 0 \tag{4.6}$$

Using the conditions (4.4), (4.5) and (4.6) the coefficients a, b, c and d can be expressed in terms of a parameter λ defined by

$$\lambda = \frac{\delta^2}{\nu} \frac{dU}{dx} \tag{4.7}$$

The parameter λ is then found as function of x from the momentum equation. Equation (4.1) for the velocity profile can be written in the form

$$\bar{u} = F(\eta) + \lambda\ G(\eta) \tag{4.8}$$

with (for $0 \leqslant \eta \leqslant 1$)

$$F(\eta) = 1 - (1 + \eta)(1 - \eta)^3 \tag{4.9}$$

and

$$G(\eta) = \frac{1}{6}\, \eta(1 - \eta)^3 \tag{4.10}$$

Holstein and Bohlen use the parameter

$$\Lambda_1 = \frac{\theta^2}{\nu} \frac{dU}{dx} \tag{4.11}$$

instead of λ . This is attractive since Λ_1 occurs in the momentum equation; Λ_1 is directly related to λ . The shape of the velocity profile depends only on λ , and hence on Λ_1. Therefore the non-dimensional quantities $\ell = \frac{\tau_o \theta}{\mu U}$ and $H = \frac{\delta^*}{\theta}$ can be considered as given functions of Λ_1. Then, using the abbreviations given in the list of symbols, the momentum equation (2.16) may be written in the form

$$\frac{d\bar{\Theta}^2}{d\bar{x}} = \frac{F(\Lambda_1)}{\bar{U}} \tag{4.12}$$

It follows that the boundary layer calculation is reduced to the solution of an ordinary differential equation. The function $F(\Lambda_1)$ is universal for Pohlhausen's method and is given as fig. 4.1; a table of $F(\Lambda_1)$ may be found in [7].

Normally the calculation is started in a stagnation point where $\bar{U} = 0$. To avoid an infinite value for $\frac{d\bar{\Theta}^2}{d\bar{x}}$ it is assumed that in the stagnation point also $F(\Lambda_1) = 0$. Then $\frac{d\bar{\Theta}^2}{d\bar{x}}$ assumes the undetermined value $\frac{0}{0}$; it can be made determinate using ℓ' Hopital's rule (see [7] , chapter 12). An inspection of fig. 4.1 shows that $F(\Lambda_1)$ has a zero for $\Lambda_1 = 0.0770$ which can be chosen to represent the stagnation point. Other important points in fig. 4.1 are $\Lambda_1 = 0$ (flat plate) and $\Lambda_1 = -0.1567$ (separation, $\tau_o = 0$).

Walz [51] has been the first to notice that equation (4.12) can be integrated directly when the relation between $F(\Lambda_1)$ and Λ_1 is of the form

$$F(\Lambda_1) = a_1 - b_1 \Lambda_1 \tag{4.13}$$

Using (4.13) the result of the integration is

$$\bar{U}\,\bar{\Theta}^2 = \frac{a_1}{\bar{U}^{b_1 -1}} \int_o^{\bar{x}} \bar{U}^{b_1 -1}\, d\bar{x} \tag{4.14}$$

where $\bar{x} = 0$ corresponds to the stagnation point. A reasonable approximation of $F(\Lambda_1)$ is obtained for a = 0.470 and b = 6 (see fig. 4.1). From applications of Pohlhausens method it is known that the results are reasonably accurate for favourable pressure gradients ($\Lambda_1 > 0$). However, for adverse pressure gradients ($\Lambda_1 < 0$) the accuracy is rather poor; in general the method predicts separation too late (see [28], chapter 5).

4.3. Other methods using the momentum equation and compatibility conditions.

Following Pohlhausen many authors developed similar methods using other compatibility conditions or different expressions for the velocity

profile. In this section some of these methods will be briefly described. The treatment cannot possibly be exhaustive due to the large number of methods available. Only the methods, to be referred to later, will be mentioned; extensive reviews may be found in [7, 28, 29].
The characteristic features of the methods to be described are collected in table 4.1; in what follows some additional remarks on these methods will be made.

Timman's method. [52] In this method the velocity profile is chosen in such a way that the right asymptotic behaviour for large values of y is obtained. Slight modifications have been introduced by Zaat [53] and Nunnink [54].
Schlichting's method. [55] Here the velocity profile is chosen in such a way that two important cases with and without suction are represented with good accuracy. For these cases the flat plate without suction and the asymptotic suction boundary layer were selected. The expression for the velocity profile, given in table 4.1, reduces to the asymptotic suction profile for $K = 0$ and to $\bar{u} = \sin(\frac{\pi}{6}\eta)$ for $K = -1$; the sine function is used as approximation to Blasius' velocity profile. A disadvantage of the method is that no unique solution is obtained near separation; to overcome this difficulty Schlichting had to introduce a rather arbitrary separation criterion. A critical review of Schlichting's method has been given by Truckenbrodt [56] who at the same time developed a different method.
A new method. The present author designed a method which may be considered as a further development of Schlichting's method. Here a third velocity profile - namely the separation profile of Timman's method - is introduced into the general expression of the velocity profile. A detailed discussion of the new method will be given in chapter 5. The method will be referred to as the "momentum method".
Thwaites' method. [57] An interesting type of method, valid for the no-suction case, has been given by Thwaites. The momentum equation is used - in a form similar to (4.12) - to find the non-dimensional momentum loss thickness $\bar{\Theta}$. It was observed by Thwaites that for this calculation

no necessity exists to specify the velocity profile in advance; all that is needed is a function similar to $F(\Lambda_1)$ of the Pohlhausen method. To obtain this function Thwaites plotted $F(\Lambda_1)$ versus Λ_1 for available exact solutions of the boundary layer equations and selected a linear relationship of the type (4.13) to represent mean values. The values $a_1 = 0.45$ and $b_1 = 6$ give a reasonably good average of the exact solutions. By plotting ℓ and H versus Λ_1 for exact solutions and deducing average curves Thwaites was able also to specify ℓ and H as functions of Λ_1. From the first compatibility condition at the wall (2.10) it follows that for the no-suction case $\Lambda_1 = -m$. Hence, once $\overline{\Theta}$ and Λ_1 are known from the momentum equation as functions of $\overline{x}$ also ℓ, m and H are known. Then, if needed, a velocity profile can be composed which has the right values for ℓ, H and m.
A slight modification of the method has been introduced by Curle and Skan [58]. Due to lack of exact solutions for cases with suction the method cannot be generalised easily to suction problems.

4.4. Methods using the kinetic energy equation in addition to the momentum equation.

The approximate methods, using only the momentum equation, described in section 4.3, do not always give an accurate description of the boundary layer especially near the separation point. To improve upon this, methods have been devised which use the kinetic energy equation (2.21) in addition to the momentum equation. Such methods have been given for instance by Walz [59], Tani [60], Wieghardt [32], Truckenbrodt [61] and most recently by Head [62, 63, 64]. Reviews of these methods may be found in [28] and [29].
The method of Head seems to be the most accurate. In this method the momentum equation (2.15), the kinetic energy equation (2.21) and the first compatibility condition (2.10) are used. A wide range of velocity profiles is defined graphically from which relations between the characteristic boundary layer parameters H, $\overline{H}$, $2D^*$, ℓ and m are derived. These relations are plotted in charts to be used for the boundary layer calculations. Available results of the method show a good agreement with

exact solutions. A disadvantage is the use of charts which makes it somewhat difficult to program the method for automatic computation.

4.5. Possible methods using moment equations of higher order.

It is a disadvantage of all the approximate methods mentioned so far that the accuracy can only be assessed by comparison with exact solutions. In the no-suction case a sufficient number of exact solutions is available for this purpose but the situation is different for suction boundary layers. In the latter case the number of available exact solutions is too small to provide a good check. Such a check is necessary however since a method which works well in the no-suction case will not necessarily be satisfactory in the case of suction. This is caused by the fact that for suction boundary layers a far larger variety of velocity profiles has to be included than in the case of no-suction.
A striking example is given by the Pohlhausen method. If in this method the momentum equation and compatibility condition are modified to include the effect of suction it is found that a complex boundary layer thickness is predicted for the asymptotic suction profile.
In order to acquire confidence in the approximate methods it should be possible to estimate their accuracy without making reference to exact solutions.
The improvement obtained by the use of the kinetic energy equation in addition to the momentum equation suggests that such a method might be constructed by using a whole series of moment equations as defined by equation (2.25) for $k = 0,1,2,..,K$. Then it can be expected that the results obtained converge to the exact solution for $K \rightarrow \infty$. As far as the author is aware no succesful method has been developed along these lines. The practical application of such a method will be cumbersome for large values of K. To see this let the velocity profile be defined by

$$\frac{u}{U} = \bar{u} = \sum_{n=0}^{N} a_n F_n(y) \qquad (4.15)$$

The δ_{k+2} occurring in the moment equations (2.25) then are algebraic expressions of degree k+2 in the coefficients a_n defined by equation

(2.26). The step by step solution of the moment equations requires the determination of the a_n once the δ_{k+2} are known for all values of k to be used. This leads to the solution of a set of non-linear algebraic equations in a_n. For K=0 essentially the Pohlhausen method appears which in its simplest form requires the solution of one quadratic equation. For K=1 a method like Head's is obtained, which requires the simultaneous solution of a quadratic and a cubic equation. In a method for which K=2 a quartic equation would be added, etc. This situation makes the application of this method difficult for large values of K.

To obtain a workable method the moments should be defined in such a way that the moment equations can be written in the form

$$\frac{d\,J_k}{dx} = M_k \tag{4.16}$$

where the J_k are linear functions of the parameters specifying the velocity profile. In this case the step by step calculation requires only the solution of a set of linear algebraic equations.

In chapter 7 a method will be described which is designed along these lines. From applications of this method, to be given in chapter 8, it appears that the results converge to the exact solution when the number of moment equations is increased.

5. An approximate method using the momentum equation for the calculation of boundary layers with and without suction.

5.1. Introductory remarks.

In this chapter an approximate boundary layer calculation method, designed for application to suction problems will be described. A preliminary version of the method has been given in [65]. The essential point of the method is that an expression for the velocity profile is chosen which contains three important velocity profiles as special cases. These profiles are selected to be

the boundary layer on a flat plate without suction,

the asymptotic suction profile,

and the separation profile from the method of Timman.

The expression contains three parameters to be determined as functions of x from the momentum equation and the first and second compatibility condition at the wall. The method can be regarded as an extension of Schlichting's method discussed in section 4.3; the extension consists of adding the separation profile and the second compatibility condition. The results of the method are in good agreement with exact solutions without suction and with weak suction. For large values of the suction velocity the method breaks down because the expression selected for the velocity profile is not flexible enough to represent the wide class of velocity profiles, needed under greatly varying suction conditions. However, in most of the cases to be discussed in the present work the suction velocities will not be so high as to raise serious difficulties. The accuracy of the method may be assessed from the examples to be given in the present chapter and in chapters 8, 10 and 11.

5.2. The expression for the velocity profile and related parameters.

For the velocity profile the following expression is assumed:

$$\overline{u} = \frac{u}{U} = F_1(\eta) + K\, F_2(\eta) + L\, F_3(\eta) \tag{5.1}$$

In this expression K and L are shape parameters; η is the non-dimensional wall distance defined by

$$\eta = \frac{y}{\sigma} \tag{5.2}$$

in which σ is a scaling factor related to the boundary layer thickness. The functions F_1, F_2 and F_3 are chosen in such a way that some special boundary layer velocity profiles are reproduced as accurately as possible for certain values of K and L. The functions F_1, F_2 and F_3 are defined by the equations (5.3) - (5.9)

$$F_1(\eta) = f_1(\eta) \tag{5.3}$$

$$F_2(\eta) = f_1(\eta) - f_2(\eta) \tag{5.4}$$

$$F_3(\eta) = f_1(\eta) - f_3(\eta) \tag{5.5}$$

with

$$f_1(\eta) = 1 - e^{a\eta} \tag{5.6}$$

$$f_2(\eta) = 2\ b\eta - 5(b\eta)^4 + 6(b\eta)^5 - 2(b\eta)^6 \quad \text{for } 0 \leqslant b\eta \leqslant 1 \tag{5.7}$$

$$f_2(\eta) = 1 \quad \text{for} \quad b\eta \geqslant 1 \tag{5.8}$$

$$f_3(\eta) = 1 - e^{-\eta^2} - \tfrac{1}{2}\,\eta^2\, e^{-\eta^2} \tag{5.9}$$

In these equations $\bar{u} = f_1(\eta)$ represents the asymptotic suction profile for $\frac{a}{\sigma} = \frac{v_o}{\nu}$; $f_2(\eta)$ is a good approximation of the Blasius profile (see section 5.4.2.) while $f_3(\eta)$ is the separation profile from Timman's method (section 4.3). The coefficients a and b are scaling factors which later on will be given the values 1.3 and 0.3 respectively. These values were determined in such a way that some important boundary layers different from the three mentioned above, will be reproduced as accurately as possible. This point is discussed in detail in section 5.8. The functions defined by equations (5.3) to (5.9) are shown in figure 5.1 for a = 1.3 and b = 0.3.

Using the expressions (5.3) to (5.9) and the definitions (2.17) and (2.18) for the displacement thickness δ^* and the momentum-loss thickness Θ it is found that

$$\frac{\delta^*}{\sigma} = p_1 + p_2 K + p_3 L \qquad (5.10)$$

and

$$\frac{\theta}{\sigma} = p_4 + p_5 K + p_6 L + p_7 K^2 + p_8 L^2 + p_9 KL \qquad (5.11)$$

The coefficients p in (5.10) and (5.11) are rather complicated expressions in a and b containing error functions. For a = 1.3 and b = 0.3 the following values are obtained

$$\begin{array}{lll} p_1 = 0.76923 & p_4 = 0.38462 & p_7 = -0.03938 \\ p_2 = -0.18315 & p_5 = -0.01925 & p_8 = -0.10771 \\ p_3 = -0.33855 & p_6 = -0.01817 & p_9 = -0.12361 \end{array} \qquad (5.12)$$

Other important relations, to be used in what follows, are (see also the list of symbols)

$$\Lambda_1 = \bar{\theta}^2 \frac{d\bar{U}}{d\bar{x}} = \frac{\theta^2}{\nu} \frac{dU}{dx} = \frac{\sigma^2}{\nu} \frac{dU}{dx} \left(\frac{\theta}{\sigma}\right)^2 = \ell_1 \left(\frac{\theta}{\sigma}\right)^2 \qquad (5.13)$$

$$_2 = \overline{v_o} . \bar{\theta} = \frac{-v_o \theta}{\nu} = \frac{-v_o \sigma}{\nu} \frac{\theta}{\sigma} = \ell_2 \frac{\theta}{\sigma} \qquad (5.14)$$

$$H = \frac{\delta^*}{\theta} = \frac{\delta^*/\sigma}{\theta/\sigma} \qquad (5.15)$$

$$\ell = \frac{\tau_o \theta}{\mu U} = \frac{\theta}{\sigma} \frac{\tau_o \sigma}{\mu U} = \frac{\theta}{\sigma} \left(\frac{\partial \bar{u}}{\partial \eta}\right)_o = \frac{\theta}{\sigma} \left[\left(\frac{\partial F_1}{\partial \eta}\right)_o + K \left(\frac{\partial F_2}{\partial \eta}\right)_o + L \left(\frac{\partial F_3}{\partial \eta}\right)_o \right]$$

$$= \frac{\theta}{\sigma} \left[a + (a - 2b)K + aL \right] \qquad (5.16)$$

For a = 1.3 and b = 0.3 the last relation becomes

$$\ell = \frac{\theta}{\sigma} (1.3 + 0.7 K + 1.3 L) \qquad (5.17)$$

5.3. The momentum equation and compatibility conditions.

The present method employs the momentum equation (2.16) which, using the abbreviations given in the list of symbols, may be written in the form

$$\frac{d\bar{\Theta}^2}{d\bar{x}} = \frac{2\ell - 2(2+H)\Lambda_1 - 2\Lambda_2}{\bar{U}} = \frac{M}{\bar{U}} \tag{5.18}$$

In addition to (5.18) the first and second compatibility conditions (2.10) and (2.11) are used. These may be written as

$$-\ell_2 \left(\frac{\partial \bar{u}}{\partial \eta}\right)_o = \ell_1 + \left(\frac{\partial^2 \bar{u}}{\partial \eta^2}\right)_o \tag{5.19}$$

$$-\ell_2 \left(\frac{\partial^2 \bar{u}}{\partial \eta^2}\right)_o = \left(\frac{\partial^3 \bar{u}}{\partial \eta^3}\right)_o \tag{5.20}$$

Together with the expressions (5.3) to (5.9) defining the velocity profile, equations (5.19) and (5.20) lead to the following relations between K, L, ℓ_1 and ℓ_2.

$$K = \frac{-a\,\ell_2^{\,2} - (a^2+1)\ell_1\ell_2 + a^3\ell_1 + a^3}{\ell_2^{\,2}(a-2a^2b-2b) + 2\,a^3b\,\ell_2 - a^3} \tag{5.21}$$

$$L = \frac{2\,a^2b\,\ell_2^{\,2} - 2\,a^3b\,\ell_2 + a^2\,\ell_1\ell_2 - a^3\ell_1}{\ell_2^{\,2}(a - 2\,a^2b - 2b) + 2\,a^3b\,\ell_2 - a^3} \tag{5.22}$$

In (5.21) and (5.22) a and b should take the values 1.3 and 0.3 respectively. The boundary condition $\bar{u} = 1$ for $\eta \to \infty$ does not introduce additional relations between the parameters involved because this condition is satisfied already through the special choice for the functions $F_1(\eta)$, $F_2(\eta)$ and $F_3(\eta)$.

5.4. Similar solutions.

5.4.1. General.

For similar boundary layers the velocity profile - if suitably made non-dimensional - has to be independent of the streamwise coordinate x (section 3.1). Then, characteristic boundary layer parameters like ℓ and H become constants. In the present method this requires constant values for K and L and hence also Λ_1, Λ_2 and M should be independent of x.

Elimination of $\bar{\Theta}$ from the following expressions

$$\Lambda_1 = \bar{\Theta}^2 \frac{d\bar{U}}{d\bar{x}} \tag{5.23}$$

and

$$\frac{d\bar{\Theta}^2}{d\bar{x}} = \frac{M}{\bar{U}} \tag{5.24}$$

leads to

$$\frac{\Lambda_1 \frac{d^2\bar{U}}{d\bar{x}^2}}{\frac{d\bar{U}}{d\bar{x}}} + \frac{M}{\bar{U}} \frac{d\bar{U}}{d\bar{x}} = 0 \tag{5.25}$$

Equation (5.25), in which M and Λ_1 are constants, defines the functions $\bar{U}(\bar{x})$ for which similar solutions may be obtained. Integration of (5.25) gives

$$\Lambda_1 \ln \left| \frac{d\bar{U}}{d\bar{x}} \right| + M \ln \bar{U} = \text{constant}$$

and after rearrangement

$$\text{constant} \,.\, \bar{U}^{\frac{M}{\Lambda_1}} \, d\bar{U} = d\bar{x} \tag{5.26}$$

A second integration leads to

$$\bar{U} = c_1 \, e^{c_2 \bar{x}} \qquad \text{if} \qquad M = -\Lambda_1 \tag{5.27}$$

and to

$$\bar{U} = u_1 \, \bar{x}^{m_1} \qquad \text{if} \qquad M \neq -\Lambda_1 \tag{5.28}$$

In (5.27) and (5.28) c_1, c_2 and u_1 are irrelevant integration constants; m_1 is a constant defined by

$$m_1 = \frac{\Lambda_1}{\Lambda_1 + M} \tag{5.29}$$

Equations (5.27) and (5.28) show, that the present approximate method leads to the same permissible pressure distributions for the occurrence of similar solutions as the exact theories, discussed in section 3.2. In what follows only the wedge-type flows, defined by (5.28) will be discussed further.

The permissible suction distribution is deduced from the requirement that also Λ_2 should be a constant. Then from (5.23) and

$$\Lambda_2 = \bar{v}_o \cdot \bar{\theta} \tag{5.30}$$

it follows, through elimination of $\bar{\theta}$, that

$$\bar{v}_o = \Lambda_2 \sqrt{\frac{\frac{d\bar{U}}{d\bar{x}}}{\Lambda_1}} \tag{5.31}$$

With (5.28) this leads to

$$\bar{v}_o = \Lambda_2 \sqrt{\frac{m_1 u_1}{\Lambda_1}} \; \bar{x}^{\frac{m_1 - 1}{2}} \tag{5.32}$$

which reproduces the exact result given by equation (3.13). In view of further use (5.32) may be rewritten in the form

$$\frac{-v_o}{U} \sqrt{\frac{Ux}{\nu}} = \frac{\Lambda_2}{\sqrt{\Lambda_1 + M}} \tag{5.33}$$

5.4.2. The similar boundary layers for $\bar{U} = u_1 \, \bar{x}^{m_1}$ without suction.

For the similar boundary layer flows corresponding to (5.28) without suction Hartree's velocity profiles are obtained. (section 3.1.2.). In the present method these boundary layers are obtained as follows.
If suction is absent $\ell_2 = 0$ and the boundary layer parameters become functions of ℓ_1 only; they can easily be calculated using the formulae given in sections 5.2 and 5.3. The value of Hartree's parameter β then follows from (5.29) and (3.4).
Results of the calculations are given in fig. 5.2 where also a comparison

is made with the exact solution. Velocity profiles are shown in fig. 5.3 for the flat plate ($\beta = 0$) and the plane stagnation point ($\beta = 1$). Numerical values for some characteristic boundary layer parameters have been collected in table 5.1.

5.4.3. The plane stagnation point flow with suction.

It follows from section 3.1.4 that for the plane stagnation point flow $m_1 = 1$; then equation (5.29) shows that M should be zero. Due to this restriction only one independent parameter remains for which ℓ_2 will be selected. Inspection of (5.32) shows that, as a consequence of $m_1 = 1$, v_o is independent of $\bar{x}$. Some results of the present method for this case are collected in table 5.2; they are plotted as a function of $\lambda_2 = \frac{-v_o}{U} \sqrt{\frac{Ux}{\nu}}$ in fig. 5.4 and compared to exact solutions by Schlichting and Bussmann. (quoted by Mangler [37]).
Comparison with section 3.1.5 shows that both the exact and approximate solution tend to the asymptotic suction layer for $\lambda_2 \rightarrow \infty$.

5.4.4. The flat plate with $v_o \backsim x^{-\frac{1}{2}}$.

For a flat plate U is constant and hence from $\ell_1 = \frac{\sigma^2}{\nu} \frac{dU}{dx}$ it follows that $\ell_1 = 0$; equation (5.28) shows that also $m_1 = 0$. Equation (5.32) then indicates that for similar boundary layer flows v_o should be proportional to $x^{-\frac{1}{2}}$. From $\ell_1 = 0$ it follows that the boundary layer parameters are functions of ℓ_2 only in this case.
Results are given in fig. 5.5 and compared to exact solutions by Schlichting and Bussmann (quoted by Mangler [37]) and Thwaites [66]; Also for this case the boundary layer tends to the asymptotic suction layer for $\lambda_2 \rightarrow \infty$.

5.5. Step by step calculation of the boundary layer starting from given initial conditions.

In the boundary layer calculations it is assumed that $\bar{U}$, $\frac{d\bar{U}}{d\bar{x}}$ and $\bar{v}_o$ are known functions of $\bar{x}$. Furthermore at an initial station $\bar{x} = \bar{x}_o$ a starting

value for $\overline{\Theta}$ should be known. (The determination of this starting value will be discussed in section 5.6).
For the step by step integration of the momentum equation (5.18) it is necessary to find M once $\overline{\Theta}$ is known. This requires the knowledge of ℓ_1 and ℓ_2 which are determined by equations (5.13) and (5.14):

$$\Lambda_1 = \ell_1 \left(\frac{\Theta}{\sigma}\right)^2 \qquad (5.34)$$

$$\Lambda_2 = \ell_2 \; \frac{\Theta}{\sigma} \qquad (5.35)$$

where Λ_1 and Λ_2 are known from $\Lambda_1 = \overline{\Theta}^2 \dfrac{d\overline{U}}{d\overline{x}}$ and $\Lambda_2 = \overline{v}_o . \overline{\Theta}$. The relations between ℓ_1, ℓ_2 and $\frac{\Theta}{\sigma}$ are rather complicated (see eqs. (5.11), (5.21) and (5.22) and it is not easy to solve (5.34) and (5.35) directly for ℓ_1 and ℓ_2. However, it was found that a simple iterative procedure can be used for this.
Starting from known values of Λ_1 and Λ_2 and an estimated value of $\frac{\Theta}{\sigma}$, values of ℓ_1 and ℓ_2 are found from (5.34) and (5.35). Then K and L follow from (5.21) and (5.22) which determine an improved value of $\frac{\Theta}{\sigma}$ using (5.11). Except very close to separation this process converges rapidly; in calculated typical examples each step in the iteration procedure increased the number of exact significant figures of $\frac{\Theta}{\sigma}$ by one. The iteration should be stopped as soon as two consecutive values of $\frac{\Theta}{\sigma}$ agree within a certain prescribed tolerance. Once this accuracy is achieved $\frac{\Theta}{\sigma}$, ℓ_1 and ℓ_2 are known, satisfying (5.13) and (5.14). Then K and L follow from (5.21) and (5.22); $\frac{\delta^*}{\sigma}$ from (5.10); H from (5.15) and ℓ from (5.17). Now, all factors occurring in M are known and hence $\overline{\Theta}$ at the next station can be found, etc. From the known values of K and L all boundary layer parameters and the velocity profile are known as functions of $\overline{x}$.
In all applications of the method, to be described in the present report, the iteration procedure outlined above was used. The step by step integration was performed by means of the four point Runge-Kutta method. In all cases the calculations were made on the Telefunken TR-4 digital computer of Delft Technological University.

It would be possible to speed up the calculation considerably if M were known directly as a function of Λ_1 and Λ_2 since then the iteration process could be left out. This can be achieved by plotting M on a large scale as function of Λ_1 and Λ_2 according to the formulae given in section 5.2 and 5.3. Fig. 5.7 shows a small scale version of such a plot. For use on a digital computer it would be necessary to feed the graph into the computer, either by fitting approximation formulae to the curves or by reading a table into the computer's memory. This method has not been used in the present work; for hand computation it would be an advantage to use the graph however.

A discussion of fig. 5.7 will be appropriate at this stage since it brings out clearly some characteristic features of the present method. The curve for $\Lambda_2 = 0$ corresponds to the case of zero suction and should be compared to fig. 4.1 for Pohlhausens $F(\Lambda_1)$ discussed in section 4.2; this will be pursued further in section 5.7.
Point P_1 corresponds to $K = -1$, $L = 0$ and hence represents the flat plate without suction; P_2 is given by $K = 0$, $L = 0$ and hence represents the asymptotic suction profile. Furthermore P_3 represents Timman's separation profile without suction for which $K = 0$ and $L = -1$.
Certain curves in fig. 5.7 represent a class of boundary layers. It has been mentioned already that all boundary layers without suction fall on the curve P_3P_4 for which $\Lambda_2 = 0$. Similarly P_1P_2, for which $\Lambda_1 = 0$, covers all flat plate boundary layers with arbitrary suction distributions. All plane stagnation point flows with suction, discussed in section 5.4.3 fall along P_2P_4.
The graph is closed on the upper left hand side by a curve which for $\Lambda_2 < 0.30$ denotes separation. For $\Lambda_2 > 0.30$ separation is not yet reached on the bounding curve but here double valued functions start to appear. To avoid this complication the calculations are deliberately stopped when this line is reached. Using the iteration process described above, the calculation stops automatically because the iteration fails to converge in this region. This difficulty is similar to the one mentioned in section 4.3 for Schlichting's method; in the present method the complication arises at larger values of Λ_2 than for

Schlichting's method.

From the similar solutions, already discussed and from some further examples to be given in chapters 8, 10 and 11 it is found that the present method can be used with some confidence for $0 \leqslant \Lambda_2 \leqslant 0.5$. This is not surprising since in the points P_1, P_2 and P_3 of fig. 5.8 this was ensured a priori by the choice for the functions F_1, F_2 and F_3. Furthermore a and b have been given such values (see also section 5.8) that the results along P_1P_2 and $P_3P_1P_4$ became as accurate as possible. The remarks given above about the accuracy of the method are not applicable to cases where large discontinuities in pressure gradient or suction velocity occur; for such problems the accuracy may be rather poor (cf. section 8.12).

5.6. Determination of the starting value for $\overline{\Theta}$.

The boundary layer calculation has to start in the stagnation point where $\overline{U} = 0$. Hence it follows from (5.18) that in the stagnation point $\frac{d\overline{\Theta}^2}{d\overline{x}} \rightarrow \infty$ unless $M = 0$. This means that the boundary layer starts as one of the plane stagnation point flows discussed in section 5.4.3.

From the relations given in table 5.2 and fig. 5.4 the starting values can be determined if $\overline{v}_o\left(\frac{d\overline{U}}{d\overline{x}}\right)^{-1}$ in the stagnation point is known. The value of $\overline{\Theta}$ follows directly from the given value of Λ_1 by using $\Lambda_1 = \overline{\Theta}^2 \frac{d\overline{U}}{d\overline{x}}$. However, $\frac{d\overline{\Theta}^2}{d\overline{x}}$ takes the undeterminate value $\frac{0}{0}$; this can be made determinate by applying L'Hopital's rule to eq. (5.18). The result is

$$\frac{d\overline{\Theta}^2}{d\overline{x}} = \frac{\overline{\Theta}^2 \frac{d^2\overline{U}}{d\overline{x}^2} \frac{\partial M}{\partial \Lambda_1} + \overline{\Theta} \cdot \frac{d\overline{v}_o}{d\overline{x}} \cdot \frac{\partial M}{\partial \Lambda_2}}{\frac{d\overline{U}}{d\overline{x}} \left(1 - \frac{\partial M}{\partial \Lambda_1}\right) - \frac{\overline{v}_o}{2\overline{\Theta}} \frac{\partial M}{\partial \Lambda_2}} \qquad (5.36)$$

where all values in (5.36) are to be taken in the stagnation point. In general suction will not be applied near the stagnation point because there is no tendency for transition or separation in this region. For the no-suction case (5.36) takes a simple form analogous to a relation obtained for the Pohlhausen method ([7], chapter 12).

$$\left(\frac{d\bar{\Theta}^2}{d\bar{x}}\right)_{st} = \frac{\bar{\Theta}^2 \dfrac{d^2\bar{U}}{d\bar{x}^2} \dfrac{\partial M}{\partial \Lambda_1}}{\dfrac{d\bar{U}}{d\bar{x}}\left(1 - \dfrac{\partial M}{\partial \Lambda_1}\right)} = \frac{\Lambda_1 \dfrac{d^2\bar{U}}{d\bar{x}^2} \dfrac{\partial M}{\partial \Lambda_1}}{\left(\dfrac{d\bar{U}}{d\bar{x}}\right)^2 \left(1 - \dfrac{\partial M}{\partial \Lambda_1}\right)} \tag{5.37}$$

or with $\Lambda_1 = 0.08572$ and $\dfrac{\partial M}{\partial \Lambda_1} = -4.844$ in the stagnation point

$$\left(\frac{d\bar{\Theta}^2}{d\bar{x}}\right)_{st} = -0.07105 \frac{\left(\dfrac{d^2\bar{U}}{d\bar{x}^2}\right)_{st}}{\left(\dfrac{d\bar{U}}{d\bar{x}}\right)^2_{st}} \tag{5.38}$$

In general the step by step calculation will require short steps near the stagnation point; moreover for experimentally determined pressure distributions $\bar{U}$ and its derivatives will not be known with great accuracy near the stagnation point. Therefore it is recommended to start the step by step solution a small distance $\bar{x}_o$ away from the stagnation point. The starting value for $\bar{\Theta}$ may then be found by applying one of the similar - or series solutions from $\bar{x} = 0$ to $\bar{x}_o$. For the case of zero suction the simple formulae (5.40) to be discussed in section 5.7 should be used.

It was found that for the typical case of an airfoil without suction the solution at larger distances from the stagnation point is rather insensitive to the starting values used. Therefore it appears that the calculation of the starting values may be rather inaccurate.

5.7. Simplification of the method for the no-suction case.

When no suction is applied eq. (5.21) and (5.22) show that $K = -1-\ell_1$ and $L = \ell_1$; this leads to a considerable simplification because only one parameter (ℓ_1) occurs and the method becomes analogous to the Pohlhausen method. Important boundary layer parameters for $\ell_2 = 0$ have been given in table 5.3 as a function of ℓ_1; the results are plotted in fig. 5.6 as a function of Λ_1. Assuming a linear relationship between M and Λ_1 of the form

$$M = a_1 - b_1 \Lambda_1 \tag{5.39}$$

(compare Walz, section 4.2) the momentum equation (5.18) can be integrated from $\bar{x}_1$ to $\bar{x}_2$ giving

$$(\bar{U}^{b_1} \bar{\Theta}^2)_{\bar{x}_2} - (\bar{U}^{b_1} \bar{\Theta}^2)_{\bar{x}_1} = a_1 \int_{\bar{x}_1}^{\bar{x}_2} \bar{U}^{b_1 - 1} \, d\bar{x} \tag{5.40}$$

From an inspection of fig. 5.6 it is seen that for the present method the best values of a_1 and b_1 are as follows

region of applicability	a_1	b_1
near stagnation point ($M = 0$)	0.415	4.84
from stagnation point ($M = 0$) to pressure minimum ($\Lambda_1 = 0$)	0.437	5.10
from pressure minimum ($\Lambda_1 = 0$) to separation ($\Lambda_1 = -0.087072$)	0.437	6

For engineering applications the results will be sufficiently accurate if the values $a_1 = 0.437$ and $b_1 = 6$ are used all the way from stagnation point to separation.

Then, if the calculation is started in the stagnation point eq. (5.40) reduces to

$$\bar{U}^6 \bar{\Theta}^2 = 0.437 \int_0^{\bar{x}} \bar{U}^5 \, d\bar{x} \tag{5.41}$$

5.8. Determination of the best values for a and b.

5.8.1. Determination of b.

In section 5.2 it was mentioned that a and b should take the values 1.3 and 0.3 respectively to obtain the best overall results of the present method. This may be discussed now in some more detail.

For boundary layer flows without suction it was found in section 5.7 that $K = -1-\ell_1$ and $L = \ell_1$. Hence (5.1) reduces to

$$\bar{u} = (1+\ell_1)\, f_2(\eta) - \ell_1\, f_3(\eta) \tag{5.42}$$

showing that $f_1(\eta)$ and hence the coefficient a no longer occur in the expression for the velocity profile. Therefore the results of the present method, for boundary layers without suction, only depend on b.
For $\ell_1 = -1$ only the separation profile $f_3(\eta)$ is obtained, which is independent of b. For $\ell_1 = 0$ only $f_2(\eta)$ remains which gives the flat plate boundary layer without suction. The expressions (5.7) and (5.8) for $f_2(\eta)$ contain b but only as a scaling factor for y which does not influence the non-dimensional boundary layer parameters like ℓ, m, H etc. Hence both for $\ell_1 = 0$ and -1 the results of the present method are independent of b. For other values of ℓ_1 however they depend rather strongly on b. The best value of b was defined as the value which leads to the best representation of the Hartree profiles (cf. section 5.4.2). It was found that b = 0.30 should be taken to obtain this.

5.8.2. Determination of a.

Once a value for the scaling factor b has been chosen only the scaling factor a remains to be determined; this was done as follows.
For the flat plate with constant suction velocity $-v_o$ an exact solution has been given by Iglisch [67]. this solution will be discussed in chapter 8. The present approximate method was used to calculate the boundary layer for this case, using different values for a. By comparison with the exact solution it was found that a = 1.30 shows the best overall results.

6. Phaseplane description of the boundary-layer flow between non-parallel plane walls.

6.1. Introductory remarks.

From the examples discussed in chapter 5 it follows that the behaviour of boundary-layer flows strongly depends on the streamwise pressure gradient and the suction velocity.

Another important example which may illustrate this is the viscous flow between non-parallel plane walls. This flow has been discussed already in 1915 and 1916 by Jeffery [23] and Hamel [24] respectively using the Navier-Stokes equations. From their work it is known that in the case of inflow between non-porous walls the Navier-Stokes equations admit a boundary layer type solution for which the radial velocity component becomes practically constant at large distances from the wall.

For inflow between impervious walls such a boundary layer type solution is also allowed by the boundary layer equations. This solution was given in closed form by Pohlhausen in 1921 [22]; it will be discussed further in section 6.3.

For outflow between diverging walls it is only possible to obtain boundary layer type solutions in case a sufficient amount of suction at the wall is applied.

This characteristic difference between the cases of inflow and outflow becomes very clear when the flow is studied in a "phase plane" where shear τ is plotted versus the velocity component u parallel to the wall.

The phase plane concept is known from the theory of oscillations of non-linear autonomous systems with one degree of freedom where speed is plotted versus displacement. These oscillations are described by a second order ordinary differential equation in the variables displacement x and time t of the form

$$\frac{d^2x}{dt^2} + g(x, \frac{dx}{dt}) = 0 \qquad (6.1)$$

As the time t does not appear explicitly in this equation it can be eliminated between (6.1) and

$$y = \frac{dx}{dt} \tag{6.2}$$

where y denotes the speed.

The resulting equation is of the form

$$\frac{dy}{dx} = \frac{P(x,y)}{Q(x,y)} \tag{6.3}$$

Singular points of this equation occur for values of x and y where both P and Q vanish; the singular points correspond to equilibrium positions of the oscillation. The type of singularity determines the character of the stability (or instability) of the oscillation.

A general theory of equation (6.3) has been given by Poincaré [68]; reviews of this theory may be found for instance in the books by Minorsky [69] and Stoker [70].

If the origin of a Cartesian coordinate system coincides with the singular point under investigation equation (6.3) may be written in the form

$$\frac{dy}{dx} = \frac{ax + by + P_1(x,y)}{cx + dy + Q_1(x,y)} \tag{6.4}$$

where $P_1(o,o) = Q_1(o,o) = 0$. If P_1 and Q_1 vanish like x^2+y^2 when x and y tend to zero and if furthermore $ad - bc \neq 0$ the type of singularity is determined by the simpler equation

$$\frac{dy}{dx} = \frac{ax + by}{cx + dy} \tag{6.5}$$

A classification of the singularities may then be given in terms of the constants a, b, c and d (see for instance Stoker [70]) and hence the different kinds of singularities of (6.3) may be determined without actually solving the equation.

In the following section it will be shown that for the flow between non-parallel plane walls the boundary layer equations can be reduced to the form (6.1) so that the phase plane method may be used to study the flow problem. It follows also that the singular points correspond to the edge of the boundary layer; solutions of the boundary layer type will only occur when the singularity is a saddle point or a stable node. The kind of singularity will depend on the amount of suction or blowing; it is found for instance that for outflow between diverging walls a minimum amount of suction has to be exceeded before a boundary layer type solution will be possible.

A similar treatment may be given for the full Navier-Stokes equations; the results are essentially the same as for the boundary layer equations. In some cases it is even possible to transform the Navier-Stokes equations into the boundary-layer equations by introducing suitable new variables; only the boundary conditions remain different. This difference in boundary conditions vanishes when the Reynoldsnumber becomes large and the solutions of the Navier-Stokes equations then tend to those of the boundary layer equations. In this thesis only the results for the boundary layer equations will be given. A more detailed review of this work, together with the phase plane description applied to the Navier-Stokes equations, may be found in [71].

As far as the author is aware, the only other phase plane representation of viscous flow has been given by Ku [72] who discussed the boundary layer flow for the flat plate and the plane stagnation point. As the equations (3.14) and (3.20) describing these flows are of the third order a phase space is needed instead of a phase plane. Since the general theory for singularities in a three dimensional space is more complicated than for the two-dimensional problem, Ku was unable to establish a relation between the types of singularities and the character of the flow.

6.2. The boundary layer equations for the flow between non-parallel plane walls.

For radial flow between non-parallel plane walls (fig. 6.1) the potential flow velocity distribution is given by

$$U = u_1 \, x^{-1} \tag{6.6}$$

where u_1 is a constant. For $u_1 > 0$ equation (6.6) represents outflow from a two-dimensional source at $x = 0$; for $u_1 < 0$ inflow into a sink is obtained. It has been mentioned already in section 3.1.1 that for $U = u_1 \, x^{-1}$ the boundary layer equation (2.7) and the continuity equation (2.5) admit a similar solution. To obtain this solution the non-dimensional wall distance η is introduced with

$$\eta = \frac{y}{x}\sqrt{\frac{|u_1|}{\nu}} \tag{6.7}$$

and the non-dimensional streamfunction $f(\eta)$ by

$$\psi = \sqrt{\nu\,|u_1|}\;f(\eta) - \lambda\sqrt{\nu|u_1|}\;\ln x \tag{6.8}$$

In equation (6.8) λ is a constant which determines the suction velocity at the wall according to equation 6.15.

With (3.7) and (6.8) the continuity equation (2.5) is satisfied; the velocity components u and v follow from

$$u = \frac{|u_1|}{x}\,f'(\eta) = |U|\;f'(\eta) \quad \text{or} \quad \bar{u} = \frac{u}{|U|} = f'(\eta) \tag{6.9}$$

$$v = \sqrt{\nu|u_1|}\;\frac{\eta}{x}\,f'(\eta) + \frac{\lambda}{x}\sqrt{\nu|u_1|} \tag{6.10}$$

In (6.9), (6.10) and subsequent equations in this chapter primes denote differentiation with respect to η.

Introduction of (6.9) and (6.10) in the boundary layer equation (2.7) leads to

$$f''' - \lambda\,f'' + (f')^2 - 1 = 0 \tag{6.11}$$

Since f does not occur in (6.11) the order of this equation may be reduced through the introduction of $f' = \bar{u}$. The resulting equation is

$$\bar{u}'' - \lambda\,\bar{u}' + \bar{u}^2 - 1 = 0 \tag{6.12}$$

Boundary conditions for solutions of (6.12) are at the wall

$$\eta = 0 : \bar{u} = 0 \tag{6.13}$$

and at the edge of the boundary layer $\eta \to \infty$:

$$\left.\begin{array}{lll} \bar{u} \to +1 & \text{for outflow} & (u_1 > 0) \\ \bar{u} \to -1 & \text{for inflow} & (u_1 < 0) \\ \bar{u}' \to 0 & \text{both for outflow and inflow} & \end{array}\right\} \tag{6.14}$$

It follows from (6.10) that the normal velocity at the wall ($\eta = 0$) is given by

$$v_o = \frac{\lambda}{x} \sqrt{\nu \, |u_1|} \tag{6.15}$$

This equation shows that v_o should be inversely proportional to x to obtain similar solutions; blowing occurs for $\lambda > 0$ and suction for $\lambda < 0$.

6.3. The non-porous wall ($\lambda = 0$).

For the non-porous wall ($\lambda = 0$) equation (6.12) can easily be integrated after multiplication with $2\,\bar{u}'$. The result is

$$(\bar{u}')^2 + \frac{2}{3}\,\bar{u}^3 - 2\,\bar{u} = A \tag{6.16}$$

where A is an integration constant.
For inflow the boundary conditions (6.14) at the edge of the boundary layer require that $A = +\frac{4}{3}$. Then it follows from (6.16) that at the wall $(\bar{u}')^2 = \frac{4}{3}$; hence the non-dimensional shear stress at the wall is given by $\bar{u}'(o) = -2/\sqrt{3}$. The negative root is taken because in the present coordinate system both the velocity and shear stress are negative for the case of inflow.
For outflow the conditions (6.14) at the edge of the boundary layer lead to $A = -\frac{4}{3}$. However, from (6.16) it follows that A should be non-negative to obtain a real value for the skin friction at the wall ($\bar{u} = 0$). Hence it is concluded that (6.16) does not allow a real boundary layer type solution for outflow.
The solution for inflow with $A = +\frac{4}{3}$ can be written in the forms

$$\frac{d\bar{u}}{d\eta} = \bar{u}' = -\sqrt{\frac{4}{3} + 2\,\bar{u} - \frac{2}{3}\,(\bar{u})^3} \tag{6.17}$$

$$\eta = -\int_o^{\bar{u}} \frac{d\bar{u}}{\sqrt{\frac{4}{3} + 2\,\bar{u} - \frac{2}{3}\,\bar{u}^3}} \tag{6.18}$$

Again the minus-signs in (6.17) and (6.18) are introduced since for the case of inflow both $\bar{u}$ and $\bar{u}'$ are negative. Integration of (6.18) leads to the following expression for the velocity profile

$$-\bar{u} = 3 \text{ tgh}^2 \left[\frac{\eta}{\sqrt{2}} + 1.146\right] - 2 \qquad (6.19)$$

A graph of the velocity profile is shown in fig. 6.2. The solution (6.19) was obtained by Pohlhausen in 1921 [22]. (see also [7], chapter 9.b).

That a corresponding solution for outflow does not exist can easily be demonstrated by studying equation (6.12) in the phase plane. Introducing the non-dimensional shear stress $\bar{\tau}$ by

$$\bar{\tau} = \bar{u}' = \frac{d\bar{u}}{d\eta} \qquad (6.20)$$

equation (6.12) may be written, for $\lambda = 0$, in the form

$$\frac{d\bar{\tau}}{d\eta} = 1 - \bar{u}^2 \qquad (6.21)$$

Elimination of η between (6.20) and (6.21) leads to the following first order differential equation

$$\frac{d\bar{\tau}}{d\bar{u}} = \frac{1-\bar{u}^2}{\bar{\tau}} \qquad (6.22)$$

Since equation (6.22) is of the form (6.3) it can easily be studied using Poincaré's general theory. Singular points are obtained for $\bar{\tau} = 0$ and $\bar{u} = -1$ or $+1$; these points in the phase plane correspond to the edge of the boundary layer in the physical plane for inflow and outflow respectively. Solutions of (6.22) are easily found to be

$$\bar{\tau}^2 = 2\,\bar{u} - \frac{2}{3}\,\bar{u}^3 + A \qquad (6.23)$$

where A is an arbitrary integration constant. Integral curves for different values of A are shown in fig. 6.3. These trajectories were obtained by solving (6.12) on an analog computer for different initial conditions; the curves in fig. 6.3 were drawn by a plotting machine coupled to the analog computer. Arrows in fig. 6.3 indicate the direction in which the trajectories are traversed with increasing wall distance η. This direction follows from (6.20) which shows that η increases with $\bar{u}$ when $\bar{\tau}$ is positive.

The singularity at (-1,0) in the phase-plane is a saddle point; it corresponds to the edge of the boundary layer for inflow. At (+1,0) a center occurs which represents the edge of the boundary layer for outflow.

A solution of (6.22) which satisfies the boundary conditions (6.13) and (6.14) should produce a trajectory in the phaseplane connecting a point on the $\bar{\tau}$-axis ($\eta = \bar{u} = 0$) with one of the singularities. It follows from fig. 6.3 that such a solution may be found for inflow; it is defined by the trajectory PS for which $A = +\frac{4}{3}$. This trajectory clearly represents Pohlhausen's solution (6.17).

The boundary layer velocity profile follows from

$$\eta = \int_0^{\bar{u}} \frac{d\bar{u}}{\bar{\tau}} \tag{6.24}$$

it can easily be produced by the analog computer. The velocity profile obtained in this way is shown in fig. 6.4 together with the profiles corresponding to some adjacent trajectories in fig. 6.3. The figure shows that Pohlhausen's solution is a unique one. It should also be noted that the solutions of (6.22) for the case of inflow show the same behaviour as the Hartree solutions for the Falkner-Skan equation in case $\beta > 0$ (cf. section 3.1.2).

It is clear from fig. 6.3 that no boundary layer type solution can be found for outflow because (+1,0) is an isolated singular point. It will be shown in the next section that for outflow boundary layer type solutions may be found only if a sufficient amount of suction is applied at the wall.

6.4. The effects of suction and blowing ($\lambda \neq 0$).

For $\lambda \neq 0$ the walls of the channel should be porous giving a normal velocity distribution in accordance with equation 6.15. This equation shows that there is suction at one wall and blowing at the other one with a normal velocity inversely proportional to x. In what follows only the lower wall will be considered for which $\lambda < 0$ or $\lambda > 0$ means suction or blowing respectively. A solution of (6.12) in closed form can not be found for $\lambda \neq 0$. According to Mangler [37] numerical solutions have been obtained by Holstein [73]; detailed numerical results will not be given in the present work however. Instead of this, equation (6.12) will be studied in the phase plane giving a better insight into the structure of the equation.

Introducing $\bar{\tau} = \frac{d\bar{u}}{d\eta}$ and eliminating η from (6.20) and (6.12) leads to the following equation

$$\frac{d\bar{\tau}}{d\bar{u}} = \frac{\lambda\bar{\tau} + 1 - \bar{u}^2}{\bar{\tau}} \tag{6.25}$$

Equation (6.25) is again of the type (6.3) and hence can easily be studied using Poincaré's theory. For all values of λ the singular points are found at $\bar{\tau} = 0$, $\bar{u} = \pm 1$ and hence are the same as in the no-suction case ($\lambda = 0$). It is easily found that the singular point (-1,0), representing the edge of the boundary layer for inflow, is always a saddle point irrespective of the amount of suction or blowing. The type of the singularity at (+1,0), corresponding to the edge of the boundary layer for outflow, depends on the value of λ according to table 6.1.

Phase plane portraits for different values of λ, obtained from the analog computer, are shown in fig. 6.5.

Since the singularity at (-1,0) is always a saddle point there is a unique boundary layer type solution for the case of inflow irrespective of the amount of suction or blowing. These solutions correspond to the trajectories connecting the $-\bar{\tau}$ axis with the singularity (-1,0). The corresponding velocity profiles are shown in fig. 6.6 for different values of λ.

A boundary layer type solution for outflow would require a trajectory in the phase plane connecting some point on the $+\bar{\tau}$-axis with the singularity (+1,0). Fig. 6.5 shows that for blowing ($\lambda > 0$) all trajectories lead away from the singular point. Hence, a boundary layer type solution is not possible for outflow with blowing at the wall. From section 6.3 it is known already that also for the impervious wall ($\lambda = 0$) no solution is possible.

For suction at the wall ($\lambda < 0$) an infinity of solutions exists; however not all these solutions are physically acceptable. For $-2\sqrt{2} < \lambda < 0$ the singularity at (+1,0) is a spiral point which produces velocity profiles of the type shown in fig. 6.7. In this case $\bar{u}$ approaches 1 in an oscillatory manner which is physically not acceptable. With increasing intensity of suction the spiral changes into a stable node for $\lambda \leqslant -2\sqrt{2}$; the corresponding velocity profiles are of the type shown in fig. 6.8. Some of the velocity profiles have an overshoot and hence are rejected as physically unacceptable. There remains however an infinity of solutions for which $\bar{u} \longrightarrow 1$ from below; it is not clear on physical grounds which of these solutions should be selected as the relevant one. This situation is analogous to the problem encountered by Hartree in his study of solutions of the Falkner-Skan equation (3.10) for $\beta < 0$ (see section 3.1.2). To obtain a unique solution Hartree introduced the extra condition that the relevant solution is the one for which $\bar{u} \longrightarrow 1$ as fast as possible without making an overshoot. If this "Hartree condition" is also accepted for the present problem it follows that the steeper main branch of the stable node should be used (fig. 6.9). Some further arguments in favour of Hartree's choice can be produced in the present case. If it is required that $\bar{u}$ approaches 1 exponentially it should be possible to develop $\bar{\tau}$ in a power series in $(\bar{u}-1)$ starting with a term of the first degree. This is only possible for the two main branches of the node; the other trajectories through the node can only be represented by non-analytical series. The power series for the steeper main branch has finite coefficients for all values of $\lambda \leqslant -2\sqrt{2}$; for the other main branch however some of the coefficients in the series may become infinite at certain values of λ. Hence if $\bar{u}$ should tend to 1 exponentially with η for all values of λ, only the steeper main branch of the node may be used; this is in agreement with Hartree's choice.

A further argument follows from an inspection of the phase plane portraits in fig. 6.5. It follows that with increasing suction the steeper main branch moves into a region with higher shear and hence produces a thinner boundary layer. For the other main branch, however, increased suction produces a smaller values of $\bar{\tau}$ and a thicker boundary layer; this conflicts with our physical ideas about the effects of suction on boundary layer flows.

If, finally, the steeper main branch of the node is selected as representing the relevant boundary layer type solution for the case of outflow a unique velocity profile is obtained for $\lambda \leqslant -2\sqrt{2}$. The velocity profiles for some values of λ are shown in fig. 6.6.

From fig. 6.5 it follows that for $\lambda \longrightarrow -\infty$ the wall shear stress becomes very high and the steeper main branch of the node tends to a straight line through (+1,0). In the same way the relevant trajectory through the saddle point becomes a straight line. This property is shown more clearly after introduction of the following transformations

$$\eta_1 = -\lambda \eta \tag{6.26}$$

$$\bar{\tau}_1 = \frac{\bar{\tau}}{-\lambda} = \frac{d\bar{u}}{d\eta_1} \tag{6.27}$$

Substituting (6.26) and (6.27) into (6.25) leads to the following equation

$$\frac{d\bar{\tau}_1}{d\bar{u}} = \frac{-\bar{\tau}_1 + \dfrac{1-\bar{u}^2}{\lambda^2}}{\bar{\tau}_1} \tag{6.28}$$

which for $\lambda \longrightarrow -\infty$ reduces to

$$\frac{d\bar{\tau}_1}{d\bar{u}} = -1 \tag{6.29}$$

From (6.29) it follows that the trajectories through the singularities ($\pm$1,0) are given by

$$\bar{\tau}_1 = 1 - \bar{u} \quad \text{for outflow} \tag{6.30}$$

$$\bar{\tau}_1 = -1 - \bar{u} \quad \text{for inflow} \tag{6.31}$$

Using (6.26), (6.27) and integrating (6.30) and (6.31) leads to

$$\left|\bar{u}\right| = 1 - e^{-\eta_1} = 1 - e^{\lambda\eta} \tag{6.32}$$

With (6.7) and (6.15) equation (6.32) may be written in the form

$$\left|\bar{u}\right| = 1 - e^{\frac{v_o y}{\nu}} \tag{6.33}$$

Equation (6.33) shows that both for outflow and for inflow with increasing suction the velocity profile tends to the asymptotic suction profile discussed in section 3.1.5. This result had been obtained already by Pretsch [74] (see Mangler [37]).

6.5. Consequences of some results of the phase plane description for practical boundary layer calculations.

For the case of inflow between impervious walls equation (6.17) shows that the relation between $\bar{\tau}^2$ and $\bar{u}$ is given by the following polynomial

$$\bar{\tau}^2 = -\frac{2}{3}\,\bar{u}^3 + 2\,\bar{u} + \frac{4}{3} \tag{6.34}$$

or

$$\bar{\tau}^2 = \frac{2}{3}\,(\bar{u} + 1)^2(2 - \bar{u}) \tag{6.35}$$

In the last part of section 6.4 it was shown that both for outflow and for inflow the asymptotic suction profile is obtained when $\lambda \rightarrow -\infty$. From equations (6.30) and (6.31) it follows that also in these cases the relation between $\bar{\tau}_1^2$ and $\bar{u}$ is a simple polynomial.

It can be shown that for the case of inflow, at arbitrary values of λ, $\bar{\tau}$ may be developed in a power series in $(\bar{u} + 1)$ of the form

$$\bar{\tau} = \gamma_1(\bar{u}+1) + \gamma_2\,(\bar{u}+1)^2 + \gamma_3(\bar{u}+1)^3 + \ldots\ldots \tag{6.36}$$

(note that for inflow $\bar{u} = -1$ at the singularity). It may be shown that the series converges rapidly for all values of λ. For $\lambda = 0$ the

series expansion of $\sqrt{\frac{2}{3}(\bar{u}+1)^2(2-\bar{u})}$ is obtained.
For the case of outflow with $\lambda \leqslant -2\sqrt{2}$ a series expansion around $\bar{u} = +1$ is possible of the form

$$\bar{\tau} = \gamma_1(1-\bar{u}) + \gamma_2(1-\bar{u})^2 + \gamma_3(1-\bar{u})^3 + \ldots. \qquad (6.37)$$

It is found that the series converges well except for values of λ near the limiting value $-2\sqrt{2}$.

The numerical results quoted above suggest the idea that a practical calculation method of the Pohlhausen type can be developed in which the velocity profile is defined by a polynomial expression of the form

$$\bar{\tau}^2 = a_o + a_1\bar{u} + a_2\bar{u}^2 + \ldots\ldots \qquad (6.38)$$

Such a method will be described in the next chapter.

7. A new multimoment method to obtain solutions of the boundary layer equations.

7.1. Introductory remarks.

It was shown in chapters 4 and 5 that - at least for cases without suction - reasonably accurate solutions of the boundary layer equations can be obtained by means of the von Kármán-Pohlhausen technique. In methods of this type a suitable expression for the velocity profile is used in combination with certain compatibility conditions and moments. Since these methods in themselves do not provide a check on their accuracy, it will only be possible to get an idea about their validity by applying them to boundary layer flows for which exact solutions are available. If such a method works well for a specific example it may reasonably be expected that the results for similar cases will also be sufficiently accurate. For widely different cases however the results may be entirely useless.

It may be expected that the accuracy of the Pohlhausen-type methods can be improved by increasing the number of parameters in the expression for the velocity profile. These extra parameters then have to be determined from additional compatibility conditions and/or moment equations. Since moment equations are relations between mean quantities in the boundary layer while compatibility conditions give relations between quantities at the wall or at the edge of the boundary layer only, it can be expected that the best results will be obtained from taking additional moment equations.

Increasing the number of moment equations leads to considerable difficulties for existing methods however; it has been explained already in section 4.5. that the difficulties arise from the fact that non-linear algebraic equations have to be solved.

Therefore if a workable Pohlhausen-type method, using many moment equations, is to be developed the moments should be defined in such a way that the moment equations reduce to relations of the form (4.16)

$$\frac{d\,J_k}{d\bar{x}} = M_k \tag{7.1}$$

where the J_k are linear in the parameters specifying the velocity profile. Such a method will be described in the present chapter; the principle idea is outlined below.

It was shown in chapter 6 that for some special configurations a simple description of the boundary layer may be given in the "phase plane", where the shear τ is plotted versus the velocity component u parallel to the wall. For the case of inflow between impervious non-parallel plane walls and for the asymptotic suction boundary layer the relation between τ^2 and u is given exactly by a simple polynomial (eqs 6.34 and 6.30-6.31 respectively). This observation suggested the idea to develop a kind of Pohlhausen method starting from the boundary layer equations written in a form, where $\bar{x} = \frac{x}{c}$ and $\bar{u} = \frac{u}{U}$ are the independent variables and $\bar{\tau}^2$ is the dependent variable. Here $\bar{\tau}$ is the non-dimensional shear stress to be defined by equations (7.11) and (7.20). The governing equation is a modified form of the well known Crocco equation [75] where τ is used instead of τ^2 and where moreover compressible flow is assumed. In what follows the new equation will be called the "modified Crocco equation"; a slightly different form has been used by Schönauer [76, 77] to develop a finite difference method.
In the present method $\bar{\tau}^2$ will be approximated by a polynomial in $\bar{u}$ of degree N. Moments are obtained by multiplication of the modified Crocco equation with $\bar{u}^k$ for k = 0, 1, 2, ... followed by integration over the interval $\bar{u}$ = 0 to $\bar{u}$ = 1. The method allows N to be increased by taking more moment equations without unduly complicating the procedure.
For special forms of the functions $\bar{U}(\bar{x})$ and $\bar{v}_o(\bar{x})$ solutions in series are possible; this series method shows many features similar to the exact series solutions discussed in section 3.2.
In the application of the method, to be discussed in subsequent chapters, the calculations were made on the Telefunken TR 4 computer of Delft Technological University.

7.2. The modified Crocco equation.

Crocco [75] was the first to introduce a form of the boundary layer equations in which x and u are used as independent variables and τ as dependent variable. This equation will be derived in the present section for the special case of incompressible flow with constant viscosity. The equations to be transformed are the boundary layer equation (2.7)

$$u \frac{\partial u}{\partial x} + v \frac{\partial u}{\partial y} = U \frac{dU}{dx} + \nu \frac{\partial^2 u}{\partial y^2} \tag{7.2}$$

and the continuity equation (2.5)

$$\frac{\partial u}{\partial x} + \frac{\partial v}{\partial y} = 0 \tag{7.3}$$

New independent variables x^* and y^* are introduced by

$$\left.\begin{aligned} x &= x^* \\ y &= y(x^*, y^*) \end{aligned}\right\} \quad (7.4)$$

From (7.4) it follows that

$$\left.\begin{aligned} \frac{\partial}{\partial x^*} &= \frac{\partial}{\partial x} + \frac{\partial}{\partial y} \frac{\partial y}{\partial x^*} \\ \frac{\partial}{\partial y^*} &= \frac{\partial}{\partial y} \frac{\partial y}{\partial y^*} \end{aligned}\right\} \quad (7.5)$$

or

$$\left.\begin{aligned} \frac{\partial}{\partial x} &= \frac{\partial}{\partial x^*} - \frac{\partial}{\partial y} \frac{\partial y}{\partial x^*} \\ \frac{\partial}{\partial y} &= \frac{\frac{\partial}{\partial y^*}}{\frac{\partial y}{\partial y^*}} \end{aligned}\right\} \quad (7.6)$$

Crocco selects y^* to be u; a partial differentiation with respect to x^* then leaves u constant. Using (7.6) and noting that U does not depend on y it follows that

$$\left.\begin{aligned}
\frac{\partial u}{\partial x} &= -\frac{\partial u}{\partial y}\frac{\partial y}{\partial x^*} \\
\frac{\partial u}{\partial y} &= \frac{1}{\frac{\partial y}{\partial u}} \\
\frac{\partial v}{\partial y} &= \frac{\frac{\partial v}{\partial u}}{\frac{\partial y}{\partial u}} \\
\frac{dU}{dx} &= \frac{dU}{dx^*}
\end{aligned}\right\} \qquad (7.7)$$

With $\tau = \mu \frac{\partial u}{\partial y}$ and introducing (7.7) into (7.2) and (7.3) the following equations are obtained

$$- u \frac{\partial y}{\partial x^*} + v = \frac{\mu}{\tau} U \frac{dU}{dx^*} + \frac{1}{\rho}\frac{\partial \tau}{\partial u} \qquad (7.8)$$

$$- \frac{\partial y}{\partial x^*} + \frac{\partial v}{\partial u} = 0 \qquad (7.9)$$

Finally v is eliminated from these equations by differentiating (7.8) with respect to u and subtracting (7.9) from the result. If in the resulting equation x^* is again replaced by x and after some rearrangement, the following equation is obtained

$$-\rho \mu u \left(\frac{\partial \tau}{\partial x}\right)_u + \tau^2 \left(\frac{\partial^2 \tau}{\partial u^2}\right)_x - \rho \mu U \frac{dU}{dx}\left(\frac{\partial \tau}{\partial u}\right)_x = 0 \qquad (7.10)$$

The subscripts u and x in equation (7.10) are added to emphasize that the differentiations have to be performed at constant u and x respectively. The equation is equivalent to Crocco's equation for the special case of constant ρ and μ.

Equation (7.10) will be transformed further by introducing non-dimensional quantities, defined as follows

$$\left.\begin{aligned}
\bar{x} &= \frac{x}{c} & \bar{\tau} &= \frac{\tau\delta}{\mu U} \\
\bar{y} &= \frac{y}{\delta} & S &= \bar{\tau}^2 \\
\bar{u} &= \frac{u}{U} & \alpha_1 &= \bar{U}\,\bar{\delta}^2 \\
\bar{U} &= \frac{U}{U_\infty} & \lambda_1 &= \bar{\delta}^2\,\frac{d\bar{U}}{d\bar{x}} \\
\bar{\delta} &= \frac{\delta}{c}\sqrt{\frac{U_\infty c}{\nu}}
\end{aligned}\right\} \qquad (7.11)$$

In (7.11) c and U_∞ represent a constant reference lenth and velocity respectively; δ is a given function of $\bar{x}$ related to the boundary layer thickness. In section 7.3 the choice for δ will be specified.
In what follows $\bar{x}$ and $\bar{u}$ are taken as independent variables while S is the dependent variable. The transformation to the non-dimensional variables follows from the following equations.

$$\left.\begin{aligned}
\left(\frac{\partial}{\partial x}\right)_u &= \frac{\partial}{\partial \bar{u}}\left(\frac{\partial \bar{u}}{\partial x}\right)_u + \frac{\partial}{\partial \bar{x}}\left(\frac{\partial \bar{x}}{\partial x}\right)_u \\
\left(\frac{\partial}{\partial u}\right)_x &= \frac{\partial}{\partial \bar{u}}\left(\frac{\partial \bar{u}}{\partial u}\right)_x + \frac{\partial}{\partial \bar{x}}\left(\frac{\partial \bar{x}}{\partial u}\right)_x
\end{aligned}\right\} \qquad (7.12)$$

in which

$$\left.\begin{aligned}
&\left(\frac{\partial \bar{u}}{\partial x}\right)_u = -\frac{u}{U^2}\,\frac{dU}{dx} \;; \quad \left(\frac{\partial \bar{x}}{\partial x}\right)_u = \frac{1}{c} \\
&\left(\frac{\partial \bar{u}}{\partial u}\right)_x = \frac{1}{U} \;; \quad \left(\frac{\partial \bar{x}}{\partial u}\right)_x = 0
\end{aligned}\right\} \qquad (7.13)$$

Introducing (7.11) and (7.13) into (7.10) leads to

$$\frac{\partial}{\partial \bar{x}}(\bar{u}\;S) = \frac{\left(\dfrac{d\alpha_1}{d\bar{x}} - 3\lambda_1\right)\bar{u}\;S + S\;S'' - \tfrac{1}{2}(S')^2 - \lambda_1(1-\bar{u}^2)S'}{\alpha_1} \qquad (7.14)$$

In equation (7.14) and in the remainder of the present chapter primes denote differentiation with respect to $\bar{u}$. Equation (7.14) will be called "the modified Crocco equation". The boundary condition for (7.14) at the edge of the boundary layer is S(1) = 0. At the wall ($\bar{u}$ = 0) a boundary condition is provided by the first compatibility condition (2.10); this will be discussed further in section 7.4.

If the requirement is made that at the edge of the boundary layer $1-\bar{u}$ tends to zero as $e^{-\bar{y}}$ the shear stress $\bar{\tau}$ behaves like $1-\bar{u}$ for $\bar{u} \rightarrow 1$ (compare section 6.4). Hence $S = \bar{\tau}^2$ tends to zero like $(1-\bar{u})^2$ for $\bar{u} \rightarrow 1$; this leads to the following boundary conditions for equation (7.14) at $\bar{u} = 1$

$$S(1) = S'(1) = 0 \tag{7.15}$$

Equation (7.14) permits the calculation of $S(\bar{u})$ provided for a certain initial value of $\bar{x}$ the profile $S(\bar{u})$ is known and $\bar{U}$ and $v_o(\bar{x})$ are known as functions of $\bar{x}$.

7.3. A special choice for δ.

Although δ may be any known function of x it is convenient to choose it in such a way that for some similar boundary layer flows the shear function S will not depend on $\bar{x}$ but only on $\bar{u}$. To point this out more clearly possible similar solutions of (7.14) will be studied first.

If S does not depend on $\bar{x}$ equation (7.14) reduces to

$$\left(\frac{d\alpha_1}{d\bar{x}} - 3\lambda_1 \right) \bar{u}S + SS'' - \tfrac{1}{2}(S')^2 - \lambda_1(1-\bar{u}^2)S' = 0 \tag{7.16}$$

This equation admits solutions independent of $\bar{x}$ only if both λ_1 and $\frac{d\alpha_1}{d\bar{x}}$ are constants. Hence it follows that

$$\alpha_1 = \bar{U}\,\bar{\delta}^2 = \alpha_2\,\bar{x} + \alpha_3 \tag{7.17}$$

$$\lambda_1 = \bar{\delta}^2 \frac{d\bar{U}}{d\bar{x}} = \text{constant} \tag{7.18}$$

where α_2 and α_3 are constants.

If $\alpha_2 \neq 0$ it is possible, without loss of generality, to make $\alpha_2 = 1$ and $\alpha_3 = 0$ by a trivial change of the variable $\bar{x}$.
Equation (7.17) then reduces to

$$\alpha_1 = \bar{U}\,\bar{\delta}^2 = \bar{x} \tag{7.19}$$

implying that

$$\bar{\delta} = \sqrt{\frac{\bar{x}}{\bar{U}}} \qquad \text{or} \qquad \frac{\delta}{x}\sqrt{\frac{Ux}{\nu}} = 1 \tag{7.20}$$

Elimination of $\bar{\delta}^2$ between (7.18) and (7.19) gives

$$\frac{\lambda_1}{\bar{x}}\,d\bar{x} = \frac{d\bar{U}}{\bar{U}} \tag{7.21}$$

and upon integration

$$\bar{U} = \text{constant} \,.\, \bar{x}^{\,\lambda_1} \tag{7.22}$$

Hence a first class of similar solutions, for which S becomes independent of $\bar{x}$, may be obtained for pressure distributions defined by

$$\bar{U} = \text{constant} \,.\, \bar{x}^{\,m_1} \tag{7.23}$$

where $m_1 = \lambda_1 =$ constant and δ is defined by equation (7.20). This is in agreement with the exact results discussed in section 3.1.
A second class of similar solutions is obtained from the case $\alpha_2 = 0$ which was hitherto excluded. This case may be shown to lead to

$$\bar{U} = \text{constant} \,.\, e^{\frac{\lambda_1 \bar{x}}{b_2}} \tag{7.24}$$

where both λ_1 and b_2 are constant. Hence also for $\alpha_2 = 0$ one of the results discussed in chapter 3 is regained; in this case δ is defined by $\alpha_1 = \bar{U}\,\bar{\delta}^2 =$ constant.

In what follows always the definition (7.20) for δ will be used; the corresponding expressions for α_1 and λ_1 then become

$$\alpha_1 = \bar{x} \quad ; \quad \lambda_1 = \bar{\delta}^2 \frac{d\bar{U}}{d\bar{x}} = \frac{\bar{x}}{\bar{U}} \frac{d\bar{U}}{d\bar{x}} \tag{7.25}$$

while equation (7.14) reduces to

$$\frac{\partial}{\partial \bar{x}} (\bar{u}\ S) = \frac{(1-3\lambda_1)\ \bar{u}\ S + SS'' - \frac{1}{2}(S')^2 - \lambda_1(1-\bar{u}^2)S'}{\bar{x}} \tag{7.26}$$

From the derivation of equation (7.26) it follows that for pressure distributions defined by equation (7.22) solutions may be found for which S is independent of $\bar{x}$.

7.4. The polynomial approximation for S and compatibility conditions of the modified Crocco equation.

It was shown in chapter 6 that for some special cases of similar boundary layer flows $S(\bar{u})$ is given by a simple polynomial. For instance for inflow between impervious non-parallel plane walls the following result was obtained (equation 6.34)

$$S = \bar{\tau}^2 = \frac{4}{3} + 2\ \bar{u} - \frac{2}{3}\ \bar{u}^3 \tag{7.27}$$

For the asymptotic suction profile equations (6.30) or (6.31) lead to

$$S = \bar{\tau}^2 = \text{constant}\ (1 - \bar{u})^2 \tag{7.28}$$

In the present method it will be attempted to obtain solutions of the modified Crocco equation (7.26) by assuming that in all cases S can be approximated by a polynomial expression of the following form

$$S = a_o + a_1\bar{u} + a_2\ \bar{u}^2 + \ldots\ldots. + a_N\ \bar{u}^N \tag{7.29}$$

In (7.29) the coefficients a_n are functions of $\bar{x}$ for general boundary layer flows and constants for the similar boundary layers defined by $\bar{U} = u_1\ \bar{x}^{m_1}$. Introducing (7.29) into (7.26) gives

$$\bar{x}\frac{\partial}{\partial \bar{x}}\left(\sum_{n=0}^{N} a_n \bar{u}^{n+1}\right) = d_o + d_1\bar{u} + d_2\bar{u}^2 + \ldots + d_e\bar{u}^e \qquad (7.30)$$

where $e = N+1$ for $N < 3$ and $e = 2N-1$ for $N \geqslant 3$.
In equation (7.30) the coefficients d are quadratic expressions in the a_n. The first few of these read as follows

$$d_o = 2\, a_o a_2 - \tfrac{1}{2}\, a_1^{\,2} - \lambda_1\, a_1 \qquad (7.31)$$

$$d_1 = a_o + 6\, a_o a_3 - \lambda_1\,(3\, a_o + 2\, a_2) \qquad (7.32)$$

$$d_2 = a_1 + 12\, a_o a_4 + 3\, a_1 a_3 - \lambda_1 (2\, a_1 + 3\, a_3) \qquad (7.33)$$

If (7.30) is valid for all values of $\bar{u}$ the coefficients of equal powers of $\bar{u}$ in the left- and right-hand sides of the equation have to be equal. This leads to

$$0 = d_o \qquad (7.34)$$

$$\bar{x}\frac{da_o}{d\bar{x}} = d_1 \qquad (7.35)$$

$$\bar{x}\frac{da_1}{d\bar{x}} = d_2. \qquad (7.36)$$

---------- ------

or using (7.31), (7.32) and (7.33)

$$0 = 2\, a_o a_2 - \tfrac{1}{2}\, a_1^{\,2} - \lambda_1 a_1 \qquad (7.37)$$

$$\bar{x}\frac{da_o}{d\bar{x}} = (1-3\,\lambda_1)a_o + 6\, a_o a_3 - 2\,\lambda_1 a_2 \qquad (7.38)$$

$$\bar{x}\frac{da_1}{d\bar{x}} = a_1 + 12\, a_o a_4 + 3\, a_1 a_3 - 2\,\lambda_1 a_1 - 3\,\lambda_1 a_3 \qquad (7.39)$$

Equations (7.37) to (7.39) are compatibility conditions at the wall for the modified Crocco equation. They are the analogues to the compatibility conditions discussed in chapter 2 for Prandtl's form of the boundary layer equations.

In the derivation of the modified Crocco equation the normal velocity v has been eliminated. In order to be able to specify a boundary condition on v at the wall and to discuss problems with suction, the normal velocity v has to be introduced again by means of the compatibility conditions of Prandtl's boundary layer equations.

The first and second of these compatibility conditions read (see section 2.3)

$$v_o \left(\frac{\partial u}{\partial y}\right)_o = U \frac{dU}{dx} + \nu \left(\frac{\partial^2 u}{\partial y^2}\right)_o \tag{7.40}$$

$$v_o \left(\frac{\partial^2 u}{\partial y^2}\right)_o = \nu \left(\frac{\partial^3 u}{\partial y^3}\right)_o \tag{7.41}$$

Writing these equations in terms of S and $\bar{u}$ leads to

$$-\lambda_2 \sqrt{S(o)} = \lambda_1 + \frac{S'(o)}{2} \tag{7.42}$$

$$-\lambda_2 \quad S'(o) = S''(o) \sqrt{S(o)} \tag{7.43}$$

in which λ_2 stands for

$$\lambda_2 = \frac{-v_o \delta}{\nu} = \frac{-v_o}{U} \sqrt{\frac{Ux}{\nu}} = \bar{v}_o . \bar{\delta} \tag{7.44}$$

while $\bar{v}_o$ is defined by

$$\bar{v}_o = \frac{-v_o}{U_\infty} \sqrt{\frac{U_\infty c}{\nu}} \tag{7.45}$$

If S(o), S'(o) and S''(o) are expressed in terms of the a_n's equations (7.42) and (7.43) can be written in the form

$$a_1 = -2 \lambda_1 - 2 \lambda_2 \sqrt{a_o} \tag{7.46}$$

$$a_2 = \frac{-\lambda_2 a_1}{2\sqrt{a_o}} \tag{7.47}$$

Elimination of λ_2 from (7.46) and (7.47) again leads to (7.37). This means that the first and second compatibility condition of Prandtl's boundary layer equation include the first compatibility condition of the modified Crocco equation. This, of course, could be expected from the derivation of the modified Crocco equation.

Some further relations between the coefficients a_n are obtained from the conditions (7.15) at the edge of the boundary layer. They lead to

$$\sum_{n=0}^{N} a_n = 0 \tag{7.48}$$

and

$$\sum_{n=1}^{N} n\, a_n = 0 \tag{7.49}$$

In what follows both conditions (7.48) and (7.49) at $\bar{u} = 1$ will be retained together with the equations (7.38), (7.46) and (7.47). In the next section these equations will be supplemented by some moment equations.

7.5. Moments of the modified Crocco equation.

In taking moments of the modified Crocco equation it should be tried - in order to fulfill the requirement set out in section 7.1 - to reduce the left-hand side of (7.26) to the form $\frac{dJ}{d\bar{x}}$ in which J is a linear combination of the a_n's. Evidently such a relation can be obtained by multiplying the equation with some function $G(\bar{u})$ and integrating the resulting equation w.r.t. $\bar{u}$ from 0 to 1.

In what follows $G(\bar{u}) = \bar{u}^k$ will be used where k in turn takes the values 0,1,2,..., K. This leads to K+1 moment equations defined by

$$\bar{x}\frac{dJ_k}{d\bar{x}} = M_k \tag{7.50}$$

$$M_k = (1-3\lambda_1)J_k - \lambda_1 P_k + Q_k \tag{7.51}$$

$$J_k = \sum_{n=0}^{N} j_{k,n}\, a_n \tag{7.52}$$

$$P_k = \sum_{n=0}^{N} P_{k,n}\, a_n \tag{7.53}$$

$$Q_k = \sum_{\ell=0}^{N} \sum_{n=\ell}^{N} q_{k,\ell,n}\, a_\ell a_n \tag{7.54}$$

$$\left.\begin{array}{lll}
j_{k,n} = \dfrac{1}{k+n+2} & & 0 \leqslant n \leqslant N \\[2ex]
p_{k,0} = 0 & & \\[2ex]
p_{k,n} = \dfrac{2n}{(k+n)(k+n+2)} & & 1 \leqslant n \leqslant N \\[2ex]
q_{k,0,0} = q_{k,0,1} = 0 & & \\[2ex]
q_{k,0,n} = \dfrac{n(n-1)}{k+n-1} & & 2 \leqslant n \leqslant N \\[2ex]
q_{k,1,1} = \dfrac{-\frac{1}{2}}{k+1} & & \\[2ex]
q_{k,1,n} = \dfrac{n(n-2)}{k+n} & & 2 \leqslant n \leqslant N \\[2ex]
q_{k,\ell,\ell} = \dfrac{\frac{1}{2}\ell^2-\ell}{k+2\ell-1} & & 2 \leqslant \ell \leqslant N \\[2ex]
q_{k,\ell,n} = \dfrac{n(n-1)-\ell n+\ell(\ell-1)}{k+\ell+n-1} & & \begin{array}{l} 2 \leqslant \ell \leqslant N \\ \ell < n \leqslant N \end{array}
\end{array}\right\} \tag{7.55}$$

7.6. Summary of the formulae to be used in the new calculation method.

This section summarizes the formulae derived in the preceding sections which have to be used in the new calculation method.
The flow outside the boundary layer is determined by $\overline{U}(\overline{x})$ and $\dfrac{d\overline{U}}{d\overline{x}}$; the suction distribution by $\overline{v}_o(\overline{x})$ with

$$\overline{v}_o = -\frac{v_o}{U_\infty}\sqrt{\frac{U_\infty c}{\nu}} \tag{7.56}$$

Furthermore the following definitions are used

$$\bar{\delta} = \sqrt{\frac{\bar{x}}{\bar{U}}} \tag{7.57}$$

$$\lambda_1 = \bar{\delta}^2 \frac{d\bar{U}}{d\bar{x}} = \frac{\bar{x}}{\bar{U}} \frac{d\bar{U}}{d\bar{x}} \tag{7.58}$$

$$\lambda_2 = \bar{v}_o . \bar{\delta} = - \frac{v_o}{U} \sqrt{\frac{Ux}{\nu}} \tag{7.59}$$

It should be noted that the pressure distribution only enters the calculation through λ_1 and λ_2 while the suction distribution only enters through λ_2. The shear stress function S is approximated by the polynomial

$$S = \sum_{n=0}^{N} a_n \bar{u}^n \tag{7.60}$$

where the coefficients a_n are determined as functions of $\bar{x}$ from the following equations.

<u>Compatibility conditions at the wall:</u>

$$\bar{x} \frac{da_o}{d\bar{x}} = (1-3 \lambda_1)a_o + 6 a_o a_3 - 2 \lambda_1 a_2 \tag{7.61}$$

$$a_1 = -2 \lambda_1 - 2 \lambda_2 \sqrt{a_o} \tag{7.62}$$

$$a_2 = - \frac{\lambda_2 a_1}{2\sqrt{a_o}} \tag{7.63}$$

<u>Conditions at the edge of the boundary layer ($\bar{u} = 1$):</u>

$$a_1 + 2 a_2 + 3 a_3 + \ldots\ldots\ldots + N a_N = 0 \tag{7.64}$$

$$a_o + a_1 + a_2 + a_3 + \ldots\ldots\ldots + a_N = 0 \tag{7.65}$$

<u>Moment equations:</u>

$$\bar{x} \frac{dJ_k}{d\bar{x}} = M_k \qquad \text{for} \qquad k = 0,1,2,\ldots\ldots,K \tag{7.66}$$

where the M_k follow from equations (7.51) - (7.55). The total number of equations (7.61) to (7.66) thus obtained is K+6. These equations should yield the N+1 coefficients a_n; hence it follows that

$$K = N - 5 \tag{7.67}$$

Some further remarks on the compatibility conditions at the wall and the moments may be made here. The choice of the moments and the compatibility conditions to be used has been made in a rather arbitrary manner. No systematic investigation has been made of the best possible choice. However there is an argument in favour of the present choice which will be given now. The compatibility conditions (7.37) through (7.39) have been obtained by equating to zero the coefficients of terms with various powers of $\bar{u}$ in (7.30). The same result will be obtained by repeated differentiation of (7.30) w.r.t. $\bar{u}$ and putting $\bar{u} = 0$ in the resulting equations. A natural complement to these compatibility conditions would be a set of moment equations obtained by repeated integrations of (7.30) w.r.t. $\bar{u}$ from $\bar{u} = 0$ to $\bar{u}$ and putting $\bar{u} = 1$ in the final results. This has in fact been precisely achieved because it can be shown that the members of the present set of moment equations are linear combinations of the equations which appear upon repeated integration of (7.30). The number of compatibility conditions was taken as small as possible because it was felt that the moment equations might be more decisive for the mean boundary layer characteristics than the compatibility conditions. However, since in the first compatibility condition (7.62) the square root of a_o already occurs it was decided to go on and to include (7.61) in the system which provides a differential equation from which a_o can easily be calculated.

7.7. Step by step solution starting from given initial conditions.

In this section it is assumed that at some station $\bar{x} = \bar{x}_o$ starting values of the a_n's are known (The determination of the starting values will be discussed in section 7.9). The a_n downstream of $\bar{x}_o$ can be determined in the following way using one of the numerical methods for the integration of a system of ordinary differential equations.

From the given starting values at $\bar{x} = \bar{x}_o$ the value of a_o at the next station is found using equation (7.61). Then a_1 and a_2 follow from (7.62) and (7.63) respectively. The values of the J_k at the next station follow from equations (7.66). The only remaining problem is to find the a_n for $n \geqslant 3$ from the values of the J_k. As the J_k are linear relations in the a_n (equation 7.52) this leads, in combination with the conditions (7.64) and (7.65) at the edge of the boundary layer, to the following set of linear equations.

$$\begin{aligned}
3\,a_3 + 4\,a_4 + 5\,a_5 + \ldots\ldots + N\,a_N &= -a_1 - 2\,a_2 = \beta_1 \\
a_3 + a_4 + a_5 + \ldots\ldots + a_N &= -a_o - a_1 - a_2 = \beta_2 \\
\frac{a_3}{k+5} \quad \frac{a_4}{k+6} \quad \frac{a_5}{k+7} + \ldots\ldots + \frac{a_N}{k+N+2} &= J_k - \frac{a_o}{k+2} - \frac{a_1}{k+3} - \frac{a_2}{k+4} = \beta_{k+3}
\end{aligned} \qquad (7.68)$$

where the coefficients β_n have been introduced to denote the known right-hand sides. The last equation should be used for $k = 0,1,2,\ldots\ldots,N-5$. The left hand sides of (7.68) do not contain specific data of the boundary layer being calculated and therefore the coefficient matrix of the equations can be inverted once for all, for all values of N to be used. As the original matrix is very orderly built the inverse can easily be obtained by hand computation for increasing values of N. Denoting with a_{ij} the coefficient of a_{i+2} in the j^{th} row of the set (7.68) the elements of the inverse matrix will be denoted by A_{ij} where i and j assume the values $1,2,3,\ldots\ldots,N-2$. The results are given in table 7.1 for N=5 to 10. It is noticed that the elements of A become very large for large values of N. This is caused by the tendency of the coefficient matrix of (7.68) to become singular at large values of N. It may be noted that the tendency to singularity had no influence on the accuracy of the inverses presented because these were obtained by hand computation in the exact number of figures.

Solutions of (7.68) can now be given in the form

$$a_n = \sum_{j=1}^{N-2} A_{n-2,j}\,\beta_j \qquad (7.69)$$

in which $n \geqslant 3$.

When the value of N is increased, only the number of linear equations to be solved increases but the method remains in principle the same. Hence it may be conjectured that the approximate solution will approach the exact solution when N is successively increased.

A practical limit to the maximum permissible value of N is imposed however by the loss of significant figures which occurs in (7.69) for large values of N. This is due to the fact that both the a_n and β_j are of order 1 while the A_{ij} are of a considerably larger order of magnitude (see table 7.1). This difficulty may be postponed to large values of N if the procedure outlined above is not applied to the a_n and J_k but only to the increments of these quantities.

When values at the initial station are denoted by a bar the increments follow from

$$\begin{aligned} \Delta a_n &= a_n - \overline{a_n} \\ \Delta J_k &= J_k - \overline{J_k} \\ \Delta \beta_j &= \beta_j - \overline{\beta_j} \end{aligned} \qquad (7.70)$$

As both the initial and final values satisfy the linear equations (7.68) it follows that also the increments are determined by the equations (7.68) when the a_n, J_k and β_j are replaced by Δa_n, ΔJ_k and $\Delta \beta_j$ respectively. Hence for $n \geqslant 3$ the Δa_n are given by

$$\Delta a_n = \sum_{j=1}^{N-2} A_{n-2,j} \, \Delta \beta_j \qquad (7.71)$$

or after separating the contributions of Δa_o, Δa_1, Δa_2 and ΔJ_k:

$$\begin{aligned} \Delta a_n = &- \Delta a_o \left[A_{n-2,2} + \sum_{j=3}^{N-2} \frac{A_{n-2,j}}{j-1} \right] \\ &- \Delta a_1 \left[A_{n-2,1} + A_{n-2,2} + \sum_{j=3}^{N-2} \frac{A_{n-2,j}}{j} \right] \qquad (7.72) \\ &- \Delta a_2 \left[2\, A_{n-2,1} + A_{n-2,2} + \sum_{j=3}^{N-2} \frac{A_{n-2,j}}{j+1} \right] \\ &+ \sum_{j=3}^{N-2} A_{n-2,j} \, \Delta J_{j-3} \end{aligned}$$

The number of significant figures retained is made as large as possible by first evaluating the terms between brackets in (7.72).
Once the Δa_n are obtained from (7.72) the values of a_n at the next station follow from (7.70). These values can be used as starting values for the next step etc.
In all examples given in the present work the integration was performed by a third order Runge-Kutta method. It should be understood that in this method a full step is made up of some sub-steps and that the procedure outlined above has to be applied in each sub-step. As in certain applications of the method the largest permissible step length may vary considerably with $\bar{x}$ use was made of one of the Runge-Kutta formulae with self-adjusting step length given by Zonneveld [78]. These formulae provide explicit expressions for the last term of the Taylor series taken into account. The step length used is adjusted in such a way that the absolute value of this last term is equal to a certain tolerance, to be specified in the program.

7.8. Similar solutions for $\bar{U} = \bar{x}^{\lambda_1}$.

It was shown in section 7.3 that for $\bar{U} = \bar{x}^{\lambda_1}$ with constant λ_1 similar solutions may occur for which the a_n are constants. From the compatibility conditions (7.62) and (7.63) it follows that also λ_2 should be constant. Therefore the permissible suction distribution for this class of similar boundary layers is given by

$$\bar{v}_o = \lambda_2 \, \bar{x}^{\frac{\lambda_1 - 1}{2}} \tag{7.73}$$

From the fact that the a_n are constant for the similar solutions under consideration it follows that all terms with $\bar{x}\frac{d}{d\bar{x}}$ vanish from the equations (7.61) to (7.66). Hence the moment equations for this case reduce to $M_k = 0$ with $k = 0,1,2,\ldots, N-5$.
Since the resulting equations contain non-linear terms they are not easy to solve directly; however, solutions can easily be obtained by interpolation or iteration. In what follows two different procedures which were used for this purpose will be described.

It should be noted that due to the non-linearity multiple solutions may occur. One of these solutions is always $a_n \equiv 0$ which of course is an unrealistic one. In all the examples to be discussed in chapter 8, only one realistic solution occurred.

A procedure to obtain similar solutions by interpolation. If values for a_o, a_7, a_8, ..., a_N are assumed, the compatibility conditions (7.61) to (7.63) with the additional condition $\bar{x} \frac{d}{d\bar{x}} = 0$ provide values for a_1, a_2 and a_3 while a_4 and a_5 can be expressed as a linear relation in a_6 using (7.64) and (7.65). In this way the moment equations $M_k = 0$ are reduced to quadratic equations in a_6; real roots of these equations provide, for each value of k, one or two values of a_6 for which $M_k = 0$. Repeating this procedure for other values of a_o, a_6, a_7, a_8, ... it is rather easy to find by interpolation values for the a_n for which all compatibility conditions and moment equations are satisfied. The method outlined above works well for $N \leqslant 7$; for higher values of N however it becomes too complicated. Therefore an iterative procedure was designed which will be outlined in the remainder of the present section.

An iteration procedure to obtain similar solutions. At first it was attempted to use the step by step method of section 7.7 for this purpose by starting from guessed initial values and running the program for constant λ_1 and λ_2 until the a_n's became constant. It was found that the required solutions were stable so that the proposed procedure was convergent. However, a large amount of computation was required to obtain the solutions with sufficient precision. It turned out that the solutions could be obtained much more rapidly by using the following iteration procedure.

For the similar solutions equations (7.61) through (7.66) reduce to:

$$\left.\begin{aligned}
E_1 &= (1-3\lambda_1)a_o + 6\, a_o a_3 - 2\lambda_1\, a_2 &&= 0\\
E_2 &= a_1 + 2\lambda_1 + 2\lambda_2 \sqrt{a_o} &&= 0\\
E_3 &= 2\, a_2 \sqrt{a_o} + \lambda_2\, a_1 &&= 0\\
E_4 &= a_1 + 2\, a_2 + 3\, a_3 + \dots + N\, a_N &&= 0\\
E_5 &= a_o + a_1 + a_2 + a_3 + \dots + a_N &&= 0\\
E_{6+k} &= M_k &&= 0
\end{aligned}\right\} \quad (7.74)$$

The last equation written down in (7.74) has to be used for $k = 0,1,2,\dots, N-5$. The equations (7.74) can be solved using an iterative procedure equivalent to Newton's method for one equation.

If initial values $\bar{a}_n$ for all a_n are assumed to be known, then also initial values $\bar{E}_i$ of the functions E_i can be calculated. Now, the $\bar{E}_i$ will in general be different from zero; to make them zero the a_n should be changed by amounts δa_n. For small variations the E_i may be replaced by their Taylor series expansions using only terms up to and including those of the first degree. Hence, if $\frac{\partial E_i}{\partial a_n}$ is denoted by e_{in} and δa_n by t_n the equations (7.74) are replaced by

$$\left.\begin{aligned}
E_1 &= \bar{E}_1 + e_{10}\, t_o + e_{12}\, t_2 + e_{13}\, t_3 &&= 0\\
E_2 &= \bar{E}_2 + e_{20}\, t_o + e_{21}\, t_1 &&= 0\\
E_3 &= \bar{E}_3 + e_{30}\, t_o + e_{31}\, t_1 + e_{32}\, t_2 &&= 0\\
E_4 &= \bar{E}_4 + \sum_{n=0}^{N} e_{4n}\, t_n &&= 0\\
E_5 &= \bar{E}_5 + \sum_{n=0}^{N} e_{5n}\, t_n &&= 0\\
E_{6+k} &= \bar{E}_{6+k} + \sum_{n=0}^{N} e_{6+k,n}\, t_n &&= 0\\
& k = 0,1,2,\dots,N-5
\end{aligned}\right\} \quad (7.75)$$

The derivatives e_{in} are given by

$$\left.\begin{array}{lll}
e_{10} = 1-3\lambda_1 + 6\,\bar{a}_3 & e_{20} = \dfrac{\lambda_2}{\sqrt{\bar{a}_o}} & e_{30} = \dfrac{\bar{a}_2}{\sqrt{\bar{a}_o}} \\
e_{12} = -2\lambda_1 & & \\
e_{13} = 6\,\bar{a}_o & e_{21} = 1 & e_{31} = \lambda_2 \\
 & & e_{32} = 2\sqrt{\bar{a}_o} \\
e_{4n} = n \quad \text{for} \quad n = 0,1,2,\ldots, N & & \\
e_{5n} = 1 \quad \text{for} \quad n = 0,1,2,\ldots, N & & \\
e_{6+k,n} = \dfrac{\partial M_k}{\partial a_n} \quad \text{for} \left\{\begin{array}{l} k = 0,1,2,\ldots, N-5 \\ n = 0,1,2,\ldots, N \end{array}\right. & &
\end{array}\right\} \quad (7.76)$$

From equations (7.51) through (7.54) it follows that

$$\frac{\partial M_k}{\partial a_n} = (1-3\lambda_1) j_{k,n} - \lambda_1 p_{k,n} + \sum_{\ell=0}^{n} q_{k,\ell,n}\,\bar{a}_\ell + \sum_{\ell=n}^{N} q_{k,n,\ell}\,\bar{a}_\ell \quad (7.77)$$

It is convenient to select the initial values $\bar{a}_n$ in such a way that the compatibility conditions at the wall (equations 7.61 to 7.63) and the conditions at $\bar{u} = 1$ (7.64) and (7.65) are satisfied which means that $\bar{E}_i = 0$ for $i = 1,2,\ldots,5$. Then, denoting $\bar{E}_{6+k}$ by $\bar{M}_k$ the equations (7.75) reduce to the following set of linear algebraic equations.

$$\left.\begin{array}{ll}
e_{10}t_o + e_{12}t_2 + e_{13}t_3 & = 0 \\
e_{20}t_o + e_{21}t_1 & = 0 \\
e_{30}t_o + e_{31}t_1 + e_{32}t_2 & = 0 \\
\sum_{n=0}^{N} e_{4n}\,t_n & = 0 \\
\sum_{n=0}^{N} e_{5n}\,t_n & = 0 \\
\sum_{n=0}^{N} \dfrac{\partial M_k}{\partial a_n}\,t_n & = -\bar{M}_k \text{ for}
\end{array}\right\} \quad (7.78)$$

$$k = 0,1,2,\ldots,N-5$$

Solving these equations for the t_n gives improved values for the a_n from $a_n = \bar{a}_n + t_n$; these values for the a_n can be used as new starting values $\bar{a}_n$ etc. It should be noted that throughout the iteration process $\bar{E}_1$ to $\bar{E}_5$ remain zero which means that the compatibility conditions are always satisfied. The iteration procedure serves to adjust the a_n such that also the moment equations are satisfied.

7.9. Series solutions for special types of the functions U(x) and $v_o(x)$.

7.9.1. General remarks.

In section 7.7 it was assumed that for a certain initial value of $\bar{x}$ starting values for the a_n were known. It will be shown now that these starting values can be determined from a series solution starting from $\bar{x} = 0$.

In the series solution a new variable z is used defined by

$$z = x^f \tag{7.79}$$

where f may be any real positive number. Series solutions for the coefficients a_n will be obtained for those functions λ_1 and λ_2 which can be developed in power series in z of the following form

$$\lambda_1 = \sum_{p=0}^{\infty} \lambda_{1,p} \quad z^p \tag{7.80}$$

$$\lambda_2 = \sum_{p=0}^{\infty} \lambda_{2,p} \quad z^p \tag{7.81}$$

The expressions (7.80) and (7.81) correspond to special forms of the pressure- and suction distributions. They are sufficiently general however to be applied near $\bar{x} = 0$ for all problems likely to be encountered. The pressure- and suction distributions which lead to (7.80) and (7.81) will be obtained first.

From (7.80) and

$$\lambda_1 = \frac{\bar{x}}{\bar{U}} \frac{d\bar{U}}{d\bar{x}} = \frac{fz}{\bar{U}} \frac{d\bar{U}}{dz} = fz \frac{d}{dz} (\ell n \; \bar{U}) \tag{7.82}$$

it follows that

$$\frac{\lambda_{1,o}}{z} + \lambda_{1,1} + \lambda_{1,2}\, z + \lambda_{1,3}\, z^2 + \ldots . + \lambda_{1,p}\, z^{p-1} + \ldots$$
$$= f \frac{d}{dz} (\ln \bar{U}) \qquad (7.83)$$

Integration of (7.83) leads to

$$\bar{U} = \text{constant} \;.\; z^{\frac{\lambda_{1,o}}{f}} \left[e^{\frac{\lambda_{1,1}}{f} z + \frac{1}{2} \frac{\lambda_{1,2}}{f} z^2 + \ldots + \frac{\lambda_{1,p}}{pf} z^p + \ldots} \right]$$
$$(7.84)$$

Development of the exponential function in a power series in z results in the following expression for $\bar{U}$

$$\bar{U} = z^{\frac{\lambda_{1,o}}{f}} \left[u_o + u_1 z + u_2\, z^2 + \ldots . + u_p\, z^p + \ldots . \right] \qquad (7.85)$$

In terms of $\bar{x}$ the permissible pressure distribution follows from (7.79) and (7.85)

$$\bar{U} = \bar{x}^{\lambda_{1,o}} (u_o + u_1\, \bar{x}^{-f} + u_2\, \bar{x}^{-2f} + \ldots . + u_p\, \bar{x}^{\,pf} + \ldots) \quad (7.86)$$

The permissible suction distribution then follows from (7.57), (7.59) and (7.86)

$$\bar{v}_o = \lambda_2\, \bar{x}^{\frac{\lambda_{1,o}-1}{2}} (u_o + u_1\, \bar{x}^{-f} + u_2\, \bar{x}^{\,2f} + \ldots .)^{\frac{1}{2}} \qquad (7.87)$$

Noting that λ_2 is represented by the series (7.81) and developing the square root in (7.87) gives the following expression for the permissible suction distribution

$$\bar{v}_o = \bar{x}^{\frac{\lambda_{1,o}-1}{2}} (s_o + s_1\, \bar{x}^{-f} + s_2\, \bar{x}^{\,2f} + \ldots . + s_p\, \bar{x}^{\,pf} + \ldots) \quad (7.88)$$

In practical applications of the series method the coefficients u_p and s_p in (7.86) and (7.88) are given while the coefficients of the series (7.80) and (7.81) have to be determined. It is possible to derive universal formulae from which these coefficients can be calculated but they will not be given here. In the examples of the method to be discussed in chapter 8 the series developments of λ_1 and λ_2 will be given directly for each case.

The series solutions are obtained from equations (7.61) to (7.66) if in these equations $\bar{x}\dfrac{d}{d\bar{x}}$ is replaced by $f\,z\,\dfrac{d}{dz}$. The equations obtained in this way read as follows:

$$\left.\begin{aligned}
fz\frac{da_o}{dz} &= (1-3\lambda_1)\,a_o + 6\,a_oa_3 - 2\lambda_1 a_2\\
a_1 &= -2\lambda_1 - 2\lambda_2\sqrt{a_o}\\
a_2 &= -\frac{\lambda_2 a_1}{2\sqrt{a_o}}\\
\sum_{n=1}^{N} n\,a_n &= 0\\
\sum_{n=0}^{N} a_n &= 0\\
fz\frac{dJ_k}{dz} &= M_k \quad \text{for} \quad k = 0,1,2,\ldots, N-5
\end{aligned}\right\} \qquad (7.89)$$

In sections 7.9.2 to 7.9.4 the solutions in series of the equations (7.89) will be given.

7.9.2. Series expressions for some functions occurring in the theory.

For pressure- and suction distributions which conform to

$$\lambda_1 = \sum_{p=0}^{\infty} \lambda_{1,p}\, z^p \qquad (7.90)$$

and

$$\lambda_2 = \sum_{p=0}^{\infty} \lambda_{2,p}\, z^p \qquad (7.91)$$

Solutions of the equations (7.89) will be sought of the form

$$a_n = \sum_{p=0}^{\infty} a_{n,p}\, z^p \qquad (7.92)$$

To do this some functions occurring in the equations have to be expressed in the form of a power series in z. This will be done in the present section.

For $\sqrt{a_o}$ the following series is used

$$\sqrt{a_o} = \sum_{p=0}^{\infty} r_p \, z^p \tag{7.93}$$

where the r_p follow from:

$$r_o = \sqrt{a_{o,o}} \tag{7.94}$$

$$r_p = \frac{a_{o,p}}{2\, r_o} - \sigma_p \quad \text{for} \quad p > 0 \tag{7.95}$$

in which for p even and $\geqslant$ 2

$$\sigma_p = \frac{(r_{p/2})^2}{2\, r_o} + \frac{1}{r_o} \sum_{i=1}^{\frac{p}{2}-1} r_i r_{p-i} \tag{7.96}$$

and for p odd and 1

$$\sigma_p = \frac{1}{r_o} \sum_{i=1}^{\frac{p-1}{2}} r_i r_{p-i} \tag{7.97}$$

The sums in (7.96) and (7.97) must be omitted when the upper bound is smaller than 1.

The series development (7.93) is not possible for $a_{o,o} = 0$; this means that the series method is not applicable in cases where the boundary layer starts at $\bar{x} = 0$ with a separation point. As such a boundary layer cannot easily be imagined this seems no real limitation of the method.

Other series expressions to be used are the following

$$\left.\begin{aligned}
J_k &= \sum_{p=0}^{\infty} J_{k,p} \, z^p \\
P_k &= \sum_{p=0}^{\infty} P_{k,p} \, z^p \\
Q_k &= \sum_{p=0}^{\infty} Q_{k,p} \, z^p \\
M_k &= (1-3\,\lambda_1) J_k - \lambda_1 P_k + Q_k = \sum_{p=0}^{\infty} M_{k,p} \, z^p
\end{aligned}\right\} \tag{7.98}$$

$$\left.\begin{aligned}
J_{k,p} &= \sum_{n=0}^{N} j_{k,n}\, a_{n,p} \\
P_{k,p} &= \sum_{n=1}^{N} p_{k,n}\, a_{n,p} \\
Q_{k,p} &= \sum_{\ell=0}^{N} \sum_{n=\ell}^{N} \sum_{i=0}^{p} q_{k,\ell,n}\, a_{\ell,i}\, a_{n,p-i} = \\
&= \sum_{\ell=0}^{N} \sum_{n=\ell}^{N} q_{k,\ell,n}\, (a_{\ell,o}\, a_{n,p} + a_{\ell,p}\, a_{n,o}) \\
&+ \sum_{\ell=0}^{N} \sum_{n=\ell}^{N} q_{k,\ell,n} \sum_{i=1}^{p-1} a_{\ell,i}\, a_{n,p-i} \\
M_{k,p} &= J_{k,p} + Q_{k,p} - 3 \sum_{i=0}^{p} \lambda_{1,i}\, J_{k,p-i} \\
&- \sum_{i=0}^{p} \lambda_{1,i}\, P_{k,p-i}
\end{aligned}\right\} \quad (7.99)$$

The coefficients $j_{k,n}$, $p_{k,n}$ and $q_{k,\ell,n}$ follow from equations (7.55). If the series expressions given above are inserted into the equations (7.89) and the coefficients of successive powers p of z are equated to zero a set of algebraic equations is obtained for each value of p. Coefficients in these equations are determined by the $a_{n,j}$ for $j < p$ and by $\lambda_{1,j}$ and $\lambda_{2,j}$ for $j \leqslant p$. For $p = 0$ the set of equations contains non-linear terms and hence is not easy to solve directly; it will be discussed further in section 7.9.3. For $p > 0$ the equations are linear in the unknown $a_{n,p}$ and can be solved easily provided the solutions of the sets of order less than p are known. This will be discussed further in section 7.9.4.

7.9.3. The zero-order terms of the series solution.

For p=0 the following set of equations is obtained

$$\left.\begin{aligned}
(1-3\lambda_{1,0})a_{o,o} + 6\, a_{o,o}\, a_{3,o} - 2\lambda_{1,o}\, a_{2,o} &= 0 \\
2\lambda_{2,0}\sqrt{a_{o,o}} + a_{1,o} + 2\lambda_{1,o} &= 0 \\
2\, a_{2,0}\sqrt{a_{o,o}} + \lambda_{2,o}\, a_{1,o} &= 0 \\
a_{1,o} + 2\, a_{2,o} + \ldots + N\, a_{N,o} &= 0 \\
a_{o,o} + a_{1,o} + a_{2,o} + \ldots\ldots + a_{N,o} &= 0 \\
M_{k,o} = (1-3\lambda_{1,o})\, J_{k,o} - \lambda_{1,o}\, P_{k,o} + Q_{k,o} &= 0 \\
(\text{for } k = 0,1,2,\ldots,N-5)
\end{aligned}\right\} \quad (7.100)$$

In the last equation $J_{k,o}$; $P_{k,o}$ and $Q_{k,o}$ follow from equations (7.99) for p = 0. The equations (7.100) are non-linear due to the occurrence of $\sqrt{a_{o,o}}$; $a_{o,o}\, a_{3,o}$ and the $Q_{k,o}$ which contain quadratic terms in the $a_{n,o}$. However, a comparison with equations (7.74) shows that the solution for p=0 corresponds to the similar solution for $\lambda_1 = \lambda_{1,o}$ and $\lambda_2 = \lambda_{2,o}$.
These similar solutions have been discussed already in section 7.8 and hence the solutions of (7.100) can be considered as known.
From the preceding remarks it follows that the present approximate method reproduces the result known from exact solutions (see chapter 3) in this respect that a boundary layer for which $\overline{U}(\overline{x})$ and $\overline{v}_o(\overline{x})$ are given by (7.86) and (7.88) with f=1, starts at $\overline{x} = 0$ as a similar boundary layer.

7.9.4. The terms of order $p > 0$ of the series solution.

For $p > 0$ the following set of equations is obtained

$$(fp-1 + 3\lambda_{1,o} - 6\, a_{3,o})a_{o,p} + 2\lambda_{1,o}\, a_{2,p} - 6\, a_{o,o}\, a_{3,p}$$
$$= -3\sum_{i=1}^{p} \lambda_{1,i}\, a_{o,p-i} + 6\sum_{i=1}^{p-1} a_{o,i}\, a_{3,p-i} - 2\sum_{i=1}^{p} \lambda_{1,i}\, a_{2,p-i}$$

$$\frac{\lambda_{2,o}}{r_o}\, a_{o,p} + a_{1,p} = 2\lambda_{2,o}\,\sigma_p - 2\lambda_{1,p} - 2\sum_{i=1}^{p} \lambda_{2,i}\, r_{p-i}$$

$$\left.\begin{array}{l}
\dfrac{a_{2,o}}{r_o} a_{o,p} + \lambda_{2,o} a_{1,p} + 2 r_o a_{2,p} = \\
\qquad = 2 \sigma_p a_{2,o} - 2 \sum_{i=1}^{p-1} a_{2,i} r_{p-i} - \sum_{i=1}^{p} \lambda_{2,i} a_{1,p-i} \\
\sum_{n=1}^{N} n a_{n,p} = 0 \\
\sum_{n=0}^{N} a_{n,p} = 0 \\
\text{and for } k = 0,1,2,\ldots, N-5 \\
(fp-1 + 3\lambda_{1,o}) \sum_{n=0}^{N} j_{k,n} a_{n,p} + \lambda_{1,o} \sum_{n=1}^{N} p_{k,n} a_{n,p} \\
\qquad - \sum_{\ell=0}^{N} \sum_{n=\ell}^{N} q_{k,\ell,n} (a_{\ell,o} a_{n,p} + a_{n,o} a_{\ell,p}) = \\
\qquad = -3 \sum_{i=1}^{p} \lambda_{1,i} J_{k,p-i} - \sum_{i=1}^{p} \lambda_{1,i} P_{k,p-i} + \\
\qquad + \sum_{\ell=0}^{N} \sum_{n=\ell}^{N} q_{k,\ell,n} \sum_{i=1}^{p-1} a_{\ell,i} a_{n,p-i}
\end{array}\right\} \quad (7.101)$$

From an inspection it follows that the equations are linear in the $a_{n,p}$ with coefficients depending only on p and the leading-edge conditions (These leading-edge conditions depend on $\lambda_{1,o}$; $\lambda_{2,o}$ and N; they are given by the quantities with second subscript equal to zero).

The conditions downstream of $\bar{x} = 0$ enter only through the right-hand sides of the equations. Therefore the coefficient matrix of the equations can be inverted once for all for given leading-edge conditions. For a specific example with the same leading-edge conditions the coefficients $a_{n,p}$ can then be obtained by simple multiplications of the right hand sides of the equations with universal constants obtained from the inverse matrix.

This is analogous to what happens in Görtler's method where universal functions are used which only depend on the leading-edge conditions.

In the present approximate method it is of no use to calculate and store the universal constants for a whole series of leading-edge conditions and values of p. It is easier to store the values of the $a_{n,o}$ corresponding to given $\lambda_{1,o}$; $\lambda_{2,o}$ and N (which in fact corresponds to the solutions for p = 0) together with a machine-program which calculates the $a_{n,p}$ for successive values of $p > 0$.

7.9.5. Comparison of the new series method with existing series methods.

From the preceding sections it follows that the series solution for the present approximate method displays several features of the exact methods discussed in chapter 3. Some important points are listed below.

Both in the exact and approximate methods the zero-order terms correspond to one of the similar solutions. In the exact methods this solution follows from a non-linear ordinary differential equation whereas in the approximate method a set of non-linear algebraic equations has to be solved.
For the exact methods further terms of the series solution are obtained from linear ordinary differential equations in which the coefficients depend on the leading-edge conditions only. The full solution is obtained by multiplication of the universal functions with constants depending on the pressure- and suction distributions downstream of $\bar{x} = 0$. In the approximate method the terms of higher order follow from a set of linear algebraic equations. The coefficient matrix of these equations only depends upon the leading-edge conditions and the order of the terms to be found.
An advantage of the present approximate method above the exact series methods is, that the calculation of higher order terms is so simple that it can be done anew for each example to be calculated whereas in the exact methods a considerable number of universal functions has to be tabulated.
A further advantage of the present series method is that the same quantities are used as in the step by step method discussed in section 7.7. Hence the series method need only be used near $\bar{x} = 0$ to start the calculation. As soon as the series is no longer sufficiently convergent the boundary layer calculation may be continued using the step by step method. In existing series methods however, an entirely different method

is used for the continuation in regions where the series is not sufficiently convergent. Such a continuation is always necessary near separation.

7.10. Calculation of some characteristic boundary layer parameters from the coefficients a_n.

In the present method the boundary layer calculation is reduced to the determination in terms of $\bar{x}$ of the coefficients a_n in the polynomial expression (7.29). The familiar boundary layer parameters can easily be calculated from these coefficients. The related formulae will be summarised in the present section.

Once the a_n are known the shear stress may be calculated from (7.29). Then the velocity profile follows from

$$\bar{y} = \frac{y}{\delta} = \frac{y}{x}\sqrt{\frac{Ux}{\nu}} = \int_0^{\bar{u}} \frac{d\bar{u}}{\bar{\tau}} \qquad (7.102)$$

The parameters δ^*, θ and as defined by (2.18), (2.19) and (2.22) are given by

$$\left.\begin{aligned}
\frac{\delta^*}{x}\sqrt{\frac{Ux}{\nu}} &= \frac{\delta^*}{\delta} = \int_0^1 \frac{(1-\bar{u})}{\bar{\tau}}\,d\bar{u} \\
\frac{\theta}{x}\sqrt{\frac{Ux}{\nu}} &= \frac{\theta}{\delta} = \int_0^1 \frac{\bar{u}(1-\bar{u})}{\bar{\tau}}\,d\bar{u} \\
\frac{\varepsilon}{x}\sqrt{\frac{Ux}{\nu}} &= \frac{\varepsilon}{\delta} = \int_0^1 \frac{\bar{u}(1-\bar{u}^2)}{\bar{\tau}}\,d\bar{u}
\end{aligned}\right\} \qquad (7.103)$$

The integrals in (7.103) can be found numerically using Simpson's rule for instance. The integrals have to be evaluated with some care near $\bar{u} = 1$ because $\bar{\tau} \longrightarrow 0$ for $\bar{u} \longrightarrow 1$. Therefore, in the examples to be discussed in chapter 8, the integrals were calculated using Simpson's rule from $\bar{u} = 0$ to $\bar{u} = 0{\cdot}99$. For $0{\cdot}99 \not\leqslant \bar{u} \leqslant 1.00$ the integrals were calculated as follows.

Because $\bar{\tau} \to 0$ like $1-\bar{u}$ for $\bar{u} \to 1$ (see section 7.2) the following approximation for $\bar{\tau}$ may be made in the interval $0.99 \leqslant \bar{u} \leqslant 1$

$$\bar{\tau} = 100\ \bar{\tau}_{0.99}\ (1-\bar{u}) \tag{7.104}$$

Now, using (7.104) the integrals in (7.102) and (7.103) can be found analytically for $0.99 \leqslant \bar{u} \leqslant 1$ and hence the equations reduce to

$$\left.\begin{aligned}
\frac{y}{x}\sqrt{\frac{Ux}{\nu}} &= \int_0^{0.99} \frac{d\bar{u}}{\bar{\tau}} - \frac{1}{100\ \bar{\tau}_{0.99}}\ \ln\ 100(1-\bar{u}) \\
\frac{\delta^*}{x}\sqrt{\frac{Ux}{\nu}} &= \int_0^{0.99} \frac{(1-\bar{u})d\bar{u}}{\bar{\tau}} + \frac{10^{-4}}{\bar{\tau}_{0.99}} \\
\frac{\theta}{x}\sqrt{\frac{Ux}{\nu}} &= \int_0^{0.99} \frac{\bar{u}(1-\bar{u})d\bar{u}}{\bar{\tau}} + \frac{0.995\ 10^{-4}}{\bar{\tau}_{0.99}} \\
\frac{\varepsilon}{x}\sqrt{\frac{Ux}{\nu}} &= \int_0^{0.99} \frac{\bar{u}(1-\bar{u}^2)d\bar{u}}{\bar{\tau}} + \frac{1.985033\ 10^{-4}}{\bar{\tau}_{0.99}}
\end{aligned}\right\} \tag{7.105}$$

Once the integrals have been calculated all parameters of interest can easily be found.

.11. Some related methods known from the literature.

In the literature two methods are found which have some features in common with the present method. However, for so far known to the author they have not been worked out in as much detail as the present method. The first one is due to Trilling [79] who starts from Crocco's equation in the form (7.10), the compatibility condition at the wall (7.42) and the condition at the edge of the boundary layer

$$\bar{\tau} = 0 \quad \text{for} \quad \bar{u} = 1 \tag{7.106}$$

Furthermore the following approximation for τ is used

$$\tau = \tau_o + \tau_1\bar{u} + \tau_2\bar{u}^2 + \ldots . + \tau_6\bar{u}^6 \tag{7.107}$$

Substituting (7.107) into (7.10) and (7.42) and using (7.106) leads to an ordinary differential equation for $\tau_o(x)$ which contains the known functions $v_o(x)$, $\frac{dU}{dx}$ and their derivatives with respect to x. The application of the method seems rather cumbersome; only one example has been given in [79].

The second method has been designed by Dorodnitsyn [80]. In his method the von Kármán-Pohlhausen momentum equation (2.15) is used together with some related moment equations of the type 2.14 . The resulting equations are written in terms of τ, $\frac{1}{\tau}$ and $\bar{u}$.
Then, solutions of the equations are sought of the form

$$\frac{1}{\tau} = \frac{1}{(1-\bar{u})} \quad (a_o + a_1\bar{u} + a_2\bar{u}^2 + \ldots\ldots) \tag{7.108}$$

$$\tau = (1-\bar{u}) \quad (b_o + b_1\bar{u} + b_2\bar{u}^2 + \ldots\ldots) \tag{7.109}$$

The coefficients a_i and b_i in (7.108) and (7.109) are expressed in the values of τ at some equidistant values of $\bar{u}$.
It is shown in [80] that a good agreement is obtained for the similar boundary layers corresponding to $\bar{U} = u_1\, \bar{x}^{m_1}$.

8. Some applications of the new calculation methods.

8.1. Introductory remarks.

The present chapter contains some applications of the new calculation methods discussed in chapters 5 and 7. The results will be compared to available exact solutions. If for a specific example no results of the momentum method are quoted they have been presented already in chapter 5.

8.2. The flat plate without suction.

For the flat plate without suction $\frac{d\bar{U}}{d\bar{x}} = v_o = 0$ and hence equations (7.58) and (7.59) show that $\lambda_1 = \lambda_2 = 0$. Equations (7.62) and (7.63) then lead to $a_1 = a_2 = 0$ while from (7.61) it follows that $a_3 = -{}^1/6$ if a similar solution with $\frac{da_o}{d\bar{x}} = 0$ is to be obtained.

The values of a_o, a_4, a_5, ... are determined by equations (7.64) to (7.66). It is noted that the equations are non-linear and therefore may possess several solutions. For instance, a solution of the complete set of equations (7.61) to (7.66) is $a_n \equiv 0$ for all values of N which however is physically unrealistic. For N = 4 no moment equations are needed and the remaining equations (7.61) to (7.65) have only one solution in addition to the irrelevant one $a_n = 0$. The solution is found to be $a_o = {}^1/24 = 0.041667$; $a_1 = a_2 = 0$; $a_3 = -{}^1/6$ and $a_4 = {}^1/8$. From Blasius' theory, discussed in section 3.1.3, it is known that $a_o = \frac{\tau_o x}{\mu U} \sqrt{\frac{\nu}{Ux}} = 0.33206$ or $a_o = 0.11026$ which shows that the approximation to the exact solution is rather poor for N = 4. A substantial improvement is obtained however for $N > 4$, which implies the use of moment equations. Results for N = 5 to 9 were obtained, using the procedures outlined in section 7.8; as starting value for a_o in the iteration method $a_o = 0.11$ was used throughout. Since the final results for the a_n show a regular pattern (see table 8.1) it was easy to estimate good starting values for the other a_n's at $N = N_1$ once the results for $N < N_1$ were known.
It may be remarked that no difficulties were encountered from the occurrence of multiple solutions; in a wide region around the relevant one there were no other solutions.

Values for the a_n's at different values of N have been collected in table 8.1. From the formulae given in section 7.10 the functions $S(\bar{u})$, the velocity profiles and some familiar boundary layer parameters were calculated. The results are given in table 8.2 and figs 8.1 and 8.3. All data show a monotonic convergence towards the exact solution with increasing values of N. However, the convergence slows down for $N > 7$ and therefore it seems to be of little use to go beyond N = 7 or 8 for practical applications. Table 8.2. and fig. 8.3. show, that in this way the usual boundary layer parameters are predicted within a few percent of the exact values.

The results, given in table 8.2, suggest that the differences with the exact solution are approximately halved if N is increased from 6 to 7 or from 7 to 8. Hence to obtain a more accurate result from the values for N = 6 and 7 corrected values for N = 7 - to be denoted by $N = 7^*$ - may be determined from

$$a_n^* = 2(a_n)_{N=7} - (a_n)_{N=6} \tag{8.1}$$

The corrected results, obtained in this way, have been included in tables 8.1 and 8.2. The $S(\bar{u})$ and velocity profiles for $N = 7^*$ are found to be so close to the exact solution that they have not been shown in fig. 8.1.

8.3. The plane stagnation point without suction.

For the plane stagnation point the potential flow velocity distribution is given by $\bar{U} = u_1\bar{x}$ (equation 3.19). Hence it follows that $\lambda_1 = 1$ and since $v_o = 0$ the suction parameter λ_2 is equal to zero.

Results for different values of N have been determined in the same way as described in section 8.2 for the flat plate. The final results have been collected in tables 8.3 and 8.4 and figs 8.2 and 8.3.

It follows that the approximation to the exact solution is better than for the flat plate. Again more accurate results can be obtained from the results for N = 6 and 7 using equation (8.1). The results for $N = 7^*$, 8, 9 and 10 are so close to the exact values that they could not be shown in fig. 8.2.

8.4. Hartree's boundary layers without suction.

For the Hartree boundary layers the pressure distribution is defined by $\bar{U} = u_1 \bar{x}^{m_1}$ (see equation 3.1 and section 3.1.2.). Hence it follows that $\lambda_1 = m_1$ and equation (3.4) then gives

$$\lambda_1 = \frac{\beta}{2-\beta} \tag{8.2}$$

For several values of β between $\beta = 1$ (plane stagnation point) and $\beta = -0.198838$ (separation according to the exact solution) calculations have been made in the same way as described in sections 8.2 and 8.3 for the special cases $\beta = 0$ and $\beta = 1$. Results for a_o, which is essentially the square of the wall shear stress, are shown in figs 8.5a and 8.5b. It follows that a_o converges monotonically towards the exact solution for $\beta > -0.06$. Near separation however, ($\beta < -0.06$) a_o first decreases when N is increased from 5 to 6 and then increases towards the exact solution. Detailed results for $\beta = -0.16$ are given in table 8.5 while the velocity profiles are shown in fig. 8.6. It follows that not only a_o but also other relevant parameters show a non-monotonic convergence to the exact solution.
Figs 8.7 and 8.8 show the exact values of $S = \bar{\tau}^2$ and $\bar{\tau}$ as function of $\bar{u}$ for a series of values for β.
From fig. 8.8 it is seen that $\bar{\tau}$ behaves like $\sqrt{\bar{u}}$ near the wall ($\bar{u} = 0$) for the separation profile. This illustrates the advantage of using $\bar{\tau}^2$ instead of $\bar{\tau}$ as dependent variable.

8.5. The flat plate with $v_o \sim x^{-\frac{1}{2}}$.

For this similar solution (see section 5.4.4) $\lambda_1 = 0$ and $\lambda_2 = \frac{-v_o}{U}\sqrt{\frac{Ux}{\nu}}$ is an arbitrary constant.
Both from the exact solution and from the momentum method (see section 5.4.4) it is known that for this flow the boundary layer tends to the asymptotic suction layer for $\lambda_2 \to \infty$. This result also holds for the multimoment method. For $\lambda_2 = 0$ of course the flat plate without suction, discussed in section 8.2, is obtained.
For other values of λ_2 calculations were performed for different values

of N; the parameter a_o for N = 5 is shown in fig. 8.4 and compared to the exact results due to Thwaites [66] and Schlichting-Bussmann (quoted by Mangler [37]). Only the results for N = 5 are shown in the figure since those for higher values of N are close to the exact solution.

8.6. The plane stagnation point with constant suction velocity.

For the plane stagnation point $\lambda_1 = 1$ (see section 8.3) and to obtain a similar solution $\lambda_2 = \frac{-v_o}{U}\sqrt{\frac{Ux}{\nu}}$ should be constant. For $\lambda_2 = 0$ the plane stagnation point without suction is obtained while for $\lambda_2 \rightarrow \infty$ the asymptotic suction layer is found.
Results of the multimoment method for N = 5 are shown in fig. 8.9 and compared to the exact solution of Schlichting-Bussmann (quoted by Mangler [37]).

8.7. Howarth' boundary layer flow for $\overline{U} = 1 - \overline{x}$ without suction.

8.7.1. General.

In [44] Howarth studied the boundary layer flow corresponding to a main stream velocity U defined by

$$U = b_o - b_1 x \tag{8.4}$$

in which b_o and b_1 are constants. Defining the reference speed U_∞ and -length c by

$$U_\infty = b_o \quad \text{and} \quad c = \frac{b_o}{b_1} \tag{8.5}$$

equation (8.4) reduces to

$$\overline{U} = 1 - \overline{x} \tag{8.6}$$

This boundary layer was calculated by Howarth using a series method with the following expansion for the stream function

$$\psi = \sqrt{2\, U_\infty \nu\, x}\,\left[f_o(\eta) + \overline{x}\, f(\eta) + \overline{x}^2\, f_2(\eta) + \ldots\right] \tag{8.7}$$

in which

$$\eta = \sqrt{\frac{U_\infty}{2\nu x}}\; y \tag{8.8}$$

(see also section 3.2.3.).

The function $f_o(\eta)$ was shown to satisfy the Blasius equation (3.14) while the functions $f_n(\eta)$ for $n > 1$ had to be calculated from a set of linear differential equations. Howarth calculated the functions f_n for $n \leqslant 6$ which however was not sufficient for an accurate determination of the separation point. Therefore the result was improved as follows. It was noted by Howarth that the functions $f_5(\eta)$ and $f_6(\eta)$ have the same shape and this led him to assume that all f_n for $n \geqslant 5$ are the same in shape so that equation (8.7) can be written in the form

$$\psi = \sqrt{2U_\infty \nu\, x}\left[\sum_{0}^{6} \bar{x}^{n}\, f_n(\eta) + A(\bar{x})\; f_6(\eta)\right] \tag{8.9}$$

The function $A(\bar{x})$ is different from zero only in regions where the series (8.7) is not sufficiently convergent using 7 terms only; this occurs near separation. The function $A(\bar{x})$ was determined by Howarth from the requirement that (8.9) should satisfy the von Kármán momentum equation (2.15). In this way separation was found at $\bar{x} = 0.120$; this result was confirmed from later calculations made by Hartree [81], Tani [45], Leigh [82] and Terrill [83].

8.7.2. The momentum method.

For $\bar{U} = 1 - \bar{x}$ the momentum equation (5.18) can be written in the form

$$\frac{d\bar{\theta}^2}{d\bar{x}} = \frac{M}{1-\bar{x}} \tag{8.10}$$

which can be integrated to

$$-\ln\,(1-\bar{x}) = \int_{o}^{\bar{\theta}^2} \frac{d\bar{\theta}^2}{M} \tag{8.11}$$

From $\bar{U} = 1 - \bar{x}$ it follows that in this case the pressure gradient

parameter $\Lambda_1 = \bar{\theta}^2 \dfrac{d\bar{U}}{d\bar{x}}$ reduces to $\Lambda_1 = -\bar{\theta}^2$. Since in the no-suction case M is a function of Λ_1 only (see table 5.3 and fig. 5.6) this parameter can also be considered as a function of $\bar{\theta}^2$. Hence the integral (8.11) can easily be calculated. Some results are shown in fig. 8.10 and compared to the exact solution due to Howarth. Separation is found at $\bar{x} = 0.123$ as compared with $\bar{x}_{sep} = 0.120$ for the exact solution.
A comparison of the velocity profiles for $\bar{x} = 0.10$ and 0.12 is shown in fig. 8.11.

8.7.3. The multi-moment method.

For $\bar{U} = 1 - \bar{x}$ the pressure gradient parameter λ_1 becomes

$$\lambda_1 = \frac{\bar{x}}{\bar{U}} \frac{d\bar{U}}{d\bar{x}} = \frac{-\bar{x}}{1-\bar{x}} \tag{8.12}$$

and hence the power series expansion (7.80) for λ_1 is easily found to be

$$\lambda_1 = -\bar{x} - \bar{x}^2 - \bar{x}^3 - \bar{x}^4 \; . \; . \; . \; . \; . \tag{8.13}$$

Since the zero-order term in (8.13) is absent it follows that the boundary layer at $\bar{x} = 0$ will start as the similar solution for which $\lambda_1 = 0$; this is the flat plate boundary layer, discussed in section 8.2. Therefore the zero-order terms of the expansion for a_n follow from table 8.1.
Results for a_o at N = 7 and different orders p of the series solution are shown in fig. 8.12. It follows that the series converges well until very close to separation. Included in the figure as a dotted line is the result of a step by step calculation started at $\bar{x} = 0.08$.
Fig. 8.12 shows that in the step by step solution zero skin friction is only asymptotically reached. This behaviour is caused by equation (7.61) which for zero suction ($a_2 = \lambda_2 = 0$) reduces to

$$\frac{da_o}{d\bar{x}} \longrightarrow 0 \qquad \text{for} \qquad a_o \longrightarrow 0 \tag{8.14}$$

This anomalous behaviour is the prize to be paid for the convenience of using equation (7.61) which gives an easy means to determine a_o. In section 8.14 this difficulty will be discussed further.
Results for different values of N have been collected in fig. 8.13; in each case the series method was used from $\bar{x} = 0$ to 0.08 including terms of the 10th degree in $\bar{x}$. Downstream of $\bar{x} = 0.08$ the step by step method was used; for all values of N differences between the series- and step by step solutions became noticeable only for $\bar{x} > 0.10$. Included in fig. 8.13 are the values of a_o according to the exact solution.
It should be noted that far from separation there is a monotonic convergence to the exact solution with increasing N. Near separation however, the convergence is of the type displayed by the Hartree flows for $\beta < -0.06$.
A comparison of figs 8.10 and 8.13 shows that the momentum method and the multimoment method with N = 8 have about the same accuracy for a_o. Results of Görtler's series for $\sqrt{a_o}$ and a_o are given in fig. 8.14 and 8.15. It follows that Görtler's method, which is exact at $\bar{x} = 0$, is not very accurate near separation due to lack of convergence. The present series method is in this region at least equally accurate and moreover easily allows a step by step continuation.
Finally fig. 8.16 shows, to a large scale, results for a_o in the region near separation according to different methods.

8.8. Tani's boundary layers for $\bar{U} = 1 - \bar{x}^j$.

Using essentially Howarth' procedure (see section 8.7.1) the boundary layer flows for

$$\bar{U} = 1 - \bar{x}^j \tag{8.15}$$

have been calculated by Tani [45] for j = 2, 4 and 8. The position of the separation point obtained in this way is shown in table 8.6.

For $\overline{U} = 1 - \overline{x}^j$ without suction $\lambda_2 = 0$ while λ_1 becomes

$$\lambda_1 = \frac{\overline{x}}{\overline{U}} \frac{d\overline{U}}{d\overline{x}} = - \sum_{i=1}^{\infty} j\left(\overline{x}^j\right)^i \qquad (8.16)$$

Introducing a new variable z according to equation (7.79) with f = j, equation (8.16) may be written in the form

$$\lambda_1 = - \sum_{p=1}^{\infty} j\ z^p \qquad (8.17)$$

Since (8.16) and (8.17) do not contain a zero-order term it follows that the multimoment method reproduces the result from exact theory that Tani's boundary layers start at $\overline{x} = 0$ in the same way as the Blasius boundary layer.

Detailed results of the multimoment method with N = 7 for $\overline{U} = 1 - \overline{x}^2$ are shown in fig. 8.17. It follows that the series solution including terms with $\overline{x}^{20}$ gives a good correspondence with the step by step solution until close to separation.

Final results for N = 5, 6 and 7 are shown in fig. 8.18 where also a comparison is made with the exact solution due to Tani. It is seen that an accurate extimate of the position of separation can be obtained from a linear extrapolation of a_o for $\overline{x} < 0.26$.

In the same way results have been obtained for j = 4 and 8. The positions of separation for j = 1, 2, 4 and 8 at N = 7 are collected in table 8.6.

8.9. The boundary layer on a circular cylinder without suction: $\overline{U} = \sin \overline{x}$.

8.9.1. General.

Boundary layer calculations for the pressure distribution corresponding to potential flow around a circular cylinder have been made by many authors. Possibly the most accurate result has been obtained to date by Terrill [83], using a numerical procedure.

For this flow the velocity U is given by (see fig. 8.19)

$$U = 2V \sin \varphi = 2V \sin\left(\frac{x}{R}\right) \qquad (8.18)$$

If the reference speed and -length U_∞ and c are defined by

$$U_\infty = 2V \quad ; \qquad c = R \tag{8.19}$$

equation (8.18) reduces to

$$\overline{U} = \sin \overline{x} \tag{8.20}$$

8.9.2. The momentum method.

For small $\overline{x}$ equation (8.20) reduces to $\overline{U} = \overline{x}$ which shows that the boundary layer on the circular cylinder starts near $\overline{x} = 0$ as the plane stagnation point flow. Hence starting values for the step by step calculation can be obtained from section 5.4.2. Results for a_o are shown in fig. 8.20 and compared to the exact solution due to Terrill. The momentum method gives separation at $\overline{x} = 1.78$ while the accurate value is 1.823.

8.9.3. The multimoment method.

With $\overline{U} = \sin \overline{x}$ the expression for λ_1 becomes

$$\lambda_1 = \frac{\overline{x}}{\overline{U}} \frac{d\overline{U}}{d\overline{x}} = \overline{x} \frac{\cos \overline{x}}{\sin \overline{x}} \tag{8.21}$$

which can be developed in the following power series

$$\lambda_1 = 1 - \frac{1}{3}\overline{x}^2 - \frac{1}{45}\overline{x}^4 - \frac{2}{945}\overline{x}^6 - \frac{1}{4725}\overline{x}^8 - \frac{2}{93555}\overline{x}^{10} \ldots\ldots \tag{8.22}$$

Since in (8.22) the zero order term is 1 the boundary layer starts at $\overline{x} = 0$ in the same way as the plane stagnation point without suction discussed in section 8.3. Hence, the zero-order terms of the series for a_n can be obtained from table 8.3. Results of the series method up till and including terms with $\overline{x}^{10}$ have been obtained for N = 5, 6 and 7. The series (8.22) contains only terms of even order and hence this is also the case with the resulting series for a_n. Results for a_o at N = 7 and different orders of the approximation are shown in fig. 8.20; the curve for p = 8 which is not shown lies between those for p = 6 and 10. Results of a step by step calculation started at $\bar{x} = 1.50$ are shown as a dotted line in fig. 8.20. It follows from the figure that only near separation the step by step solution differs from the series solution for p = 10. It should be emphasized that - in principle - the present series method can be used to much higher orders p which certainly would improve the correspondence between the step by step- and the series solution. However, this has not been done in the present example since it is very easy to continue with the step by step calculation.

Results for N = 5 and 6 are very close to those for N = 7 and therefore have not been given in fig. 8.20. Only near separation the solutions for N = 5 and 6 lay slightly above those for N = 7.

Included in fig. 8.20 are the exact results due to Terrill; for this solution separation occurs at $\bar{x} = 1.823$. It is seen that the multimoment method for N = 7 accurately approximates the exact solution except very near separation. However, with a short linear extrapolation of a_o for $\bar{x} < 1.80$ an accurate estimate of the separation point is obtained.

Results obtained from Görtler's series are shown in fig. 8.21 and 8.22; the figure for $\sqrt{a_o}$ is included since Görtler's method employs variables which express the wall shear stress in a parameter equivalent to $\sqrt{a_o}$ instead of a_o.

A comparison of figs 8.21 and 8 22 clearly shows the advantage of using $\bar{\tau}^2$ instead of $\bar{\tau}$ (and hence a_o instead of $\sqrt{a_o}$) as dependent variable. Near a separation point $\bar{x}_{sep}$, the function a_o behaves like

$$a_o \backsimeq (\bar{x} - \bar{x}_{sep})^1 \tag{8.23}$$

and hence

$$\sqrt{a_o} \backsimeq (\bar{x} - \bar{x}_{sep})^{\frac{1}{2}} \tag{8.24}$$

(see also Goldstein [84] and Terrill [83]).

Of course it is easier to approximate (8.23) with a series than (8.24). From a comparison of figs 8.20 and 8.21 it follows that both the momentum method and the multimoment method give a better accuracy near separation than Görtler's method.

.10. Curle's boundary layer flow for $\overline{U} = \overline{x} - \overline{x}^3$.

.10.1. General.

The boundary layer flow for the pressure distribution defined by

$$\overline{U} = \overline{x} - \overline{x}^3 \tag{8.25}$$

has been calculated by Curle [85] using Howarth' procedure, described in section 8.7.1. For this boundary layer separation was found at $\overline{x} = 0.655$.

.10.2. The momentum method.

For small values of $\overline{x}$ equation (8.25) reduces to $\overline{U} = \overline{x}$ and hence the boundary layer starts as the plane stagnation point. Hence the step by step calculation can be started at a small distance from the stagnation point ($\overline{x} = 0$) with a starting value for $\overline{\Theta}$ obtained from section 5.4. Results for a_o are shown in fig. 8.23 and compared to the exact solution; separation is predicted at $\overline{x} = 0.640$.

.10.3. The multi-moment method.

With $\overline{U} = \overline{x} - \overline{x}^3$ the series expansion for λ_1 becomes

$$\lambda_1 = 1 - 2\,\overline{x}^2 - 2\,\overline{x}^4 - 2\,\overline{x}^6 \;.\;.\;.\;. \tag{8.26}$$

which again shows that the boundary layer starts at $\overline{x} = 0$ as the plane stagnation point. Calculations have been performed for N = 5, 6 and 7 using the series method from $\overline{x} = 0$ to 0.55 and the step by step method downstream of $\overline{x} = 0.55$. Final results for N = 7 are shown in fig. 8.23 where also the exact solution is shown. Results for N = 5 and 6 are so close to those for N = 7 that the differences cannot be shown in the figure except very close to separation. Only the results for N = 5 are shown, those for N = 6 are between those for N = 5 and 7. It follows that the multimoment method gives a very good approximation to the exact solution. Also near separation the accuracy is gradually improved with increasing N. Although for this example again separation is reached with

$\frac{da_o}{d\bar{x}} \rightarrow 0$ the curve for a_o bends so sharply into the horizontal axis, especially for N = 7, that a short linear extrapolation is sufficient to provide an accurate determination of the separation point. From a large scale version of fig. 8.23 the value of $\bar{x}$ at separation was found to be $\bar{x}$ = 0.652 which is very close to the exact value 0.655.

8.11. Iglisch' solution for the flat plate with constant suction velocity.

8.11.1. General.

For the flat plate with constant suction velocity v_o, an exact solution of the boundary layer equations has been given by Iglisch [67]. In this solution a new independent variable $\bar{x}$ is introduced by

$$\bar{x} = \frac{x}{c} = \left(\frac{-v_o}{U}\right)^2 \frac{Ux}{\nu} \tag{8.27}$$

which implies that the reference length c is defined by

$$c = \frac{U\nu}{(-v_o)^2} \tag{8.28}$$

If for the reference speed U_∞ the constant main stream velocity U is used it follows that

$$\bar{U} = \frac{U}{U_\infty} = 1 \tag{8.29}$$

From Iglisch' solution it is known that at $\bar{x}$ = 0 the boundary layer starts as the Blasius boundary layer while for $\bar{x} \rightarrow \infty$ the asymptotic suction layer is obtained.

8.11.2. The momentum method.

Using equations (8.27) to (8.29) it follows that for the present case

$$\bar{v}_o = \frac{-v_o}{U_\infty}\sqrt{\frac{U_\infty c}{\nu}} = 1 \tag{8.30}$$

$$\Lambda_1 = \bar{\theta}^2 \frac{d\bar{U}}{d\bar{x}} = 0 \tag{8.31}$$

and $$\Lambda_2 = \bar{v}_o \, \bar{\Theta} = \bar{\Theta} \tag{8.32}$$

Hence the momentum equation (5.18) reduces to the simple form

$$\frac{d(\Lambda_2^{\,2})}{d\bar{x}} = \ell - \Lambda_2 \tag{8.33}$$

which can be written as

$$\bar{x} = \int_o^{\Lambda_2} \frac{\Lambda_2}{\ell - \Lambda_2} \, d\Lambda_2 \tag{8.34}$$

Since for the flat plate $\Lambda_1 = 0$, the parameter ℓ is a known function of Λ_2 (see chapter 5) and equation (8.34) can easily be integrated numerically. It follows from equation (8.34) that $\bar{x} \rightarrow \infty$ for $\ell \rightarrow \Lambda_2$; this occurs for $\ell = \Lambda_2 = 0.50$ which represents the asymptotic suction profile. Since the momentum method was designed to represent the asymptotic suction layer exactly it follows that the method gives exact results for $\bar{x} \rightarrow \infty$.

For $\bar{x} = 0$ the momentum loss thickness Θ is zero and hence $\Lambda_2 = \frac{-v_o \Theta}{\nu} = 0$; which implies that the boundary layer starts at $\bar{x} = 0$ as that on a flat plate without suction.

Different parameters are shown as a function of $\sqrt{\bar{x}}$ in fig. 8.24 and compared to Iglisch' exact solution and an approximate solution due to Schlichting [55] (see also section 4.3).

.11.3. The multimoment method.

From equations (8.27) and (8.29) it follows that

$$\lambda_1 = \frac{\bar{x}}{\bar{U}} \frac{d\bar{U}}{d\bar{x}} = 0 \tag{8.35}$$

and $$\lambda_2 = \frac{-v_o}{U} \sqrt{\frac{Ux}{\nu}} = \sqrt{\bar{x}} \tag{8.36}$$

This shows that for $\bar{x} = 0$ both λ_1 and λ_2 are zero and hence the multimoment method reproduces the exact result that at $\bar{x} = 0$ the boundary layer starts as that for the flat plate without suction.

It can easily be shown that for $\lambda_1 = 0$ and $\lambda_2 = \sqrt{\bar{x}}$ a solution of equations (7.61) to (7.66) for all $N \geqslant 2$ is

$$\left.\begin{aligned} a_o &= \bar{x} \\ a_1 &= -2\bar{x} \\ a_2 &= \bar{x} \\ a_n &= 0 \qquad \text{for } n \geqslant 3 \end{aligned}\right\} \qquad (8.37)$$

With (7.60) this leads to

$$S = \bar{\tau}^2 = \bar{x}(1-\bar{u})^2 \qquad (8.38)$$

or

$$\frac{\partial \bar{u}}{\partial \frac{y}{x}\sqrt{\frac{Ux}{\nu}}} = \bar{\tau} = \sqrt{\bar{x}}(1-\bar{u}) \qquad (8.39)$$

After integration of (8.39) and using (8.27) it is found that

$$\bar{u} = 1 - e^{\frac{v_o y}{\nu}} \qquad (8.40)$$

This reproduces the asymptotic suction profile discussed in section 3.1.5. Formally the solution (8.37) is valid from $\bar{x} = 0$ to $\bar{x} \rightarrow \infty$; however this would lead to the unrealistic solution $a_n = 0$ for $\bar{x} = 0$ discussed in section 8.2 for the flat plate without suction. Therefore it is expected that the solution (8.37) is only approached asymptotically for $\bar{x} \rightarrow \infty$; this is confirmed by further calculations, to be discussed below.

In view of (8.36) a new variable $z = \sqrt{\bar{x}}$ was used in the series method. Results of the series method for N = 7 are shown in fig. 8.25 where also results of a step by step calculation and the exact solution are shown.

Since $a_o \longrightarrow \bar{x}$ for large values of $\bar{x}$ it is advantageous to plot the quantity $\bar{x}/a_o$ versus $\sqrt{\bar{x}}$. This has been done in fig. 8.26 where results for N = 5, 6 and 7 are compared to the exact solution. In the same figure results of the momentum method have been included for comparison.

From the definitions of a_o and $\overline{x}$ (equation 8.27) it follows that

$$\frac{\overline{x}}{a_o} = \left[\frac{\frac{-v_o \delta^*}{\nu}}{\frac{\tau_o \delta^*}{\mu U}} \right]^2 \qquad (8.41)$$

and hence $\overline{x}/a_o$ can easily be found from the results of fig. 8.24. It is seen from fig. 8.26 that the result of the multimoment method converges well to the exact solution for increasing N. The accuracy for N = 7 is comparable to that of the momentum method. The advantage of the multimoment method is that its accuracy can be improved by increasing N; results for N = 8 are very close to the exact solution.

.12. Rheinboldt's boundary layer on a flat plate with discontinuous suction.

.12.1. General.

Rheinboldt [86] designed a special procedure for the calculation of suction boundary layers with discontinuities in the suction velocity; the method was illustrated with several examples.
The first example discusses the boundary layer on a flat plate with non-porous entry length c followed by a porous region with constant suction for $x > c$ (see fig. 8.27a).
In a second example there is only suction for $c < x < 1.15c$ with a suction velocity v_o given by $\frac{-v_o}{U}\sqrt{\frac{Uc}{\nu}} = 1.5$ (see fig. 8.27b). In what follows c and U will be used as reference length and velocity and hence

$$\overline{x} = \frac{x}{c} \quad \text{and} \quad \overline{U} = 1 \qquad (8.42)$$

.12.2. The momentum method.

The momentum method is found to be unable to cope with large discontinuities in the suction velocity; this may be seen as follows.
For the present case of zero pressure gradient only one independent parameter occurs in the momentum method (see chapter 5); it is convenient to select $\Lambda_2 = \frac{-v_o \theta}{\nu}$ for this parameter.

For the non-porous entry length the flat plate boundary layer without suction occurs which is represented by $\Lambda_2 = 0$. From this solution it is known that $\frac{\Theta}{x}\sqrt{\frac{Ux}{\nu}} = 0.661$ (see table 5.1) and hence $\overline{\Theta} = \frac{\Theta}{c}\sqrt{\frac{Uc}{\nu}} = 0.661$ at $\overline{x} = 1$.

At discontinuities in v_o the momentum loss thickness Θ is supposed to be continuous and hence directly downstream of $\overline{x} = 1$ it is found that

$$\Lambda_2 = \overline{v}_o . \overline{\Theta} = 0.661\ \overline{v}_o$$

If the suction velocity has such a magnitude that $\overline{v}_o = \frac{0.50}{0.661}$ it follows that $\Lambda_2 = 0.50$; this implies that directly downstream of $\overline{x} = 1$ suddenly the asymptotic suction profile would be established. (compare also section 8.11). It can be expected however that in reality the boundary layer will only gradually approach asymptotic conditions.
Similarly the momentum method produces the erroneous result that the boundary layer velocity profile immediately returns to the Blasius shape if the suction is suddenly stopped at some station.
The way in which the boundary layer develops according to the momentum method can easily be calculated as follows.

$$\left.\begin{aligned} &\text{From} && \overline{U} = 1 \\ & && \Lambda_2 = \frac{-v_o\Theta}{\nu} = \overline{v}_o \,.\, \overline{\Theta} \\ & && \Lambda_1 = 0 \\ &\text{and} && \overline{v}_o = \frac{-v_o}{U}\sqrt{\frac{Uc}{\nu}} = \text{constant} \end{aligned}\right\} \qquad (8.44)$$

it is found that the momentum equation (5.18) can be written in the form

$$\overline{v}_o^{\,2}\, d\overline{x} = \frac{\Lambda_2}{\ell - \Lambda_2}\, d\Lambda_2 \qquad (8.45)$$

or after integration

$$\overline{v}_o^{\,2}\,(\overline{x}-1) = \int_{0.661\overline{v}_o}^{\Lambda_2} \frac{\Lambda_2}{\ell - \Lambda_2}\, d\Lambda_2 \qquad (8.46)$$

The integration constant in (8.46) has been chosen in such a way that for $\bar{x} = 1$ the suction parameter Λ_2 has the value 0.661 $\bar{v}_o$ (see equation 8.43). Values of the shape factor H, as determined from equation 8.46; for different values of $\bar{v}_o$ are shown in fig. 8.28 and compared to available results from Rheinboldt's calculation. It is seen that the momentum method is very inaccurate directly downstream of large discontinuities in the suction velocity.

12.3. The multimoment method.

To check the accuracy of the multimoment method for discontinuously varying suction velocity only Rheinboldt's second example will be used. This is the most severe case of the two since here suction is started suddenly at $\bar{x} = 1$ and stopped again at $\bar{x} = 1.15$.

In the non-porous entry length $\bar{x} < 1$ the flat plate boundary layer without suction, discussed in section 8.2, is found. Hence table 8.1 provides the starting values at $\bar{x} = 1$ for the step by step solution. Since the boundary layer changes very rapidly near $\bar{x} = 1$ very small steps had to be used in this region. Fig. 8.29 shows a_o in the suction region for N = 5, 6 and 7; also the exact solution is given in the figure. It is seen that the results for N = 5 and 6 are not very accurate; those for N = 7 agree with the exact solution within the accuracy to which Rheinboldt's results can be read from the graphs in [86].

For the non-porous region downstream of $\bar{x} = 1.15$ only results for N = 7 are shown; a reasonably good correspondence with the exact solution is obtained. It should be noted that far downstream of the porous region again $a_o \longrightarrow 0.106$ which is the value obtained for the flat plate without suction.

13. Schubauer's elliptic cylinder.

13.1. General.

A detailed experimental observation of the laminar boundary layer on an elliptic cylinder has been made by Schubauer [25]. The lengths of the major and minor axes of the cylinder were 11.78 and 3.98 inches respectively. The cylinder was placed in a wind tunnel with its major axis parallel to the flow. The measurements were performed at a windspeed of 11.5 ft/sec which resulted in the low value 72000 for the Reynolds number R_c based on the length of the major axis.

The pressure distribution around the cylinder was measured by means of orifices in the surface. Velocity profiles in the boundary layer were determined using hot wires. From the experiments Schubauer concluded that separation occurred at $\bar{x} = 1.99 \pm 0.02$ where $\bar{x} = x/c$ and c is the length of the minor axis of the cylinder. It was shown by Schubauer that application of Pohlhausen's method to the observed pressure distribution failed to show separation. Later an accurate numerical solution of the boundary layer equations for the observed pressure distribution was obtained by Hartree [26]. Again the theoretical results did not show separation. However, it was also shown by Hartree that a slight modification of the observed pressure distribution was sufficient to predict separation near $\bar{x} = 1.99$.

Due to the uncertainty about the experimentally determined pressure distributions to be used for the calculations it has - for so far the author knows - never been shown conclusively whether or not the boundary layer equations will be able to predict separation for experimentally determined pressure distributions.

In chapter 10 some new measurements will be described which - in agreement with Schubauer's data - show that it is very difficult to assess the validity of the boundary layer equations close to separation from measured pressure distributions. In the next section some results will be presented of calculations with the momentum method and the multimoment method for Schubauer's observed pressure distribution and for the modified distribution.

8.13.2. Results of boundary layer calculations.

Calculations have been made with both new methods for the observed and the modified pressure distribution. To facilitate the computations, values of $\bar{U}$ and $\frac{d\bar{U}}{d\bar{x}}$ taken from [26] have been plotted on a large scale. Then $\bar{U}$ and $\frac{d\bar{U}}{d\bar{x}}$ have been read from the graph for equidistant values of $\bar{x}$;

the results have been colledted in table 8.7. In the table also values for $\lambda_1 = \frac{\bar{x}}{\bar{U}} \frac{d\bar{U}}{d\bar{x}}$, to be used in the multimoment method, are given.
It has been shown by Hartree that near the stagnation point ($\bar{x} = 0$) the values of $\bar{U}$ can be approximated by

$$\bar{U} = 8.7\,\bar{x} - 24\,\bar{x}^2 + 24\,\bar{x}^3 + \ldots. \tag{8.47}$$

which leads to the following expression for λ_1

$$\lambda_1 = 1 - 2.75862\,\bar{x} - 2.0927\,\bar{x}^2 + 1.837\,\bar{x}^3 + 10.84\,\bar{x}^4 + 24.8\,\bar{x}^5 + \ldots. \tag{8.48}$$

To facilitate calculations with the multimoment method the values of λ_1 further downstream have been approximated by polynomial expressions of the form

$$\lambda_1 = \sum_{n=0}^{6} e_n\,\bar{x}^n \tag{8.49}$$

The coefficients e_n have been collected in table 8.8. Fig. 8.30 shows the functions $\bar{U}$, $\frac{d\bar{U}}{d\bar{x}}$ and λ_1 in graphical form.

Results of boundary layer calculations with the momentum method and the multimomentmethod are presented in figs 8.31 to 8.32. Fig. 8.31 shows a_o for the observed pressure distribution according to the momentum method and to the multimoment method for N = 7. Results for N = 5 and 6 are close to those for N = 7 and therefore are not shown in the figure. The same curves are drawn to a larger scale in fig. 8.32 for $1.6 \leqslant \bar{x} \leqslant 2.10$; now also results of the multimoment method for N = 5 and 6 are included.
It can be concluded that the results of the multimoment method for increasing N converge well to Hartree's solution. The accuracy of the momentum method is somewhat less than for the multimoment method at N = 7. However, all methods agree in this respect that they do not show separation.
Similar results for the modified pressure distribution are included.

in fig. 8.32. It is noticed that the momentum method predicts separation at $\bar{x} = 1.92$ as compared to 1.983 for Hartree's calculation and 1.99 ± 0.02 for the experiment. As usual the multimoment method gives no clear indication of separation.
However, if the results for N = 6 and 7 are extrapolated using equation (8.1) the resulting curve comes very close to Hartree's values until near separation.

8.14. Concluding remarks on the new calculation methods.

From the examples discussed in the present chapter the following conclusions may be drawn.

1. The momentum method leads to accurate results as long as no large discontinuities in the suction velocity occur.
2. The accuracy of the multimoment method for N = 7 or 8 is comparable to or better than the accuracy of the momentum method. If discontinuities in the suction velocity occur, the multimoment method retains its accuracy while the momentum method (and all comparable methods) will fail.
3. A more rapid convergence of the multimoment method with increasing N would be desirable near separation.
4. A disadvantage of the multimoment method in the case of no suction is the following.

For the no-suction case $\lambda_2 = 0$ and hence equation (7.61) reduces to

$$\bar{x}\,\frac{da_o}{d\bar{x}} = a_o(1 - 3\lambda_1 + 6\,a_3) \qquad (8.50)$$

This equation shows that near separation where $a_o \longrightarrow 0$ also $\frac{da_o}{d\bar{x}}$ will tend to zero unless $\left|1 - 3\lambda_1 + 6\,a_3\right|$ tends to infinity.
From the results presented in this chapter it may be noticed that indeed $\frac{da_o}{d\bar{x}} \longrightarrow 0$ near separation making it difficult to give an accurate estimate of the position of separation. For some examples (see for instance figs 8.20 and 8.23) it is observed that the curve for a_o bends sharply into the $\bar{x}$-axis especially at high values of N so that

the position of separation can easily be determined from a short extrapolation of the straight part of the curve.

It is suggested by these results that for $N \to \infty$ the derivative $\frac{da_o}{d\bar{x}}$ may tend to a constant non-zero value when separation is approached. This would be in agreement with Goldstein's theory [84]. Equation (8.61) shows that in this case $\left|1-3\,\lambda_1 + 6\,a_3\right|$ has to approach infinity near separation. As an example fig. 8.33 shows $-(1-3\lambda_1 + 6a_3)$ as function of $\bar{x}$ and a_o for $\bar{U} = \sin\bar{x}$ near separation. It is found indeed that $-(1-3\lambda_1 + 6a_3)$ becomes very large for $a_o \to 0$.

In view of these remarks it seems to be worth while to inquire whether the results near separation can be improved by omitting equation (7.61) and replacing it by an additional moment equation.

The modification will slightly complicate the application of the method for the case of suction since then the non-linear factor $\sqrt{a_o}$ appears as unknown parameter in equations (7.62) and (7.63). This possible modification of the method will not be pursued further in the present work however.

9. Stability and transition.

9.1. Introductory remarks.

In the preceding chapters laminar boundary layers have been discussed only. It is known from experiments however, that solutions of the laminar boundary layer equations cannot always be realised in practice because transition to turbulent flow may occur. Fig. 3.3 for instance showed a comparison with experimental results of Blasius' theory for the laminar boundary layer on a flat plate. It is seen that the theory is confirmed by experiments only when the leading-edge of the plate has not been disturbed by a tripping wire and if only those stations on the plate are considered for which the Reynoldsnumber $\frac{Ux}{\nu}$ is less than 3×10^6. At higher Reynoldsnumbers or when the flow is disturbed a turbulent boundary layer is found. From detailed experiments by Schubauer and Skramstad [87] on a smooth plate in a wind tunnel with a degree of turbulence less than 0.1 °/o it is known that the flow is completely laminar when $\frac{Ux}{\nu}$ is less than 2.8×10^6 and fully turbulent for $\frac{Ux}{\nu} > 3.9 \times 10^6$. For intermediate values of $\frac{Ux}{\nu}$ a transition region occurs where the flow passes from laminar to turbulent. A similar behaviour is shown by the flow around airfoil sections or through pipes. Although the phenomenon of transition has been known already since Reynolds' famous experiments on pipe flow in 1883 [88] the mechanism of transition is not yet completely understood. Neither is it possible to predict theoretically for an arbitrary body the position where transition will occur.

For a long time there have been two conflicting opinions about the mechanism of transition. One school of thought supposes that disturbances in the flow outside the boundary layer cause fluctuations inside the boundary layer which lead to local and instantaneous separation followed by transition (Taylor [89]). A different explanation is given by the so called stability theory as developed by Rayleigh, Tollmien, Schlichting, Lin, etc. (see [90] and [7], chapter 16).

In this theory it is shown that small harmonic disturbances in the boundary layer may become unstable and amplify. It is supposed that these disturbances cause transition as soon as they have gained a sufficient amplification. The unstable oscillations, predicted by the stability theory were discovered in wind tunnel experiments on the boundary layer of a flat plate by Schubauer and Skramstad in 1940 [87]. It was found that the stability theory is valid only if the degree of turbulence in the airstream is less than 0.1°/o. For high turbulence levels Taylor's theory is more appropriate. In 1951 the existence of unstable oscillations was also shown in free flight by Malotaux et al. [91]. In the free atmosphere and in modern low speed wind tunnels the degree of turbulence is considerably less than 0.1°/o and it is commonly accepted now that under these circumstances transition on smooth bodies - at least initially - is governed by the stability theory. An exception should be made for cases where the laminar boundary layer separates from the surface due to an adverse pressure gradient. It may be possible that a short distance upstream of the separation point Taylor's transition mechanism is the relevant one. Also transition in the separated layer may be governed by a different mechanism.

This theory shows under which circumstances the laminar boundary layer may become unstable and predicts the initial growth of the disturbances. Since most of the existing theories are linearised by assuming small disturbances they cannot describe the complete transition to the irregular turbulent flow with relatively large disturbances.

Our knowledge of transition has been steadily enlarged however through experiments starting with the investigations by Schubauer and Skramstad. A review of this work may be found in [29]. Some recent results have been described by Hinze et al. [92].

From the experiments it is known that in the transition region suddenly "turbulent spots" are generated. These spots grow and merge as they move downstream until finally at a certain position the flow is fully turbulent [93]. According to Klebanoff and Tidstrom [94] the spots seem to develop from threedimensional concentrations of disturbance energy in the originally two-dimensional disturbance waves.

In the first few sections of the present chapter the main principles and results of linear stability theory will be collected for later use. In the final sections it will be shown that the stability theory may be used to develop a semi-empirical method for the calculation of the transition position on smooth bodies in an airstream with low degree of turbulence. Throughout the present work it is assumed that surface roughness is so small that it will have no influence on transition.

9.2. Principles of linear stability theory.

9.2.1. General.

The stability theory considers a given laminar main flow upon which small disturbances are superimposed. It is assumed that both the undisturbed and the disturbed flow satisfy the Navier-Stokes equations. After linearisation a perturbation equation is obtained which under certain circumstances may possess unstable solutions. It is found that important factors determining the stability or instability are:

the shape of the boundary layer velocity profile

the Reynoldsnumber $\frac{U\delta^*}{\nu}$ and

the frequency or wavelength of the disturbances.

9.2.2. The Orr-Sommerfeld equation.

In what follows a two-dimensional flow is considered which is subjected to a two-dimensional disturbance. It is possible to omit three dimensional disturbances since, according to Squire [95], the instability of incompressible boundary layer flows is initially determined by the two dimensional disturbances. For the stability investigation it is assumed that the u-velocity component of the undisturbed main flow depends only on the wall distance y and that the v component is zero; the pressure p only depends on the streamwise coordinate x. These assumptions hold exactly for pipe- or channel flow and also with a good approximation for boundary layers because here u changes much more rapidly with y than with x. (Pretsch [96]).

On the main flow a disturbance is superimposed with velocity components $u'(x,y,t)$ and $v'(x,y,t)$; the fluctuating pressure component is $p'(x,y,t)$. Hence the combined flow is given by

$$u^*(x,y,t) = u(y) + u'(x,y,t)$$
$$v^*(x,y,t) = \qquad v'(x,y,t) \tag{9.1}$$
$$p^*(x,y,t) = p(x) + p'(x,y,t)$$

If (see for instance [7], chapter 16)

a) equations (9.1) are introduced into the Navier-Stokes equations (2.1) and (2.2) and the continuity equation (2.3);
b) the resulting equations are linearised in the disturbance components;
c) it is observed that also the undisturbed flow should fulfil equations 2.1 - 2.3;
d) the fluctuating pressure component p' is eliminated from two of the resulting expressions;

the following equations remain:

$$\frac{\partial^2 u'}{\partial t \partial y} - \frac{\partial^2 v'}{\partial t \partial x} + u\left(\frac{\partial^2 u'}{\partial x \partial y} - \frac{\partial^2 v'}{\partial x^2}\right) + v' \frac{\partial^2 u}{\partial y^2} =$$

$$\nu\left(\frac{\partial^3 u'}{\partial x^2 \partial y} + \frac{\partial^3 u'}{\partial y^3} - \frac{\partial^3 v'}{\partial x^3} - \frac{\partial^3 v'}{\partial x \partial y^2}\right) \tag{9.2}$$

$$\frac{\partial u'}{\partial x} + \frac{\partial v'}{\partial y} = 0 \tag{9.3}$$

Now a periodic disturbance is assumed with a stream function ψ defined by

$$\psi\,(x,y,t) = \varphi(y)e^{i(\bar{\alpha}x - \bar{\beta}t)} \tag{9.4}$$

which, using

$$u' = \frac{\partial\psi}{\partial y} \quad \text{and} \quad v' = -\frac{\partial\psi}{\partial x} \tag{9.5}$$

directly satisfies the continuity equation (9.3). Since (9.2) and (9.3) are linear in the fluctuating quantities more general periodic disturbances may be obtained by superposition of a number of components of the form (9.4).

In the expression (9.4) it is assumed that $\bar{\alpha}$ is a real quantity; it determines the wave length λ of the disturbance by $\lambda = \frac{2\pi}{\bar{\alpha}}$; $\bar{\beta}$ is complex with $\overline{\beta} = \beta_r + i\,\beta_i$ where $\frac{\beta_r}{2\pi}$ is the frequency of the disturbance. The sign of β_i determines whether the disturbance is stable or unstable. For stable or unstable disturbances β_i is negative or positive respectively; neutrally stable disturbances correspond to $\beta_i = 0$. The amplitude function $\varphi(y)$ is complex and is assumed to depend on y only. Furthermore use will be made of

$$\overline{c} = c_r + i\,c_i = \frac{\beta_r}{\overline{\alpha}} + i\,\frac{\beta_i}{\overline{\alpha}} \tag{9.6}$$

the sign of c_i again determines the stability of the disturbance; c_r is the wave speed.

Using (9.4) and (9.5) equation (9.2) may be reduced to

$$(u-\overline{c})\left[\frac{\partial^2\varphi}{\partial y^2} - \overline{\alpha}^2\varphi\right] - \frac{\partial^2 u}{\partial y^2}\,\varphi = - \frac{i\nu}{\overline{\alpha}}\left[\frac{\partial^4\varphi}{\partial y^4} - 2\,\overline{\alpha}^2\,\frac{\partial^2\varphi}{\partial y^2} + \overline{\alpha}^4\varphi\right] \tag{9.7}$$

This equation can be written in non-dimensional form by using the velocity U at the edge of the boundary layer and the displacement thickness δ^* as reference velocity and -length respectively. The result is

$$\left(\frac{u}{U} - \frac{\overline{c}}{U}\right)\left[\frac{\partial^2\varphi}{\partial y^2}\,\frac{\delta^*}{U} - (\overline{\alpha}\delta^*)^2\left(\frac{\varphi}{U\delta^*}\right)\right] - \frac{\partial^2 u}{\partial y^2}\,\frac{\delta^{*2}}{U}\,\frac{\varphi}{U\delta^*} =$$

$$\frac{-\,i}{(\alpha\delta^*)\,\frac{U\delta^*}{\nu}}\left[\frac{\partial^4\varphi}{\partial y^4}\,\frac{\delta^{*3}}{U} - 2\,(\overline{\alpha}\delta^*)^2\,\frac{\partial^2\varphi}{\partial y^2}\,\frac{\delta^*}{U} + (\overline{\alpha}\delta^*)^4\,\frac{\varphi}{U\delta^*}\right] \tag{9.8}$$

Equation (9.7) or (9.8) is known as the Orr-Sommerfeld equation. It is homogeneous in φ and hence admits the solution $\varphi \equiv 0$; this of course represents the undisturbed flow. The stability investigation is concerned with non-zero solutions satisfying equation (9.7) or (9.8) together with some boundary conditions. These solutions are found by solving the resulting eigenvalue problem. This will not be pursued further here; extensive reviews may be found in [7, 29, 90].

In the following sections only those results of stability theory will be presented which are used in the remainder of the present work.

9.2.3. The stability diagram.

For a given laminar boundary layer $\frac{U\delta^*}{\nu}$ and the velocity profile $\bar{u}\left(\frac{y}{\delta^*}\right)$ are known. Then in equation (9.8) $\bar{\alpha}\delta^*$, $\frac{c_r}{U}$ and $\frac{c_i}{U}$ remain as parameters. Usually $\frac{c_r}{U}$ and $\frac{c_i}{U}$ are replaced by $\frac{\beta_r}{U^2}$ and $\frac{\beta_i\delta^*}{U}$ using the following expressions.

$$\frac{c_r}{U} = \frac{\beta_r\nu}{U^2} \cdot \frac{1}{\bar{\alpha}\delta^*} \cdot \frac{U\delta^*}{\nu} \qquad (9.9)$$

and

$$\frac{c_i}{U} = \frac{\beta_i\delta^*}{U} \cdot \frac{1}{\bar{\alpha}\delta^*} \qquad (9.10)$$

Now, when a value for one of these parameters is assumed (for instance $\bar{\alpha}\delta^*$) the values of the other ones may be determined for which (9.8) allows non-zero solutions. Results of these calculations are usually presented in an $\bar{\alpha}\delta^*$ - $\frac{U\delta^*}{\nu}$ plane: the "stability diagram". As an example fig. 9.1 shows the stability diagram for the flat plate boundary layer. The curve for $\frac{\beta_i\delta^*}{U} = 0$ denotes the neutrally stable disturbances. Inside the loop β_i is positive and outside negative. This means that unstable disturbances will be found only for combinations of $\bar{\alpha}\delta^*$ and $\frac{U\delta^*}{\nu}$ inside the loop. Below a certain value of $\frac{U\delta^*}{\nu}$ there are no values of $\bar{\alpha}\delta^*$ for which unstable disturbances are possible; this value of $\frac{U\delta^*}{\nu}$ is called the critical Reynoldsnumber.

The Orr-Sommerfeld equation (9.8) has been obtained for parallel flows only where u(y) - and hence $\frac{u}{U}\left(\frac{y}{\delta^*}\right)$ and $\frac{U\delta^*}{\nu}$ - do not change with x. It is general practice to apply results of stability calculations also to flows where u(y) changes slowly with x. This implies that at each station x the actual flow is replaced by a parallel flow with the same non-dimensional velocity profile $\frac{u}{U}\left(\frac{y}{\delta^*}\right)$ and Reynoldsnumber $\frac{U\delta^*}{\nu}$.

For a similar boundary layer the "shape of the velocity profile" $\frac{u}{U}\left(\frac{y}{\delta^*}\right)$ is independent of x and hence the same stability diagram applies at all values of x. If now a disturbance with a constant value of $\frac{\beta_r\nu}{U^2}$ is considered which is convected downstream with the flow, it follows

? how physically

- because $\frac{U\delta^*}{\nu}$ increases with x - that the disturbance may at first be stable, then become unstable and finally become stable again. The same happens for non-similar boundary layers where however the stability diagram changes with x.

It can be seen from the Orr-Sommerfeld equation (9.8) that the stability diagram depends on the shape of the velocity profile. It turns out that the curvature of the profile is very important: profiles with a point of inflexion have a much lower critical Reynoldsnumber and hence are much less stable than velocity profiles without inflexion point (fig. 9.2). Moreover, the height of the unstable loop is finite when $\frac{U\delta^*}{\nu} \longrightarrow \infty$ for velocity profiles with an inflexion point while the height tends to zero if there is no inflexion point. Hence it follows that factors determining the occurrence of an inflexion point have much influence on stability and hence on transition.

An inflexion point occurs if $\frac{\partial^2 u}{\partial y^2}$ at the wall is positive. From the first compatibility condition at the wall (equation 2.10) it follows that $\left(\frac{\partial^2 u}{\partial y^2}\right)_o$ depends on the pressure gradient term $U \frac{dU}{dx}$ and the suction velocity v_o. An "adverse" pressure gradient ($\frac{dU}{dx} < 0$) or blowing ($v_o > 0$) tend to make $\left(\frac{\partial^2 u}{\partial y^2}\right)_o > 0$ and hence are destabilising factors. A "favourable" pressure gradient ($\frac{dU}{dx} > 0$) or suction ($v_o < 0$) tend to make $\left(\frac{\partial^2 u}{\partial y^2}\right)_o < 0$ and hence are stabilising factors. This point will be discussed further in section 9.3.

9.2.4. The amplification factor.

It was shown in section 9.2.3. that the amplification or damping of disturbances in the boundary layer is determined by the magnitude of β_i. In what follows an equation will be derived which governs the growth of the amplitude of the disturbances. This equation follows from the expression (9.4) for the stream function. Of course, only the real part of the stream function ψ_r is physically significant.

From (9.4), together with $\varphi = \varphi_r + i\,\varphi_i$, it follows that

$$\psi_r = e^{\beta_i t}\left[\varphi_r \cos(\bar{\alpha}x - \beta_r t) - \varphi_i \sin(\bar{\alpha}x - \beta_r t)\right]$$

or denoting $\frac{\varphi_r}{\varphi_i}$ by tg γ

$$\psi_r = -e^{\beta_i t}\ \frac{\varphi_i}{\cos\gamma} \sin\,(\bar{\alpha}x - \beta_r t - \gamma) \qquad (9.11)$$

For the velocity components u' and v' of the disturbance similar expressions are found. Because φ and hence γ depend only on y the amplitudes a and a + da for a fixed value of y at times t and t + dt are related by

$$d(\ln a) = \beta_i\ dt \qquad (9.12)$$

Hence if the amplitude for the neutral oscillation at time t_o is denoted by a_o, the amplitude at a later time t follows from

$$\ln \frac{a}{a_o} = \int_{t_o}^{t} \beta_i\ dt \qquad (9.13)$$

or

$$\frac{a}{a_o} = e^{\sigma_a} \quad \text{where} \quad \sigma_a = \int_{t_o}^{t} \beta_i\ dt \qquad (9.14)$$

In what follows σ_a will be called the "amplification factor".
For parallel flows the parameter β_i in (9.14) is constant but it may vary with x for non-parallel flow.
Since the integration variable t in (9.14) is a little obscure for instability calculations in boundary layers a change will be made to the variable x by using

$$\frac{dx}{dt} = c_r \qquad (9.15)$$

This means that a disturbance is followed on its way downstream. Using (9.15) equation (9.14) for σ_a may be written as

$$\sigma_a = \int_{x_o}^{x} \frac{\beta_i}{c_r}\ dx$$

or after introducing convenient non-dimensional quantities

$$\sigma_a = \frac{U_\infty c}{\nu} \cdot 10^{-6} \int_{\bar{x}_o}^{\bar{x}} T.\bar{U}\, d\bar{x} \qquad (9.16)$$

In equation (9.16) T denotes

$$T = \frac{\frac{\beta_i \delta^*}{U} \cdot \bar{\alpha}\delta^* .10^6}{\frac{\beta_r \nu}{U^2} . \left(\frac{U\delta^*}{\nu}\right)^2} \qquad (9.17)$$

and $\bar{x} = \frac{x}{c}$ where c is a constant reference length. The quantity T may be calculated as a function of $\bar{x}$ for a given value of $\frac{\beta_r \nu}{U^2}$ if the shape of the velocity profile and $\frac{U\delta^*}{\nu}$ are known as functions of $\bar{x}$. Moreover stability diagrams have to be known for the velocity profiles encountered.

The lower integration limit $\bar{x}_o$ in (9.16) denotes the value of $\bar{x}$ at which for the frequency considered $\frac{\beta_i \delta^*}{U} = 0$ for the first time.

9.3. Some available stability diagrams.

As the stability calculations are rather laborious not many stability diagrams have been calculated. A review of these results may be found in [7], chapter 16 and [29], section IX; a selection of these results will be given below.

For the flat plate boundary layer without suction critical Reynoldsnumbers from different sources have been collected in table 9.1, stability diagrams are shown in fig. 9.3. It is seen that the results of various calculations show considerable differences. This is caused on the one hand by the different procedures followed for the stability calculations. On the other hand the Blasius profile has been approximated by different analytical expressions; in many cases the velocity profile for the flat plate boundary layer from some Pohlhausen type method has been used. Since these velocity profiles and especially their curvature may be different, the stability diagrams are not necessarily identical.

Some available stability diagrams for the plane stagnation point flow without suction have been compared in fig. 9.4; again considerable differences are shown.

Calculations for a whole series of Hartree profiles (see section 3.1.2) have been made by Pretsch [96, 97, 98]. Stability diagrams are shown in fig. 9.5; the critical Reynoldsnumber is given in fig. 9.6 as a function of β. Figures 9.5 and 9.6 clearly show the stabilising influence of a favourable pressure gradient ($\beta > 0$). Also amplification calculations have been made by Pretsch; these results will be discussed in more detail in section 9.5.

The neutral stability curves for some cases with suction and blowing have been calculated by Ulrich [99]. The flows considered are

1. the flat plate with constant suction velocity
2. the flat plate with $v_o \sim x^{-\frac{1}{2}}$
3. the plane stagnation point with constant suction velocity.

The cirtical Reynoldsnumber is shown as a function of $\lambda_2 = \frac{-v_o}{U}\sqrt{\frac{Ux}{\nu}}$ in fig. 9.7 which clearly shows the strong stabilising influence of suction. From the examples discussed in chapter 8 it is known that for the boundary layer flows considered by Ulrich the velocity profile tends to the asymptotic suction profile if the suction velocity $-v_o$ becomes infinitely large ($\lambda_2 \rightarrow \infty$). According to Ulrich's calculations the critical Reynoldsnumber $\frac{U\delta^*}{\nu}$ becomes as high as 70000 for this case; a recalculation by Freeman [100] gave 78000. Fig. 9.8 shows some stability diagrams selected from Ulrich's results for different boundary layer flows. This figure shows that if $(\frac{U\delta^*}{\nu})_{crit}$ is equal for two different boundary layers also the remainder of the neutral stability curve is roughly the same, irrespective of the pressure gradient or suction velocity.

Comparison of this result with figs 9.3 and 9.4 reveals that the stability diagrams calculated by different authors for the same flow show as much variation as the stability diagrams obtained by the same author for different velocity profiles with the same value of the critical Reynoldsnumber.

In the remainder of the present work the amplification factor for boundary layers with arbitrary pressure- and suction distributions will be calculated. For this calculation stability diagrams including information about the amplification rate at $\beta_i > 0$ have to be known.

To the best of the author's knowledge these results are only provided by Pretsch's stability diagrams and it will be attempted to apply these diagrams to arbitrary boundary layers.

In view of the comparisons of different stability diagrams made above, the following procedure seems to be justified for assigning a stability diagram to a certain velocity profile. From an approximate formula due to Lin (section 9.4) the critical Reynoldsnumber is found. Then the stability diagram from Pretsch's series with the same critical Reynolds number is assumed to be valid for the velocity profile under investigation. This implies that all possible stability diagrams are considered to form a one-parameter family with the critical Reynoldsnumber as parameter.

If only the critical Reynoldsnumber is needed a quick estimate may be made using a formula of Wieghardt [101].

$$\left(\frac{U\delta^*}{\nu}\right)_{crit} = H \left(\frac{U\Theta}{\nu}\right)_{crit} = H\, e^{26.3 - 8H} \qquad (9.18)$$

where $H = \frac{\delta^*}{\Theta}$. Fig. 9.9 shows that indeed equation (9.18) gives a reasonably good approximation to the critical Reynoldsnumber for a variety of boundary layers. For relatively strong suction however Wieghardts relation seems to become invalid (Head, [63]); and it is safer to use Lin's formula for all cases.

Since in boundary layer calculations using the momentum equation the momentum loss thickness Θ is the proper thickness parameter it is advantageous in many cases to use a critical Reynoldsnumber based on Θ. From fig. 9.9 it follows that for the boundary layers, which have been considered in the present section, equal values of H mean equal values of $\left(\frac{U\Theta}{\nu}\right)_{crit}$ and hence also of $\left(\frac{U\delta^*}{\nu}\right)_{crit}$. Therefore the comparisons of the stability diagrams made in the present section can also be made in terms of $\bar{\alpha}\Theta$ and $\frac{U\Theta}{\nu}$, instead of $\bar{\alpha}\delta^*$ and $\frac{U\delta^*}{\nu}$, without altering the conclusions.

9.4. Lin's formulae for the critical Reynoldsnumber.

A simple approximate formula for the calculation of the critical Reynoldsnumber has been given by Lin [90], and reads

$$\left(\frac{Ud}{\nu}\right)_{crit} = \frac{25\left(\frac{\partial \bar{u}}{\partial y/d}\right)_o}{\bar{u}_c^{\;4}} \qquad (9.19)$$

In this equation d may be any length which is used to make the wall distance y non-dimensional.

$\bar{u}_c$ is the value of $\bar{u}$ for which the following equation is satisfied

$$-\pi\left(\frac{\partial \bar{u}}{\partial y/d}\right)_o \frac{\bar{u}\,\frac{\partial^2 \bar{u}}{\partial (y/d)^2}}{\left(\frac{\partial \bar{u}}{\partial y/d}\right)^3} = 0.58 \qquad (9.20)$$

For the momentum method discussed in chapter 5 it is appropriate to take $d = \sigma$ leading to $\frac{y}{d} = \eta$. Then equations (9.19) and (9.20) lead to

$$\left(\frac{U\theta}{\nu}\right)_{crit} = \frac{25 . \frac{\tau_o \sigma}{\mu U} . \frac{\theta}{\sigma}}{\bar{u}_c^{\;4}} \qquad (9.21)$$

and

$$\frac{-\bar{u}\,\frac{\partial^2 \bar{u}}{\partial \eta^2}}{\left(\frac{\partial \bar{u}}{\partial \eta}\right)^3} = \frac{0.58}{\pi\,\frac{\tau_o \sigma}{\mu U}} \qquad (9.22)$$

For the multimoment method given in chapter 7 it is useful to make d equal to δ as defined by equation (7.20). In that case (9.19) and (9.20) reduce to

$$\left(\frac{U\theta}{\nu}\right)_{crit} = \frac{25\sqrt{a_o}}{\bar{u}_c^{\;4}}\;\frac{\theta}{x}\sqrt{\frac{Ux}{\nu}} \qquad (9.23)$$

$$\frac{-\bar{u}\,\frac{\partial S}{\partial \bar{u}}}{S\sqrt{S}} = \frac{1.16}{\pi\sqrt{a_o}} \qquad (9.24)$$

The equations (9.22) and (9.24) can easily be solved by iteration for a given velocity- or S-profile. It is even possible to include Lin's formulae in a computer program for the boundary layer calculation.

A comparison of results obtained with Lin's formulae and those from other calculations may be found in section IX of [29]. Some results for the flat plate boundary layer without suction have been collected in table 9.2. For the asymptotic suction profile the formula leads to $(\frac{U\theta}{\nu})_{crit} = 40000$ or $\frac{U\delta^*}{\nu}_{crit} = 80000$ as compared to 70000 according to Ulrich and 78000 obtained by Freeman. It follows from these comparisons that the accuracy of Lin's formula is quite satisfactory.

9.5. Reduction of Pretsch's results to a form suitable for use on a digital computer.

Detailed stability calculations for some of the Hartree profiles have been made by Pretsch [96-98]. The stability diagrams are shown in fig. 9.5, while some characteristic parameters of the profiles have been collected in table 9.3. Stability diagrams for some other values of β have been obtained by Smith and Gamberoni [1] from interpolation in Pretsch's diagrams. In what follows these diagrams will be used to calculate the amplification factor σ_a. It follows from equation (9.16) that the only information needed from the diagrams is the quantity T as defined by (9.17). Values of T for a range of values of $\frac{\beta_r \nu}{U^2}$ and $\frac{U\delta^*}{\nu}$ have been obtained from Pretsch's work for $\beta = 1, 0.6, 0, -0.10, -0.198$ and for $\beta = 0.2, 0.1, -0.05$ from [1].

In fig. 9.10 for example the results are shown for the flat plate ($\beta = 0$) plotted as function of ${}^{10}\log \frac{U\theta}{\nu}$. It is seen from the figure that the curves for constant values of $\frac{\beta_r \nu}{U^2}$ may be approximated by parabola's of the form

$$T = T_o - K_1 \left({}^{10}\log \frac{U\theta}{\nu} - K_2\right)^2 \qquad (9.25)$$

where the coefficients T_o, K_1 and K_2 depend on β and $\frac{\beta_r \nu}{U^2}$. Values for these coefficients have been obtained for all values of β and a range of values for $\frac{\beta_r \nu}{U^2}$. The results for $\beta = 0$ are shown in figure 9.11 as function of ${}^{10}\log \frac{\beta_r \nu}{U^2}$. The approximation given by (9.25) to the actual

values is shown in fig. 9.10. Finally cross plots have been made to find T_o, K_1 and K_2 as functions of β for constant values of $\frac{\beta_r \nu}{U^2}$. Since a unique relation exists between β and $(\frac{U\Theta}{\nu})_{crit}$ (see fig. 9.6) it is possible to consider T_o, K_1 and K_2 as functions of $^{10}\log(\frac{U\Theta}{\nu})_{crit}$.
Since it may be expected that Pretsch's results will not be very accurate, linear interpolation in $^{10}\log(\frac{U\Theta}{\nu})_{crit}$ seems to be justified to find the coefficients of (9.25) for arbitrary values of $^{10}\log(\frac{U\Theta}{\nu})_{crit}$. Table 9.4 gives T_o, K_1 and K_2 for different values of $\frac{\beta_r \nu}{U^2}$ at equidistant values of $^{10}\log(\frac{U\Theta}{\nu})_{crit}$. The numbers quoted in the table have been chosen in such a way that by linear interpolation in $^{10}\log(\frac{U\Theta}{\nu})_{crit}$ the values obtained from Pretsch's diagrams will be regained.
For convenience the reduced frequencies $\frac{\beta_r \nu}{U^2}$ have been denoted by a number f in table 9.4; results for intermediate values of $\frac{\beta_r \nu}{U^2}$ can be obtained by linear interpolation in the parameter f.
In view of the remarks made at the end of section 9.3 it will be assumed that table 9.4 can be applied to boundary layer flows with arbitrary suction- and pressure distributions.

9.6. Some existing methods for the calculation of the transition point.

In preceding sections it has been shown that it is possible to determine theoretically whether a particular boundary layer flow is stable or unstable. For instance for the flat plate the boundary layer becomes unstable as soon as $\frac{U\delta^*}{\nu}$ exceeds a critical value of about 575 corresponding to $\frac{Ux}{\nu} = 0.11 \times 10^6$. From experiments it is known however (see section 9.1) that actual transition starts at $\frac{Ux}{\nu} = 2.8 \times 10^6$ only. This means that a considerable distance will exist between the point of instability and the transition point.
From fig. 3.3 it follows that the instability has no direct effect on the friction drag; only when transition occurs the friction drag increases. It follows that for the calculation of the characteristics of airfoil sections it is important to possess a method for predicting

the possible occurrence of transition. Since the transition process is not yet sufficiently understood these methods will necessarily be semi-empirical in nature. Some of these methods are mentioned below.

In some methods the results of different transition measurements are plotted in such a way that all points fall on a single curve. For a new case transition may be "predicted" by assuming that the new case will also fall on this universal curve. An important example of these methods is due to Michel [106]. In his method $\frac{U\theta}{\nu}$ at the transition point is plotted versus the corresponding value of $\frac{Ux}{\nu}$; indeed results of different experiments fall reasonably well on a single curve. The method is based on experiments without suction and can not easily be generalised to suction problems.
A different method has been given by Granville [107]. Here a universal curve is obtained by plotting $(\frac{U\theta}{\nu})_{tr} - (\frac{U\theta}{\nu})_{i}$ versus the mean value $\overline{\Lambda}_1$ of the Pohlhausen parameter Λ_1, defined by

$$\overline{\Lambda}_1 = \frac{1}{\overline{x}_{tr} - \overline{x}_i} \int_{\overline{x}_i}^{\overline{x}_{tr}} \Lambda_1 \, d\overline{x} \qquad (9.26)$$

The subscripts "tr" and "i" denote transition and instability respectively. Another suggested method is to assume that transition occurs at a constant value of $\frac{U\delta^*}{\nu}$. This results in a very rough estimate of the transition point only.
To improve upon the above methods the determination of the transition point should not be based on local quantities only but the history of the boundary layer should be taken into account, since this determines the amplification of unstable disturbances. Such a method has been designed by the present author; it will be presented in the next section.

9.7. A new method for the semi-empirical determination of the transition region.

9.7.1. General.

It was shown by the present author in [3-5] and at the same time independently by Smith and Gamberoni [1,2] that different experiments on transition without suction can be correlated on the basis of the amplification factor σ_a. It was shown that the maximum value of σ_a which was reached at the transition position was roughly equal for all cases investigated. Hence in new cases an accurate estimate of the transition position may be found using the assumption that transition occurs as soon as the calculated value of $(\sigma_a)_{max}$ reaches this critical value. In the references cited above the method was shown to be valid for the no-suction case. It will be presented here in a modified form; furthermore it will be shown that the method is also applicable to cases with suction.

9.7.2. The amplification factor for the flat plate without suction.

Teh amplification factor σ_a is defined by equation (9.16)

$$\sigma_a = 10^{-6} \frac{U_\infty c}{\nu} \int_{\bar{x}_o}^{\bar{x}} T.\bar{U}\, d\bar{x} \qquad (9.27)$$

If for the flat plate the reference velocity U_∞ and the reference length c are chosen as U and $\frac{\nu}{U}$ respectively, equation (9.27) reduces to

$$\sigma_a = 10^{-6} \int_{\frac{Ux_o}{\nu}}^{\frac{Ux}{\nu}} T\, d\left(\frac{Ux}{\nu}\right) \qquad (9.28)$$

For the flat plate the relation between $\frac{U\Theta}{\nu}$ and $\frac{Ux}{\nu}$ is known and it is possible to calculate σ_a for different frequencies $\frac{\beta_r \nu}{U^2}$ using table 9.4 and the formulae given in section 9.5. For this calculation a value of $\left(\frac{U\Theta}{\nu}\right)_{crit}$ has to be assumed; as some uncertainty exists here (see table 9.1) a range of values for the critical Reynoldsnumber has been used. For $\left(\frac{U\Theta}{\nu}\right)_{crit} = 260$, which is the value obtained by Pretsch for $\beta = 0$, some results are shown in figs 9.12 and 9.13. Values of T are shown in fig. 9.12; the amplification factor σ_a is shown in fig. 9.13 where also the envelope giving the maximum amplification factor $(\sigma_a)_{max}$ has been drawn.

Similar calculations have been performed for other values of $\left(\frac{U\Theta}{\nu}\right)_{crit}$

from table 9.1; the results for $(\sigma_a)_{max}$ have been collected in fig. 9.14. Of course the calculation of the amplification factor can be extended to arbitrary high Reynoldsnumbers. However, it is known from experiments (see section 9.1) that transition sets in at $\frac{Ux}{\nu} = 2.8 \times 10^6$ and that the boundary layer is completely turbulent for $\frac{Ux}{\nu} > 3.9 \times 10^6$. These limits have been inserted in fig. 9.14; it follows that to these values of $\frac{Ux}{\nu}$ certain values of $(\sigma_a)_{max}$ correspond which are shown as function of $(\frac{U\Theta}{\nu})_{crit}$ in fig. 9.15 and table 9.5.

If Pretsch's value is used it is found that beginning and end of the experimentally determined transition region correspond to $(\sigma_a)_{max} = 7.6$ and 9.7 respectively. In the earlier version of the method [3-5] the values 7.8 and 10 were obtained. The slight differences with the present values are easily explained by the fact that at that time only small scale versions of Pretsch's charts were available to the author which could not be read very accurately.

In most of the further calculations the momentum method of chapter 5 will be used in combination with Lin's formulae for the critical Reynoldsnumber. Table 9.5 shows that this leads to $(\sigma_a)_{max} = 9.2$ and 11.2 at the beginning and end of the transition region respectively. In what follows it will be shown that nearly the same values are obtained for other boundary layers. It should be noted that the linear stability theory has been used to calculate σ_a up till transition. Of course not too much significance should be attached to the details of these calculations. The maximum amplification factor has to be considered only as a convenient parameter correlating different factors which influence the transition.

9.7.3. The amplification factor for the EC 1440 airfoil section without suction.

For airfoil sections the boundary layer is not similar and hence for different values of $\bar{x}$ different stability diagrams have to be used. If $(\frac{U\Theta}{\nu})_{crit}$ is known as a function of $\bar{x}$, for instance from Lin's formulae, it is easily possible to calculate σ_a also for these cases using table 9.4.

In [3-5] results of transition measurements and calculations of the amplification factor for the EC 1440 airfoil section have been presented. In this work Pohlhausen's method was used for the boundary layer calculations; critical Reynoldsnumbers for the velocity profiles were found by relating Pohlhausen's λ to Hartree's β. This relation was obtained by calculating the Hartree boundary layers for $U = u_1\, x^{\frac{\beta}{2-\beta}}$ with Pohlhausen's method. The examples discussed in [3-5] will be recalculated here using the momentum method of chapter 5 in combination with Lin's formulae. Fig. 9.16 shows $\bar{U}$ as a function of $\bar{s}$ and the results of the boundary layer calculations for different values of the angle of attack α. Results of the amplification calculation for $\alpha = 0^{\circ}$ are shown in figs 9.17 and 9.18. Similar calculations have been performed for other values of α; the results have been used to construct fig. 9.19 where also the experimentally determined transition region is shown. The curve $(\sigma_a)_{max} = 0$ in fig. 9.19 denotes the instability point; it follows that both the instability point and transition move forward with increasing angle of attack.

However, the distance between the instability point and transition can be very large. If the beginning of transition is assumed to occur for $(\sigma_a)_{max} = 9.2$ it may be seen from fig. 9.19 that the beginning of transition is predicted accurately within $5^{\circ}/o$ of the chord length for $\alpha > -2^{\circ}$.

For $\alpha < -2^{\circ}$ transition is preceded by laminar separation; in this case the distance between the predicted and actual positions where transition starts may grow to $10^{\circ}/o$ of the chord length.

Smith and Gamberoni [1,2] applied a similar analysis to a great number of experimental data including results of free flight measurements. They calculated the laminar boundary layer by means of a method which for the flat plate produces Hartree's velocity profile for $\beta = 0$. Hence, using Pretsch' value for the critical Reynoldsnumber, they should find $(\sigma_a)_{max} = 7.6$ and 9.7 at the beginning and end of the transition region. The conclusion of their analysis was that $(\sigma_a)_{max} = 9$ would correlate the experimental data very well. Since no distinction was made between beginning and end of the transition region the agreement with the values 7.6 and 9.7 is very good. A difference between the present method and the method of Smith and Gamberoni is that the last authors calculate the amplification at constant values of $\frac{\beta_r \nu}{U_\infty^2}$ while for the present method constant values of $\frac{\beta_r \nu}{U^2}$ are used. Since $\overline{U} = U/U_\infty$ does not change very much in the regions of interest and moreover only the envelope of σ_a for different frequencies is used this difference apparently has no effect on the results.

It has been mentioned already that the method becomes less accurate if transition occurs close to or even downstream of the calculated separation point. Some possible explanations for these discrepancies are listed below.

1. Near separation the transition mechanism assumed in stability theory may not be the relevant one so that a method which is based on this theory may become less accurate.
2. Especially close to separation the shape of the calculated boundary layer velocity profiles may be in error so that a wrong value for $(\frac{U\Theta}{\nu})_{crit}$ is found.
3. In cases where the critical Reynoldsnumber is low - which occurs close to separation - really nothing is known about the accuracy of Lin's formulae or Pretsch' stability diagrams.
4. There is no clear reason why the critical values of $(\sigma_a)_{max}$ at transition should be constants. An exact correspondence between experiment and theory for the results shown in fig. 9.19 might have been obtained for instance by assuming that the critical values are suitable functions of the critical Reynoldsnumber at transition. However, in further experiments no systematic variation of $(\sigma_a)_{max}$ with $(\frac{U\Theta}{\nu})_{crit}$ at transition was found and hence in what follows constant critical values for $(\sigma_a)_{max}$ have been used.

9.7.4. The amplification factor for boundary layers with suction through a porous surface.

Anticipating the results of an experimental investigation on the effects of suction through a porous surface - to be described in chapter 11 - it is stated here that the method is also applicable in the case of suction.

9.8. Some results for the flat plate with different suction laws.

9.8.1. The flat plate with constant suction velocity.

In section 8.11 the boundary layer on a flat plate with constant suction velocity has been discussed. It was found that the non-dimensional parameter $\Lambda_2 = \frac{-v_o \Theta}{\nu}$ and the shape of the velocity profile only depend on the variable $\bar{x}$ defined by

$$\bar{x} = \left(\frac{-v_o}{U}\right)^2 \frac{Ux}{\nu} \tag{9.29}$$

Since the critical Reynoldsnumber depends on the shape of the velocity profile only it also depends only on $\bar{x}$.
Values of $\frac{U\Theta}{\nu}$ may be found as function of $\bar{x}$ for different values of the suction coefficient $c_q = \frac{-v_o}{U}$ from

$$\frac{U\Theta}{\nu} = \frac{\frac{-v_o\Theta}{\nu}}{\frac{-v_o}{U}} \tag{9.30}$$

Results of some calculations using the momentum method in combination with Lin's formulae for the critical Reynoldsnumber, are shown in fig. 9.20. It follows that for $\frac{-v_o}{U} > 0.980 \times 10^{-4}$ nowhere along the length of the plate $\frac{U\Theta}{\nu}$ will exceed $\left(\frac{U\Theta}{\nu}\right)_{crit}$ and hence the boundary layer is stable at all values of $\bar{x}$. For values of $\frac{-v_o}{U}$ less than 0.980×10^{-4} the boundary layer becomes unstable in a certain interval.
A similar calculation has been made by Ulrich [99] using Iglisch' exact solution for $\frac{U\Theta}{\nu}$ and the results for $\left(\frac{U\Theta}{\nu}\right)_{crit}$ shown in figure 9.7. He found that the suction coefficient c_q should exceed the value 1.18×10^{-4} to ensure a stable boundary layer for all values of $\bar{x}$. The difference between the values 1.18 and 0.980 is easily explained by the different procedures used to determine the critical Reynoldsnumber.

Fig. 9.21a and b show the drag of a flat plate with the constant suction velocity $-v_o = 1.18 \times 10^{-4}$ U. Appendix 1 should be consulted for an explanation of the terms "wake drag", "suction drag" and "total drag" which are mentioned in figure 9.21. Included in the figure is the drag for the flat plate without suction for both laminar and turbulent flow (section 3.1.3). It is seen that the total drag with suction is higher than for the Blasius boundary layer. However, it remains much smaller than the drag of the flat plate with turbulent boundary layer which would occur at high values of $\frac{Ux}{\nu}$ without suction.
The percentage reduction in total drag which would result from keeping the boundary layer laminar is shown in figure 9.22. It follows that drag reductions of 85 $^o/o$ will be possible at the value 25×10^6 for the Reynoldsnumber $\frac{Ux}{\nu}$ which is representative for the wing of a modern jet airliner in cruising flight.
The drag reduction shown in fig. 9.22 has been calculated on the assumption of a constant suction velocity with such a magnitude that the boundary layer remains stable along the full length of the plate. It may be expected that less suction will be required if the boundary layer is allowed to become unstable to such a degree that the maximum amplification factor remains slightly below 9.2. This will be pursued further in the remainder of the present section. A further reduction of the suction quantity may be obtained by allowing the suction velocity to vary along the length of the plate. This will be discussed further in section 9.8.2.

For the case of a constant suction velocity the amplification factor can easily be calculated as follows.
If the definition (9.29) for $\bar{x}$ is used it is implied that the reference length c has been defined as

$$c = \frac{U\nu}{(-v_o)^2} \tag{9.31}$$

If the reference speed U_∞ is made equal to the constant free stream speed U then the Reynoldsnumber $R_c = \frac{U_\infty c}{\nu}$ becomes

$$R_c = \left(\frac{U}{-v_o}\right)^2 = c_q^{-2} \tag{9.32}$$

and equation (9.16) reduces to

$$\sigma_a = 10^{-6} c_q^{-2} \int_{\bar{x}_o}^{\bar{x}} T \, d\bar{x} \tag{9.33}$$

Results of amplification calculations for different values of c_q have been collected in fig. 9.23 where $(\sigma_a)_{max}$ is shown as function of $\bar{x}$.
The peak value of the amplification factor is plotted in fig. 9.24 as function of c_q. If it is assumed that transition starts as soon as $(\sigma_a)_{max}$ reaches the critical value 9.2, then it may be concluded from fig. 9.24 that transition will not occur unless c_q falls below the value 0.485×10^{-4}. This value is only 50°/o of the suction coefficient required to keep the boundary layer stable. Then it may be concluded that the suction coefficient can be much smaller than was assumed for the calculation of the drag reduction shown in fig. 9.22. This implies that the possible drag reduction may be much larger than shown in fig. 9.22.
Furthermore it should be noted that using a constant value of $-v_o$ results in a suction intensity which is too high at most stations on the plate. Only in the critical region this suction velocity is really necessary to prevent transition. To obtain a minimum suction quantity the suction velocity should be adjusted to the local needs of the boundary layer. This will be discussed further in section 9.8.2.

9.8.2. The flat plate with varying suction velocity.

Using the momentum method in combination with Lin's formulae for the critical Reynoldsnumber, it is easy to calculate the suction distribution which will maintain a neutrally stable boundary layer characterized by

$$\frac{U\Theta}{\nu} = \left(\frac{U\Theta}{\nu}\right)_{crit} \tag{9.34}$$

Since the momentum method and Lin's formulae lead to $\frac{U\Theta}{\nu} = 0.661\sqrt{\frac{Ux}{\nu}}$ and $(\frac{U\Theta}{\nu})_{crit} = 221$ for the boundary layer on a flat plate without suction, it follows that instability arises downstream of the position where $\frac{Ux}{\nu} = 0.11 \times 10^6$. If suction is started at this point and the requirement (9.34) is fulfilled, further downstream the suction distribution shown in fig. 9.25 results. It may be seen from this figure that only locally a high suction intensity is needed. For $\frac{Ux}{\nu} \rightarrow \infty$ the suction velocity takes the constant value $0.125 \times 10^{-4} U$. This value easily follows from the observation that for $\frac{Ux}{\nu} \longrightarrow \infty$ the asymptotic suction profile is found for which $\frac{-v_o\Theta}{\nu} = 0.50$ and $(\frac{U\Theta}{\nu})_{crit} = 40000$ so that to satisfy equation (9.34) the suction velocity should be given by

$$\frac{-v_o}{U} = \frac{\frac{-v_o\Theta}{\nu}}{\frac{U\Theta}{\nu}} = \frac{0.5}{4 \times 10^4} = 0.125 \times 10^{-4}$$

The total suction quantity obtained in this case is much less than for the case of constant suction velocity. A further reduction will be obtained if the amplification factor $(\sigma_a)_{max}$ is allowed to reach the critical value 9.2. However, this will not be pursued further in the present work.

Experimental investigation of the laminar boundary layer on an impervious 28°/o thick airfoil section.

Introductory remarks.

In section 8.13 the experiments of Schubauer on the laminar boundary layer of an elliptic cylinder have been discussed. It was mentioned that some controversy exists about these measurements since it was definitely shown in the experimental investigation that separation of the laminar boundary layer occurred while some boundary layer calculation methods fail to predict separation using the measured pressure distribution.
It was shown by Hartree that a slight modification of the measured pressure distribution is sufficient to obtain separation. However, it is not known for certain whether or not the change assumed by Hartree remains within experimental error.
Due to the uncertainty about the exact pressure distribution to be used, this experiment failed to definitely answer the question whether boundary layer theory is capable of predicting laminar separation using the measured pressure distribution.
Therefore it was thought worth while to undertake an independent investigation to provide additional - and possibly still more accurate - material to be used for a comparison between boundary layer theory and experiment.
A disadvantage of Schubauer's investigation is the small size of the model (11.78 inch chord) and the low speed (11.5 ft/sec) at which the measurements were performed, resulting in the low value of 72000 for the Reynoldsnumber R_c based on chord. Due to this low Reynolds number a fully separated laminar boundary layer occurred without subsequent turbulent reattachment.
Since the Reynoldsnumbers in aeronautical practice are much higher than 72000 it was thought worth while to perform the new investigation at a much larger value of R_c. The measurements were made on the upper surface of a 28°/o thick symmetrical airfoil section with a chord length of 1 meter. All measurements were made at zero angle of attack and a wind speed of 28 m/sec corresponding to $R_c = 1.37 \times 10^6$. This value of R_c was selected to ensure that a separated laminar boundary layer occurred

with subsequent turbulent reattachment.
Details of the test set-up and the apparatus used are mentioned in section 10.2; the test methods are described in section 10.3. Results of the measurements and a comparison with boundary layer theory are given in sections 10.4 and 10.5 respectively.

10.2. Description of the experimental apparatus.

10.2.1. The wind tunnel.

The experiments were performed in the low speed wind tunnel of the Department for Aeronautical Engineering at Delft Technological University. The test section of the wind tunnel has an octagonal cross section, 1.80 m wide and 1.25 m high; the maximum windspeed is 120 m/sec. At the speed employed for the present investigation (28 m/sec) the degree of turbulence is about 0.04 °/o. Further details of this wind tunnel may be found in [108] and [109].

10.2.2. The model.

The wing model was not built for the present investigation but happened to be available. It had earlier been used by the N.L.L. at Amsterdam for some drag measurements.
The model is built up from two wooden spars and a number of wooden ribs spaced 140 mm apart. Furthermore the 2 mm thick multiplex skin is, at 135 mm intervals, supported by spanwise stringers.
The airfoil section used is NACA0028-64; the dimensions of which are given in table 10.1.
The model was placed vertically between the floor and ceiling of the test section; the geometric span obtained in this way being 1.25 m. A sketch, showing the test set-up is given as fig. 10.1.
Two rows of pressure orifices were provided in the upper surface of the model extending for some distance around the leading-edge to the lower surface. Positions of the orifices are given in table 10.2; those numbered 1-34 have been present during the whole series of measurements; the numbers 35 to 41 were added later during the investigation.

0.2.3. Hot-wire equipment.

Mean velocity profiles of the laminar boundary layer were measured with hot-wires at different positions in chord number III (fig. 10.1). Platinum wires, 0.003 mm Ø and about 2.5 mm long were used together with some transistorized equipment operating in the constant temperature mode. This equipment has been described in detail in [110].
The probe holding the hot-wire could be traversed across the boundary layer by means of a screw spindle (pitch 1 mm) running through a stream-lined tube and extending through a hole in the sidewall of the wind tunnel. A dial at the end of the spindle enabled the displacement of the hot-wire, from an arbitrary reference position outside the boundary layer, to be read within 0.01 mm. The distance between this reference position and the model surface was determined by a special technique to be described in section 10.3.3.

0.2.4. Other apparatus.

The free stream speed U_∞ in the test section was measured by means of a pitot-static tube mounted some distance above the floor of the test section (fig. 10.1).
For all pressure measurements inclined tube manometers were used, frequently calibrated against a Betz-type manometer.
Besides the orifices in the model surface a small static tube - which could be taped to the surface - was used for the pressure distribution measurements. Total pressures inside the boundary layer at a fixed small distance from the wall were measured with a small flattened total head tube which could also be taped to the surface. Both tubes were soldered to a common base plate to form one instrument as shown in fig. 10.2.

0.3. Test methods and reduction of data.

0.3.1. Pressure distribution measurements.

At a free stream speed U_∞ = 28 m/sec the pressure distribution around the model was measured relative to the free stream total head p_t. Since for subsequent boundary layer calculations the velocity U at the edge of the boundary layer is needed, the measured surface pressures p_x were converted to U. Using the assumption that the difference in static pressure between the wall and the edge of the boundary layer can be neglected, U follows from

$$\tfrac{1}{2}\rho U^2 = p_t - p_x \tag{10.1}$$

The values of U obtained in this way were made non-dimensional with the free stream velocity U_∞.

It was found that inserting the hot-wire probe and the streamlined tube had some influence on the pressure distribution. Therefore some measurements were repeated with the hot-wire placed at two different chordwise positions in the lower chord with orifices.

Since the size of the model is rather large compared with the dimensions of the test section there must be an appreciable tunnel wall effect on the pressure distribution. Moreover the speed at the position of the pitot-static tube can not be regarded as true free stream speed since it will be influenced by the presence of the model and the walls. These effects present no real problem since it is the only object of the present investigation to compare boundary layer theory and experiment for the same - but otherwise arbitrary - pressure distribution. The "free-stream speed" U_∞ is only used as a reference speed to obtain non dimensional quantities.

It is clear however, that the present investigation will not predict the free-flight characteristics of the airfoil section.

10.3.2. Hot-wire measurements.

All hot-wire measurements were made in the mid-span chord. During these measurements frequent calibrations were obtained using the following procedure. The hot-wire was placed in the midspan position well outside the boundary layer at the same chordwise position as orifice number 23. Assuming two-dimensional flow and constant static pressure across the boundary layer the speed U at the position of the hot-wire follows from $\tfrac{1}{2}\rho U^2 = p_t - p_{23}$, where p_{23} is the static pressure at the position of

orifice number 23 and p_t is the free stream total head. By varying the tunnel speed and recording both $\frac{1}{2}\rho U^2$ and the output of the hot-wire apparatus a calibration curve is easily obtained.
Once the calibration is known a velocity profile can be measured by moving the hot-wire in small steps from well outside the boundary layer to about 0.10 mm from the model surface. There is no point in measuring closer to the wall since the corrections to be applied to hot-wire readings obtained near a wall are uncertain. Fortunately it is not necessary to perform measurements near the wall since the velocity profile in this region can easily be calculated as soon as the pressure distribution is known (see section 10.3.3.).
Although the displacement of the hot-wire can accurately be measured with reference to an arbitrary starting position, its absolute distance from the wall can not so easily be determined directly. It was found however that the compatibility conditions of the boundary layer equations provide an easy method to find this distance. This procedure will be described in the next sub-section.

).3.3. Determination of the position of the hot-wire relative to the wall.

From the hot-wire measurements and the subsequent data reduction the non-dimensional velocity $\overline{u} = u/U$ in the boundary layer is found as function of the distance y_r measured from an arbitrary reference position outside the boundary layer (fig. 10.3). A problem remaining to be solved is to determine the distance between this reference position and the wall. This was done as follows using the compatibility conditions (2.10) and (2.11).

$$v_o \left(\frac{\partial u}{\partial y} \right)_o = U \frac{dU}{dx} + \nu \left(\frac{\partial^2 u}{\partial y^2} \right)_o \qquad (10.2)$$

$$v_o \left(\frac{\partial^2 u}{\partial y^2} \right)_o = \nu \left(\frac{\partial^3 u}{\partial y^3} \right)_o \qquad (10.3)$$

Equations (10.2) and (10.3) show that $\left(\frac{\partial^2 u}{\partial y^2} \right)_o$ and $\left(\frac{\partial^3 u}{\partial y^3} \right)_o$ can be calculated when v_o, $U \frac{dU}{dx}$ and $\left(\frac{\partial u}{\partial y} \right)_o$ are known. This implies that in the

Taylor series expansion of the velocity near the wall

$$u = \left(\frac{\partial u}{\partial y}\right)_o \frac{y}{1\,!} + \left(\frac{\partial^2 u}{\partial y^2}\right)_o \frac{y^2}{2!} + \left(\frac{\partial^3 u}{\partial y^3}\right)_o \frac{y^3}{3!} + \ldots\ldots \qquad (10.4)$$

the coefficients of y^2 and y^3 are known if - apart from the pressure- and suction distribution - the coefficient $\left(\frac{\partial u}{\partial y}\right)_o$ is given.

The procedure adopted now is to calculate the velocity profile near the wall from equation (10.4) for some assumed values of $\left(\frac{\partial u}{\partial y}\right)_o$. These velocity profiles are then plotted on a sheet of transparant paper which is placed on the measured curve in such a way that one of the calculated profiles coincides with the measured profile over some distance near the wall. Using this procedure not only the position of the wall is found but also a value for the wall shear stress is obtained. It may be noted from equation 10.2 and 10.3 that for the present case of impervious walls ($v_o = 0$) the derivatives $\left(\frac{\partial^2 u}{\partial y^2}\right)_o$ and $\left(\frac{\partial^3 u}{\partial y^3}\right)_o$ follow directly from

$$\left(\frac{\partial^2 u}{\partial y^2}\right)_o = -\frac{U}{\nu}\frac{dU}{dx} \qquad (10.5)$$

$$\left(\frac{\partial^3 u}{\partial y^3}\right)_o = 0 \qquad (10.6)$$

10.3.4. Measurements with the surface tubes.

From the difference in pressure indicated by the flattened total head tube and the static tube, shown in fig. 10.2, the value of $\frac{1}{2}\rho u^2$ at a small distance from the wall is found. This device may then be used to obtain a rough estimate of the wall shear stress and the position of separation. It is not possible to get accurate values in this way due to the fact that the distance between the wall and the effective center of the total-head tube is not known.

10.3.5. Flow visualization experiments.

It was attempted to determine the separation point of the laminar boundary layer by means of the oil film technique and using smoke. No sharp indication of separation could be obtained in this way. The position of reattachment of the turbulent boundary layer, however, was clearly indicated by the oil film.

0.4. Results of the experiments.

0.4.1. The pressure distribution.

Detailed results of the pressure measurements have been collected in table 10.3. Fig. 10.4 shows $\overline{U}$ as function of $\overline{x}$ for the lower chord with orifices without the boundary layer traversing gear present. Values of $\overline{U}$ obtained with the static tube are consistently about 0.5^{o}/o lower than those determined from the orifices. Therefore the results of the static tube have been used only as an aid to draw a proper curve through the points resulting from the orifices. The full curves drawn in fig. 10.4 give the relations between $\overline{U}$, $\frac{d\overline{U}}{d\overline{x}}$ and $\overline{x}$ which finally have been adopted for the boundary layer calculations (See also table 10.4). Near the leading-edge ($-0.04 < \overline{x} < +0.04$) the measurements may be approximated by

$$\overline{U} = 21.987\ \overline{x} - 2218.8\ \overline{x}^{3} + 221907\ \overline{x}^{5} \qquad (10.7)$$

In the interval $0.12 < \overline{x} < 0.18$ an irregularity in $\overline{U}(\overline{x})$ occurs; this region is shown to a larger scale in fig. 10.5. It is possible that the oscillation in $\frac{d\overline{U}}{d\overline{x}}$ is caused by inaccurate manufacturing of the model but it may equally well originate from the procedure by which the airfoil sections are designed. It is usual to compute the coordinates of a limited number of points of a section which in general is not sufficient to fix the shape in every detail. Especially in the region near the leading-edge, where rapid changes in curvature occur, the pressure distribution may be very sensitive to small deviations from the desired contour. Support to this idea is given by the fact that for the suction model, to be described in chapter 11, a similar irregularity occurred.

There is a sharp discontinuity in the pressure distribution near $\overline{x} = 0.71$; this is caused by transition of the separated laminar

boundary layer and subsequent turbulent reattachment. Separation occurs upstream of this point at about $\overline{x} = 0.64$ (see section 10.4.2).
The region from $\overline{x} = 0.40$ to 0.80 is shown to a larger scale in fig. 10.6. This figure reveals a second discontinuity in the slope of the curve near $\overline{x} = 0.635$. It will be shown in section 10.4.2. that this irregularity corresponds to the separation point of the laminar boundary layer.
Results for the upper row of orifices are very nearly the same as those for the lower row (see table 10.3); therefore in what follows it will be assumed that the pressure distribution is two-dimensional.
Inserting the boundary layer traversing gear in the wind tunnel lowers the values of $\overline{U}$ upstream of the hot-wire by about $0.5^{o}/o$. The shape of $\overline{U}(\overline{x})$ however remains essentially the same. The values of $\overline{U}$, with the traversing gear present, can be made equal to those without it by decreasing U_{∞} by about $0.5^{o}/o$; this implies adopting a $0.5^{o}/o$ lower value of the Reynoldsnumber R_c. Remembering that the boundary layer parameters $\overline{\delta^*}$, $\overline{\Theta}$, H and the non-dimensional wall shear stress ℓ only depend on the function $\overline{U}(\overline{x})$, and not on the value of R_c, it is clear that changing R_c will have no influence on the position of separation. The boundary layer thickness is inversely proportional to $(R_c)^{\frac{1}{2}}$ and hence the boundary layer thickness will increase $0.25^{o}/o$ due to the presence of the boundary layer traversing gear. It can not be expected that this difference will be noticed in the experiments.
Therefore in all subsequent analyses of the experimental results and boundary layer calculations the pressure distribution as determined for the lower chord, without the traversing gear present, has been used (table 10.4).
The values of $\overline{U}$ quoted in table 10.4 have been obtained from large scale versions of fig. 10.4 to 10.6; the derivatives $\frac{d\overline{U}}{d\overline{x}}$ have been found by numerical differentiation. It is emphasized at this point that slight changes in $\overline{U}(\overline{x})$ may produce large variations in $\frac{d\overline{U}}{d\overline{x}}$. There is scope for a different fairing of the experimental results, especially near the irregularity at $\overline{x} = 0.15$ and near separation. This may have an appreciable effect on the boundary layer calculations.

0.4.2. Results of the boundary layer measurements.

The measured velocity profiles are shown in fig. 10.7; the values of $\overline{u}$ as determined from equation 10.4 have been included to show how this equation fits the measurements. Some points measured very near the wall should be disregarded since these results may have been influenced by some disturbing factors. In the first place the calibration of the hot-wire is not valid when measuring very near a wall. In the second place the prongs holding the wire may have been in contact with the wall leading to an extra heat loss of the wire. Moreover - and this is probably the most important factor - the prongs may bend, leading to an erroneous value for y. Included in fig. 10.7 are the velocity profiles determined from the boundary layer calculations to be discussed in section 10.5. Fig. 10.8 shows a comparison between the experimentally determined and calculated values of $\overline{\delta^*}$, $\overline{\theta}$ and H. The wall shear stress, obtained from the procedure outlined in section 10.3.3, is shown in fig. 10.9 where the results of boundary layer calculations are also given. The measurements seem to indicate that zero skin friction, and hence separation, will occur near $\overline{x} = 0.64$.

Included in fig. 10.9 are the results of measurements with the combined total head- and static tubes. For comparison the values of $\overline{u}$ at constant distances from the wall, as obtained from a cross plot of fig. 10.7, have also been given. The results indicate that the effective distance of the total head tube from the wall is nearly constant at a value between 0.25 and 0.30 mm for $x < 0.44$. For $x > 0.45$ the effective distance in general increases in the downstream direction especially when separation is approached. The velocity indicated by the tube tends to zero for $\overline{x} \rightarrow 0.665$ implying that the tube enters the region with backflow for $\overline{x} > 0.655$.

It has been shown by Goldstein [84] (see also section 8.9) that near a separation point τ_o should behave like $(\overline{x} - \overline{x}_s)^{\frac{1}{2}}$ where $\overline{x}_s$ denotes the separation point. Therefore it is appropriate to plot τ_o^2 versus $\overline{x}$ near separation. This has been done in fig. 10.10; it is found indeed that a straight line can be drawn through the measured points. Extrapolating to zero shear stress indicates separation at $\overline{x} = 0.637$;

this is so close to the value $\overline{x} = 0.635$ where a discontinuity in $\frac{d\overline{U}}{d\overline{x}}$ occurs, that it may be assumed that the irregularity in $\overline{U}(\overline{x})$ is due to the presence of the separation bubble.
Also shown in fig. 10.10 is $\overline{u}_p^{\,2}$; where $\overline{u}_p$ is the value indicated by the total head- and static tube combination. It follows that $\overline{u}_p^{\,2}$ becomes zero at $\overline{x} = 0.655$; remains negative until $\overline{x} = 0.716$; rises very fast downstream of $\overline{x} = 0.716$ and levels off again at about $\overline{x} = 0.80$. It is noted that $\overline{u}_p^{\,2}$ is not to be interpreted as the square of a velocity when negative; since the total head tube will not indicate total head but nearly static pressure when placed in a reversed flow.
Combining the information obtained from all the measurements described above suggests the following description of the flow near separation (see also fig. 10.11). Separation of the laminar boundary layer occurs at $\overline{x} = 0.635 - 0.637$ causing a small kink in the $\overline{U}(\overline{x})$ curve. At $\overline{x} = 0.655$ the effective center of the total head tube passess through the upper boundary of the region with reversed flow. Near $\overline{x} = 0.71$ transition of the separated layer occurs resulting in a sudden decrease of the displacement thickness and consequently in a large discontinuity in the curve for $\overline{U}(\overline{x})$. Near $\overline{x} = 0.716$ reattachment of the turbulent layer sets in while at $\overline{x} = 0.80$ a fully attached turbulent boundary layer occurs.

10.4.3. Results of the flow visualisation experiments.

Oil film technique. Due to the low speed at which the experiments were performed the aerodynamic forces on the oil were very small especially near separation. On the other hand, since the model surface was vertical, there was a strong influence of gravity forces on the direction of the oil flow. Therefore no reliable indication of separation could be obtained; from various trials it was conjectured however that separation occurs at $\overline{x} = 0.65 \pm 0.01$. Turbulent reattachment was shown very clearly to start at $\overline{x} = 0.71$ while a fully reattached turbulent boundary layer flow appeared to occur downstream of $\overline{x} = 0.74$.

Smoke injection. As the results of the oil film experiments were not conclusive it was tried to find the separation point by introducing smoke into the downstream end of the separation bubble. A very thin layer with reversed flow became clearly visible due to forward movement of the smoke in the bubble. Due to its small thickness the forward edge of the bubble was difficult to estimate; it was certainly upstream of $\bar{x} = 0.66$ however.

10.5. Boundary layer calculations using the measured pressure distribution.

10.5.1. The momentum method.

The pressure distribution used for the boundary layer calculations has been defined by equation (10.7) for $0 \leqslant \bar{x} \leqslant 0.04$ and by table 10.4 for $0.04 \leqslant \bar{x} \leqslant 0.70$. From $\bar{x} = 0$ to 0.04 equation (5.40) was employed with $\bar{x}_1 = 0$, $a_1 = 0.415$ and $b_1 = 4.84$; a step by step solution starting from $\bar{x} = 0.01$ gave essentially the same results at $\bar{x} = 0.04$. At $\bar{x} = 0.04$ a step by step calculation was started using steps of 0.01; from $\bar{x} = 0.12$ to 0.18 and 0.46 to 0.51 also calculations have been made using half the original step length without changing the results.

Comparisons of the theory with the experimental results have been given in figs 10.7 to 10.10. A good correspondence is shown in the interval $0.28 < \bar{x} < 0.47$. The differences between theory and experiment in the interval $0.15 < \bar{x} < 0.25$ may be due to different reasons. In the first place it is possible that the momentum method overestimates the effects of an oscillation in $\frac{d\bar{U}}{d\bar{x}}$ since - for cases without suction - it is essentially a one-parameter method. In the second place it is very difficult to obtain accurate values for $\frac{d\bar{U}}{d\bar{x}}$ in this region; the values given in table 10.4 and fig. 10.4 for $0.15 < \bar{x} < 0.25$ may be appreciably in error.

Between $\bar{x} = 0.46$ and 0.58 the momentum method produces values for $\overline{\delta^*}$ and H which are too high while the wall shear stress is too low. From $\bar{x} = 0.58$ to 0.635 the values for $\overline{\delta^*}$ and H are predicted too low and the wall shear stress is overestimated. Consequently the theory does not show separation. However, if the calculation is extended downstream of $\bar{x} = 0.635$ suddenly separation is obtained; this can easily be seen as follows.

In the momentum method separation occurs at $\Lambda_1 = \overline{\Theta}^2 \frac{d\overline{U}}{d\overline{x}} = -0.0871$ for the no-suction case (see table 5.3). Directly upstream of $\overline{x} = 0.635$ the calculation gives $\overline{\Theta} = 0.45$ and $\Lambda_1 = -0.0525$ with $\frac{d\overline{U}}{d\overline{x}} = -0.26$. Since in the theory $\overline{\Theta}$ is assumed to be continuous, even when discontinuities in the boundary conditions occur, $\overline{\Theta} = 0.45$ also directly downstream of $\overline{x} = 0.635$. At this position table 10.4 indicates that $\frac{d\overline{U}}{d\overline{x}} = -0.7255$ and hence $\Lambda_1 = -0.147$; which is already far beyond the separation value of -0.0871.

It is interesting to investigate whether a small change to $\overline{U}(\overline{x})$ may be made upstream of $\overline{x} = 0.635$ which remains within experimental error and for which the momentum method predicts separation at $\overline{x} = 0.635$.

If only a very local modification is made it is easy to indicate a function $\overline{U}(\overline{x})$ which produces the desired result; this may be seen as follows.

First it is noted that due to a small change in $\overline{U}(\overline{x})$ the value of $\overline{\Theta}$ at $\overline{x} = 0.635$ will not change in first approximation while $\frac{d\overline{U}}{d\overline{x}}$ and hence $\Lambda_1 = \overline{\Theta}^2 \frac{d\overline{U}}{d\overline{x}}$ may change considerably. Therefore it may be assumed that $\overline{\Theta}$ at $\overline{x} = 0.635$ keeps the value 0.45 so that to obtain separation at this position $\frac{d\overline{U}}{d\overline{x}}$ should assume such a value that $\Lambda_1 = \overline{\Theta}^2 \frac{d\overline{U}}{d\overline{x}} = -0.0871$.

This leads to $\frac{d\overline{U}}{d\overline{x}} = -0.43$. Since for the pressure distribution given in table 10.4 and fig. 10.4 the derivative $\frac{d\overline{U}}{d\overline{x}}$ changes discontinuously from -0.26 to -0.7255 at $\overline{x} = 0.635$ it is not difficult to imagine a function $\overline{U}(\overline{x})$ which produces the desired result. It is sufficient to round off the kink in $\overline{U}(\overline{x})$ at $\overline{x} = 0.635$ (see fig. 10.13). Such a modification is certainly within experimental error.

Since a local modification of $\overline{U}(\overline{x})$ does not improve the agreement between theory and experiment further upstream it is interesting to solve the more general problem of finding the function $\overline{U}(\overline{x})$ for which the momentum method reproduces the experimentally determined wall shear stress throughout a certain interval. Such a function will be indicated in the remainder of the present section.

Fig. 10.13 shows the values of $\ell = \frac{\tau_o \Theta}{\mu U}$ which have been determined from the experimental results. In what follows the function $\overline{U}(\overline{x})$ will be derived for which the momentum method exactly reproduces these experimental values. Since in the momentum method for the no-suction case there is only one free parameter (see table 5.3) the known function $\ell(\overline{x})$ directly determines Λ_1 and M as function of $\overline{x}$. Then the definition of Λ_1 and the momentum equation (5.18) lead to the following differential equations for $\overline{\Theta}$ and $\overline{U}$

$$\frac{d\overline{U}}{d\overline{x}} = \frac{\Lambda_1(\overline{x})}{\overline{\Theta}^2} \tag{10.8}$$

$$\frac{d\overline{\Theta}^2}{d\overline{x}} = \frac{M(\overline{x})}{\overline{U}(\overline{x})} \tag{10.9}$$

These equations have been solved with initial values for $\overline{U}$ and $\overline{\Theta}$ at $\overline{x} = 0.46$ determined from the earlier calculation with the momentum method. The resulting function $\overline{U}(\overline{x})$ is shown in fig. 10.13. It may be seen that the difference with the original curve is certainly larger than experimental error.
However, if a similar calculation is made starting at $\overline{x} = 0.59$ the momentum method may be made to accurately predict the measured wall shear stress with a resulting change in $\overline{U}(\overline{x})$ which might be less than experimental error.

10.5.2. The multimoment method.

Near the stagnation point ($0 < \overline{x} < 0.04$) equation (10.7) supplies a good approximation of the measured pressure distribution. Hence the pressure gradient parameter λ_1 may be approximated in $0 \leqslant \overline{x} \leqslant 0.04$ by

$$\lambda_1 = 1 - 201.83\,\overline{x}^2 + 20003\,\overline{x}^4 + 4055600\,\overline{x}^6 + 207380000\,\overline{x}^8 + \ldots . \tag{10.10}$$

Using (10.10) the series method has been used to calculate the boundary layer for $0 \leqslant \overline{x} \leqslant 0.03$; the step by step method was employed for $\overline{x} \geqslant 0.03$. To be able to perform the calculations with variable step length the values of λ_1 from table 10.4 were approximated by analytic expressions of the form (8.49). The coefficients e_n are collected in table 10.5.

Results for N = 5,6 and 7 are included in figs 10.7 - 10.12; in general a good agreement between theory and experiment is shown. It follows that the multimoment method is slightly superior to the momentum method. For instance it may be noted that a better prediction of the wall shear stress is obtained for $0.48 < \bar{x} < 0.58$. However, the deviation from the experimental values downstream of $\bar{x} = 0.58$ is very similar to the behaviour shown by the momentum method. Again no separation is indicated upstream of $\bar{x} = 0.635$. If however the calculation is extended beyond $\bar{x} = 0.635$ suddenly separation occurs.

Again small changes in $\bar{U}(\bar{x})$ upstream of $\bar{x} = 0.635$ are sufficient to let the theory "predict" the wall shear stress with good accuracy in the interval shortly upstream of $\bar{x} = 0.635$.

0.6. Concluding remarks on the experiments without suction.

From the comparisons between theory and experiment for the boundary layer without suction the following conclusions may be drawn.

1. Both the momentum method and the multimoment provide results which are in good agreement with the experiments except close to separation. The multimoment method is slightly superior to the momentum method.
2. Both methods fail to predict separation if the pressure distribution from fig. 10.4 and table 10.4 is used. Both theories may be forced to approach separation with the right shear stress distribution by changing $\bar{U}(\bar{x})$ with a small amount. Although this change might be within experimental error no firm conclusion has been reached on this point.
3. To provide a definite answer to the question whether boundary layer theory is valid near separation the experiments should be performed with greater accuracy than has been achieved in the present investigation.

1. Experimental investigation of a 15°/o thick laminar flow airfoil section with distributed suction.

1.1. Introductory remarks.

In the present chapter some experimental work will be described which was performed on a NACA 64_2-A-215 airfoil section with boundary layer suction through a porous surface. The chord length of the model is 1.35 m; both the upper and the lower surface are porous between the 30°/o and 90°/o chord positions.

The model was tested in the low speed wind tunnel of the Department for Aeronautical Engineering at Delft. Measurements have been performed for angles of attack from -6 to +6 degrees and at Reynoldsnumbers R_c up till 8×10^6. The characteristics of the model without suction were determined by sealing the porous surface with a thin sheet of self-adhesive plastic.

The aims of the investigations were as follows:

a) To collect data on transition of two-dimensional boundary layers with suction. The results are to be used to check whether the method for predicting the transition point - proposed in chapter 9 - is applicable also for boundary layers with suction.

b) To obtain experimental data on the velocity distribution in a two-dimensional laminar boundary layer with suction including a separation point. These data are to be used for a comparison of boundary layer theory with experiment in the case of suction.

c) To collect some data on the amount of drag reduction obtained from laminarisation by means of suction.

Section 11.2 describes the experimental apparatus; the test methods and data reduction procedures are given in section 11.3 while results of the investigations are presented in sections 11.4 to 11.8.

In 11.4 the results of pressure distribution measurements are given. Section 11.5 describes the results of detailed boundary layer surveys on the upper surface of the model at $\alpha = 0^o$ and $R_c = 2.75 \times 10^6$. The results are presented both for the no-suction case and for one case with suction. The suction distribution for this case was chosen in such a way that laminar separation occurred in the suction region. Results of the

measurements are compared with boundary layer calculations using the momentum method and the multimoment method.
In section 11.6 some data on transition position and drag of the unsucked model are presented. Included are results of boundary layer calculations obtained from the momentum method together with calculated values of the amplification factor σ_a. Similar results for some cases with suction are discussed in section 11.7.
Finally, section 11.8 summarizes the results for the wake drag, suction drag and total drag for the configurations tested.

Since the experimental work has been very extensive no attempt will be made to describe it here in every detail. Only the main results will be quoted and especially those which are of significance for a comparison with laminar boundary layer theory and for the verification of the proposed method to compute the transition point.

11.2. Description of the experimental apparatus.

11.2.1. General.

The experiments were performed in the wind tunnel mentioned in section 10.2.1. The hot-wire equipment, described in section 10.2.3, was used again for the present investigation. In what follows some additional equipment will be described.

11.2.2. The model.

The airfoil section of the model is NACA 64_2-A-215 with a chord length of 1.35 m; coordinates of the airfoil section follow from table 11.1. The model was placed vertically between turntables in the ceiling and floor of the test section; the span obtained in this way being 1.25 m (see fig. 11.1).
The model is built up from two heavy steel spars connected by means of 10 ribs, in the suction region about 115 mm apart in the spanwise direction.

Suction is provided both for the upper and the lower surface between the $30^{\circ}/o$ and $90^{\circ}/o$ chord positions; the spanwise extent of the porous surface is 0.805 m. Pressure orifices are present in one chord 344mm above the floor of the testsection (fig. 11.1); the positions of the orifices in chordwise direction follow from table 11.2. Two additional orifices (number 26 for the upper surface and number 25 for the lower surface) are placed in the midspan chord close to the trailing edge (see also table 11.2).

The inside of the model is divided into 40 different suction compartments, each with its own suction line, flow-regulating valve and -measuring device. A cross-section of the model is shown in fig. 11.2; the positions of the compartments in streamwise direction - measured along the contour of the model - have been given in table 11.3. In fig. 11.3 an enlargement of a part of fig. 11.2 is presented to show more clearly the construction of the porous surface. It consists of two layers of filtering paper supported by a metal screen which in turn rests on the ribs and between the ribs on wide-mesh paper honeycomb. Both the screen and the honeycomb have such a large open area that they provide a negligible resistance to the airflow and only act as support for the filtering paper.

Since at the position of the ribs the metal screen is supported directly on the ribs some obstruction to the suction flow is present here. However due to the fact that some leakage occurred between the two layers of filtering paper the inflow velocity at the position of the ribs was not so low as to cause important spanwise variations of the boundary layer characteristics. In typical cases transition to turbulent flow occurred on the ribs about 3 $^{o}/o$ of the chordlength earlier than in sections midway between two ribs.

Some photographs of the model in various stages of construction are shown in figs 11.4-11.6. A schematic drawing of the suction compartments with the related suction equipment is shown in fig. 11.7.

The top surface of the compartments consists of 7 brass plates each containing 8 small metering holes (diameters ranging from 0.5 to 1 mm for different compartments). The 56 holes in each compartment have been drilled very accurately to the same diameter in order to obtain a constant inflow velocity over the span. The constancy is slightly impaired by local variations in porosity of the filtering paper amounting to about 10 °/o. Since two layers of filtering paper have been used and since the major part of the resistance is provided by the metering holes, the actual variations in inflow velocity will have been far less than 10 °/o.

Figure 11.7 shows that the suction flow is measured at different stages. First of all the pressure drop is measured over the 8 metering holes in the plate covering the middle $^{1}/7$th part of the span of a compartment. Then, from a calibration curve the suction flow into this middle section is known. The total flow into the compartment is measured by means of an orifice plate P_i and finally the flow into all 20 compartments in the upper or lower surface of the model is measured by means of a large orifice plate P_u or P_L (fig. 11.7). All these orifice plates have been calibrated individually before the tests.

Since the height of the compartments 19 and 20 in both the upper and lower surface is rather small it was not possible to provide them with plates containing metering holes.

The suction flow into individual compartments can be varied by means of the regulating valves V_i (fig. 11.7); the total flow from the model may be changed by means of a central valve V_c in the suction line to the pump.

For the experiments without suction the two layers of filtering paper were replaced by a large sheet of self-adhesive plastic.

From preliminary measurements of the pressure distribution on this model it was found that near the leading-edge an irregularity in the pressure distribution occurred which was related to an oscillation in the curvature of the model (fig. 11.8). Before starting the tests, described in the present work, the irregularity was removed to a great extent by smoothing the curvature of the model. This was accomplished by adding a thin plastic bump to the contour of the model. The largest thickness of this bump was 0.4 mm and occurred at $s/c = 0.05$ (see fig. 11.8).

11.2.3. Boundary layer traversing apparatus.

For the measurement of boundary layer velocity profiles the traversing gear, mentioned in section 10.2.3. was used. For some measurements the hot-wire probe was replaced by a total head tube with a flattened opening (0.4 mm high).

1.2.4. Instruments for transition detection.

For transition detection two different devices have been employed. For measurements on the sealed model a small total head tube was used which could be moved in chordwise direction along the surface of the model by means of a small carriage. Transition from laminar to turbulent flow is indicated by this device through a sudden rise in total head.
For transition detection on the model with suction a "stethoscope" was used consisting of a total head tube connected to a microphone. Pressure fluctuations in the turbulent boundary layer could be made audible in this way. The device was mounted on a thin long pole which was handled by the observer to put the tube in contact with the model surface at different positions. In this way a quick estimate of the transition position could be obtained.

1.2.5. Other equipment.

For the measurement of wake drag a wake survey rake was used in combination with an "integrating manometer" (see for instance Pankhurst and Holder [111]).
For the pressure distribution measurements Betz-type manometers and inclined tubes have been used. The large number of pressures determining the suction distribution was measured on multiple type manometer banks. These pressures were recorded by photographing the manometers.

1.3. Test methods and reduction of data.

1.3.1. General.

Test methods and data reduction procedures have been - for so far possible - equal to those described in section 10.3. Some other methods will be described in the remainder of the present section.

11.3.2. The pressure distribution and "free stream speed".

The surface pressure distribution was measured in the same way as described in section 10.3.1. for the impervious model. The pressures were reduced to the velocity U at the edge of the boundary layer using equation (10.1). U was made non-dimensional with the "free stream speed" U_∞ defined by

$$\tfrac{1}{2}\rho U_\infty^{\,2} = p_t - p_m \qquad (11.1)$$

with p_t indicating the total pressure of the pitot-static tube in the test-section (fig. 11.1). The free stream static pressure p_m is defined by

$$p_m = \frac{p_{w_+} + p_{w_-}}{2} \qquad (11.2)$$

where p_{w_+} and p_{w_-} are the static pressures, measured at two positions in the side walls of the testsection opposite the model. (fig. 11.1).
It should be noted that this definition of the free stream static pressure differs from the one used in chapter 10.
The model is rather large compared with the dimensions of the testsection and therefore the remarks about tunnel wall influence on pressure distribution and free stream speed, made in section 10.3.1, apply also to the present case.

11.3.3. Determination of the suction distribution and suction drag coefficient.

The suction distribution. All orifice plates have been calibrated before the tests; the calibration curves were approximated by analytical expressions in order to simplify the subsequent data reduction procedure. The airflow into each compartment i was reduced to the suction flow coefficient c_{q_i} defined by

$$c_{q_i} = \frac{Q_i}{U_\infty b\ c} \qquad (11.3)$$

where Q_i = the total flow into compartment number i (m^3/sec)

U_∞ = free stream speed (m/sec)

b = span of porous surface (0.805 m)

c = airfoil chord (1.35 m).

Furthermore the total suction flow coefficients c_{q_u} and c_{q_ℓ} for the upper and the lower surfaces were found either from

$$c_{q_u} \text{ or } c_{q_\ell} = \frac{\sum_1^{20} Q_i}{U_\infty b\ c} = \sum_1^{20} c_{q_i} \qquad (11.4)$$

or from a direct measurement with orifice plate P_u or P_ℓ in figure 11.7.
The mean suction velocity into each compartment follows from

$$\left(\frac{-v_o}{U_\infty}\right)_i = \frac{Q_i}{U_\infty b(\Delta s)_i} = \frac{c_{q_i}\ c}{(\Delta s)_i} \qquad (11.5)$$

in which $(\Delta s)_i$ denotes the width of the suction compartment given in table 11.3.

A typical suction distribution is shown in fig. 11.9; the measured points indicated in the figure are the mean suction velocities defined by equation (11.5). Within each compartment a slight variation of v_o may occur due the chordwise gradient of the surface pressure which gives rise to a chordwise variation of the pressure difference across the filtering paper. The resulting suction distribution is shown as a broken line in fig. 11.9. The actual inflow distribution will have been smoothed out due to leakage between the layers of filtering paper and between the paper and the metal screen. Hence for subsequent boundary layer calculations a continuous curve through the measured mean values was used as an approximation to the actual suction distribution.

The suction drag coefficient. In appendix 1 it is shown that the power required to induce the suction flow and to expell the air at free stream total head can be expressed in terms of a "suction drag coefficient" c_{d_s} defined by

$$c_{d_s} = c_p c_q \qquad (11.6)$$

In (11.6) c_p is given by

$$c_p = \frac{\Delta p}{\frac{1}{2}\rho U_\infty^2} \qquad (11.7)$$

where Δp is the pressure rise, to be provided by the suction pump. In practical applications Δp will be the sum of the following pressure losses:

a. the loss in total head of the air in the boundary layer

b. the pressure drop through the porous surface

c. the pressure losses in the suction ducts inside the aircraft.

In what follows an ideal suction drag coefficient will be used including only the pressure drop mentioned under a. It will be assumed that the boundary layer air will have lost all its dynamic head before entering the porous surface.

For practical applications it certainly will be necessary to include the pressure drops b and c which will increase the suction drag. On the other hand the simple expression (11.6) will have to be replaced by a more accurate expression taking into account the difference in efficiency of the suction pump and the prime propulsion system of the aircraft (see appendix 1). This may lead to an appreciable reduction in suction drag and it may therefore be assumed that the ideal suction drag coefficient (11.6) gives a reasonable approximation of the suction drag to be expected in practice.

In analyzing the measurements a suction drag coefficient $c_{d_{s_i}}$ for each compartment was determined from

$$c_{d_{s_i}} = c_{p_i}\, c_{q_i} = \frac{\Delta p_i}{\frac{1}{2}\rho U_\infty^2}\, c_{q_i} \qquad (11.8)$$

In (11.8) Δp_i is the difference between the free stream total head p_t and the surface static pressure p_i at the position of the i^{th} compartment. Hence

$$c_{p_i} = \frac{p_t - p_i}{\frac{1}{2}\rho U_\infty^2} = \bar{U}_i^{\,2} \qquad (11.9)$$

where $\overline{U}_i$ is the maximum value of $\overline{U}$ occurring at the outer surface of compartment number i.

The suction drag coefficient for the whole upper or lower surface of the model follows from a summation of $c_{d_{s_i}}$ for the 20 compartments related to that surface and hence

$$c_{d_{s_u}} \text{ or } c_{d_{s_\ell}} = \sum_{i=1}^{20} c_{d_{s_i}} \quad . \tag{11.10}$$

A mean pressure loss coefficient for each surface follows from

$$c_{p_u} \text{ or } c_{p_\ell} = \frac{\sum_{i=1}^{20} c_{p_i} c_{q_i}}{\sum_{i=1}^{20} c_{q_i}} \tag{11.11}$$

1.3.4. Determination of the wake drag.

From wake traverses. The drag of an airfoil without suction may be determined from the momentum loss in the wake; see for instance Pankhurst and Holder [111], Pfenniger [112] and Schlichting ([7], chapter 24). In appendix 1 the principle of this method is illustrated for a flat plate. It is also shown that the drag coefficient in the case of suction can not be found from the momentum loss in the wake only but that a "suction drag coefficient" has to be added.

The part of the drag determined from the momentum loss in the wake is called "wake drag". The wake drag is determined from the distribution of total head and static pressure through the wake which is measured by means of the wake survey rake. The results of the measurements have been converted to the wake drag coefficient using Pfennigers method [112].

Determination of the wake drag from the boundary layer velocity profile at the trailing-edge. Equation (A.5) in appendix 1 shows that the wake drag coefficient of one side of a flat plate at zero angle of attack follows from

$$c_{d_w} = \frac{2\,\Theta_{t.e.}}{c} \tag{11.12}$$

where $\Theta_{t.e.}$ denotes the momentum loss thickness of the boundary layer at the trailing and c is the length of the plate. Of course the drag coefficient for both surfaces is found from (11.12) by adding the momentum loss thicknesses at the trailing-edge for both surfaces. Equation (11.12) also holds for an airfoil section if $\Theta_{t.e.}$ is replaced by Θ_∞ which is the momentum loss thickness of the wake at an infinite distance downstream of the trailing-edge. Due to the streamwise pressure gradient in the wake Θ_∞ differs from $\Theta_{t.e.}$. A relation between Θ_∞ and $\Theta_{t.e.}$ was derived by Squire and Young [113] using the momentum equation (2.15) and an empirical correlation between $\overline{U}$ and H in the wake. This leads to the following expression for the wake drag coefficient

$$c_{d_w} = 2\,\frac{\Theta_{t.e.}}{c}\,(\overline{U}_{t.e.})^{\frac{H_{t.e.}+5}{2}} \tag{11.13}$$

which reduces to (11.12) for the flat plate at zero angle of attack ($\overline{U}_{t.e.} = 1$). The derivation of (11.13) may be found for instance in Schlichting ([7], chapter 24).

The advantage of using (11.13) over the wake traverse method is that it may be applied to the upper and lower surface of the model separately so that changes in wake drag may easily be correlated with changes in transition position or suction intensity for either surface.

For the experiments without suction the boundary layer at the trailing edge was sufficiently thick to measure accurately the velocity profiles with a small rake of total head and static tubes fixed to the trailing-edge. For the experiments with suction the boundary layer thickness at the trailing-edge is greatly reduced (see fig. 11.17 for instance) and hence measurements with a rake are not sufficiently accurate. Therefore in all experiments with suction the velocity profiles at the trailing-edge have been measured with the flattened total head tube in combination with the traversing gear, described in section 11.2.3. No corrections for displacement effect of the tube have been applied. From

the measured velocity profiles δ^*, Θ and H were determined and substituted in (11.13) to find the wake drag coefficient.
The velocity profiles were not measured exactly at the trailing-edge but at the position of the most rearward pressure orifice. Since this orifice is placed at 98.5°/o of the chord the wake drag coefficient found from equation (11.13) may be slightly too small.

A comparison of the wake drag found from equation (11.13) and from the wake survey method is shown in fig. 11.10 for some typical cases. In general a good correspondence is obtained.

11.4. Results of the pressure distribution measurements.

Results of the pressure distribution measurements for the no-suction case expressed in terms of $\overline{U}$ have been given in fig. 11.11 for different values of the angle of attack and a Reynoldsnumber based on chord of 5.5×10^6. Similar results have been obtained at other values of R_c ranging from 1×10^6 to 8.7×10^6. No systematic changes of $\overline{U}$ with R_c have been noted except for $R < 1.5 \times 10^6$. This change may be due to an appreciable thickening of the boundary layer at low speeds. Since in the subsequent experiments the main interest lies at the higher Reynoldsnumbers it will be assumed that the pressure distributions shown in fig. 11.11 can be used for boundary layer calculations at all values of the Reynoldsnumber R_c.
Some experiments with different amounts of suction were performed at $\alpha = 0^o$. No systematic influence of suction on the pressure distribution was found except near the trailing edge.
It may be noted that the suction velocities required to keep the boundary layer laminar are of the order of $10^{-4} U_\infty$ so that a direct influence of suction on the pressure distribution is difficult to imagine. An indirect effect of suction may have arisen as follows.
It was shown in chapter 10 that a discontinuity in the pressure gradient may occur where laminar separation is followed by turbulent reattachment. Since due to suction the positions of separation and transition may change, also the corresponding irregularities in the pressure distribution may change their positions. Since it was difficult

to install a large number of pressure orifices in the porous surface, the pressure distribution could not be determined very accurately and possible irregularities in the pressure distribution, referred to above, were not noticed. It has therefore been assumed that for all boundary layer calculations with and without suction the pressure distributions, shown in fig. 11.11, may be used.

11.5. Results of boundary layer surveys on the upper surface with and without suction.

Detailed surveys of the boundary layer in the midspan chord on the upper surface of the model were made at $\alpha = 0^o$ and $R_c = 2.75 \times 10^6$. For measurements in the laminar boundary layer with and without suction hot-wires have been used. Velocity profiles in the turbulent boundary layer, existing over the rear part of the surface in the no-suction case, have been measured with the flattened total head tube.
The results of the experiments will be discussed in the present section together with results of calculations using the momentum method of chapter 5 and the multimoment method of chapter 7.
Details of the pressure- and suction distributions used for the boundary layer calculations are shown in fig. 11.12 and table 11.4. For the calculations with the multimoment method λ_1 and λ_2 were approximated by polynomial expressions of the form

$$\lambda_1 \text{ or } \lambda_2 = \sum e_n \bar{x}^n \tag{11.14}$$

The coefficients e_n have been listed in table 11.5. Results of the measurements and calculations are shown in figs 11.13 to 11.19.
Velocity profiles at some stations are shown in fig. 11.13; it follows that the laminar profiles with and without suction are reproduced reasonably well by the momentum method and the multimoment method. For the momentum method the correspondence is better than for the measurements discussed in chapter 10. It may be assumed that the better results in the present case stem from the fact that changes in $\frac{d\bar{U}}{d\bar{x}}$ are more gradual than for the impervious model.
The velocity profiles in the turbulent boundary layer without suction

are included in fig. 11.13. However, due to the large boundary layer thickness they could not be shown completely. Therefore, fig. 11.14 presents the velocity profiles in this region to a smaller scale. It is noticed that, as expected, a considerable reduction in boundary layer thickness and skin friction results from the application of suction.

Values of $\overline{\delta^*}$ and $\overline{\Theta}$ are shown in fig. 11.15 for the laminar boundary layers; a good correspondence between theory and experiment is shown. The experimentally determined values of the wall shear stress and the shape factor H for the laminar boundary layers with and without suction, are compared with the theoretical predictions in fig. 11.16. Again a good agreement is shown. It has to be remembered that the measured values of the wall shear stress were not obtained directly but resulted from the data reduction procedure, outlined in section 10.3.3.

According to the experiments laminar separation occurs at $\overline{x} = 0.56$ for the no-suction case and at $\overline{s} = 0.89$ in the case of suction. It may be seen that the momentum method predicts separation a bit early at $\overline{s} = 0.55$ and 0.88 respectively. As in earlier examples the multimoment method gives no clear indication of separation in the no-suction case. However, a short extrapolation of the calculated shear stress upstream of $\overline{s} = 0.50$ indicates separation at $\overline{s} = 0.55$. For the boundary layer with suction ($\lambda_2 \neq 0$) it follows from equation (7.63) that $a_2 \neq 0$ and hence equation (7.61) shows that $\frac{da_o}{d\overline{x}}$ may assume a non-zero value near separation. This is confirmed by fig. 11.17 from which it may be seen that the multimoment method predicts separation at $\overline{s} = 0.88$.

It is remarkable that in both cases with and without suction no difficulties were encountered in predicting the separation point. This situation is quite different from that for the boundary layer on the impervious model discussed in chapter 10. Possible explanations for this phenomenon are the following.

In the first place the better results may be due to the less accurate determination of the pressure distribution for the present case. This can best be explained by returning to fig.10.6 which shows the pressure distribution in the separation region for the impervious model. If it should have been tried to determine this pressure distribution with a small number of orifices, then it is very likely that a mean curve would have been selected showing a more adverse pressure gradient upstream of separation than the actual curve. This may help the calculation method to predict separation.

Since in both cases with and without suction laminar separation was followed by transition further downstream it may be expected that the actual pressure distribution will appear like the one shown in fig. 10.5. With the available orifices this could not be observed however.

A second explanation, only applicable to the case with suction, is the following. The development of boundary layers with suction is not only determined by the pressure gradient but also by the suction velocity. Since the suction velocity is measured directly it can be determined much more accurately than the pressure gradient. Therefore it can be expected that the calculation of boundary layers with suction will be less sensitive to experimental error than boundary layers without suction.

In fig. 11.18 the results for δ^* and Θ are replotted on a smaller scale to accomodate the experimental results for the turbulent boundary layer without suction. In this presentation δ^* and Θ were not made non-dimensional to give an impression of the actual thicknesses involved. It is shown that a considerable reduction of the momentum loss thickness at the trailing-edge is obtained due to suction. According to equation (11.13) this implies a similar reduction in the wake drag coefficient. A further discussion of the drag reduction due to suction will be given in section 11.8.

In chapter 5 the characteristics of the momentum method have been discussed by means of the diagram in fig. 5.7. It was shown that known exact solutions, for which the momentum method supplies good results, are represented by the curves $P_3P_1P_4$, P_1P_2 and P_2P_4 in the diagram. It was therefore expected that the momentum method will give reasonably accurate solutions for those cases, which are represented in fig. 5.7 by a curve in the vicinity of $P_3P_1P_4$, P_1P_2 and/or P_2P_4. This is confirmed by the examples discussed in chapter 8 and 10 provided the cases with large discontinuities in pressure gradient or suction velocity are excluded.

Another curve can now be indicated in the vicinity of which the momentum method can be used with some confidence. It is the path traced out in the diagram by the boundary layer with suction discussed in the present section. This path is shown in fig. 11.19; numbers on the curve denote corresponding stations on the airfoil contour.

In view of the preceding remarks it seems justified to use the momentum method in those cases for which the corresponding curves in the M-Λ_1 plane are above or only a small distance below the curve in fig. 11.19. Since it was found that this requirement is fulfilled by most of the boundary layer flows encountered in the further analysis of the experiments with suction, it was decided only to use the momentum method for this analysis.

11.6. Transition and drag of the unsucked airfoil.

11.6.1. General.

The results of drag measurements with the wake survey rake are shown in fig. 11.20 for different values of the angle of attack as function of the Reynoldsnumber R_c.

A cross plot of fig. 11.20 is given in fig. 11.21; it shows the drag coefficient as function of α for different values of R_c. It can be seen that a "low-drag bucket" appears in the curves at low values of α and R_c. The drag rise at high values of $|\alpha|$ is caused by the fact that a pressure peak develops near the leading-edge which tends to move the transition forward. This is illustrated in fig. 11.22 where the results of transition measurements for different values of R_c are shown. In sections 11.6.2 and 11.6.3 some more detailed results will be given for the upper surface of the model at $\alpha = 0$ and 3 degrees.

11.6.2. Transition and drag for the upper surface at $\alpha = 0^o$ without suction.

The transition position and wake drag coefficient for the upper surface of the model at $\alpha = 0^o$ are shown as function of the Reynoldsnumber R_c in fig. 11.23. It is seen that transition moves forward rather slowly with increasing values of R_c.
Calculations of the boundary layer characteristics including the amplification of unstable disturbances were made in the same way as described in section 9.8. Results are included in fig. 11.23 where curves are shown for constant values of the amplification factor $(\sigma_a)_{max}$ together with the calculated position of laminar separation (which is independent of the Reynoldsnumber). If, as in chapter 9, it is assumed that transition occurs for $(\sigma_a)_{max} = 9.2 - 11.2$ it follows that the method predicts the beginning of transition too early by an amount of about $6^o/o$ of the chord length at low values of R_c. This could be expected from the results shown for the EC 1440 airfoil in section 9.8.
It will be found in more examples that cases where transition occurs downstream or a short distance upstream from separation are predicted with less accuracy than those where transition occurs far upstream of separation. Possible explanations for this feature have been given already in section 9.8.
For the present case at higher values of R_c transition moves forward of the separation point (and of course separation is prevented then). At the highest value of R_c for which calculations have been made the distance between the calculated and the measured position of the beginning of transition is $2.5^o/o$ of the chord length.

11.6.3. Transition and drag for the upper surface at $\alpha = 3^o$ without suction.

In the present section detailed results will be presented for the upper surface at $\alpha = 3^o$. They will clearly illustrate the influence of changes

in the Reynoldsnumber R_c on transition position.
Fig. 11.24 shows results of boundary layer calculations using the momentum method; included is the critical Reynoldsnumber, according to Lin's formulae, which is independent of the Reynoldsnumber R_c. The values of $\frac{U\Theta}{\nu}$ depend on R_c according to the equation

$$\frac{U\Theta}{\nu} = \bar{U}.\bar{\Theta}.(R_c)^{\frac{1}{2}} \qquad (11.15)$$

obtained from the definitions of $\bar{U}$, $\bar{\Theta}$ and R_c. In equation (11.15) both $\bar{U}$ and $\bar{\Theta}$ are independent of R_c.
The results, shown in fig. 11.24, reveal an unstable region near the leading-edge caused by the adverse pressure gradient downstream of the peak in $\bar{U}$ at $\bar{s} = 0.04$ (see fig. 11.11). At $R_c = 1.94 \times 10^6$ for instance, the boundary layer becomes first unstable at $\bar{s} = 0.047$, then becomes stable again at $\bar{s} = 0.129$ and definitely unstable at $\bar{s} = 0.189$. Whether or not the unstable region may provoke transition near the leading-edge will depend on the value of the Reynoldsnumber R_c. It can be expected that only at high values of R_c the amplification rate will be high enough for this. This is confirmed by the results of further calculations described below.
The values of the amplification factor σ_a are shown in fig. 11.25a and b for several frequencies at two different values of R_c. The envelope of the curves for different frequencies gives the maximum amplification factor $(\sigma_a)_{max}$. Similar calculations have been made for other values of R_c, the resulting envelopes have been collected in fig. 11.26. It can be seen from this figure that for high values of R_c the amplification factor reaches the critical value 9.2 very close to the leading-edge and hence transition can be expected to occur very early. This is confirmed by the experimental results shown in fig. 11.27. Included in the figure are the calculated positions of separation and curves for constant values of $(\sigma_a)_{max}$. Again it is shown that, when transition is preceded by laminar separation, the distance between the measured and predicted position of transition is of the order of $10^o/o$ of the chord. For increasing R_c however, transition moves forward of the calculated laminar separation point and the predicted separation position becomes

more accurate. Even the rather sudden shift forward at $R_c > 6 \times 10^6$ is predicted with reasonable accuracy.

11.7. Transition and drag with suction at $\alpha = 0^o$.

11.7.1. General.

In the present section (11.7) some data will be presented on transition position, wake drag, ideal suction drag and total drag for 7 series of measurements at $\alpha = 0$ with suction. Results of boundary layer calculations will be presented and the measured transition positions will be compared with results of amplification calculations. Some specific details of the 7 series have been given in table 11.6.
For series 1, to be described in section 11.7.2, the flow regulating valves V_i (see fig. 11.7) have been set in such a way that the resulting suction distribution - according to a very rough calculation - would be sufficient to prevent transition. Then the setting of the central valve (V_c in fig. 11.7) was changed to collect data at different values of c_q for the same type of suction distribution.
In series 2 (section 11.7.3) all valves V_i were left open and hence the suction distribution was determined by the built-in resistances of orifice plates and suction ducts. Again the total amount of flow was changed by means of the central valve V_c.
For series 3 (section 11.7.4) the valves have been set in such a way that the pressure underneath the filtering paper was the same for all compartments in the upper surface. Hence a continuous suction distribution was obtained. The constant pressure was given such a value that transition occurred at the end of the porous surface.
In the experiments, mentioned above, it was found to be impossible to keep the boundary layer laminar at values of R_c above 3.5×10^6. At higher speeds the inherent surface roughness of the filtering paper became supercritical causing transition due to roughness. Therefore, in some further experiments, the filtering paper was covered by a sheet

of tightly stretched fine mesh nylon (see fig. 11.6). In this way it became possible to keep the boundary layer laminar up till $R_c = 6.5 \times 10^6$. Some measurements on the upper surface, with the nylon present, have been described as series 4,5,6 and 7 in section 11.7.5. For these series the valves V_i were set by trial and error in such a way that transition occurred at the end of the porous surface with the smallest possible amount of suction. Once this was achieved the total amount of flow was changed by means of the central valve.
Finally in section 11.7.6 a comparison will be given between the calculated and measured transition positions for series 1-7.

11.7.2. Transition and drag with suction; series 1.

Values of the wake drag, ideal suction drag and total drag for the upper and lower surfaces combined are shown in fig. 11.28. The wake drag decreases and the suction drag increases with increasing values of c_q. The total drag shows a minimum value at $c_q = 7.5 \times 10^{-4}$; this corresponds to the situation when transition occurs close to the trailing-edge. This is shown clearly in figs 11.29 and 11.30, where the drag has been given for the upper and lower surface separately and a comparison is made with the measured transition position.
The suction velocity distribution for the upper surface is shown in fig. 11.31 for some values of c_{q_u}. Included as a dotted line is the suction distribution required at this value of R_c to keep the boundary layer neutrally stable downstream of the beginning of the porous region ($\bar{s} = 0.32$). This suction distribution is easily found from the momentum method and Lin's formulae (section 9.4) if the requirement is made that $\frac{U\Theta}{\nu}$ and $\left(\frac{U\Theta}{\nu}\right)_{crit}$ are equal.
Fig. 11.31 shows that in the beginning the suction velocity at all values of c_{q_u} is much higher than required for stabilisation. Further downstream the suction intensity is less than required for stabilisation.
Results of boundary layer calculations using the experimentally determined suction distributions for different values of c_{q_u} are plotted in the M-Λ_1 plane shown in fig. 11.32. It is seen that in all cases the path traced out in the diagram ends up on the left-hand-side

boundary. This implies that eventually the laminar boundary layer separates from the surface unless transition occurs earlier. Indicated in the figure are the values of M and Λ_1 corresponding to the measured *transition positions. It follows that only for* $c_{q_u} = 0$ *and for very* high values of c_{q_u} separation is actually reached. For intermediate suction quantities laminar separation is prevented by transition. Values of ${}^{10}\log \frac{U\Theta}{\nu}$ and ${}^{10}\log \left(\frac{U\Theta}{\nu}\right)_{crit}$ are shown in fig. 11.33 for different values of c_{q_u}. It can be seen that for $c_{q_u} = 0$ the boundary layer becomes unstable at $\bar{s} = 0.33$ coinciding almost with the beginning of the porous surface. For the non-zero values of c_{q_u} the suction in *the first part of the porous region is so intense that a strong* stabilising influence occurs. (${}^{10}\log \left(\frac{U\Theta}{\nu}\right)_{crit} \gg {}^{10}\log \frac{U\Theta}{\nu}$). However, downstream of the pressure minimum at $\bar{s} = 0.42$ (see fig. 11.31) the adverse pressure gradient rapidly compensates the effect of suction and the boundary layer becomes unstable. Only at very high values of c_{q_u} would the boundary layer remain stable as far as the trailing-edge.
An interesting feature follows from a comparison of fig. 11.31 and 11.33. It is noticed that the boundary layer becomes unstable very close to the position where $|v_o|$ falls below the value needed to obtain a neutrally stable boundary layer over the full length of the porous surface. This implies that boundary layer stability - at least according to the momentum method - has a very poor memory for its upstream history. This may be explained by observing that the influence of suction on stability lies principally in the change of the critical Reynoldsnumber while the changes in $\frac{U\Theta}{\nu}$ are much less. (fig. 11.33). Since $\frac{U\Theta}{\nu}$ depends on the history of the boundary layer but the shape of the velocity profile - and hence $\left(\frac{U\Theta}{\nu}\right)_{crit}$ - is primarily determined by the local pressure gradient and suction velocity, it is clear that the upstream history is of secondary importance only. Therefore it is clearly not economic to apply suction to early; the most economic suction distribution will be obtained by carefully tailoring the suction velocity distribution to the local needs of the boundary layer.

Using $\frac{U\theta}{\nu}$ and $(\frac{U\theta}{\nu})_{crit}$ from fig. 11.33 for different values of c_{q_u} amplification calculations have been made for different frequencies. The resulting envelopes, denoting the maximum amplification factor, are shown in fig. 11.34. It follows that only for $c_{q_u} < 3.39 \times 10^{-4}$ the critical value 9.2 is reached in the porous region. This implies that transition can only be expected to occur in the suction region for $c_{q_u} < 3.39 \times 10^{-4}$.

In figure 11.35 the measured transition region is compared with the calculated positions for which $(\sigma_a)_{max} = 9.2$ and 11.2. Although the calculated positions are a little further downstream than the measured transition position, a satisfactory prediction of the transition region will be obtained for $c_{q_u} < 3.5 \times 10^{-4}$ if it is assumed that transition occurs as soon as $(\sigma_a)_{max}$ reaches the values 9.2-11.2. At higher values of c_{q_u} transition is caused by a preceding separation in which case the proposed method for the prediction of transition can not be expected to provide accurate results. This is confirmed by the results shown in fig. 11.35.

1.7.3. Transition and drag with suction; series 2.

For this series the same measurements and calculations have been performed as for series 1; results are presented in figs 11.36 - 11.39.

1.7.4. Transition and drag with suction; series 3.

This case is included since it shows one of the examples for which the distance between the measured and calculated transition positions is rather large. Final results are shown in fig. 11.40; it follows that transition is preceded by laminar separation for all values of c_{q_u} explaining the unsatisfactory agreement between theory and experiment.

1.7.5. Transition and drag with suction: series 4-7: $\alpha = 0^\circ$ upper surface only; filtering paper covered with nylon.

For series 4-7 the filtering paper was covered with a sheet of fine mesh nylon. In the present section some results of measurements and calculations for the upper surface will be presented. For series 4-7

the valve settings were found by trial and error. It was attempted to obtain, with the minimum amount of suction, a boundary layer for which transition occurred at the end of the porous surface.
The suction distributions obtained in this way for different values of R_c are shown in fig. 11.41. Also shown for two values of R_c is the v_o-distribution required to keep the boundary layer neutrally stable throughout the suction region. It can be seen that in all cases too much suction has been applied in the forward part of the porous region. This may be explained as follows. If the suction velocities are chosen very low it is possible that - inadvertently - local outflow occurs giving rise to premature transition. Apparently the suction velocities used in the experiments were chosen on the safe side.
Near the trailing-edge the suction intensity is in general less than that needed for stabilisation.
Boundary layer calculations, using the momentum method, have been made for the experimentally determined suction distributions shown in fig. 11.41. Results of the calculations have been plotted in the M-Λ_1 diagram (fig. 11.42) where also the measured transition position is indicated. It follows that in all cases transition near the end of the porous surface is caused by laminar separation. It is interesting to note that for $R_c = 3.37 \times 10^6$ the boundary layer nearly separates at $\bar{s} = 0.68$ but downstream of this point the suction intensity is increased which postpones separation to a position further downstream.
Measurements at other values of c_{q_u} have been made for all values of R_c by changing the setting of the central valve V_c (see fig. 11.7). At the lower values of c_{q_u} transition may be preceded by laminar separation. This is shown in figs 11.43 - 11.46 where results of transition measurements have been compared with calculated positions. It can be seen that transition is predicted within 5 or 10 °/o chord accurately except when transition is preceded by separation. Especially at $R_c = 3.37 \times 10^6$ large discrepancies between theory and experiment occur (fig. 11.43). However, fig. 11.42 shows that in this case for the suction distribution obtained by trial and error the boundary layer is on the verge of separation over a long distance and hence an inaccurate result may be expected.

A similar remark applies for other values of c_{q_u} at $R_c = 3.37 \times 10^6$. Finally figures 11.47 - 11.50 show the drag coefficients and transition positions as function of c_{q_u} for series 4 to 7. There is a good correlation between drag and transition position. This is shown more clearly in fig. 11.51 where the total drag coefficient for the upper surface is plotted as a function of the position where transition starts. It is noticed that the minimum value of the total drag coefficient is obtained when transition occurs near the end of the porous region.

..7.6. Summary of the comparisons between the measured and calculated transition positions.

Fig. 11.52 has been prepared to summarize all results obtained in the preceding comparisons of the measured and predicted transition positions. The figure shows the position where $(\sigma_a)_{max}$ reaches the critical value 9.2 as function of the beginning of the experimentally determined transition region. Where transition is preceded by laminar separation a full symbol has been used. Data are shown for all values of c_q for which in the preceding figures a measured transition region has been indicated by the symbol $\vdash\!\!\!\longrightarrow\!\!\!\dashv$. Experiments in which transition occurred downstream of the porous region have been omitted.
It may be concluded from the figure that the beginning of transition is predicted within $\pm$ 10°/o of the chord length when transition is not preceded by laminar separation. Where separation is the cause of transition the distance between the predicted and actual beginning of transition may become larger.
It should be remembered that in most of the experiments with suction transition moves downstream very rapidly with increasing c_q. For these cases a satisfactory agreement between theory and experiment may have been obtained although fig. 11.52 shows a large distance between the measured and predicted transition positions. Of course a better correlation will be shown for these cases if a comparison is made between the theoretically and the experimentally determined value of c_q which is required to bring transition back to a certain position.

11.8. Summary of the drag coefficients obtained with and without suction.

In the preceding section some results of drag measurements at $\alpha = 0^o$ with suction have been presented. It was found that the minimum total drag is obtained when transition occurs near the end of the porous surface. In the present section results will be presented for an extended series of measurements including values of $\alpha \neq 0$. The presentation will be confined to those values of c_q for which transition occurred at the end of the porous surface. It may be assumed that these situations correspond to the condition with minimum total drag at the given value of α and R_c.
Fig. 11.53a and b show the results for the upper surface covered with nylon (series 4-7) both in the familiar logarithmic presentation and to a linear scale. A comparison is made with the drag of a flat plate with constant suction velocity $\frac{-v_o}{U} = 1.18 \times 10^{-4}$ discussed in section 9.8.1. It may be seen that the drag of the airfoil decreases with increasing R_c in the same way as for the flat plate. An appreciable drag reduction due to suction is obtained; the amount of the reduction is plotted vs R_c in fig. 11.54. At the highest value of R_c for which measurements have been made (6.16×10^6) the reduction in total drag is 63^o/o.
Although a comparison with the flat plate results is not entirely justified due to the difference in pressure distribution, it may be seen that the drag reduction with increasing R_c shows the same trend for the airfoil as for the flat plate. Extrapolating the results of the experiments to full scale values of R_c ($\approx 25 \times 10^6$) shows that the drag reduction obtained may be of the order of 75^o/o. This agrees with results obtained in different experiments mentioned in chapter 1.
Results for the upper and lower surface combined, for the experiments without the nylon covering, are shown in fig. 11.55 for different values of $R_c \leqslant 3.37 \times 10^6$. Included in the figure is the drag of the model with the sealed porous surface. It may be seen that drag reductions of the order of 50^o/o are obtained at these low values of R_c.

11.9. Concluding remarks on the experiments with suction.

From the results discussed in the present chapter it follows that both the momentum method and the multimoment method provide a good agreement with the experiments. The multimoment method is slightly superior to the momentum method. It is remarkable that separation is predicted rather accurately but - strange enough - this may be due to inaccuracies in the determination of the pressure distribution.

The proposed method for the prediction of transition is reasonably accurate also in cases with suction.

The drag reduction due to suction obtained in the experiments is of the order expected from calculations for the flat plate with constant suction velocity or from earlier investigations by different authors. At full scale values of the Reynoldsnumber based on chord ($R_c \approx 25 \times 10^6$) reductions in total drag of about 75°/o may be expected.

12. Conclusions

From the investigations described in this thesis the following general conclusions may be drawn. For more detailed concluding remarks the final sections of different chapters may be consulted.

Two methods for the calculation of laminar boundary layers with and without suction have been presented in chapters 5 and 7 respectively. It is shown in chapters 10 and 11 by comparison with experiments that both methods provide a good prediction of the actual boundary layer characteristics. Near separation difficulties may arise however, since in this region the boundary layer calculation is very sensitive to changes in the pressure gradient which is difficult to determine with sufficient precision. The results of the experiments discussed in chapter 11 suggest that no difficulties may arise when the pressure distribution is measured with less accuracy. It is likely that in this case a mean value for the adverse pressure gradient is assumed, which is on the high side upstream of separation so that separation is found earlier than for the accurate pressure distribution.
A remaining problem is to answer the question whether the boundary layer equations will predict separation at the right position if the pressure gradient is determined with the utmost precision. This problem has arisen already in connection with Schubauer's experiments on the boundary layer flow around an elliptic cylinder. Also the present experiments do not provide an answer to this question. It appears that the measurements have to be performed with still more accuracy than has been achieved in the present work.

A method has been designed which enables the calculation of the transition position for two dimensional laminar boundary layers with and without suction. In typical cases the beginning of transition is predicted within $\pm$ 10°/o of the chord length if transition is not preceded by laminar separation. Some improvement of the method will be welcome however. To achieve this it will be necessary to calculate more accurate stability diagrams for an extended range of velocity profiles.

Using the proposed method it becomes possible to design economic suction distributions for arbitrary airfoil sections. Also the design of suitable airfoils with and without suction may be improved by using this method.

13. References.

1. Smith, A.M.O., Gamberoni, N.: Transition, pressure gradient, and stability theory. Report ES 26388, Douglas Aircraft Co, 1956.
2. Smith, A.M.O.: Transition, pressure gradient and stability theory. Proc. 9th Int. Congr. Appl. Mech, Brussels, 4, p 234-244, 1956.
3. Ingen, J.L. van: Een semi-empirische methode voor de bepaling van de ligging van het omslaggebied van de grenslaag bij onsamendrukbare tweedimensionale stromingen (in Dutch). Rept VTH-71. Dept. Aeron. Eng. Delft, 1956.
4. Ingen, J.L. van: A suggested semi-empirical method for the calculation of the boundary layer transition region. Rept VTH-74, Dept. Aeron. Eng., Delft, 1956.
5. Ingen, J.L. van: (same title as [4]); Proc. Second. European Aeron. Congr., Scheveningen, Netherlands, 1956.
6. Melvill Jones, B.: The streamline aeroplane. Journal Royal Aeron. Soc. 33, p 357, 1929.
7. Schlichting, H.: Grenzschichttheorie. G.Braun, Karlsruhe, third edition, 1958. (see also Boundary layer theory, English edition, Pergamon Press, London, 1955).
8. Griffith, A.A., Meredith, F.W.: The possible improvement in aircraft performance due to the use of boundary layer suction. ARC Rept 2315, 1936.
9. Lachmann, G.V.: Boundary layer and flow control; its principles and applications. 2 vols, Pergamon Press, 1961.
10. Lachmann, G.V.: Aspects of design, engineering and operational economy of low drag aircraft. pp 1123-1165 of [9].
11. Holstein, H.: Versuche zur Grenzschichtbeeinflussung. Göttinger Monograph, part B4, 1945.
12. Pfenniger, W.: Untersuchungen über Reibungsverminderungen an Tragflügeln insbesondere mit Hilfe von Grenzschichtabsaugung. Mitt. Inst. Aerodyn., E.T.H. Zürich, no 13, 1946 (see also N A.C.A.TM 1181, 1947).
13. Kay, J.M.: Boundary-layer flow along a flat plate with uniform suction. A.R.C. R and M 2628, 1948.
14. Head, M.R.: The boundary layer with distributed suction. A.R.C., R and M 2783, 1951.

15. Head, M.R., Johnson, D. and Coxon, M.: Flight experiments on boundary layer control for low drag. A.R.C. R and M 3025, 1955.

16. Pfenniger, W. and Groth, E.: Low drag boundary layer suction experiments in flight on a wing glove of an F-94A airplane with suction through a large number of fine slots. p 981-999 in [9].

17. Pfenniger, W. and Bacon, J.W.: About the development of swept laminar suction wings with full chord laminar flow. p 1007-1032 in [9].

18. Gregory, N.: Research on suction surfaces for laminar flow. pp 924-960 of [9].

19. - : Recent developments in boundary layer research. Proceedings of Agard Specialist Meeting, Naples, may 1965, Agardograph 97.

20. Pfenniger, W.: Some results of the X-21 program, Part 1: Flow phenomena at the leading edge of swept wings. In [19].

21. Fowell, L.R. and Antonatos, P.P.: Some results of the X-21 A program, Part 2: Laminar flow flight test results on the X-21A. In [19].

22. Pohlhausen, K.: Zur näherungsweisen Integration der Differentialgleichung der laminaren Grenzschicht. Z.A.M.M. 1, p 252-268, 1921

23. Jeffery, G.B.: The two-dimensional steady motion of a viscous fluid. Phil. Mag. 6, 29, p 455-465, 1915.

24. Hamel, G.: Spiralförmige Bewegungen zäher Flüssigkeiten. Jahrbuch deutsch. Math. Ver. 25, 1916, p 34-60.

25. Schubauer, G.B.: Air flow in a separating laminar boundary layer. N.A.C.A. Rept 527, 1935.

26. Hartree, D.R.: The solution of the equations of the laminar boundary layer for Schubauer's observed pressure distribution for an elliptic cylinder. A.R.C., R and M 2427, 1939.

27. Prandtl, L.: Über Flüssigkeitsbewegung bei sehr kleiner Reibung. Verh. III int. Math. Kongr., Heidelberg, p 484-491, 1904.

28. Curle, N.: The laminar boundary layer equations. Clarendon Press, Oxford 1962.

29. Rosenhead, L.: Laminar boundary layer theory. Clarendon Press, Oxford 1963.

30. Kármán, Th. von: Über laminare und turbulente Reibung. Z.A.M.M. 1, p 233-252, 1921.

31. Leibenson, L.S.: The energy form of the integral condition in the theory of the boundary layer. Dokl. Ak. Nauk. S.S.S.R. 2, p 22-24, 1935.

32. Wieghardt, K.: Über einen Energiesatz zur Berechnung laminarer Grenzschichten. Ingen.-arch. 16, p 231-242, 1948.

33. Blasius, H.: Grenzschichten in Flüssigkeiten mit kleiner Reibung. Z. Math. Phys. 56, p 1-37, 1908. (see also NACA TM 1256).

34. Hiemenz, K.: Die Grenzschicht an einem in den gleichförmigen Flüssigkeitsstrom eingetauchten geraden Kreiszylinder. Diss. Göttingen 1911, Dingl. Polytechn. J.326, 32, 1911.

35. Goldstein, S.: A note on the boundary layer equations. Proc. Cambr. Phil. Soc. 35, 338, 1939.

36. Mangler, W.: Die ähnlichen Lösungen der Prandtlschen Grenzschicht-gleichungen. Z.A.M.M. 23, p 241-251, 1943.

37. Mangler, W. Special exact solutions, section 1.2 of Boundary Layers, Göttinger Monograph, 1948.

38. Falkner, V.M., Skan, S.W.: Some approximate solutions of the boundary-layer equations. A.R.C., R and M 1314, 1930. (see also Solutions of the boundary-layer equations. Phil. Mag. 7, 12, p 865-896, 1931).

39. Hartree, D.R.: On an equation occurring in Falkner and Skan's approximate treatment of the equations of the boundary layer. Proc. Camb. Phil. Soc. 33, p 223-239, 1937.

40. Goldstein, S.: On backward boundary layers and flow in converging passages. J. Fluid Mech. Vol. 21, part 1, pp 33-45, 1965.

41a Hegge Zijnen, B.G. van der: Measurements of the velocity distribution in the boundary layer along a plane surface. Thesis, Delft, 1924.

41b Burgers, J.M.: Proc. First. Int. Congr. Appl. Mech., Delft 1924.

42. Hansen, M.: Die Geschwindigkeitsverteilung in der Grenzschicht an einer eingetauchten Platte. ZAMM, 8, 185, 1928. (see also NACA TM 585, 1930).

43. Howarth, L.: On calculation of the steady flow in the boundary layer near the surface of a cylinder in a stream. A.R.C. R and M 1632, 1934.

44. Howarth, L.: On the solution of the laminar boundary layer equations. Proc. Roy. Soc. A. 164, 547-579, 1938.

45. Tani, I.: On the solution of the laminar boundary layer equations. Journ. Phys. Soc. Japan, 4, 149-154, 1949.

46. Görtler, H.: A new series for the calculation of steady laminar boundary layer flows. J. Math. Mech. 6, p 1-66, 1957.

47. Görtler, H. and Witting, H.: Zu den Tanischen Grenzschichten, Österr. Ing. Arch. 11, 111-122, 1957.

48. Görtler, H.: Zahlentafeln universeller Funktionen zur neuen Reihe für die Berechnung laminarer Grenzschichten. D.V.L.-Bericht 34, 1957.

49. Görtler, H.: On the calculation of steady laminar boundary layer flows with continuous suction. J. Math. Mech. 6, p 323-340, 1957.

50. Holstein, H., Bohlen, T.: Ein einfaches Verfahren zur Berechnung laminarer Reibungsschichten, die dem Näherungsansatz von K.Pohlhausen genügen. Bericht Lilienthal Ges. Luftfahrtf. S10, p 5-16.

51. Walz, A.: Ein neuer Ansatz für das Geschwindigkeitsprofil der laminaren Reibungsschicht. Lilienthal-Bericht 141, 8, 1941.

52. Timman, R.: A one-parameter method for the calculation of laminar boundary layers. N.L.L. Rept F-35, 1949.

53. Zaat, J.A.: A one parameter method for the calculation of the temperature profile of laminar incompressible boundary layer flow with a pressure gradient. Rept F-127, Nat. Aeron. Res. Inst. (N.L.L.), Amsterdam, 1953.

54. Nunnink, H.J.C.A.: One parameter methods for the calculation of laminar boundary layers of two-dimensional incompressible flows. Rept 18, Institute for Applied Math, Delft, 1957.

55. Schlichting, H.: Ein Näherungsverfahren zur Berechnung der laminaren Reibungsschicht mit Absaugung. Ing. Arch. 16, p 201, 1948.

56. Truckenbrodt, E. Ein einfaches Näherungsverfahren zum Berechnen der laminaren Reibungsschicht mit Absaugung. Forsch. Ing. Wes. 22, p 147, 1956.

57. Thwaites, B.: Approximate calculation of the laminar boundary layer. Aeron. Quart. 1, p 245-280, 1949.

58. Curle, N. and Skan, S.W.: Approximate methods for predicting separation properties of laminar boundary layers. Aeron. Quart. 8, 257-268, 1957.

59. Walz, A.: Anwendung des Energiesatzes von Wieghardt auf einparametrige Geschwindigkeitsprofile in laminaren Grenzschichten. Ing. Arch. 16, 243-248, 1948.

60. Tani, I.: On the approximate solution of the laminar boundary layer equations. J. Aero. Sci. 21, 487-495, 504, 1954.

61. Truckenbrodt, E.: Ein Quadraturverfahren zur Berechnung der laminaren und turbulenten Reibungsschichten bei ebener und rotations-symmetrischer Strömung. Ingen.-Arch. 20, 211-228, 1952.

62. Head, M.R.: An approximate method of calculating the laminar boundary layer in two-dimensional incompressible flow. A.R.C., R and M 3123, 1957.

63. Head, M.R.: Approximate calculations of the laminar boundary layer with suction, with particular reference to the suction requirements for boundary layer stability on aerofoils of different thickness-chord ratio. A.R.C., R and M 3124, 1957.

64. Head, M.R.: Approximate methods of calculating the two-dimensional laminar boundary layer with suction. pp 801-841 of [9].

65. Ingen, J.L. van: Een tweeparametermethode voor de berekening van de laminaire grenslaag met afzuiging. (in Dutch). Memorandum M1, Dept. Aeron. Eng., Delft, 1958.

66. Thwaites, B.: An exact solution of the boundary layer equations under particular conditions of porous surface suction. A.R.C. R and M 2241, 1946.

67. Iglisch, R.: Exakte Berechnung der laminaren Grenzschicht an der längsangeströmten ebenen Platte mit homogener Absaugung. Schr. dtsch. Akad. Luftfahrtf. 8B,p1-51. (see also N.A.C.A. T.M. 1205).

68. Poincaré, H.: Sur les courbes définies par une equation differentielle. Oeuvre, Gauthier-Villars, Paris Vol 1, 1892.

69. Minorsky, N.: Nonlinear oscillations. Van Nostrand Co. Princeton,1962.

70. Stoker, J.J.: Nonlinear vibrations in mechanical and electrical systems. Intersc. Publ. 1950.

71. Ingen, J.L. van: Phaseplane representation of the incompressible viscous flow between non-parallel plane walls. Rept VTH-118, Dept. Aeron. Eng. Delft, 1964.

72. Ku, Y.K.: Boundary layer problems solved by the method of non-linear mechanics. Proc. 9th Intern. Congr. Appl. Mech., Brussels, 1956, p 132-144.

73. Holstein, H. Ähnliche laminare Reibungsschichten an durchlässigen Wänden. UM 3050, 1943.

74. Pretsch, J.: Die laminare Grenzschicht bei starkem Absaugen und Ausblasen. UM 3091, 1944.

75. Crocco, L.: A characteristic transformation of the equations of the boundary layer in gases. A.R.C., London, Rept 4582 (translated from Atti di Guidonia 17, no 7, p 118, 1939).

76. Schönauer, W.: Ein Differenzenverfahren zur Lösung der Croccoschen Grenzschichtgleichung für laminare inkompressible Strömung. Diss. Karlsruhe, 1960.

77. Schönauer, W.: Ein Differenzenverfahren zur Lösung der Croccoschen Grenzschichtgleichung für laminare inkompressible Strömung, ZAMM, Band 42, Sonderheft p 162-164, 1962.

78. Zonneveld, J.A.: Automatic numerical integration. Mathematical Centre Tracts, 8, Amsterdam 1964.

79. Trilling, L.: The incompressible boundary layer with pressure gradient and suction. J.Aeron. Sci, 17, p 335-342, 1950.

80. Dorodnitsyn, A.A.: General method of integral relations and its application to boundary layer theory. Proc. Sec. Int. Congress Aeron. Sciences, Zürich, sept 1960,vol.3, p 207-219.

81. Hartree, D.R.: A solution of the laminar boundary-layer equation for retarded flow. A.R.C., R and M 2426, 1939.

82. Leigh, D.C. The laminar boundary-layer equation: A method of solution by means of an automatic computer. Proc. Camb. Phil. Soc. 51, p 320-332, 1955.

83. Terrill, R.M.: Laminar boundary-layer flow near separation with and without suction. Phil. Trans. A 253, p55-100, 1960.

84. Goldstein, S.: On laminar boundary-layer flow near a position of separation. Quart. J.Mech. 1, p 43-69, 1948.

85. Curle, N.: Accurate solutions of the laminar-boundary-layer equations, for flows having a stagnation point and separation. ARC, R and M 3164.

86. Rheinboldt, W.: Zur Berechnung stationärer Grenzschichten bei kontinuierlicher Absaugung mit unstetig veränderlicher Absaugegeschwindigkeit. J. Rat. Mech. Anal. 5, p 539-604, 1956.

87. Schubauer, G.B., Skramstad, H.K. Laminar boundary layer oscillations and transition on a flat plate. N.A.C.A. Rept 909, 1947.

88. Reynolds, O.: An experimental investigation of the circumstances which determine whether the motion of water shall be direct or sinuous, and of the law of resistance in parallel channels. Phil. Trans. 174, p 935-982, 1883.

89. Taylor, G.I.: Statistical theory of turbulence. V. Effect of turbulence on boundary layer. Proc. Roy. Soc. London, Ser. A, vol. 156, no 888, 1936, p 307-317.

90. Lin, C.C.: The theory of hydrodynamic stability. Cambridge University Press, 1955.

91. Malotaux, P.C.A. et. al.: A method for qualitative boundary layer investigations by means of hot-wires without disturbing the flow. Rept. VTH-45, Dept. Aeron. Eng., Delft, 1951 (in Dutch with English summary).

92. Hinze, J.O. et.al. Contribution a la transition dans la couche limite. Compt. Rend. 8èmes Journées de l'Hydraulique. Société Hydrotechnique de France, Lille, 1964.

93a Schubauer, G.B., Klebanoff, P.S.: Contributions on the mechanics of boundary layer transition. Proc. Symp. boundary layer effects in Aerodyn. N.P.L. 1955.

93b Schubauer, G.B.: Mechanism of transition at subsonic speeds. Proc. Symp. Boundary Layer Research, Int. Union theoret. appl. Mech. Freiburg p 85-109, 1957.

94. Klebanoff, P.S., Tidstrom, K.D.: The evolution of amplified waves leading to transition in a boundary layer with zero pressure gradient. N.A.C.A. T.N. D-195, 1959.

95. Squire, H.B. On the stability for three-dimensional disturbances of viscous fluid flow between parallel walls. Proc. Roy. Soc. A 142, p 621-628, 1933.

96. Pretsch, J.: Die Stabilität einer ebenen Laminarströmung bei Druckgefälle und Druckanstieg. Jb. dtsch. Luftfahrtforsch. 1, p 158-75, 1941.

97. Pretsch, J.: Die Anfachung instabiler Störungen in einer laminaren Reibungsschicht. Jb. dtsch. Luftfahrtf. p 154-171, 1942.

98. Pretsch, J.: Berechnung der Stabilitätsgrenze von Grenzschichtprofilen und der Anfachung von Störungen. Göttinger Monograph. Part B.3.2. 1945.

99. Ulrich, A.: Theoretische Untersuchungen über die Widerstandsersparnis durch Laminarhaltung mit Absaugung. Schr. dtsch. Akad. Luftfahrtf. 83, p 53 (see also N.A.C.A. TM 1121).

100. Freeman, J.C. and Chiarulli, P.: Stability of the boundary layer. Tech. Rep. H.Q. Air Material Command. F-T/R-1197-1A, 1948.

101. Wieghardt, K.: Zur Berechnung ebener und drehsymmetrischer Grenzschichten mit kontinuierlicher Absaugung. Ing. Arch. 22, 368, 1954.

102. Lin, C.C.: On the stability of two-dimensional parallel flows. Quarterly Appl. Math. Vol 3, july 1945, p 117-142; vol 3, oct. 1945, p 218-234; Vol 3, jan. 1946, p 277-301.

103. Shen, S.F. Calculated amplified oscillations in plane Poiseuille and Blasius flows. J. Aero. Sci. 21, p 62-64, 1954.

104. Timman, R., Zaat, J.A., Burgerhout, Th. J.: Stability diagrams for laminar boundary layer flow. N.L.L. Rept F 193, 1956.

105. Tollmien, W.: Über die Entstehung der Turbulenz. 1. Mitteilung, Nachr. Ges. Wiss. Göttingen, Math. Phys. Klasse. 21-44, 1929 (also NACA TM 609, 1931).

106. Michel, R.: Détermination du point de transition et calcul de la trainée des profils d'ailes en incompressible. O.N.E.R.A. Rept no 58, 1952.

107. Granville, P.S. The calculation of viscous drag of bodies of revolution. David Taylor Model Basin, Rept 849, 1953.

108. Dobbinga, E. and Ghesel Grothe, J.A. van: De lage snelheidswindtunnel van de subafdeling Vliegtuigbouwkunde der Technische Hogeschool (in Dutch), De Ingenieur, 23 sept 1955, p A461.

109. Maas, H.J. van der: Aeronautical research in the Netherlands. J.Roy. Aeron. Soc. Vol 61, 1957, p 295-334.

110. Tennekes, H.: Beknopte handleiding voor het meten van de snelheid en de turbulentiegraad van luchtstromingen met de constante temperatuurapparatuur van de onderafdeling Vliegtuigbouwkunde. VTH-handleiding 56, 1961.

111. Pankhurst, R.C. and Holder, D.W.: Wind tunnel technique. Pitman, London, 1952.

112. Pfenniger, W.: Vergleich der Impulsmethode mit der Wägung bei Profilwiderstandsmessungen. Mitt. Inst. Aerodyn. ETH, Zürich no 8, 1943.

113. Squire, H.B., Young, A.D.: The calculation of the profile drag of aerofoils. A.R.C., R and M 1838, 1937.

114. Smith, A.M.O.: Improved solutions of the Falkner and Skan boundary-layer equation. Sherman M.Fairchild Fund Paper FF-10, Inst. Aero. Sci, 1954.

115. Schlichting, H. and Ulrich, A.: Zur Berechnung des Umschlages laminar-turbulent. Jahrbuch d. dt. Luftfahrtforschung I, 8, 1942.

4. Overzicht (summary in Dutch): Theoretische en experimentele onderzoekingen van onsamendrukbare laminaire grenslagen met en zonder afzuiging.

In dit proefschrift worden de resultaten beschreven van enige theoretische en experimentele onderzoekingen van tweedimensionale laminaire grenslagen met en zonder afzuiging. Het onderzoek werd beperkt tot onsamendrukbare stromingen en was opgezet met het doel meer inzicht te verkrijgen in de problemen welke verband houden met het laminair houden van de grenslaag door middel van afzuiging. Verschillende van de verkregen resultaten hebben echter evenzeer betrekking op grenslagen zonder afzuiging.

In een algemene inleiding (hoofdstuk 1) wordt gewezen op de mogelijke verbetering van de vliegtuigprestaties door het toepassen van afzuiging voor het laminair houden van de grenslaag.

In de hoofdstukken 2 tot en met 4 worden bekende resultaten uit de grenslaagtheorie samengevat welke hebben gediend als uitgangspunt voor het werk beschreven in latere hoofdstukken.

Een eerste theoretisch onderzoek (hoofdstuk 5) heeft betrekking op de berekening van laminaire grenslagen door middel van benaderingsmethoden zoals die door Pohlhausen werden geintroduceerd. Een nieuwe methode werd ontwikkeld welke nauwkeurige resultaten levert in gevallen waarin de afzuigintensiteit niet al te groot is.

Het tweede theoretische onderzoek is beschreven in hoofdstuk 6 en handelt over een "fasevlak beschrijving" van de laminaire grenslaagstroming tussen niet-evenwijdige vlakke wanden. In dit geval wordt het stromingsprobleem beschouwd in een vlak waarin de schuifspanning τ wordt uitgezet tegen de snelheidscomponent u evenwijdig aan de wand. Deze procedure is bekend uit de theorie der niet-lineaire trillingen van autonome systemen met één graad van vrijheid. Voor deze systemen wordt in het "fasevlak" de snelheid uitgezet tegen de verplaatsing waardoor een duidelijk beeld van het gedrag van het systeem wordt verkregen. Singuliere punten in het fasevlak corresponderen met evenwichtstoestanden van het systeem. In dit proefschrift wordt aangetoond dat voor de stroming tussen niet-evenwijdige vlakke wanden de singuliere punten in het fasevlak (τ-u vlak) corresponderen met de buitenkant van een grenslaag. Oplossingen van de bewegingsvergelijkingen kunnen slechts een grenslaagkarakter vertonen indien de corresponderende singulariteit in het fasevlak van een bepaald type is.

Het type van de singulariteit - en daarmee de mogelijkheid tot het optreden van grenslaagoplossingen - is afhankelijk van eventuele afzuiging of aanblazing aan de wanden.
Het blijkt dat voor de stroming tussen niet-evenwijdige vlakke wanden zonder afzuiging τ^2 wordt voorgesteld door een derdegraadspolynoom in u. Dit resultaat leidde tot de ontwikkeling van een tweede benaderingsmethode voor de berekening van laminaire grenslagen (hoofdstuk 7). In deze methode wordt τ^2 benaderd door een polynoom in u van de graad N. De coëfficiënten van dit polynoom zijn functies van de coördinaat x in stromingsrichting en worden bepaald door de benaderingswijze van Pohlhausen toe te passen op een enigszins gewijzigde vorm van Crocco's grenslaagvergelijking. De methode is zodanig opgezet dat de graad N van het polynoom eenvoudig kan worden verhoogd zonder dat toepassing van de methode daardoor in principe moeilijker wordt. Een aantal voorbeelden, gegeven in hoofdstuk 8, toont aan dat met toenemende N de resultaten van de benaderingsmethode convergeren naar de exacte oplossing van de grenslaagvergelijkingen.

Het experimentele gedeelte van het onderzoek omvat metingen aan twee vleugelmodellen in de lage snelheidswindtunnel van de onderafdeling Vliegtuigbouwkunde van de Technische Hogeschool te Delft.
Het eerste model heeft een 28^o/o dik "laminair" profiel met een nietporeus oppervlak; de koordelengte bedraagt 1 meter. Voor dit model werden drukverdelingen gemeten en snelheidsprofielen in de grenslaag bepaald met behulp van een gloeidraadanemometer. Speciale aandacht werd gegeven aan de bepaling van de ligging van het loslatingspunt van de laminaire grenslaag. In hoofdstuk 10 worden de resultaten van deze metingen beschreven en vergeleken met theoretische resultaten volgens beide nieuwe methoden. Bij deze berekeningen werd uitgegaan van de experimenteel bepaalde drukverdeling om het profiel.
Als belangrijk resultaat kan worden vermeld dat de theorie geen loslating van de grenslaag voorspelt terwijl bij de metingen duidelijk loslating werd geconstateerd. Dit verschijnsel is reeds eerder in de literatuur onderzocht in verband met het bekende onderzoek van Schubauer aan een elliptische cylinder. Zowel bij Schubauer's metingen als in het huidige

onderzoek is een kleine wijziging van de experimenteel bepaalde drukverdeling voldoende om de theorie loslating te doen aangeven op de juiste plaats. Het is nog niet geheel duidelijk of deze wijziging toelaatbaar is op grond van mogelijke meetfouten.
Blijkbaar moet de drukverdeling extreem nauwkeurig worden gemeten voordat de vraag kan worden beantwoord of de grenslaagvergelijkingen in staat zijn om uitgaande van een experimenteel bepaalde drukverdeling loslating van de laminaire grenslaag te voorspellen.

Het tweede vleugelmodel dat werd onderzocht, heeft een laminair profiel van 15°/o dikte bij een koordelengte van 1.35 m. Het oppervlak van dit profiel is aan beide zijden poreus van 30°/o tot 90°/o van de koorde.
Het inwendige van het model is verdeeld in 40 verschillende compartimenten, elk voorzien van een eigen afzuigleiding en apparatuur voor de regeling en meting van de hoeveelheid afgezogen lucht. Door middel van de regelkranen kan de verdeling van de afzuigintensiteit over de vleugelkoorde binnen wijde grenzen worden veranderd. De onderzoekingen aan dit poreuze model worden beschreven in hoofdstuk 11 van het proefschrift.
De metingen omvatten o.m. de bepaling van de weerstand en de ligging van het omslagpunt van de grenslaag voor verschillende afzuigsnelheidsverdelingen. Tevens werden gedetailleerde snelheidsverdelingen in de grenslaag bepaald met behulp van een gloeidraadanemometer. De resultaten van de grenslaagmetingen werden vergeleken met de theorie; de overeenkomst is in het algemeen goed.
Door afzuiging werden weerstandsbesparingen tot 60°/o bereikt. Uit een extrapolatie van de meetresultaten naar de hoge getallen van Reynolds welke optreden in de kruisvlucht van moderne verkeersvliegtuigen blijkt dat in deze gevallen een weerstandsbesparing tot 75°/o kan worden verwacht.

Voor de berekening van de eigenschappen van vleugelprofielen met en zonder afzuiging is het noodzakelijk te kunnen voorspellen waar omslag van de grenslaag zal optreden. Voor gevallen zonder afzuiging werd reeds eerder een dergelijke methode aangegeven door Smith en Gamberoni [1,2] en de schrijver van dit proefschrift [3,4,5]. Deze methode wordt beschreven in hoofdstuk 9 van het proefschrift. Uit een analyse van de metingen aan het poreuze vleugelmodel blijkt dat de methode ook met redelijke benadering geldt voor het geval van afzuiging door een poreus oppervlak. Gebruik makend van de gegeven methoden kan, nauwkeuriger dan voorheen, voor een gegeven vleugelprofiel de meest economische verdeling van de afzuigintensiteit over de koorde worden aangegeven. Evenzo kan de berekening van profielvormen met voorgeschreven aerodynamische eigenschappen nauwkeuriger worden uitgevoerd.

15. Appendix 1: The drag of a flat plate with suction.

The drag of the flat plate with suction can easily be found from the momentum equation in the form (2.16)

$$\frac{U\Theta}{\nu}\frac{d\Theta}{dx} + (2+H)\frac{\Theta^2}{\nu}\frac{dU}{dx} - \frac{v_o\Theta}{\nu} = \frac{\tau_o\Theta}{\mu U} \qquad (A.1)$$

For a flat plate U is constant and equal to the reference speed U_∞ so that (A.1) may be simplified to

$$2\frac{d\Theta}{dx} - 2\frac{v_o}{U_\infty} = \frac{\tau_o}{\frac{1}{2}\rho U_\infty^2} \qquad (A.2)$$

In what follows a flat plate with unit span will be considered. Then defining the drag coefficient c_d and the suction flow coefficient c_q by

$$c_d = \frac{\int_o^c \tau_o \, dx}{\frac{1}{2}\rho U_\infty^2 c} \qquad (A.3)$$

and

$$c_q = \int_o^c \frac{-v_o}{U_\infty} \, d\frac{x}{c} \qquad (A.4)$$

equation (A.2) may be integrated to give:

$$c_d = 2\frac{\Theta}{c} + 2c_q \qquad (A.5)$$

In (A.5) c is the length of the plate, c_d is the total drag coefficient experienced by the plate; $2\frac{\Theta}{c}$ is the "wake drag" coefficient c_{d_w} which would be found from a wake survey method as described in section 11.3.4. The term $2c_q$ represents the so-called "sink drag" coefficient and expresses the fact that an amount of air of $c_q U_\infty c$ m^3/sec is brought to rest in the boundary layer causing a momentum loss which is experienced as drag. The sink drag can be disregarded if the air is expelled in downstream direction with the free stream speed, since in this case a thrust will be obtained which balances the sink drag. However, to overcome the pressure drops through the porous surface, suction ducts etc. a suction pump is required which consumes some power. If an amount of air of Q m^3/sec is sucked, which has to be given a pressure rise Δ p, then assuming incompressible flow this requires a pumping power of

$$P_p = \frac{Q \Delta p}{\eta_p} \tag{A.6}$$

where η_p is the efficiency of the pump.

If the suction power would have been used for propulsion of the plate a drag component ΔD could have been overcome which is given by

$$P_p = \frac{U_\infty \Delta D}{\eta_T} \tag{A.7}$$

In (A.7) η_T is the efficiency of the propulsion system; ΔD is called the "equivalent suction drag".

Usually a pressure loss coefficient c_p and a suction drag coefficient c_{d_s} are defined by

$$c_p = \frac{\Delta p}{\frac{1}{2}\rho U_\infty^2} \tag{A.8}$$

and

$$c_{d_s} = \frac{\Delta D}{\frac{1}{2}\rho U_\infty^2 c} \tag{A.9}$$

Equating the right hand sides of (A.6) and (A.7) and using (A.8) and (A.9) leads to the following expression for the suction drag coefficient

$$c_{d_s} = c_p c_q \frac{\eta_T}{\eta_p} \tag{A.10}$$

Assuming for convenience equal efficiencies η_T and η_p gives

$$c_{d_s} = c_p c_q \tag{A.11}$$

The total drag coefficient for the flat plate is now given by

$$c_{d_t} = c_{d_w} + c_p c_q \tag{A.12}$$

where $c_{d_w} = 2 \frac{\Theta}{c}$.

Equation (A.12) may also be used to describe the total drag for an airfoil with suction if c_{d_w} represents the drag coefficient found from the wake traverse method.

Table 4.1: Characteristic features of some approximate methods.

Author and ref.	Expression for the velocity profile	Definition of η	Compatibility conditions used
Timman, [52]	$\frac{u}{U} = 1-e^{-\eta^2}(b + d\eta^2 + \ldots.) - \int_{\eta}^{\infty} e^{-\eta^2}(a+c\eta^2+\ldots)d\eta$	$\eta = \alpha y$; α^{-1} is related to the boundary layer thickness	first (eq. 2.10), second (eq. 2.11), and to some extent the third (eq. 2.12)
Schlichting, [55]	$\frac{u}{U} = F_1(\eta) + K\,F_2(\eta)$; $F_1(\eta) = 1-e^{-\eta}$ $F_2(\eta) = F_1(\eta) - \sin(\frac{\pi}{6}\eta)$ for $0 \leqslant \eta \leqslant 3$ $F_2(\eta) = F_1(\eta) - 1$ for $\eta \geqslant 3$	$\eta = \frac{y}{\delta_1(x)}$; $\delta_1(x)$ is related to the boundary layer thickness	first (eq. 2.10)

Table 5.1: Some characteristic parameters for the flat plate (β=0) and the plane stagnation point (β=1).

Method	$\frac{\delta^*}{x}\sqrt{\frac{Ux}{\nu}}$		$\frac{\Theta}{x}\sqrt{\frac{Ux}{\nu}}$		$H = \frac{\delta^*}{\Theta}$		$\frac{\tau_o \Theta}{\mu U}$	
	β=0	β=1	β=0	β=1	β=0	β=1	β=0	β=1
Pohlhausen	1.750	0.641	0.686	0.278	2.55	2.31	0.235	0.331
Schlichting	1.742	0.630	0.655	0.266	2.66	2.37	0.215	0.310
Timman	1.715	0.636	0.660	0.267	2.60	2.38	0.218	0.312
present	1.728	0.659	0.661	0.293	2.61	2.25	0.219	0.364
exact	1.721	0.648	0.664	0.292	2.59	2.21	0.221	0.360

Table 5.2: Results of the momentum method for the plane stagnation point with constant suction.

ℓ_2	ℓ_1	K	L	δ^*/σ	Θ/σ	H	ℓ	Λ_1	Λ_2	λ_2
0	0.5835	-1.5835	0.5835	0.8617	0.3833	2.248	0.3642	0.08572	0.0000	0
0.1	0.5359	-1.5555	0.5843	0.8563	0.3842	2.229	0.3729	0.07910	0.03842	0.1366
0.2	0.4893	-1.5195	0.5821	0.8505	0.3851	2.209	0.3824	0.07256	0.07702	0.2859
0.3	0.4437	-1.4738	0.5761	0.8441	0.3862	2.186	0.3928	0.06620	0.1159	0.4504
0.4	0.3991	-1.4165	0.5652	0.8373	0.3872	2.162	0.4039	0.05983	0.1549	0.6333
0.5	0.3554	-1.3455	0.5482	0.8301	0.3881	2.139	0.4156	0.05352	0.1941	0.8392
0.6	0.3127	-1.2582	0.5239	0.8223	0.3889	2.114	0.4279	0.04728	0.2333	1.0731
0.7	0.2707	-1.1519	0.4904	0.8142	0.3896	2.090	0.4407	0.04109	0.2727	1.3453
0.8	0.2290	-1.0238	0.4460	0.8058	0.3900	2.066	0.4536	0.03483	0.3120	1.6711
0.9	0.1873	-0.8712	0.3887	0.7972	0.3900	2.044	0.4662	0.02849	0.3510	2.0794
1.0	0.1448	-0.6922	0.3166	0.7888	0.3896	2.025	0.4780	0.02198	0.3896	2.6271
1.1	0.1004	-0.4858	0.2281	0.7810	0.3886	2.010	0.4882	0.01516	0.4275	3.4728
1.2	0.0527	-0.2536	0.1224	0.7743	0.3870	2.001	0.4959	0.00789	0.4644	5.2297
1.3	0.0000	-0.0000	0.0000	0.7692	0.3846	2.000	0.5000	0.00000	0.5000	∞

Table 5.3: Some characteristic parameters of the momentum method for the no-suction case ($\Lambda_2 = 0$).

ℓ_1	Θ/σ	δ^*/σ	H	$\ell = \frac{\tau_o \Theta}{\mu U}$	Λ_1	$M(\Lambda_1)$
-1.3	0.26510	1.1544	4.3546	-0.047718	-0.091361	1.0657
-1.2	0.27556	1.1389	4.1330	-0.033067	-0.091120	1.0515
-1.1	0.28556	1.1233	3.9337	-0.017134	-0.089699	1.0302
-1.0	0.29508	1.1078	3.7542	0	-0.087072	1.0021
-0.9	0.30413	1.0922	3.5912	+0.018248	-0.083246	0.96738
-0.8	0.31272	1.0767	3.4430	0.037526	-0.078235	0.92672
-0.7	0.32083	1.0612	3.3077	0.057749	-0.072052	0.88036
-0.6	0.32848	1.0456	3.1831	0.078835	-0.064739	0.82876
-0.5	0.33566	1.0301	3.0689	0.10070	-0.056334	0.77250
-0.4	0.34236	1.0145	2.9633	0.12325	-0.046883	0.71188
-0.3	0.34860	0.99900	2.8657	0.14641	-0.036457	0.64760
-0.2	0.35436	0.98346	2.7753	0.17009	-0.025114	0.58004
-0.1	0.35966	0.96792	2.6912	0.19422	-0.012936	0.50982
0	0.36449	0.95238	2.6129	0.21869	0	0.43738 = a_1 5.39
+0.1	0.36885	0.93684	2.5399	0.24344	+0.013605	0.36334
+0.2	0.37274	0.92130	2.4717	0.26837	+0.027787	0.28822
+0.3	0.37616	0.90576	2.4079	0.29340	+0.042449	0.21258
0.4	0.37911	0.89022	2.3482	0.31845	0.057490	0.13694
0.5	0.38159	0.87468	2.2922	0.34343	0.072805	0.061872
0.6	0.38360	0.85914	2.2397	0.36826	0.088289	-0.012118
0.7	0.38514	0.84360	2.1904	0.39284	0.10383	-0.084493
0.8	0.38621	0.82806	2.1441	0.41711	0.11933	-0.15481

Table 6.1: Type of the singularity for equation (6.25) at (+1,0)

λ	type of singularity
$\leq -2\sqrt{2}$	stable node
$-2\sqrt{2} < \lambda < 0$	stable spiral
0	center
$0 < \lambda < 2\sqrt{2}$	unstable spiral
$\geq 2\sqrt{2}$	unstable node

Table 7.1: $A_{i,j}$ for different values of N.

$$N = N_1 \quad \begin{bmatrix} A_{11} & A_{12} & \cdots\cdots & A_{1,N_1-2} \\ A_{21} & & & \\ \vdots & & & \\ A_{N_1-2,1} & & & A_{N_1-2,N_1-2} \end{bmatrix}$$

$$N = 5 \quad \begin{bmatrix} +2.5 & -27.5 & +105 \\ -6 & +60 & -210 \\ +3.5 & -31.5 & +105 \end{bmatrix}$$

$$N = 6 \quad \begin{bmatrix} -5 & +100 & +1680 & -2520 \\ +21 & -399 & -5880 & +9072 \\ -28 & +504 & +6720 & -10584 \\ +12 & -204 & -2520 & +4032 \end{bmatrix}$$

$$N = 7 \quad \begin{bmatrix} +8.75 & -271.25 & +13230 & -44100 & +34650 \\ -56 & +1680 & -70560 & +241920 & -194040 \\ +126 & -3654 & +136080 & -476280 & +388080 \\ -120 & +3360 & -113400 & +403200 & -332640 \\ +41.25 & -1113.75 & +34650 & -124740 & +103950 \end{bmatrix}$$

$$N = 8 \quad \begin{bmatrix} -14 & +616 & +70560 & -388080 & +665280 & -360360 \\ +126 & -5418 & -529200 & +2993760 & -5239080 & +2882880 \\ -420 & +17640 & +1512000 & -8731800 & +15523200 & -8648640 \\ +660 & -27060 & -2079000 & +12196800 & -21954240 & +12355200 \\ -495 & +19800 & +1386000 & -8232840 & +14968800 & -8494200 \\ +143 & -5577 & -360360 & +2162160 & -3963960 & +2265120 \end{bmatrix}$$

$$N = 9 \quad \begin{bmatrix} +21 & -1239 & +291060 & -2328480 & +6486480 & -7567560 & +3153150 \\ -252 & +14616 & -2910600 & +23950080 & -68108040 & +80720640 & -34054020 \\ +1155 & -65835 & +11434500 & -96049800 & +277477200 & -332972640 & +141891750 \\ -2640 & +147840 & -22869000 & +195148800 & -570810240 & +691891200 & -297297000 \\ +3217.5 & -176962.5 & +24774750 & -214053840 & +632431800 & -772972200 & +334459125 \\ -2002 & +108108 & -13873860 & +121080960 & -360720360 & +443963520 & -193243050 \\ +500.5 & -26526.5 & +3153150 & -27747720 & +83243160 & -103062960 & +45090045 \end{bmatrix}$$

Table 8.1: The coefficients a_n for the flat plate without suction; $a_1 = a_2 = 0$, $a_3 = -{}^1/6$

N	a_o	a_4	a_5	a_6	a_7	a_8	a_9
4	0.041666	+0.125000	-	-	-	-	-
5	0.100602	-0.169677	+0.235742	-	-	-	-
6	0.102937	+0.193777	-0.505175	+0.375128	-	-	-
7	0.106509	-0.227102	+0.995693	-1.388978	+0.680544	-	-
8	0.107822	+0.250871	-1.637534	+3.871663	-3.863447	+1.437293	-
9	0.108526	-0.263250	+2.395702	-8.149445	+13.338101	-10.471178	+3.208202

Table 8.2: Some characteristic parameters for the boundary layer on a flat plate without suction according to the multimoment method.

N	a_o	$^o/o$	$\frac{\delta^*}{x}\sqrt{\frac{Ux}{\nu}}$	$^o/o$	$\frac{\Theta}{x}\sqrt{\frac{Ux}{\nu}}$	$^o/o$	$H = \frac{\delta^*}{\Theta}$	$^o/o$	$\ell = \frac{\tau_o \Theta}{\mu U}$	($^o/o$)
4	0.041666	37.8	3.123	181.5	1.3260	199.7	2.356	90.9	0.2707	122.7
5	0.100602	91.2	1.918	111.5	0.7882	118.7	2.433	93.9	0.2500	113.4
6	0.102937	93.4	1.822	105.9	0.7248	109.1	2.514	97.0	0.2325	105.4
7	0.106509	96.6	1.779	103.4	0.7001	105.4	2.541	98.1	0.2285	103.6
8	0.107822	97.8	1.758	102.2	0.6879	103.6	2.556	98.7	0.2259	102.4
9	0.108526	98.4	1.748	101.6	0.6817	102.6	2.565	99.0	0.2246	101.8
7*	0.110081	99.8	1.741	101.1	0.6791	102.3	2.563	98.9	0.2253	102.2
exact, Smith [114]	0.110262	100.0	1.721	100.0	0.6641	100.0	2.591	100.0	0.2205	100.0

Table 8.3: The coefficients a_n for the plane stagnation point without suction; $a_1 = -2$, $a_2 = 0$, $a_3 = +{}^1/3$.

N	a_o	a_4	a_5	a_6	a_7	a_8	a_9
4	1.416667	+0.250000	-	-	-	-	-
5	1.498997	-0.161653	0.329322	-	-	-	-
6	1.510251	+0.296525	-0.654560	+0.514450	-	-	-
7	1.514489	-0.204411	+1.274888	-1.871296	+0.952997	-	-
8	1.516397	+0.328998	-1.904711	+4.852614	-5.104930	+1.978298	-
9	1.517393	-0.230753	+2.833957	-10.120913	+17.328192	-14.132244	+4.471035

Table 8.4: Some characteristic parameters for the plane stagnation point without suction according to the multimoment method.

N	a_o	$^o/_o$	$\frac{\delta^*}{x}\sqrt{\frac{Ux}{\nu}}$	$^o/_o$	$\frac{\theta}{x}\sqrt{\frac{Ux}{\nu}}$	$^o/_o$	$H = \frac{\delta^*}{\theta}$	$^o/_o$	$\ell = \frac{\tau_o \theta}{\mu U}$	$^o/_o$
4	1.416667	93.3	0.7296	112.6	0.3475	118.9	2.099	94.7	0.4136	114.8
5	1.498997	98.7	0.6808	105.1	0.3179	108.7	2.142	96.6	0.3892	108.0
6	1.510251	99.4	0.6652	102.7	0.3066	104.9	2.169	97.9	0.3768	104.6
7	1.514489	99.7	0.6586	101.6	0.3014	103.1	2.185	98.6	0.3709	102.9
8	1.516397	99.8	0.6551	101.1	0.2986	102.1	2.194	99.0	0.3677	102.0
9	1.517393	99.9	0.6531	100.8	0.2969	101.6	2.200	99.3	0.3657	101.5
7^*	1.518725	100.0	0.6525	100.7	0.2967	101.5	2.199	99.2	0.3656	101.5
exact, Smith [114]	1.519278	100.0	0.6479	100.0	0.2923	100.0	2.216	100.0	0.3603	100.0

Table 8.5: Some characteristic parameters for the Hartree boundary layer with $\beta = -0.16$.

N	a_o	$^o/_o$	$\frac{\delta^*}{x}\sqrt{\frac{Ux}{\nu}}$	$^o/_o$	$\frac{\theta}{x}\sqrt{\frac{Ux}{\nu}}$	$^o/_o$	$H = \frac{\delta^*}{\theta}$	$^o/_o$	$\ell = \frac{\tau_o \theta}{\mu U}$	$^o/_o$
5	0.012325	73.2	2.795	111.4	0.9452	116.5	2.957	95.7	0.1049	99.6
6	0.007625	45.3	2.905	115.8	0.9103	112.2	3.191	103.2	0.0795	75.5
7	0.014790	87.8	2.613	104.2	0.8553	105.4	3.055	98.8	0.1040	98.8
exact, Smith [114]	0.016850	100.0	2.508	100.0	0.8116	100.0	3.091	100.0	0.1053	100.0

Table 8.6: Separation positions for Tani's boundary layers $\overline{U} = 1 - \overline{x}^j$

method	$\overline{x}$ at separation for j =			
	1	2	4	8
exact	0.120	0.271	0.462	0.640
momentum method	0.123	0.264	0.446	0.621
multimoment method, N=7	0.121	0.268	0.465	0.648

Table 8.7: The pressure distribution used in the boundary layer calculations for Schubauer's elliptic cylinder.

$\bar{x}$	$\bar{U}$	$\frac{d\bar{U}}{d\bar{x}}$	λ_1
0.16	—	—	+0.5220
0.18	—	—	+0.4835
0.20	+0.966	+1.925	+0.4090
0.22	+1.002	+1.626	+0.3565
0.24	+1.031	+1.392	+0.3241
0.26	+1.057	+1.210	+0.2977
0.28	+1.080	+1.050	+0.2723
0.30	+1.100	+0.925	+0.2522
0.32	+1.118	+0.821	+0.2350
0.34	+1.133	+0.729	+0.2188
0.36	+1.147	+0.654	+0.2053
0.38	+1.160	+0.588	+0.1926
0.40	+1.171	+0.534	+0.1824
0.42	+1.180	+0.486	+0.1730
0.44	+1.190	+0.444	+0.1641
0.46	+1.198	+0.406	+0.1559
0.48	+1.206	+0.372	+0.1481
0.50	+1.213	+0.344	+0.1418
0.52	+1.220	+0.318	+0.1355
0.54	+1.226	+0.295	+0.1299
0.56	+1.232	+0.275	+0.1250
0.58	+1.237	+0.256	+0.1200
0.60	+1.242	+0.240	+0.1159
0.62	+1.247	+0.223	+0.1109
0.64	+1.251	+0.207	+0.1059
0.66	+1.255	+0.192	+0.1010
0.68	+1.258	+0.178	+0.0962
0.70	+1.262	+0.165	+0.0915
0.72	+1.265	+0.152	+0.0865
0.74	+ 1.268	+0.141	+0.0823
0.76	+1.270	+0.130	+0.0778
0.78	+1.273	+0.119	+0.0729
0.80	+1.275	+0.110	+0.0690
0.82	+1.278	+0.100	+0.0642
0.84	+1.280	+0.092	+0.0604
0.86	+1.281	+0.084	+0.0564
0.88	+1.283	+0.077	+0.0528
0.90	+1.285	+0.070	+0.0490
0.92	+1.286	+0.064	+0.0458
0.94	+1.287	+0.057	+0.0416
0.96	+1.288	+0.051	+0.0380
0.98	+1.289	+0.046	+0.0350
1.00	+1.290	+0.040	+0.0310
1.02	+1.291	+0.036	+0.0284
1.04	+1.292	+0.032	+0.0258
1.06	+1.293	+0.029	+0.0238
1.08	+1.294	+0.026	+0.0217
1.10	+1.294	+0.023	+0.0196
1.12	+1.294	+0.020	+0.0173
1.14	+1.295	+0.018	+0.0158
1.16	+1.295	+0.016	+0.0143
1.18	+1.295	+0.014	+0.0128
1.20	+1.295	+0.012	+0.0111
1.22	+1.295	+0.009	+0.0085
1.24	+1.295	+0.006	+0.0057
1.26	+1.295	+0.003	+0.0029
1.28	+1.295	+0.000	+0.0000
1.30	+1.295	-0.003	-0.0030
1.32	+1.295	-0.006	-0.0061
1.34	+1.295	-0.009	-0.0093
1.36	+1.295	-0.013	-0.0136
1.38	+1.295	-0.017	-0.0181
1.40	+1.295	-0.021	-0.0227
1.42	+1.295	-0.026	-0.0285
1.44	+1.294	-0.031	-0.0345
1.46	+1.293	-0.036	-0.0407
1.48	+1.292	-0.042	-0.0481
1.50	+1.291	-0.047	-0.0546
1.52	+1.290	-0.053	-0.0624
1.54	+1.289	-0.058	-0.0693
1.56	+1.288	-0.064	-0.0775
1.58	+1.287	-0.070	-0.0859
1.60	+1.285	-0.076	-0.0946
1.62	+1.283	-0.082	-0.1035
1.64	+1.282	-0.087	-0.1113
1.66	+1.280	-0.093	-0.1206
1.68	+1.278	-0.098	-0.1288
1.70	+1.276	-0.102	-0.1359
1.72	+1.274	-0.106	-0.1431
1.74	+1.272	-0.110	-0.1505
1.76	+1.270	-0.113	-0.1566
1.78	+1.268	-0.115	-0.1614
1.80	+1.265	-0.117	-0.1665
1.82	+1.262	-0.118	-0.1702
1.84	+1.260	-0.119	-0.1738
1.86	+1.258	-0.119	-0.1759
1.88	+1.254	-0.118	-0.1769
1.90	+1.253	-0.118	-0.1789
1.92	+1.251	-0.117	-0.1796
1.94	+1.249	-0.115	-0.1786
1.96	+1.246	-0.113	-0.1777
1.98	+1.244	-0.110	-0.1750
2.00	+1.242	-0.107	-0.1723
2.02	+1.240	-0.104	-0.1694
2.04	+1.238	-0.100	-0.1648
2.06	+1.236	-0.095	-0.1583
2.08	+1.234	-0.090	-0.1517

Table 8.7: Continued; Modified pressure distribution.

$\bar{x}$	$\bar{U}$	$\frac{d\bar{U}}{d\bar{x}}$	λ_1
1.80	+1.265	-0.117	-0.1665
1.82	+1.262	-0.119	-0.1716
1.84	+1.260	-0.122	-0.1782
1.86	+1.258	-0.126	-0.1863
1.88	+1.254	-0.130	-0.1949
1.90	+1.2525	-0.133	-0.2018
1.92	+1.250	-0.136	-0.2089
1.94	+1.248	-0.138	-0.2145
1.96	+1.245	-0.140	-0.2204
1.98	+1.242	-0.142	-0.2264
2.00	+1.239	-0.143	-0.2308
2.02	+1.237	-0.145	-0.2368
2.04	+1.235	-0.146	-0.2412

Table 8.8: Coefficients e_n in equation (8,49) for Schubauer's ellips.

(0.35 + 2 denotes $0.35 \times 10^{+2}$).

n	$0.10 \leq \bar{x} < 0.50$	$0.50 \leq \bar{x} < 0.90$	$0.90 \leq \bar{x} < 1.30$	$1.30 \leq \bar{x} < 1.70$	$1.70 \leq \bar{x} < 2.10$	modified $1.80 \leq \bar{x} < 2.10$
0	+0.2229526 + 0	+0.878004 + 0	-0.344650 + 0	+0.118466 + 1	-0.272018 + 0	+0.482076 + 1
1	+0.1779934 + 2	-0.399223 + 1	+0.543894 + 0	-0.237210 + 1	+0.131212 + 1	-0.344721 + 1
2	-0.2101468 + 3	+0.891446 + 1	+0.370504 + 1	+0.714958 + 0	-0.565421 + 0	-0.273478 + 1
3	+0.1020643 + 4	-0.103245 + 2	-0.102364 + 2	+0.106592 + 1	-0.513816 + 0	+0.197142 + 1
4	-0.2526967 + 4	+0.583033 + 1	+0.970133 + 1	-0.335165 + 0	+0.246656 + 0	+0.997831 + 0
5	+0.3152842 + 4	-0.137626 + 1	-0.382806 + 1	-0.385864 + 0	+0.191498 - 1	-0.962272 + 0
6	-0.1575414 + 4	+0.107946 + 0	+0.490446 + 0	+0.152730 + 0	-0.111240 - 1	+0.184954 + 0

Table 9.1: Critical Reynoldsnumber for the flat plate boundary layer.

$(\frac{U\delta^*}{\nu})_{crit}$	$(\frac{U\theta}{\nu})_{crit}$	$^{10}\log(\frac{U\theta}{\nu})_{crit}$	references
321	124	2.093	Timman et al [104]
420	162	2.210	Tollmien [105]
420	162	2.210	Lin [102]
480	185	2.268	Lin, equations 9.19 - 9.20
575	222	2.346	Ulrich [99]
645	249	2.396	Schlichting-Ulrich [115]
680	260	2.416	Pretsch, β=0 [96]

Table 9.2: Results of Lin's formulae for different approximation to the velocity profile on a flat plate.

$(\frac{U\delta^*}{\nu})_{crit}$	$(\frac{U\theta}{\nu})_{crit}$	$^{10}\log(\frac{U\theta}{\nu})_{crit}$	Velocity profile
480	185	2.268	exact
577	221	2.345	momentum method
754	310	2.492	multimoment method N = 5
493	196	2.292	" " N = 6
508	200	2.301	" " N = 7
519	203	2.307	" " N = 8
498	194	2.288	" " N = 9

Table 9.3: Characteristic parameters of the Hartree velocity profiles including the critical Reynoldsnumber according to Pretsch.

β	H	$(\frac{U\delta^*}{\nu})_{crit}$	$(\frac{U\theta}{\nu})_{crit}$	$^{10}\log(\frac{U\delta^*}{\nu})_{crit}$	$^{10}\log(\frac{U\theta}{\nu})_{crit}$
1	2.22	12400	5603	4.094	3.748
0.6	2.27	8640	3795	3.936	3.579
0.2	2.41	2955	1225	3.471	3.088
0.1	2.48	1658	669	3.219	2.825
0	2.59	680	260	2.832	2.416
-0.05	2.67	354	133	2.549	2.123
-0.10	2.80	126	45	2.100	1.654
-0.198	4.03	0	0	-	-

Table 9.4: Coefficients of equation (9.25) obtained from Pretsch' diagrams.

	f = 1, $\frac{\beta_r \nu}{U^2} = 10^{-6}$			f = 2, $\frac{\beta_r \nu}{U^2} = 2.5\ 10^{-6}$			f = 3, $\frac{\beta_r \nu}{U^2} = 5.10^{-6}$		
$^{10}\log(\frac{U\theta}{\nu})_{crit}$	T_o	K_1	K_2	T_o	K_1	K_2	T_o	K_1	K_2
1	.04	6.00	4.270	13.05	116.00	3.750	25.60	169	3.115
1.5	.75	0	4.200	8.00	87.00	3.670	15.10	136	3.250
2	1.20	10.50	3.988	2.95	58.00	3.590	4.60	105	3.385
2.5	.55	10.50	3.800	.81	21.50	3.578	1.10	35	3.390
3	.22	10.50	3.900	.40	21.50	3.640	.80	35	3.450
3.5	.22	10.50	4.000	.23	30.00	3.731	0	35	3.510
4	.22	16.00	4.100	-0.22	38.50	3.825	-0.80	35	3.570

	f = 4, $\frac{\beta_r \nu}{U^2} = 7.5\ 10^{-6}$			f = 5, $\frac{\beta_r \nu}{U^2} = 10^{-5}$			f = 6, $\frac{\beta_r \nu}{U^2} = 2.5\ 10^{-5}$		
$^{10}\log(\frac{U\theta}{\nu})_{crit}$	T_o	K_1	K_2	T_o	K_1	K_2	T_o	K_1	K_2
1	33.80	212	3.020	39.90	245	2.966	62.70	401	2.790
1.5	19.70	180	3.140	23.10	213	3.068	36.60	365.5	2.845
2	5.60	148.5	3.260	6.30	181	3.170	10.50	331	2.900
2.5	1.55	54	3.270	2.15	76	3.200	3.90	196	2.945
3	1.10	44	3.338	1.10	54	3.260	-0.10	51.5	3.030
3.5	-0.275	44	3.402	-0.735	33	3.315	-4.10	0	3.113
4	-1.10	44	3.466	-2.40	11	3.370	-8.10	0	3.196

	f = 7, $\frac{\beta_r \nu}{U^2} = 5.10^{-5}$			f = 8, $\frac{\beta_r \nu}{U^2} = 7.5\ 10^{-5}$			f = 9, $\frac{\beta_r \nu}{U^2} = 10^{-4}$		
$^{10}\log(\frac{U\theta}{\nu})_{crit}$	T_o	K_1	K_2	T_o	K_1	K_2	T_o	K_1	K_2
1	83.40	890	2.660	104.00	1224	2.560	125.80	1720	2.480
1.5	50.50	685	2.660	63.10	921	2.560	74.00	1234	2.480
2	17.60	480	2.700	21.20	620	2.570	22.20	760	2.490
2.5	3.30	345	2.750	1.40	511	2.640	0	705	2.555
3	- 1.60	200	2.850	- 1.10	400	2.710	- 1.10	650	2.625
3.5	- 6.50	60	2.950	- 3.60	300	2.780	- 2.20	600	2.695
4	-11.40	0	3.050	- 6.10	200	2.850	- 3.30	550	2.765

Table 9.4: (continued)

$^{10}\log(\frac{U\Theta}{\nu})_{crit}$	f = 10, $\frac{\beta_r \nu}{U^2} = 2.5\ 10^{-4}$			f = 11, $\frac{\beta_r \nu}{U^2} = 5.10^{-4}$			f = 12, $\frac{\beta_r \nu}{U^2} = 7.5\ 10^{-4}$		
	T_o	K_1	K_2	T_o	K_1	K_2	T_o	K_1	K_2
1	182.00	3025	2.240	218.80	4215	2.040	213	4930	1.945
1.5	100.50	1965	2.240	111.40	2670	2.040	104.5	3120	1.945
2	19.00	880	2.240	4.00	1800	2.040	- 4	1330	1.945
2.5	- 7.70	845	2.400	-103.40	1045	2.040	- 4	0	1.945
3	- 7.70	810	2.560	-103.40	200	2.040	- 4	0	1.945
3.5	- 7.70	770	2.720	-103.40	0	2.040	- 4	0	1.945
4	- 7.70	730	2.880	-103.40	0	2.040	- 4	0	1.945

$^{10}\log(\frac{U\Theta}{\nu})_{crit}$	f = 13, $\frac{\beta_r \nu}{U^2} = 10^{-3}$		
	T_o	K_1	K_2
1	202.80	5350	1.865
1.5	95.40	3475	1.865
2	- 12	1560	1.865
2.5	- 12	0	1.865
3	- 12	0	1.865
3.5	- 12	0	1.865
4	- 12	0	1.865

Table 9.5: Amplification factors at transition for the flat plate without suction.

Value assumed for		$(\sigma_a)_{max}$ at the experimentally determined transition region	
$^{10}\log(\frac{U\Theta}{\nu})_{crit}$	$(\frac{U\Theta}{\nu})_{crit}$	beginning	end
2.416	260	7.6	9.7
2.345	222	9.2	11.2
2.268	185	11.0	12.8
2.093	124	15.0	16.8

Table 10.1: Coordinates of impervious airfoil section.

$x_{p/c}$ %	$y_{p/c}$ %	$x_{p/c}$ %	$y_{p/c}$ %	$x_{p/c}$ %	$y_{p/c}$ %
0	0	20	12.25	70	10.32
0.5	2.58	25	12.98	75	9.10
1	3.69	30	13.48	80	7.70
2	5.03	35	13.82	85	6.09
3	6.07	40	13.92	90	4.32
4	6.89	45	13.80	95	2.41
5	7.55	50	13.50	100	0.26
7.5	8.90	55	13.00		
10	9.83	60	12.30		
15	11.21	65	11.41		

Table 10.2: Position of pressure orifices in the impervious model.

	Chord I			Chord II
no	$x_{p/c}$ %	$y_{p/c}$ %	s/c %	s/c %
1	1.84	-4.92	-5.42	-5.41
2	0.46	-2.53	-2.68	-2.70
3	0.25	-2.00	-2.20	--
4	0.16	-1.50	-1.58	--
5	0.09	-1.03	-1.09	-1.08
6	0.03	-0.50	-0.48	-0.49
7	0	0	0	0
8	0.03	+0.50	+0.53	+0.49
9	0.10	1.10	1.11	--
10	0.26	1.68	1.61	--
11	0.40	2.18	2.21	--
12	0.53	2.59	2.72	2.72
13	0.74	3.08	3.24	--
14	1.31	4.03	4.32	--
15	2.75	5.78	6.52	6.49
16	4.75	7.44	9.19	--
17	6.20	8.29	10.88	10.83
18	10.67	10.06	15.64	--
19	16.35	11.55	21.67	21.63
20	21.18	12.45	26.52	--
21	26.95	13.20	32.41	32.44

	Chord I			Chord II
no	$x_{p/c}$ %	$y_{p/c}$ %	s/c %	s/c %
22	32.30	13.65	37.85	37.87
23	35.55	13.82	40.97	--
24	43.18	13.90	48.61	--
25	48.58	13.63	54.04	54.02
26	53.91	13.18	59.42	--
27	59.25	12.44	64.82	64.81
28	65.13	11.43	70.83	--
29	69.85	10.37	75.62	75.62
30	75.10	9.11	81.04	--
31	80.25	7.63	86.44	86.41
32	85.42	5.98	91.79	--
33	90.35	4.23	97.20	97.22
34	95.41	2.25	102.63	--
35	--	--	49.51	--
36	--	--	53.47	--
37	--	--	54.97	--
38	--	--	58.77	--
39	--	--	61.27	--
40	--	--	65.36	--
41	--	--	67.35	--
tr.edge	100	0.26	107.90	107.75

Table 10.3. Results of pressure distribution measurements on the impervious model

$\bar{U}$ from orifices			$\bar{U}$ from surface tubes in chord I (in the same order as measured)			
no	chord I	chord II	$\bar{x}$	$\bar{U}$	$\bar{x}$	$\bar{U}$
1	-0.9713	-0.9665	0.780	1.2101	0.449	1.3628
2	-0.5670	-0.5659	0.757	1.2222	427	1.3607
3	-0.4718	-	0.734	1.2367	408	1.3576
4	-0.3454	-	0.729	1.2407	387	1.3543
5	-0.2411	-0.2416	725	1.2456	368	1.3524
6	-0.1110	-0.1196	718	1.2534	328	1.3490
7	+0.0575	+0.0648	709	1.2806	288	1.3447
8	+0.1196	+0.1273	699	1.2963	266	1.3417
9	+0.2416	-	690	1.2979	248	1.3405
10	+0.3415	-	679	1.3001	328	1.3487
11	0.4631	-	669	1.3027	229	1.3379
12	0.5513	+0.5582	659	1.3063	209	1.3311
13	0.6424	-	649	1.3091	189	1.3258
14	0.8078	-	644	1.3118	189	1.3232
15	1.0693	+1.0742	6395	1.3135	168	1.3170
16	1.2340	-	6335	1.3162	149	1.3146
17	1.2866	1.2803	609	1.3233	149	1.3154
18	1.3224	-	618	1.3204	139	1.3163
19	1.3432	-	578	1.3324	128	1.3154
20	1.3467	-	538	1.3464	128	1.3102
21	1.3576	1.3585	519	1.3540	118	1.3039
22	1.3631	1.3678	4985	1.3629	107	1.2778
23	1.3649	-	487	1.3649	097	1.2504
24	1.3735	-	479	1.3656	063	1.0490
25	1.3553	1.3602	468	1.3658	199	1.3276
26	1.3350	-	449	1.3635	178	1.3197
27	1.3187	1.3167			158	1.3158
28	1.2881	-				
29	1.2221	1.2276				
30	1.1855	-				
31	1.1371	1.1413				
32	1.0751	-				
33	0.9950	0.9970				
34	0.8983	-				
35	1.3722	-				
36	1.3579	-				
37	1.3512	-				
38	1.3392	-				
39	1.3318	-				
40	1.3156	-				
41	1.3085	-				

Table 10.4: Pressure distribution used in the boundary layer calculations for the impervious model.

$\bar{x}$	$\bar{U}$	$\frac{d\bar{U}}{d\bar{x}}$	$\lambda_1 = \frac{\bar{x}}{\bar{U}}\frac{d\bar{U}}{d\bar{x}}$	$\bar{x}$	$\bar{U}$	$\frac{d\bar{U}}{d\bar{x}}$	$\lambda_1 = \frac{\bar{x}}{\bar{U}}\frac{d\bar{U}}{d\bar{x}}$
0.04	0.7610	14.180	0.7453	0.35	1.35825	0,0995	0.0256
0.05	0.9070	11.770	0.6488	0.36	1.35925	0.1015	0.0269
0.06	1.0194	9.565	0.5630	0.37	1.36025	0.1055	0.0287
0.07	1.1046	7.541	0.4779	0.38	1.36135	0.1115	0.0311
0.08	1.1720	5.988	0.4087	0.39	1.36255	0.1200	0.0343
0.09	1.2251	4.643	0.3411	0.40	1.36375	0.1305	0.0383
0.10	1.2653	3.4224	0.2705	0.41	1.36510	0.1430	0.0429
0.11	1.2939	2.3027	0.1958	0.42	1.36655	0.1540	0.0473
0.12	1.3120	1.4777	0.1356	0.43	1.36815	0.1610	0.0506
0.13	1.32235	0.6082	0.0598	0.44	1.36975	0.1640	0.0527
0.14	1.32465	-0.1057	-0.0112	0.45	1.37135	0.1630	0.0535
0.15	1.32270	-0.1421	-0.0161	0.46	1.37285	0.1500	0.0503
0.16	1.32235	+0.0623	+0.0075	0.47	1.37395	0.0700	0.0239
0.17	1.3239	0.2394	0.0308	0.48	1.37425	-0.0192	-0.0067
0.18	1.3269	0.3565	0.0484	0.49	1.37325	-0.1806	-0.0644
0.19	1.3308	0.4133	0.0590	0.50	1.37075	-0.3152	-0.1150
0.20	1.33495	0.4089	0.0613	0.51	1.36730	-0.3709	-0.1383
0.21	1.3388	0.3476	0.0545	0.52	1.36340	-0.4050	-0.1556
0.22	1.3418	0.2587	0.0424	0.53	1.35930	-0.4111	-0.1603
0.23	1.3441	0.2030	0.0347	0.54	1.35520	-0.4059	-0.1617
0.24	1.3459	0.1630	0.0291	0.55	1.35125	-0.3799	-0.1546
0.25	1.3474	0.1405	0.0261	0.56	1.34765	-0.3452	-0.1434
0.26	1.34875	0.1275	0.0246	0.57	1.34430	-0.3240	-0.1374
0.27	1.34995	0.1170	0.0234	0.58	1.34115	-0.3048	-0.1318
0.28	1.35115	0.1090	0.0226	0.59	1.33819	-0.2900	-0.1279
0.29	1.35225	0.1041	0.0223	0.60	1.33534	-0.2793	-0.1254
0.30	1.35325	0.1005	0.0223	0.61	1.33260	-0.2709	-0.124
0.31	1.35425	0.0990	0.0227	0.62	1.32991	-0.2646	-0.1234
0.32	1.35525	0.0980	0.0231	0.63	1.32730	-0.2608	-0.1238
0.33	1.35625	0.0980	0.0238	0.635	1.32600	-0.2600	-0.1245
0.34	1.35725	0.0980	0.0245	0.635	1.32600	-0.7255	-0.34743

Table 10.5: Coefficients in equation (8.49): $\lambda_1 = \sum_{n=0}^{6} e_n \bar{x}^n$ for the impervious model (0.543 + 2 denotes $0.543 \times 10^{+2}$)

n	e_n for				
	$0.04 \leq \bar{x} < 0.14$	$0.14 \leq \bar{x} < 0.24$	$0.24 \leq \bar{x} < 0.456$	$0.456 \leq \bar{x} < 0.54$	$0.54 \leq \bar{x} < 0.635$
0	+0.4777781+0	+0.468318718+2	+0.283142524+2	-0.441984929+3	+0.62238306+2
1	+0.4725992+2	-0.108946502+4	-0.521724645+3	+0.275812516+4	-0.343194183+2
2	-0.1947334+4	+0.903993722+4	+0.396976398+4	-0.492329408+4	+0.62179067+3
3	+0.3319732+5	-0.267304210+5	-0.159384857+5	-0.458252779+3	-0.46537777+3
4	-0.2968925+6	-0.319871038+5	+0.355911081+5	+0.667306127+4	+0.60355487+3
5	+0.1349858+7	+0.332606988+6	-0.418994924+5	+0.604744491+3	-0.12214455+4
6	-0.2467063+7	-0.498304819+6	+0.203209638+5	-0.544276543+4	+0.79281632+3

Table 11.1: Coordinates of suction model (NACA 64_2-A-215)

x_p mm	y_p upper mm	y_p lower mm
0	0.13	0
10	23.91	16.80
20	29.57	23.42
50	45.62	36.06
75	55.50	43.32
100	63.63	49.28
150	77.01	58.81
200	87.94	66.16
250	96.65	71.97
300	103.59	76.48
350	109.13	79.91
400	113.40	82.38
450	116.40	83.84
500	118.06	84.28
550	118.24	83.59
600	116.77	81.44
650	113.97	78.21
700	110.03	74.12
750	105.13	69.30
800	99.27	63.928
850	92.68	straight between $x_p = 817.5$; $y_p = 61.93$ and $x_p = 1350$; $y_p = 0.43$
900	85.34	
950	77.36	
1000	68.89	
1050	60.02	
1100	50.68	
1150	40.80	
1200	30.82	
1250	20.75	
1300	10.56	
1350	0.43	0.43

Table 11.2: Position of pressure orifices in impervious model.

no	upper surface $\bar{x}$ %	upper surface $\bar{s}$ %	lower surface $\bar{x}$ %	lower surface $\bar{s}$ %
0	0	0	0	0
1	0.49	1.45	0.50	1.21
2	1.02	2.16	1.01	1.89
3	1.42	2.69	1.16	2.07
4	2.03	3.40	2.00	3.03
5	2.50	3.94	2.47	3.56
6	3.01	4.50	2.98	4.09
7	4.04	5.63	4.00	5.17
8	5.03	6.70	5.01	6.22
9	6.36	8.10	5.22	6.44
10	7.11	8.81	7.02	8.30
11	7.52	9.33	7.50	8.87
12	10.04	11.93	9.94	11.33
13	15.02	17.06	13.20	14.61
14	15.16	17.19	14.97	16.39
15	20.01	22.14	19.99	21.45
16	29.92	32.12	29.93	31.39
17	39.95	42.16	39.97	41.44
18	49.99	52.23	50.05	51.56
19	60.02	62.31	60.06	61.63
20	65.00	67.33	70.02	71.68
21	70.01	72.39	73.28	74.96
22	78.18	80.82	80.01	81.72
23	80.02	82.70	86.64	88.40
24	89.40	92.28	89.82	91.59
25	90.03	92.92	98.55	100.34
26	98.54	101.58	–	
tr.edge	100.00	103.07	100.00	101.81

Table 11.3: Dimensions of suction compartments

no	upper surface $\bar{s}$ beginning	upper surface $\bar{s}$ mean	upper surface $\bar{s}$ end	upper surface $\Delta\bar{s}$	lower surface $\bar{s}$ beginning	lower surface $\bar{s}$ mean	lower surface $\bar{s}$ end	lower surface $\Delta\bar{s}$
1	0.3210	0.3362	0.3513	0.0303	0.3151	0.3299	0.3446	0.0295
2	0.3513	0.3662	0.3811	0.0298	0.3446	0.3597	0.3748	0.0302
3	0.3811	0.3960	0.4109	0.0298	0.3748	0.3895	0.4041	0.0293
4	0.4109	0.4257	0.4405	0.0296	0.4041	0.4189	0.4336	0.0295
5	0.4405	0.4555	0.4705	0.0300	0.4336	0.4480	0.4624	0.0288
6	0.4705	0.4854	0.5003	0.0298	0.4624	0.4775	0.4925	0.0301
7	0.5003	0.5150	0.5297	0.0294	0.4925	0.5074	0.5222	0.0297
8	0.5297	0.5448	0.5598	0.0301	0.5222	0.5373	0.5523	0.0301
9	0.5598	0.5746	0.5893	0.0295	0.5523	0.5671	0.5818	0.0295
10	0.5893	0.6044	0.6195	0.0302	0.5818	0.5970	0.6122	0.0304
11	0.6195	0.6343	0.6490	0.0295	0.6122	0.6270	0.6417	0.0295
12	0.6490	0.6644	0.6798	0.0308	0.6417	0.6570	0.6723	0.0306
13	0.6798	0.6946	0.7094	0.0296	0.6723	0.6871	0.7018	0.0295
14	0.7094	0.7247	0.7399	0.0305	0.7018	0.7170	0.7321	0.0303
15	0.7399	0.7546	0.7692	0.0293	0.7321	0.7467	0.7613	0.0292
16	0.7692	0.7845	0.7998	0.0306	0.7613	0.7764	0.7915	0.0302
17	0.7998	0.8141	0.8283	0.0285	0.7915	0.8053	0.8190	0.0275
18	0.8283	0.8463	0.8643	0.0360	0.8190	0.8370	0.8550	0.0360
19	0.8643	0.8837	0.9030	0.0387	0.8550	0.8737	0.8924	0.0374
20	0.9030	0.9217	0.9404	0.0374	0.8924	0.9110	0.9295	0.0371

Table 11.4: Details of the pressure- and suction distributions used in the boundary layer calculations of section 11.5.

$\bar{s}$	$\bar{U}$	$\frac{d\bar{U}}{d\bar{x}}$	λ_1	λ_2	$\frac{-V_0}{U_\infty}\ 10^4$
0	0.110000	66.48276	0.95480		
0.01	0.61520	34.20576	0.62836		
0.02	0.82390	14.54562	0.37600		
0.03	0.93920	7.53191	0.25104		
0.04	0.99240	4.06891	0.16935		
0.05	1.02470	2.57748	0.12903		
0.06	1.04767	1.93405	0.11316		
0.07	1.06526	1.56981	0.10507		
0.08	1.07944	1.28452	0.09675		
0.09	1.09133	1.07352	0.08981		
0.10	1.10127	0.93110	0.08565		
0.11	1.11031	0.83970	0.08417		
0.12	1.11840	0.77081	0.08360		
0.13	1.12582	0.71542	0.08344		
0.14	1.13271	0.66286	0.08269		
0.15	1.13907	0.60924	0.08092		
0.16	1.14492	0.56052	0.07897		
0.17	1.15031	0.51390	0.07653		
0.18	1.15528	0.47010	0.07377		
0.19	1.15980	0.42976	0.07088		
0.20	1.16391	0.39348	0.06805		
0.21	1.16770	0.36357	0.06579		
0.22	1.17119	0.33529	0.06335		
0.23	1.17442	0.30938	0.06093		
0.24	1.17738	0.28395	0.05819		
0.25	1.18010	0.26091	0.05556		
0.26	1.18262	0.24333	0.05376		
0.27	1.18498	0.22948	0.05254		
0.28	1.18721	0.21576	0.05112		
0.29	1.18930	0.20472	0.05014		
0.30	1.19130	0.19514	0.04936		
0.31	1.19320	0.18500	0.04826		
0.32	1.19500	0.17500	0.04705	0.06405	0.745
0.33	1.19670	0.16500	0.04568	0.10513	1.205
0.34	1.19830	0.15500	0.04415	0.15061	1.702
0.35	1.19980	0.14600	0.04275	0.19567	2.181
0.36	1.20121	0.13514	0.04065	0.23643	2.600
0.37	1.20249	0.12000	0.03705	0.27409	2.975
0.38	1.20360	0.10129	0.03209	0.30983	3.320
0.39	1.20451	0.08124	0.02639	0.34398	3.640
0.40	1.20520	0.05581	0.01858	0.37838	3.955
0.41	1.20560	0.02195	0.00749	0.41275	4.262
0.42	1.20560	-0.02391	-0.00835	0.44713	4.562
0.43	1.20508	-0.07981	-0.02856	0.48157	4.855
0.44	1.20401	-0.13481	-0.04941	0.51554	5.135
0.45	1.20239	-0.18552	-0.06963	0.54914	5.406
0.46	1.20031	-0.23052	-0.08859	0.58259	5.668
0.47	1.19779	-0.27052	-0.10644	0.61466	5.910
0.48	1.19491	-0.30552	-0.12306	0.64820	6.160
0.49	1.19169	-0.33567	-0.13839	0.67978	6.202
0.50	1.18821	-0.36024	-0.15198	0.71509	6.640
0.51	1.18450	-0.38190	-0.16485	0.74619	6.850
0.52	1.18060	-0.40230	-0.17764	0.78444	7.120

Table 11.4: Continued; Details of the pressure- and suction distributions used in the boundary layer calculations of section 11.5.

$\bar{s}$	$\bar{U}$	$\frac{d\bar{U}}{d\bar{x}}$	λ_1	λ_2	$\frac{-V_o}{U_\infty} 10^4$
0.53	1.17650	-0.42114	-0.19018	0.81911	7.357
0.54	1.17219	-0.43986	-0.20312	0.85402	7.580
0.55	1.16772	-0.45576	-0.21517	0.88859	7.800
0.56	1.16308	-0.47076	-0.22719	0.92351	8.018
0.57	1.15831	-0.48486	-0.23914	0.95620	8.212
0.58	1.15340	-0.49614	-0.25005	0.98520	8.370
0.59	1.14840	-0.50620	-0.26064	1.00793	8.472
0.60	1.14330	-0.51529	-0.27100	1.02565	8.530
0.61	1.13809	-0.52120	-0.27995	1.03712	8.535
0.62	1.13281	-0.53010	-0.29074	1.04493	8.510
0.63	1.12751	-0.53460	-0.29932	1.05057	8.468
0.64	1.12191	-0.53930	-0.30827	1.05623	8.426
0.65	1.11679	-0.54310	-0.31673	1.06041	8.375
0.66	1.11131	-0.54640	-0.32514	1.06411	8.320
0.67	1.10580	-0.54980	-0.33377	1.06602	8.252
0.68	1.10030	-0.55330	-0.34260	1.06694	8.178
0.69	1.09481	-0.55670	-0.35152	1.06691	8.098
0.70	1.08929	-0.56050	-0.36086	1.06534	8.008
0.71	1.08369	-0.56520	-0.37098	1.06252	7.910
0.72	1.07802	-0.56990	-0.38132	1.05865	7.805
0.73	1.07228	-0.57452	-0.39183	1.05430	7.700
0.74	1.06652	-0.58010	-0.40321	1.05111	7.605
0.75	1.06069	-0.58614	-0.41517	1.04776	7.508
0.76	1.05479	-0.59080	-0.42641	1.04446	7.415
0.77	1.04881	-0.59580	-0.43816	1.04220	7.330
0.78	1.04281	-0.60030	-0.44976	1.03975	7.245
0.79	1.03678	-0.60238	-0.45975	1.03813	7.167
0.80	1.03072	-0.60924	-0.47363	1.03676	7.092
0.81	1.02459	-0.61414	-0.48630	1.03630	7.024
0.82	1.01841	-0.62371	-0.50299	1.03302	6.938
0.83	1.01209	-0.63886	-0.52474	1.03531	6.890
0.84	1.00561	-0.65886	-0.55121	1.03577	6.830
0.85	0.99889	-0.68371	-0.58270	1.03745	6.778
0.86	0.99191	-0.71414	-0.62011	1.03978	6.730
0.87	0.98458	-0.75024	-0.66395	1.04266	6.685
0.88	0.97691	-0.78438	-0.70761	1.04645	6.645
0.89	0.96890	-0.81529	-0.74999	1.05114	6.610
0.90	0.96060	-0.84486	-0.79270	1.05595	6.575
0.91	0.95200	-0.87600	-0.83855	1.06247	6.543
0.92	0.94309	-0.90514	-0.88423	1.06778	6.516
0.93	0.93391	-0.92910	-0.92651	1.07322	6.482
0.94	0.92450	-0.95100	-0.96828	1.07993	6.455
0.95	0.91490	-0.97260	-1.01130	1.08710	6.430
0.96	0.90510	-0.99230	-1.05391	1.09357	6.400
0.97	0.89510	-1.01100	-1.09707	1.10019	6.370
0.98	0.88490	-1.02750	-1.13945	1.10696	6.340
0.99	0.87451	-1.04120	-1.18025	1.11388	6.310
1.00	0.86400	-1.05600	-1.22381	1.12091	6.280
1.01	0.85340	-1.06500	-1.26205	1.12805	6.250
1.02	0.84270	-1.07500	-1.30284	1.13549	6.221
1.03	0.83190	-1.08500	-1.34506	1.14363	6.195
1.04	0.82100	-1.09500	-1.38882	1.15115	6.165

Table 11.5: Coefficients e_n in eq. (11.14) for the suction model (0.123 + 4 denotes 0.123 x 10^{+4})

$\bar{x} = \bar{s} + 0.0013$

	e_n for λ_1			
n	$0.0413 \leq \bar{x} < 0.3213$	$0.3213 \leq \bar{x} < 0.6013$	$0.6013 \leq \bar{x} < 0.8313$	$0.8313 \leq \bar{x} < 1.0413$
0	+0.487766 + 0	+0.1662923 + 2	-036908471 + 1	+0.22592310 + 3
1	-0.134523 + 2	-0.1986979 +3	+0.23718205 + 2	-0.10055939 + 4
2	+0.181436 + 3	+0.9103331 + 3	-0.45759292 + 2	+0.14528307 + 4
3	-0.125194 + 4	-0.1938422 + 4	-0.58434123 + 1	-0.24580937 + 3
4	+0.463313 + 4	+0.1738382 + 4	+0.11366534 + 3	-0.13063590 + 4
5	-0.880172 + 4	-0.1237675 + 3	-0.12648480 + 3	+0.12080765 + 4
6	+0.676231	-0.4795547 + 3	+0.43524752 + 2	-0.33028708 + 3

	e_n for λ_2		
n	$0.3213 \leq \bar{x} < 0.6013$	$0.6013 \leq \bar{x} < 0.8313$	$0.8313 \leq \bar{x} < 1.0413$
0	+0.29218010 + 1	-0.10669276 + 2	-0.36265370 + 2
1	-0.53116491 + 2	+0.41452406 + 2	+0.17009344 + 3
2	+0.28212314 + 3	-0.32546333 + 2	-0.24884816 + 3
3	-0.59331533 + 3	-0.19311793 + 2	+0.40613195 + 2
4	+0.37822004 + 3	+0.22741090 + 1	+0.22746742 + 3
5	+0.34827455 + 3	+0.47776766 + 2	-0.20825789 + 3
6	-0.41868191 + 3	-0.27946329 + 2	+0056318055 + 2

Table 11.6: Some specific details of 7 series of measurements with suction.

series	α	$R_c \times 10^{-6}$	porous surface	valve settings V_i
1	0	3.37	filtering paper	for roughly calculated stability
2	0	3.37	"	open
3	0	2.75	"	continuous V_o
4	0	3.37	paper + nylon	trial and error
5	0	4.50	"	"
6	0	5.50	"	"
7	0	6.16	"	"

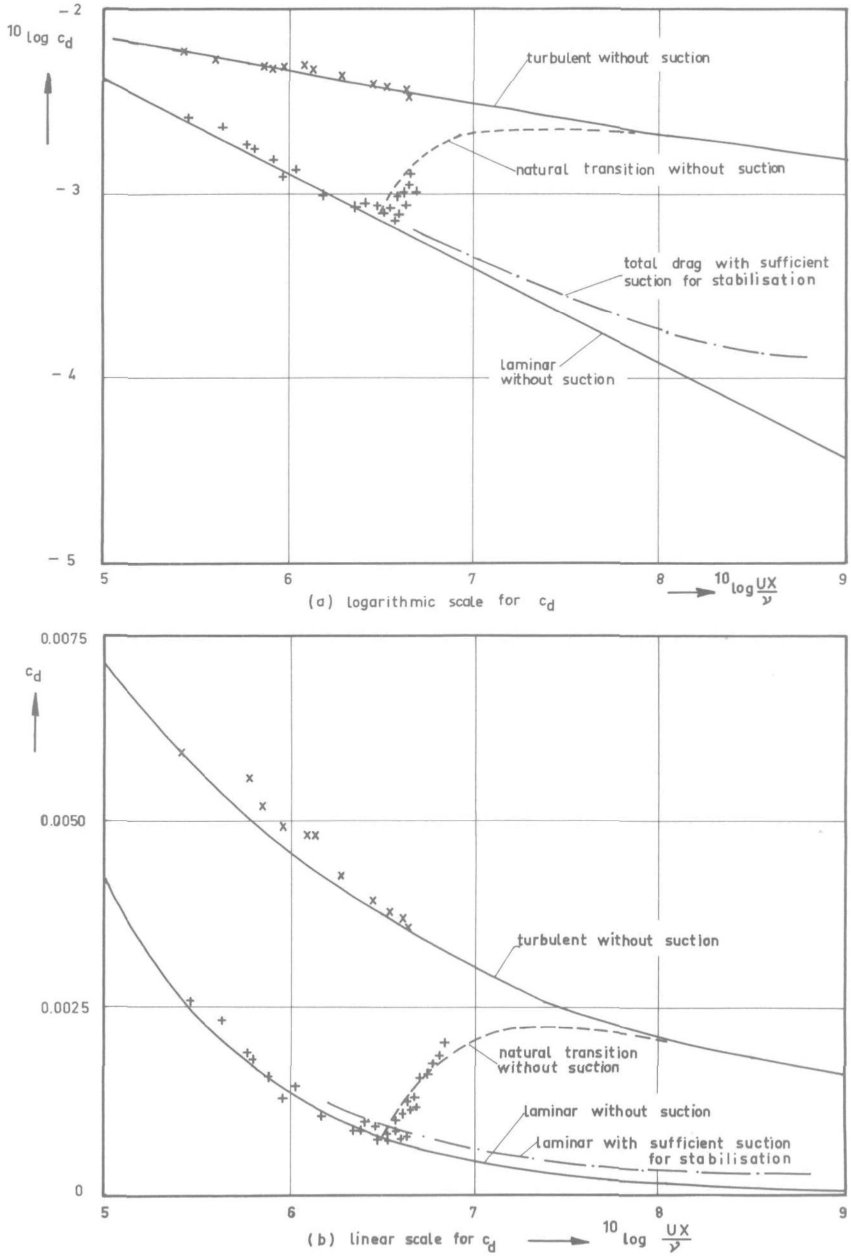

FIG. 1.1: DRAG OF FLAT PLATE WITH AND WITHOUT SUCTION
(see also fig. 9.21)

+ experiment, smooth plate
x " , with tripping wire

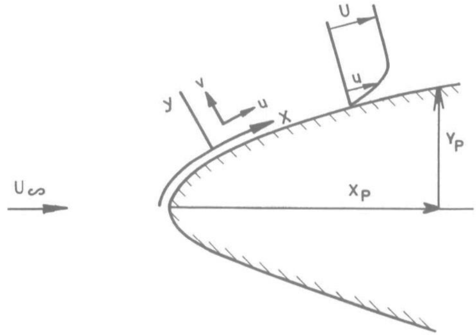

FIG. 2.1: COORDINATE SYSTEEM FOR BOUNDARY LAYER THEORY.

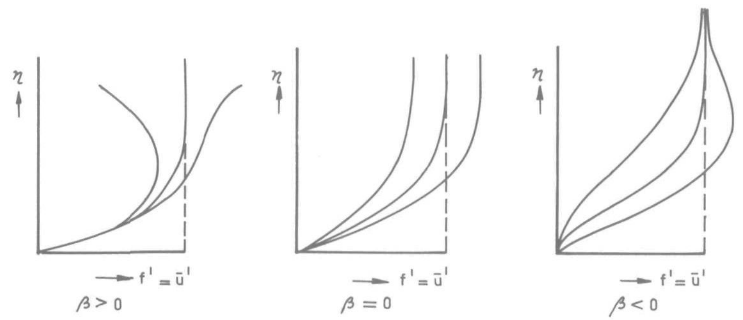

FIG. 3.1: TYPICAL SOLUTIONS OF THE FALKNER-SKAN EQUATION (3.10)

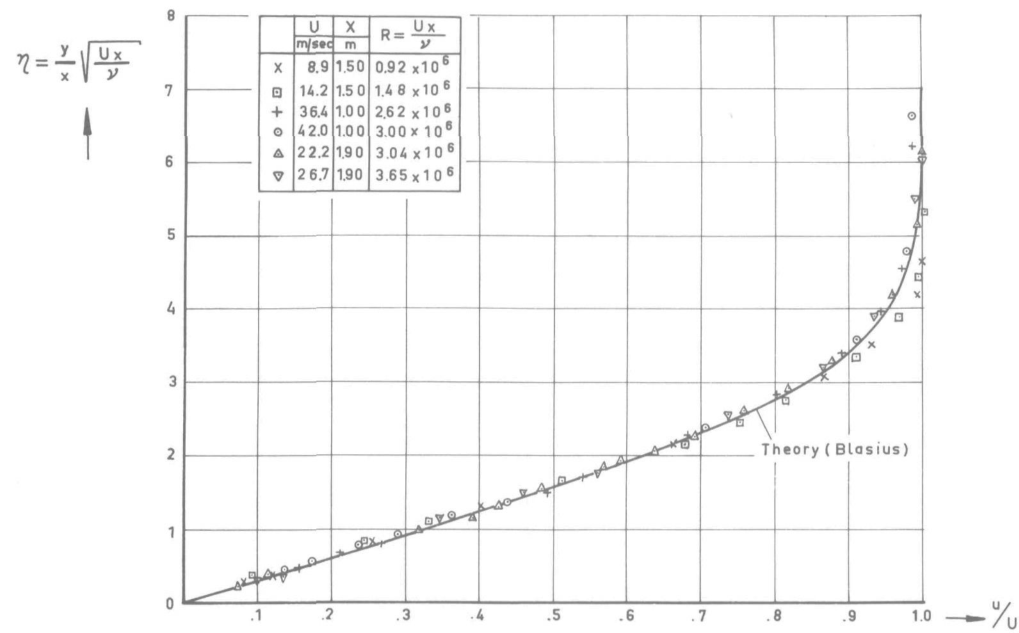

FIG. 3.2: THE VELOCITY PROFILE IN THE LAMINAR BOUNDARY LAYER ON A FLAT PLATE WITHOUT SUCTION.

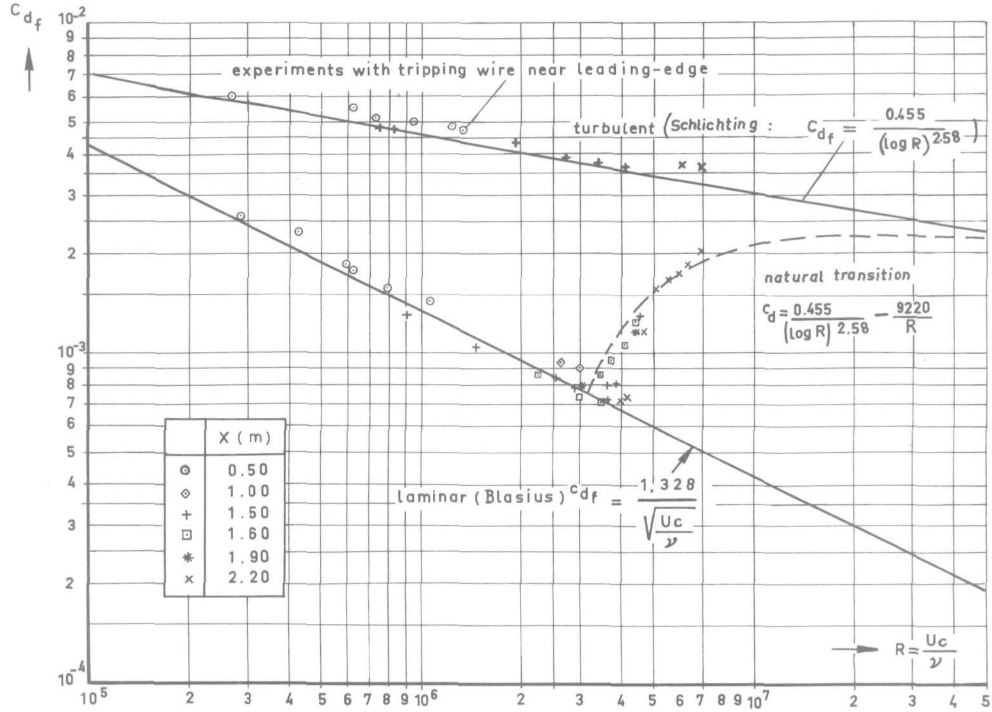

FIG. 3.3 : SKIN FRICTION COEFFICIENT FOR THE FLAT PLATE WITHOUT SUCTION.

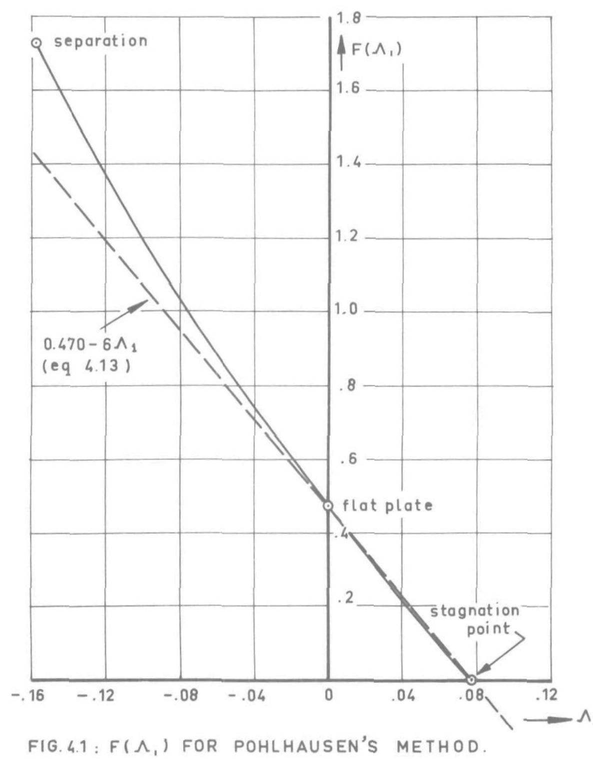

FIG. 4.1 : $F(\Lambda_1)$ FOR POHLHAUSEN'S METHOD.

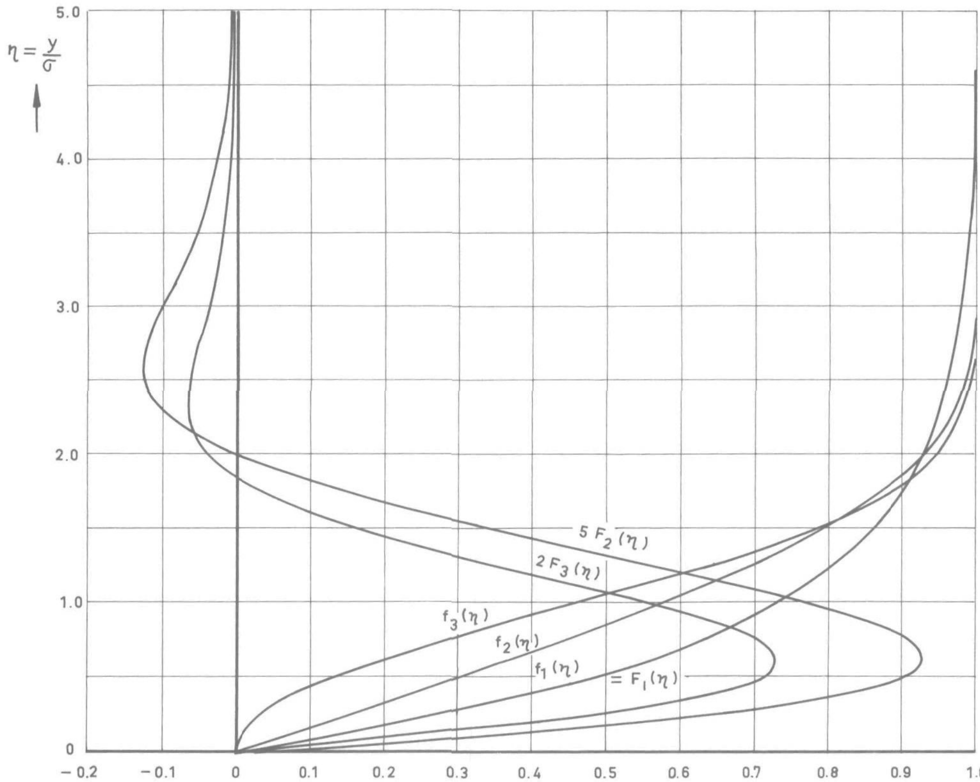

FIG. 5.1: THE FUNCTIONS DEFINED BY EQUATIONS (5.3) TO (5.9) FOR a = 1.3 AND b = 0.3

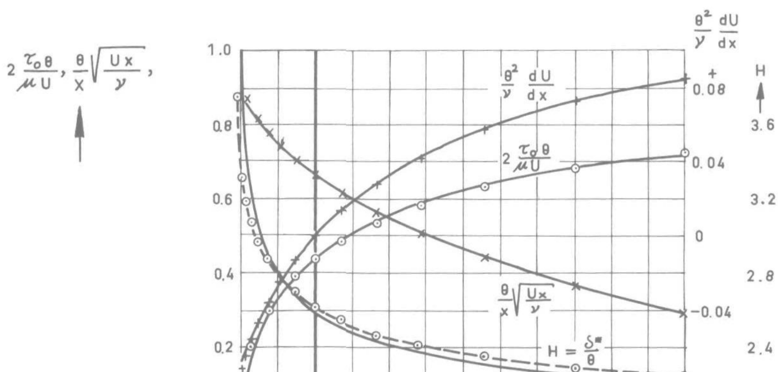

FIG. 5.2: RESULTS OF THE MOMENTUM METHOD FOR HARTREE'S BOUNDARY LAYERS.

——— exact Hartree — — — , +, x, ⊙ approximate method

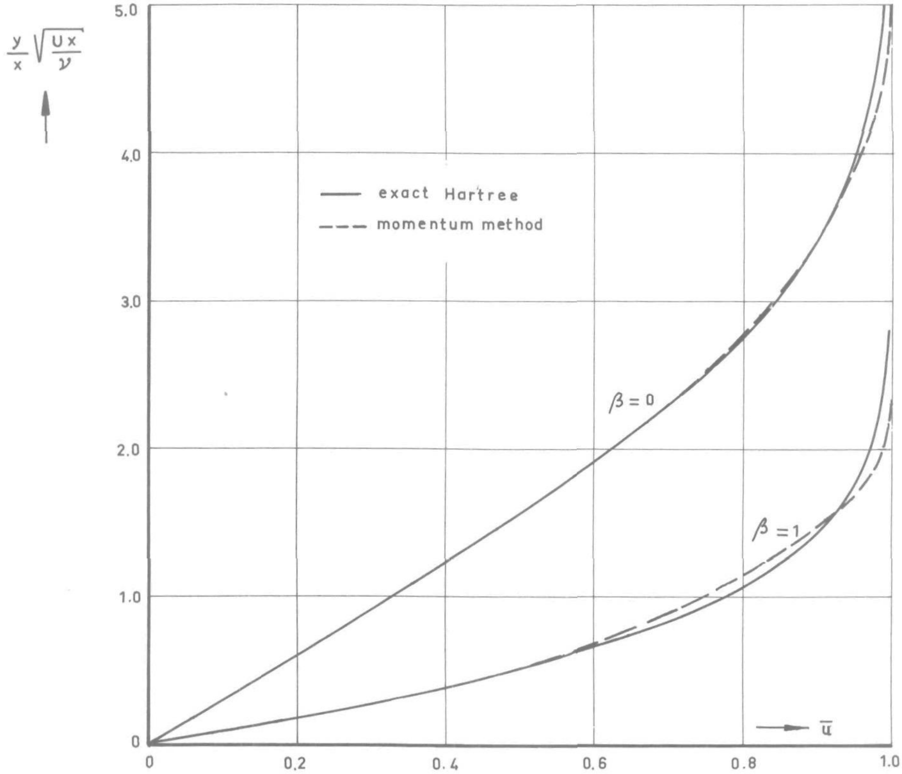

FIG. 5.3: VELOCITY PROFILES FOR THE FLAT PLATE ($\beta = 0$) AND THE PLANE STAGNATION POINT ($\beta = 1$), BOTH WITHOUT SUCTION.

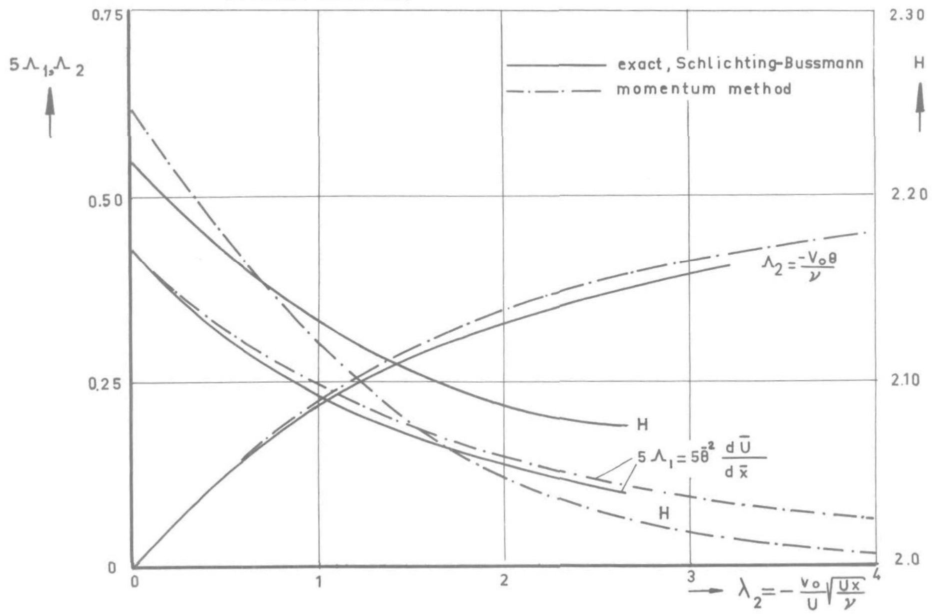

FIG. 5.4: SOME RESULTS FOR THE PLANE STAGNATION POINT WITH CONSTANT SUCTION VELOCITY.

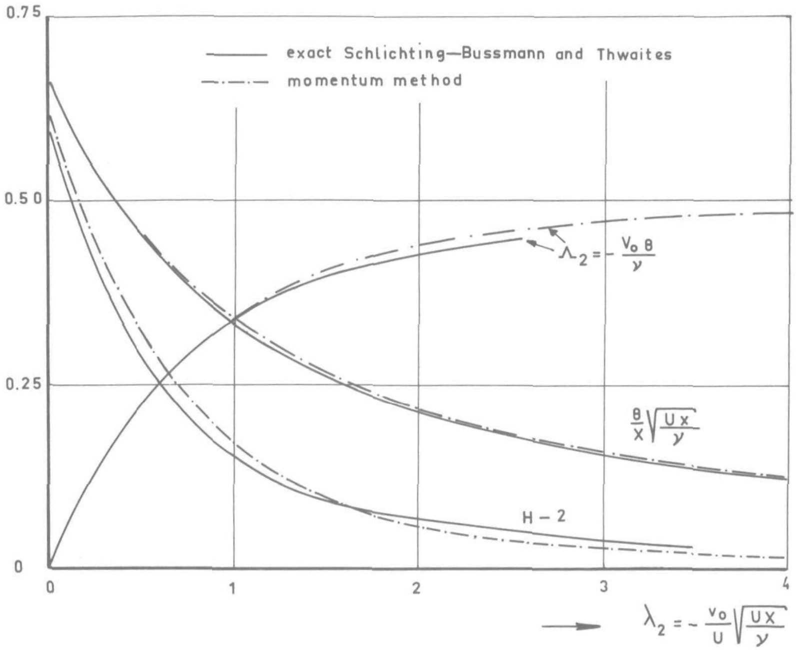

FIG. 5.5: SOME RESULTS FOR THE FLAT PLATE WITH $V_0 \backsim X^{-1/2}$

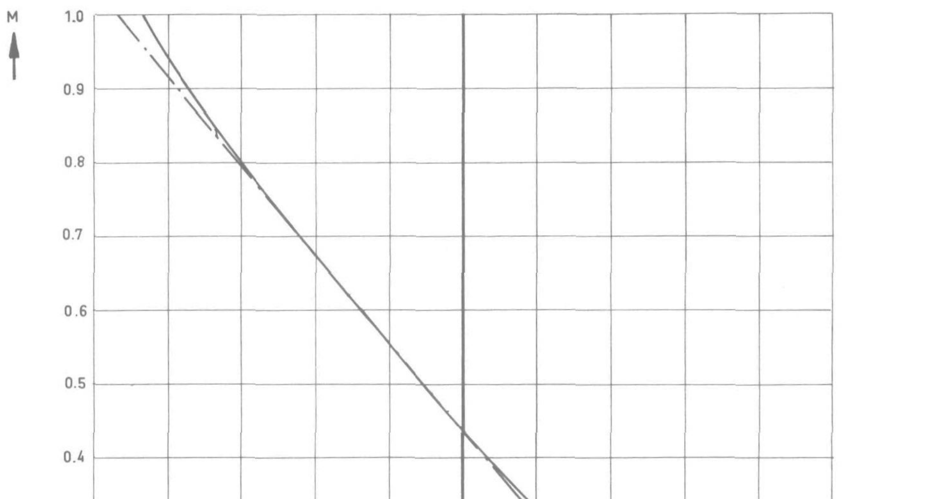

FIG. 5.6 : M (Λ_1) FOR THE MOMENTUM METHOD WITHOUT SUCTION

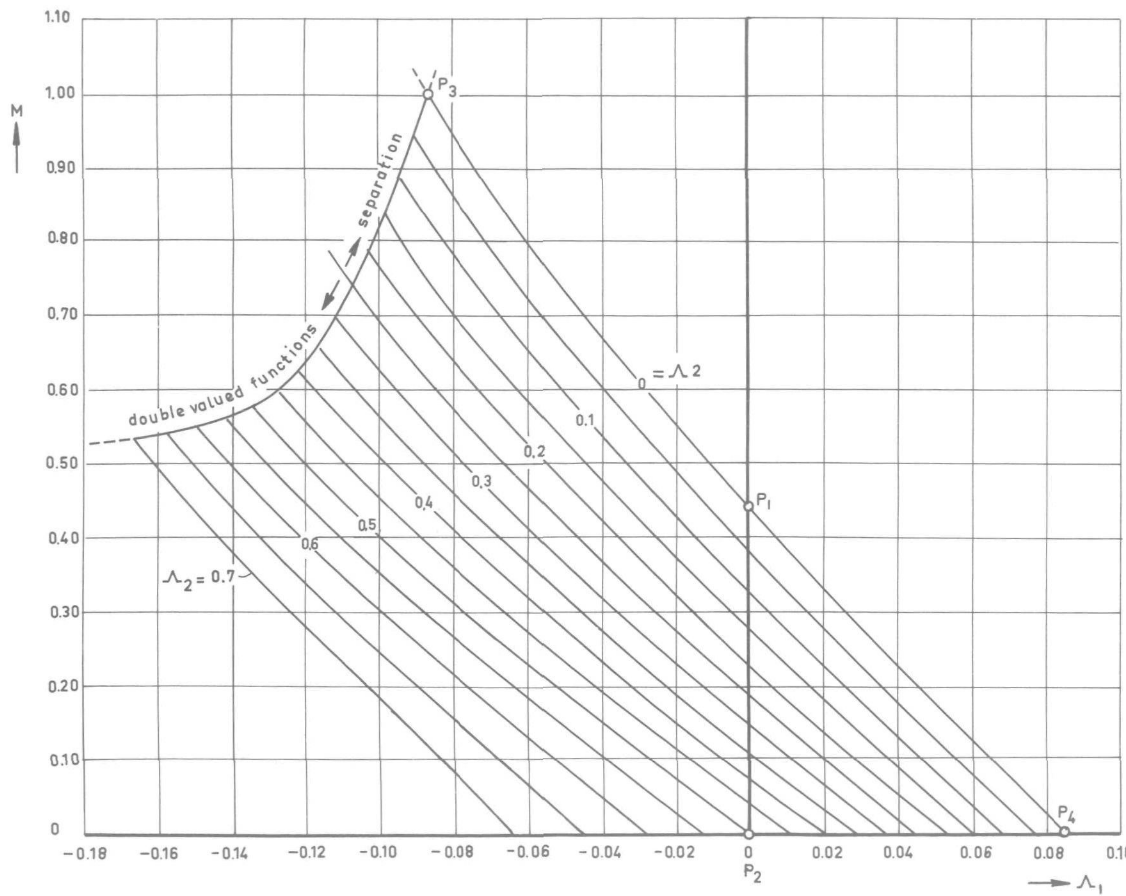

FIG. 5.7 : M (Λ_1, Λ_2) FOR THE MOMENTUM METHOD.

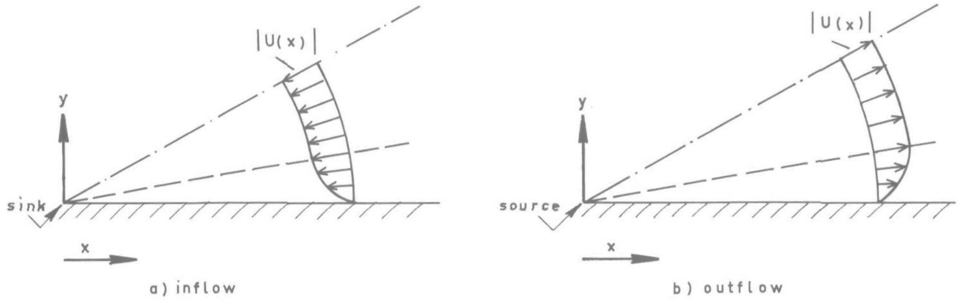

FIG. 6.1: THE FLOW BETWEEN NON-PARALLEL PLANE WALLS.

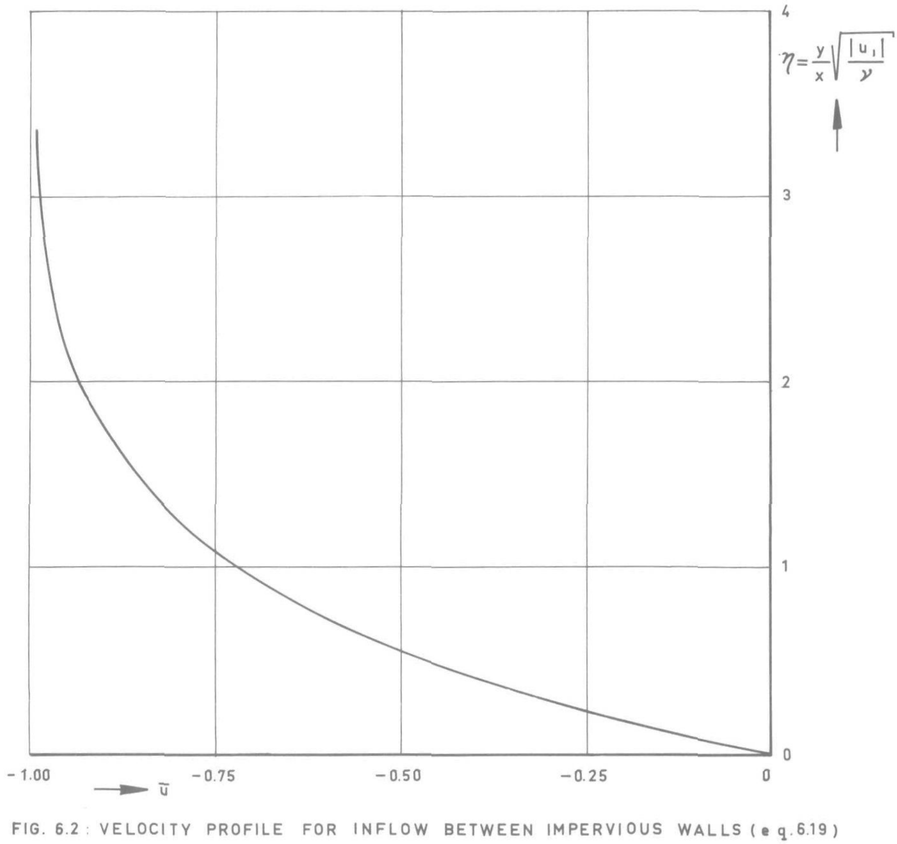

FIG. 6.2: VELOCITY PROFILE FOR INFLOW BETWEEN IMPERVIOUS WALLS (eq. 6.19)

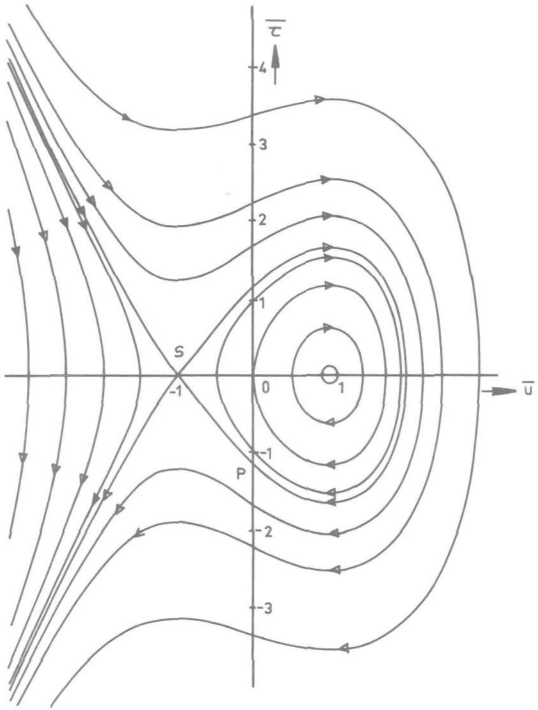

FIG. 6.3: PHASE PLANE PORTRAIT FOR THE BOUNDARY LAYER FLOW BETWEEN IMPERVIOUS NON-PARALLEL PLANE WALLS ($\lambda = 0$)

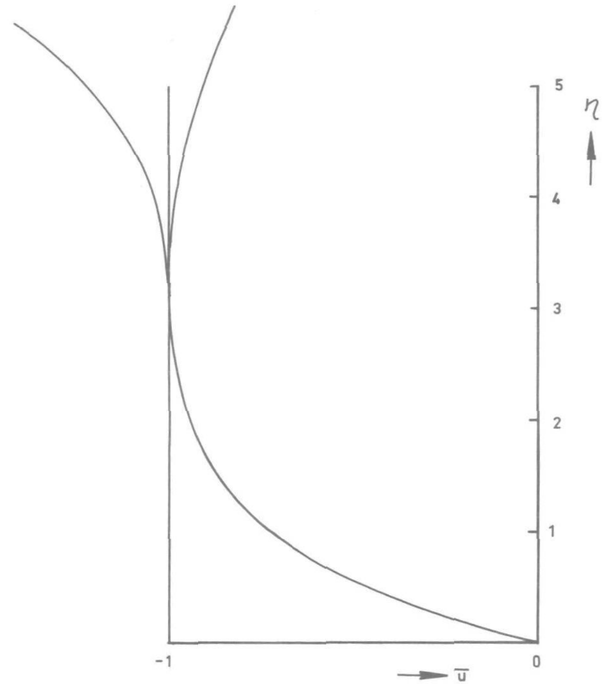

FIG. 6.4: VELOCITY PROFILES CORRESPONDING TO THE SADDLE POINT (−1.0) FOR $\lambda = 0$.

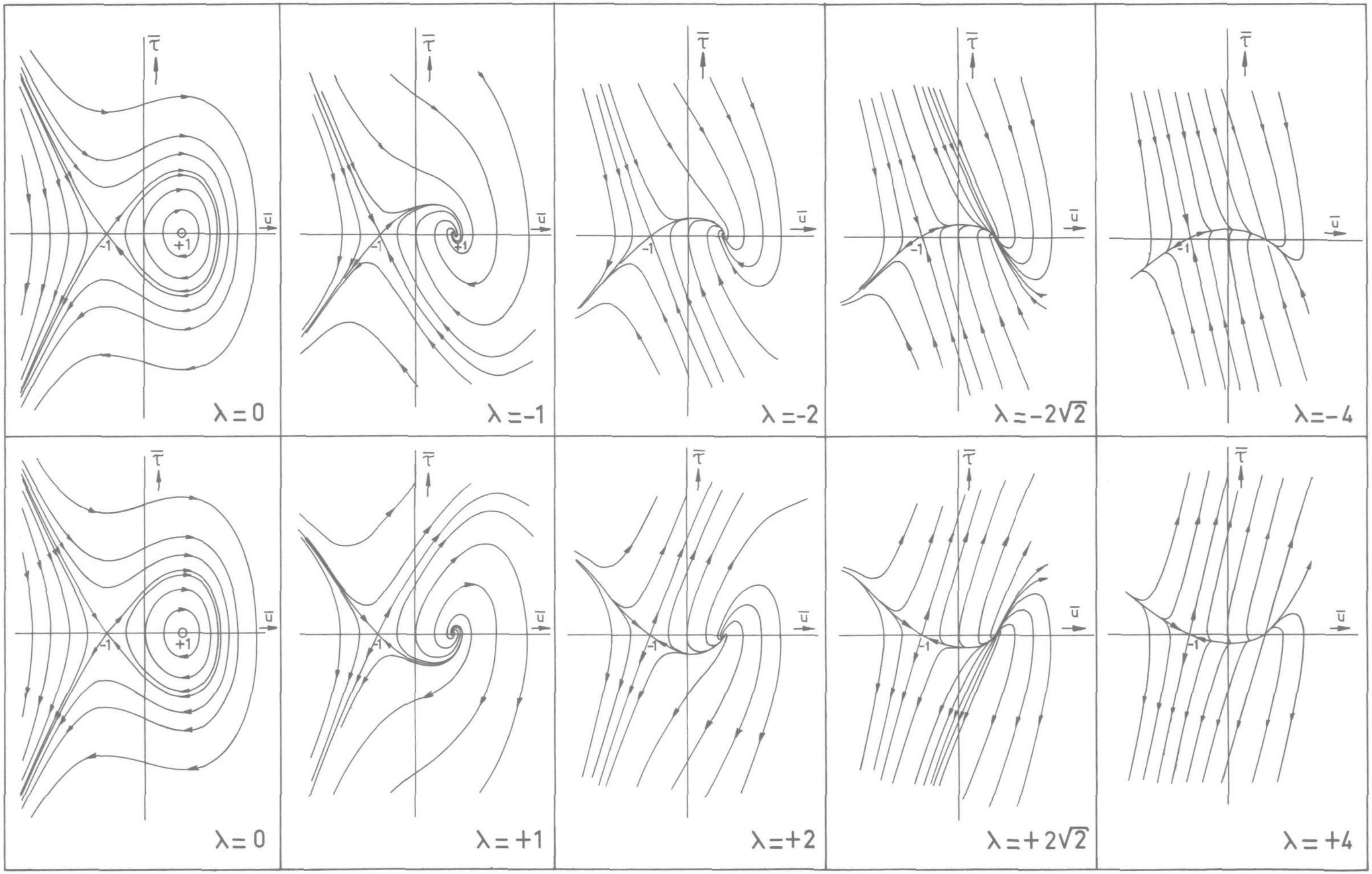

FIG. 6.5: PHASE PLANE PORTRAITS FOR THE BOUNDARY LAYER FLOW BETWEEN POROUS WALLS.

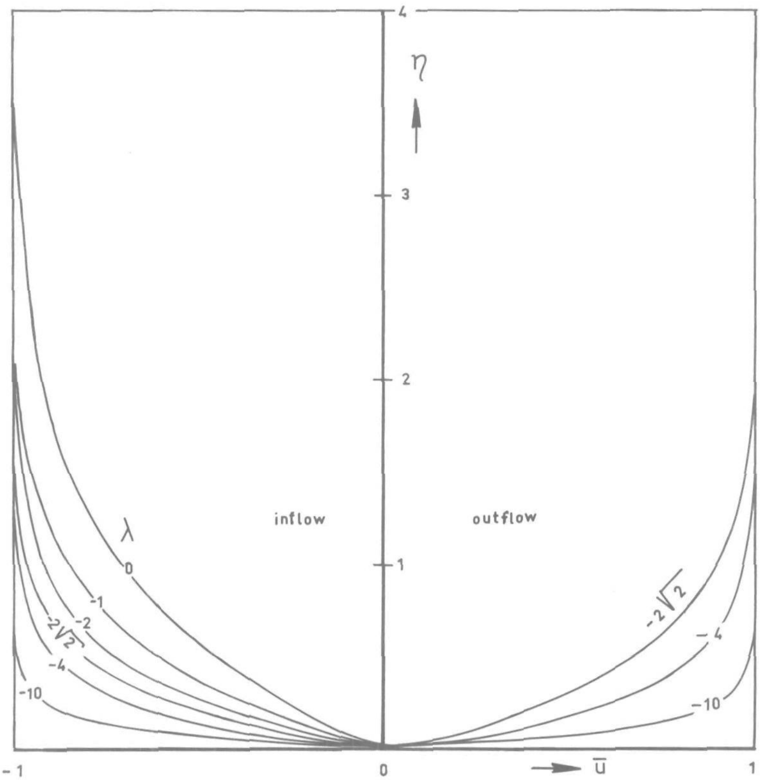

FIG. 6.6: VELOCITY PROFILES FOR INFLOW AND OUTFLOW AT DIFFERENT VALUES OF λ.

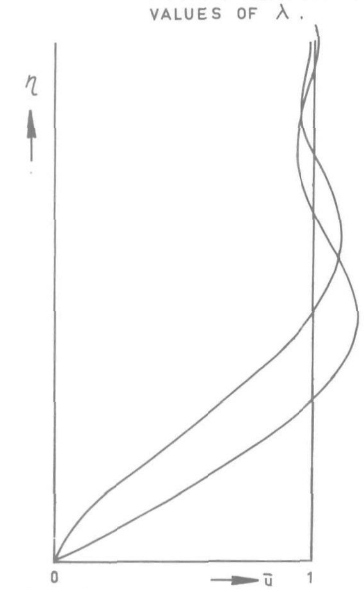

FIG. 6.7: VELOCITY PROFILES FOR OUTFLOW CORRESPONDING TO A STABLE SPIRAL IN THE PHASE PLANE

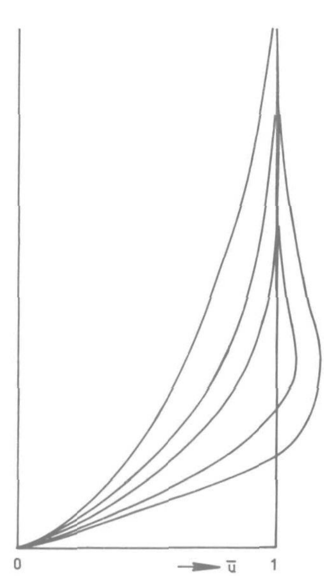

FIG. 6.8: VELOCITY PROFILES FOR OUTFLOW CORRESPONDING TO A STABLE NODE IN THE PHASE PLANE.

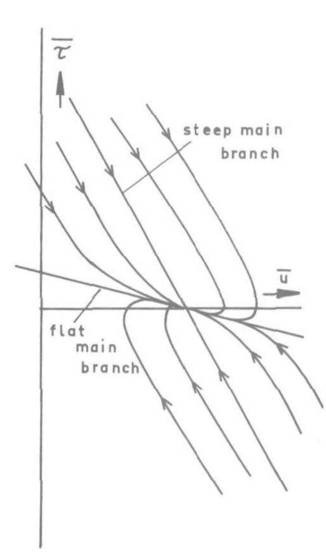

FIG. 6.9: CHARACTERISTICS OF A STABLE NODE.

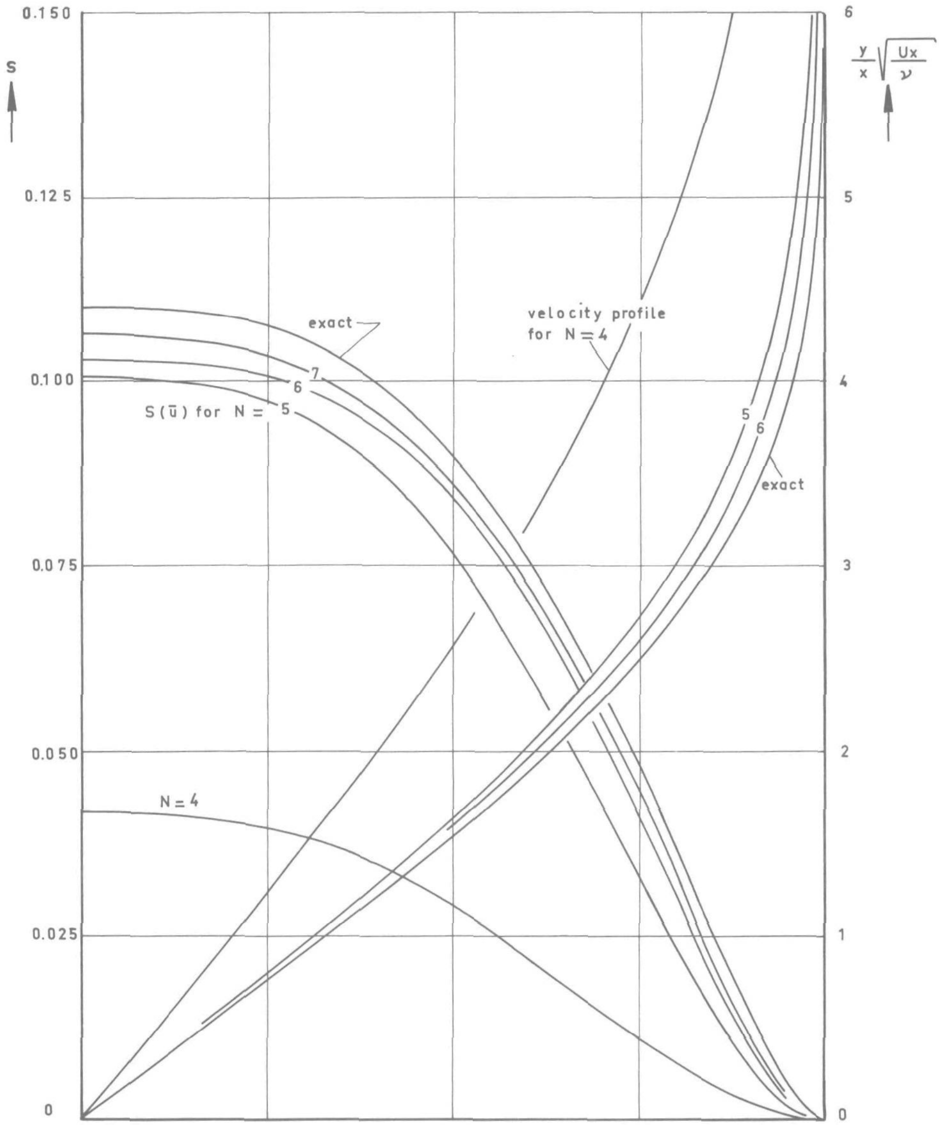

FIG. 8.1: S(ū) AND VELOCITY PROFILES FOR THE FLAT PLATE WITHOUT SUCTION AT DIFFERENT VALUES OF N.

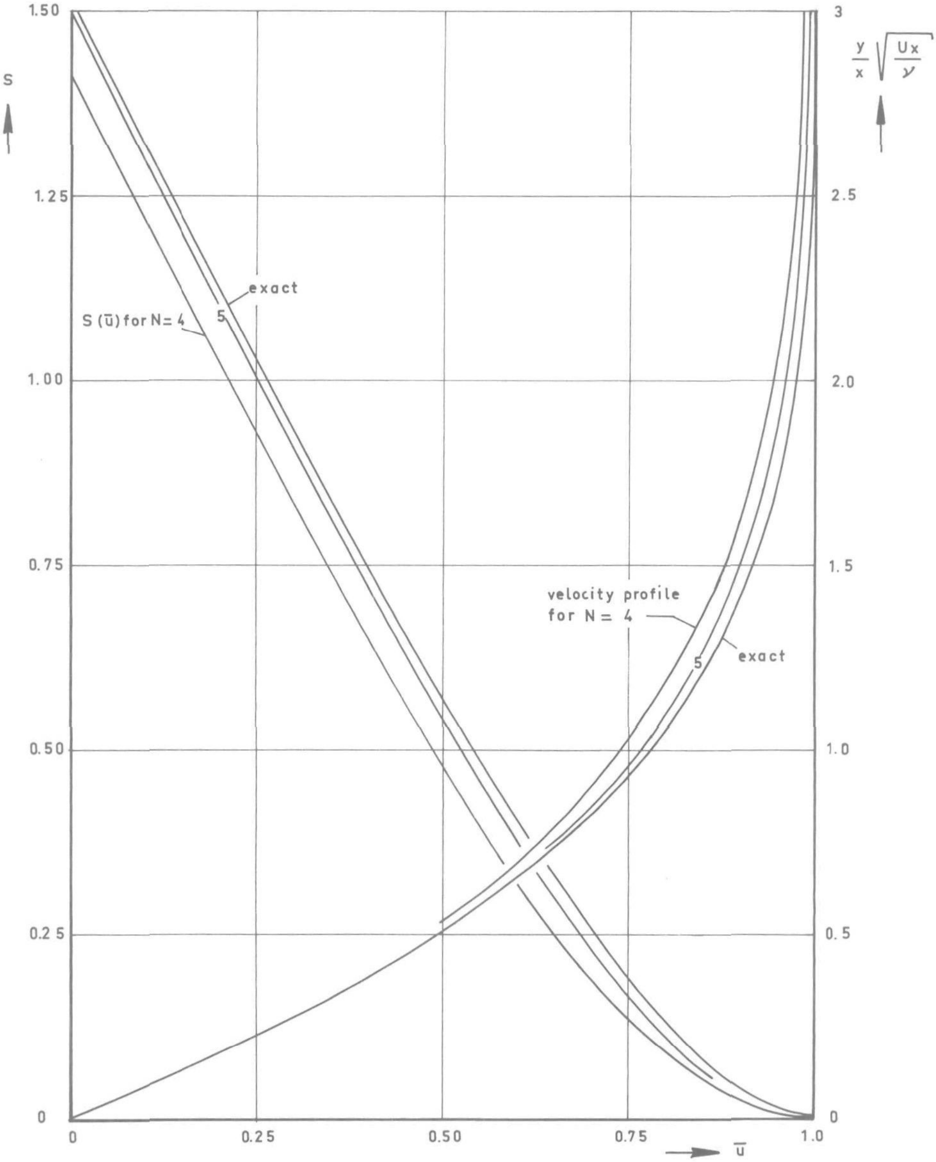

FIG. 8.2: S ($\bar{u}$) AND VELOCITY PROFILES FOR THE PLANE STAGNATION POINT WITHOUT SUCTION AT DIFFERENT VALUES OF N.

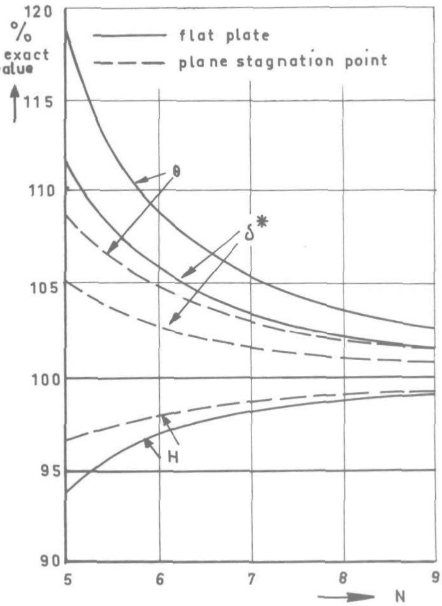

FIG. 8.3 : SOME RESULTS OF THE MULTIMOMENT METHOD FOR THE FLAT PLATE & STAGNATION POINT WITHOUT SUCTION.

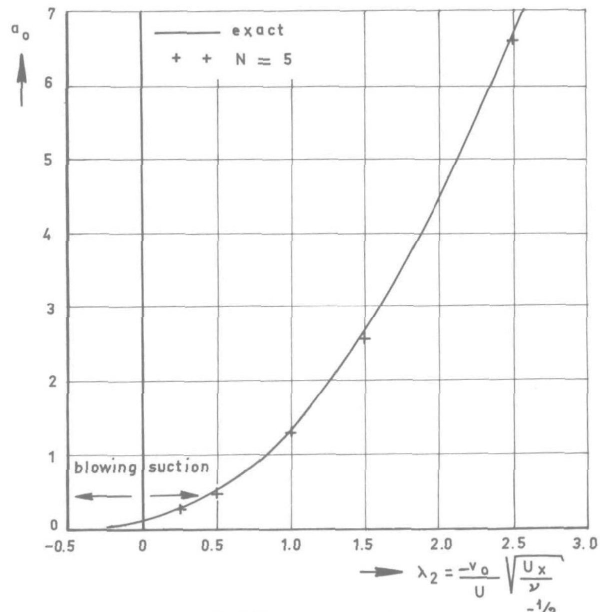

FIG. 8.4 : a_0 FOR THE FLAT PLATE WITH $v_0 \backsim x^{-1/2}$

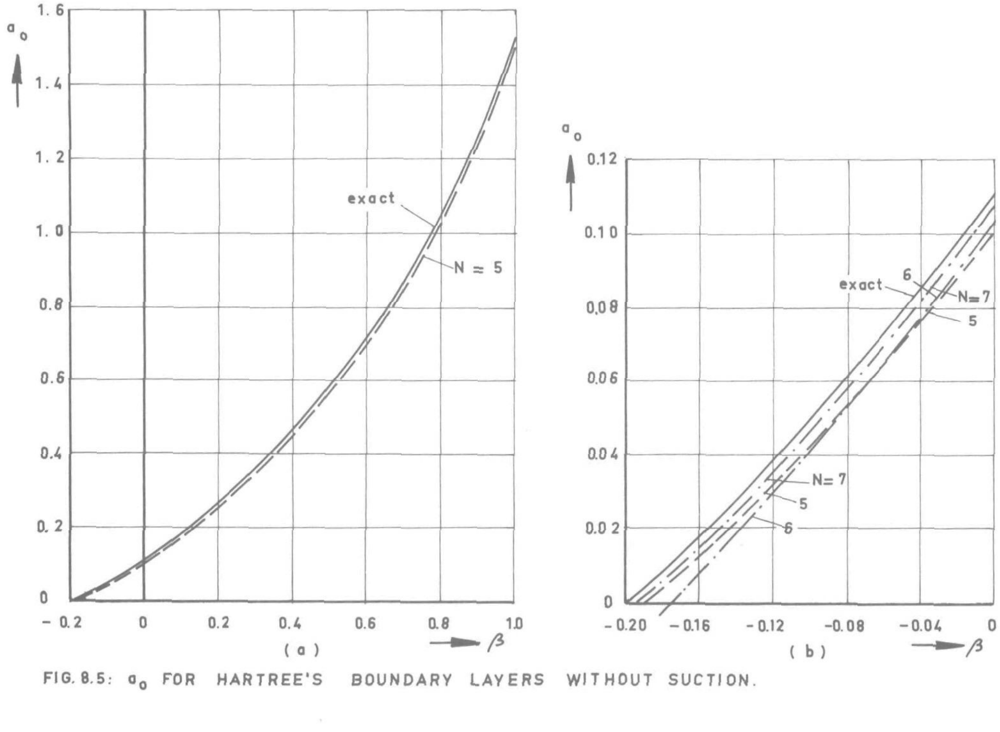

FIG. 8.5: a_0 FOR HARTREE'S BOUNDARY LAYERS WITHOUT SUCTION.

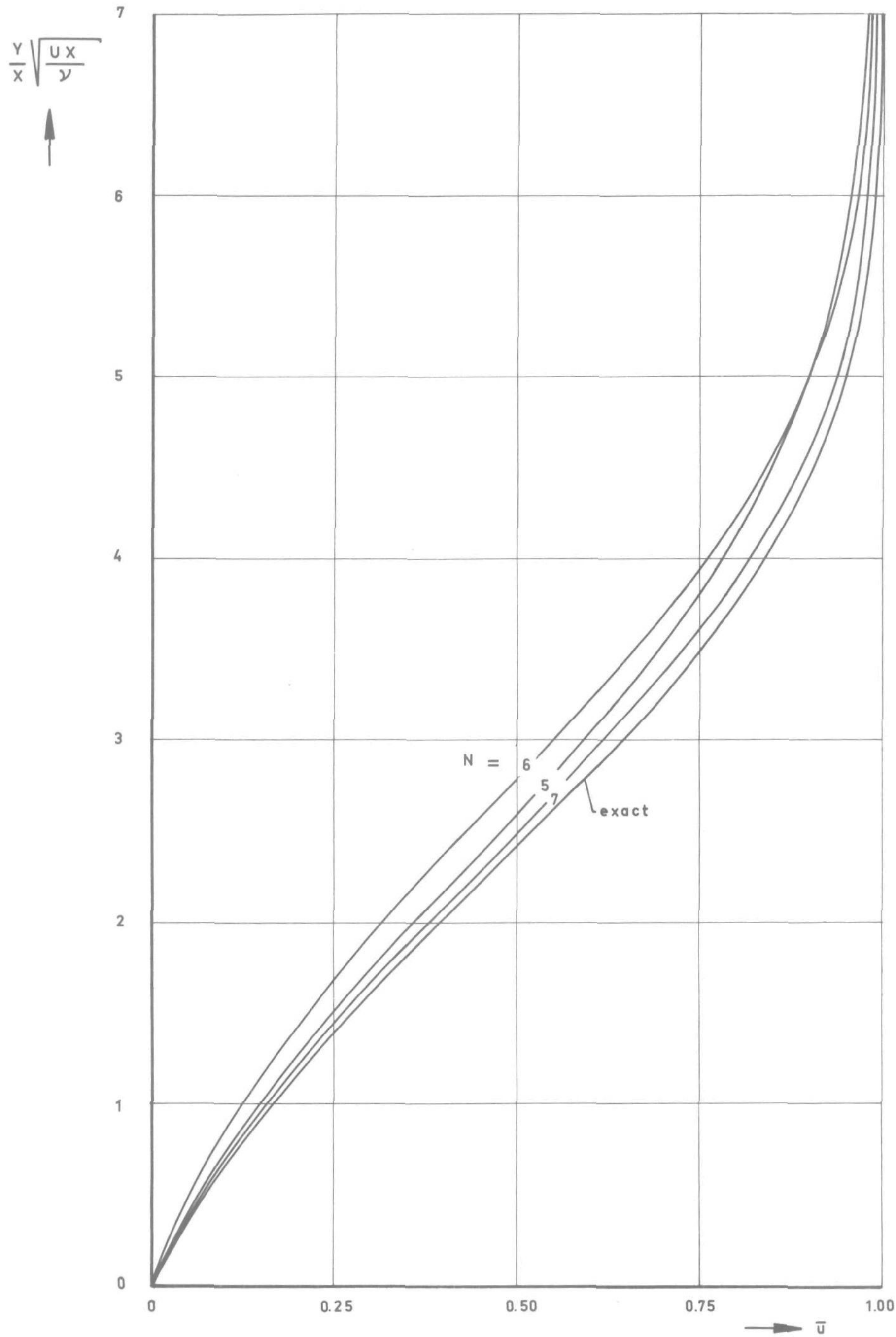

FIG. 8.6: VELOCITY PROFILES FOR THE HARTREE BOUNDARY LAYER WITH $\beta = -0.16$

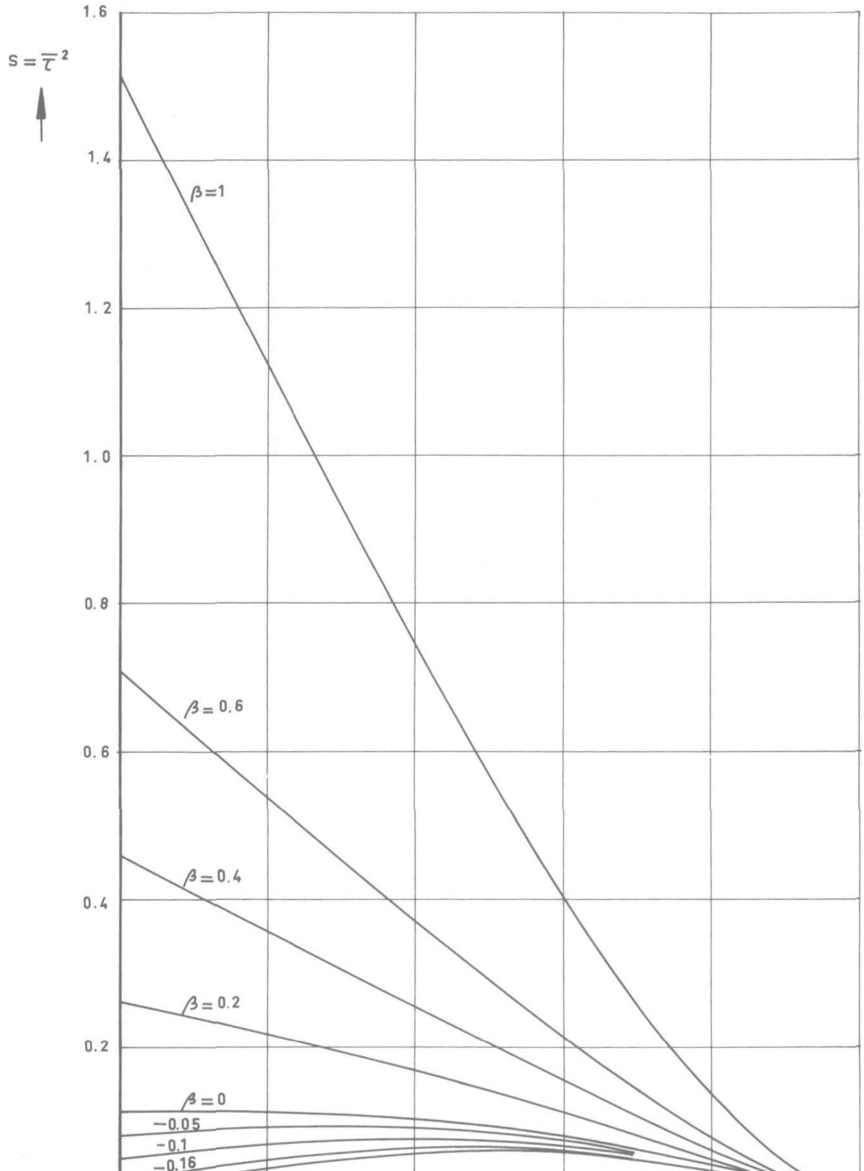

FIG. 8.7: $S(\overline{u})$ PROFILES FOR THE HARTREE BOUNDARY LAYERS ACCORDING TO THE EXACT SOLUTION BY SMITH [114].

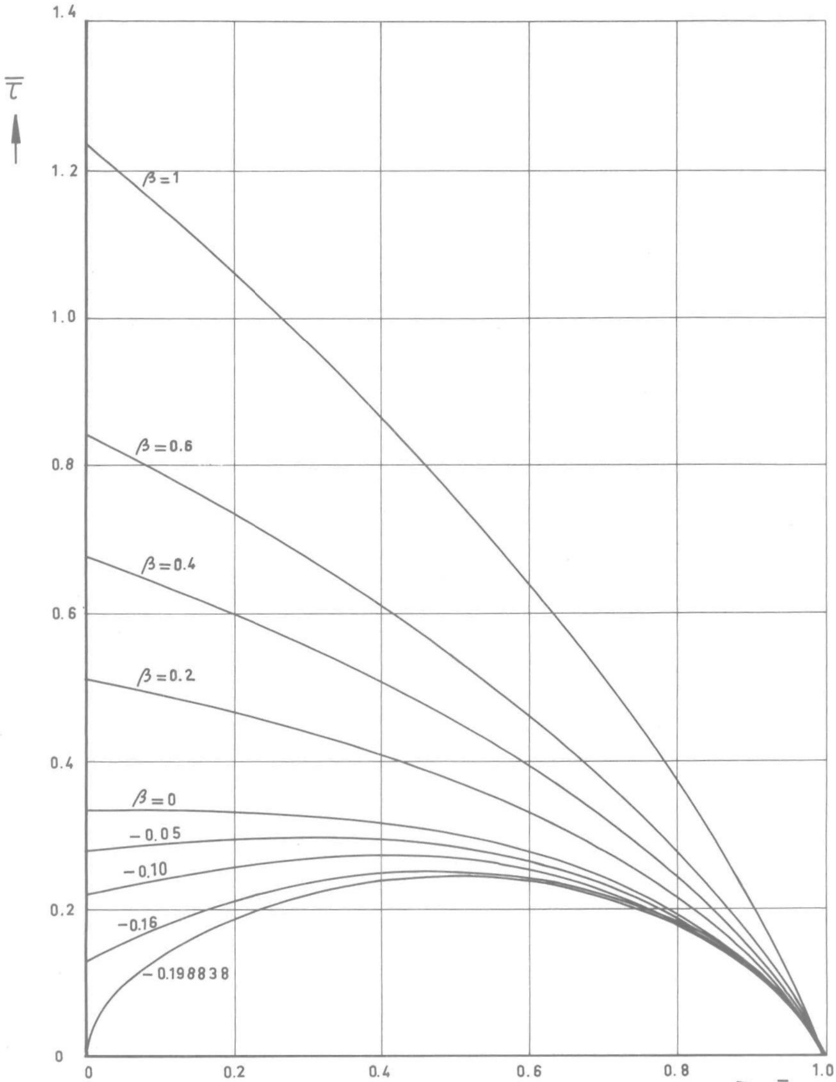

FIG. 8.8: SHEAR STRESS PROFILES FOR THE HARTREE BOUNDARY LAYERS ACCORDING TO THE EXACT SOLUTION BY SMITH [14]

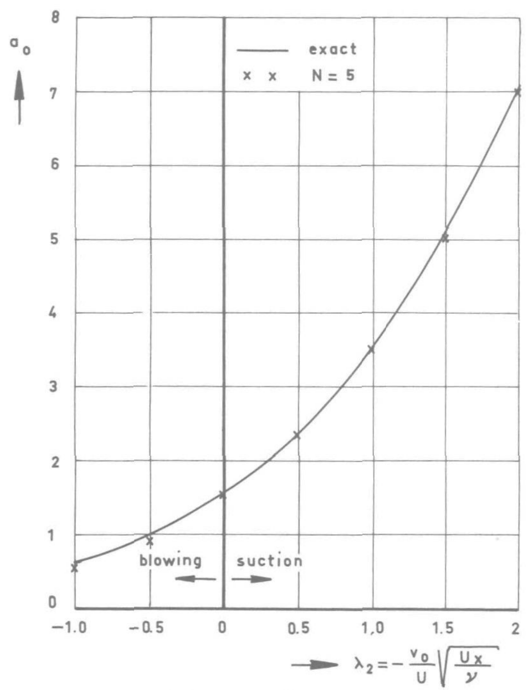

FIG. 8.9: a_o FOR THE PLANE STAGNATION POINT WITH CONSTANT SUCTION VELOCITY.

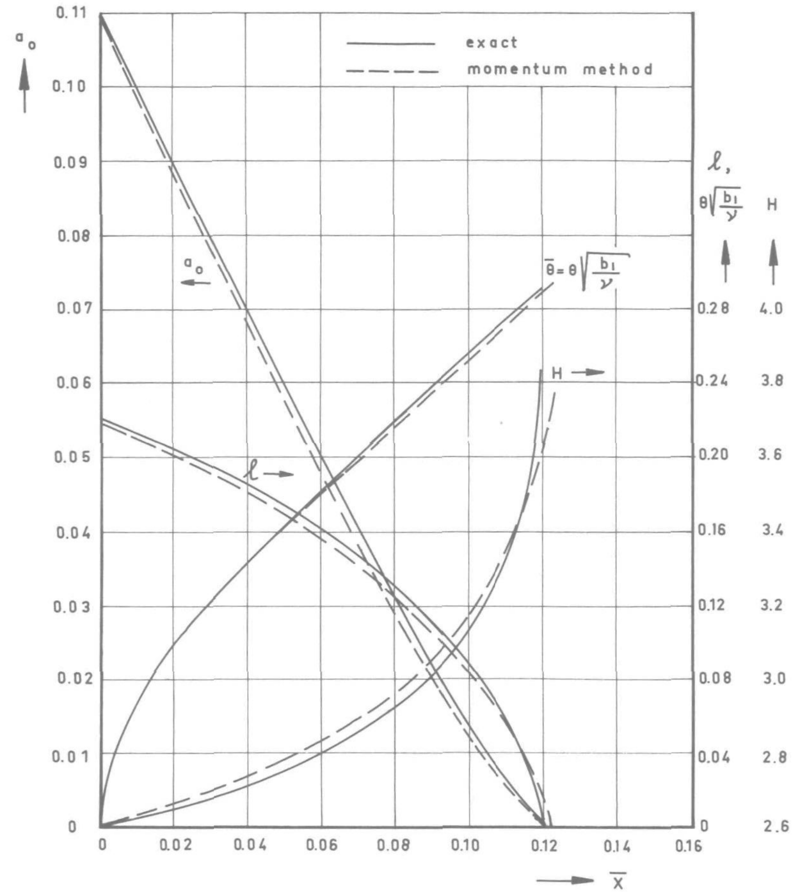

FIG. 8.10: RESULTS OF THE MOMENTUM METHOD FOR $\bar{U} = 1 - \bar{x}$.

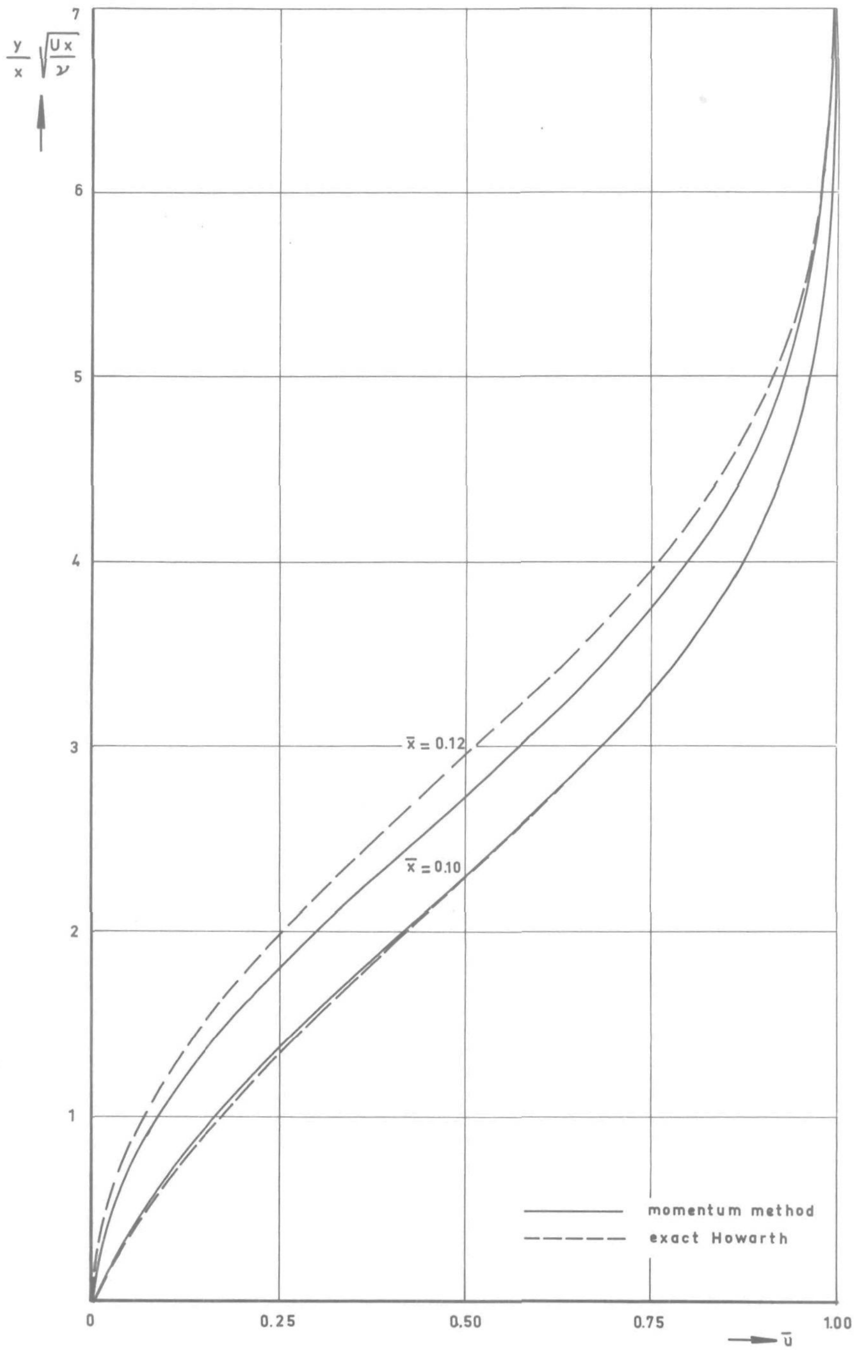

FIG. 8.11: VELOCITY PROFILES FOR $\bar{U} = 1 - \bar{x}$ AT $\bar{x} = 0.10$ AND 0.12 ACCORDING TO THE MOMENTUM METHOD.

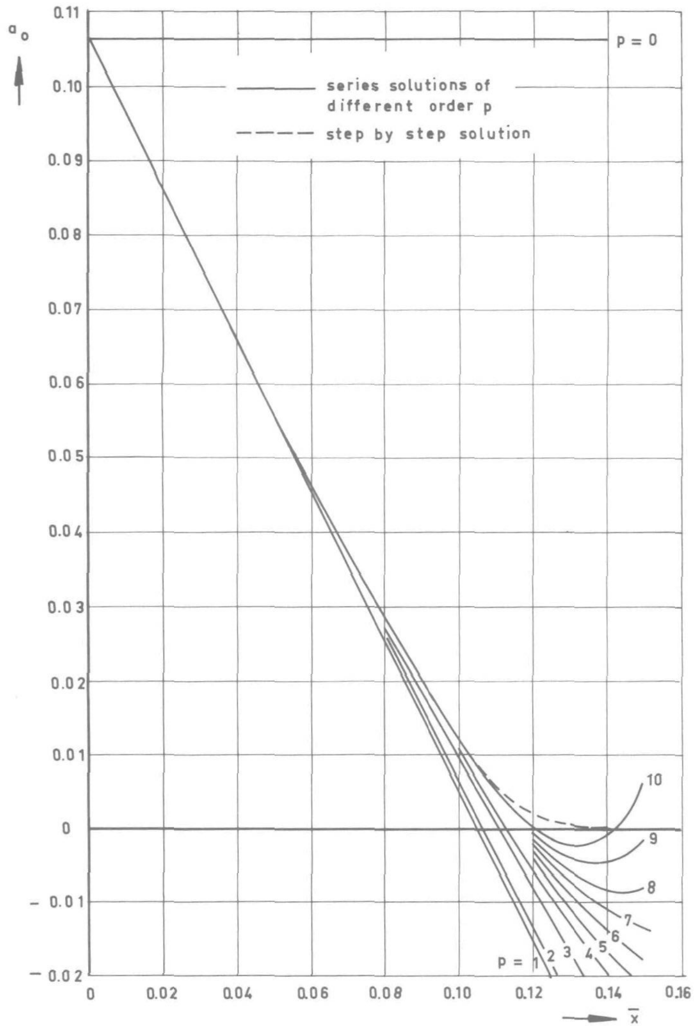

FIG. 8.12: THE MULTIMOMENT METHOD FOR $\bar{U} = 1 - \bar{x}$; N = 7

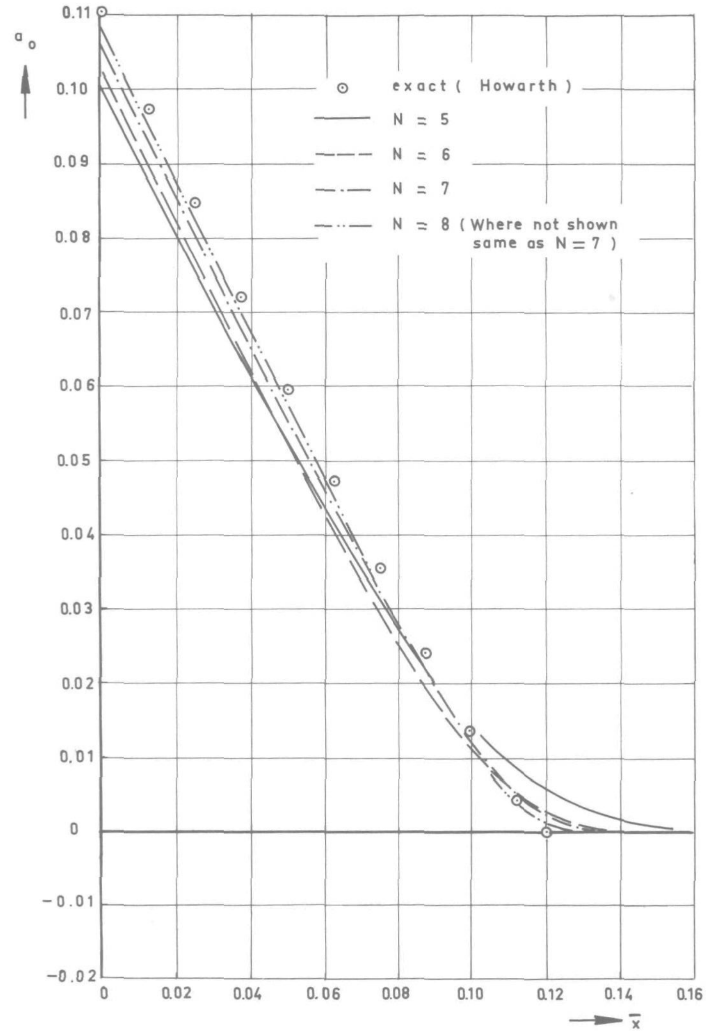

FIG. 8.13: a_0 FOR $\bar{U} = 1 - \bar{x}$

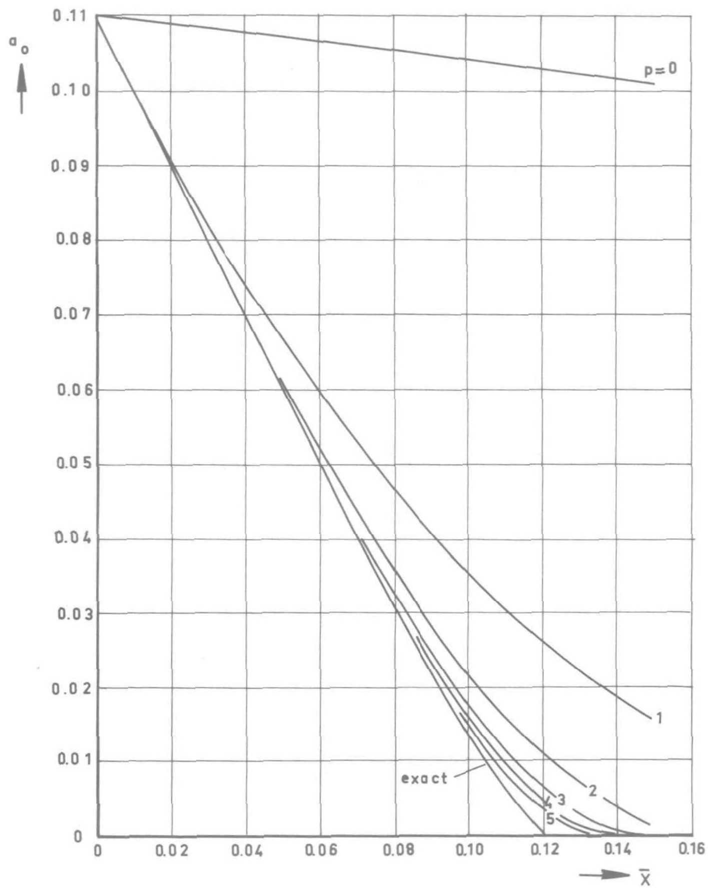

FIG. 8.14: RESULTS OF GÖRTLER'S SERIES METHOD FOR $\bar{U} = 1-\bar{x}$

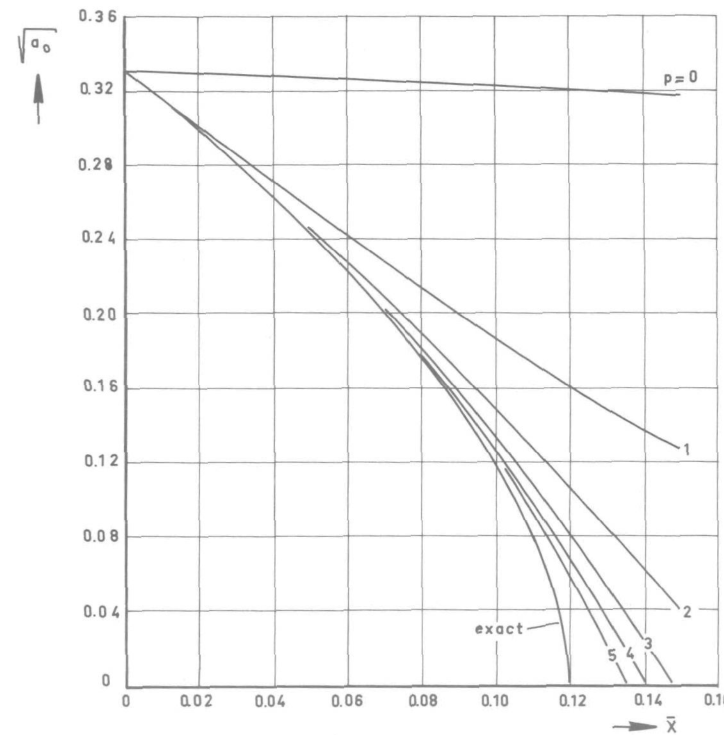

FIG. 8.15: RESULTS OF GÖRTLER'S SERIES METHOD FOR $\bar{U} = 1-\bar{x}$

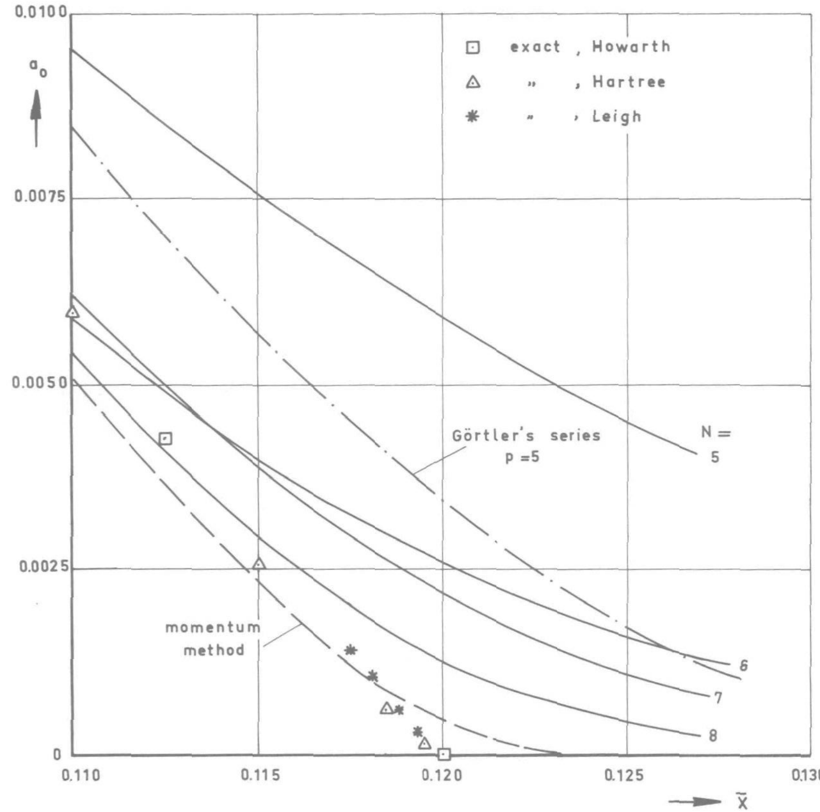

FIG. 8.16: a_o NEAR THE SEPARATION POINT FOR $\bar{U} = 1 - \bar{x}$ ACCORDING TO DIFFERENT CALCULATION METHODS

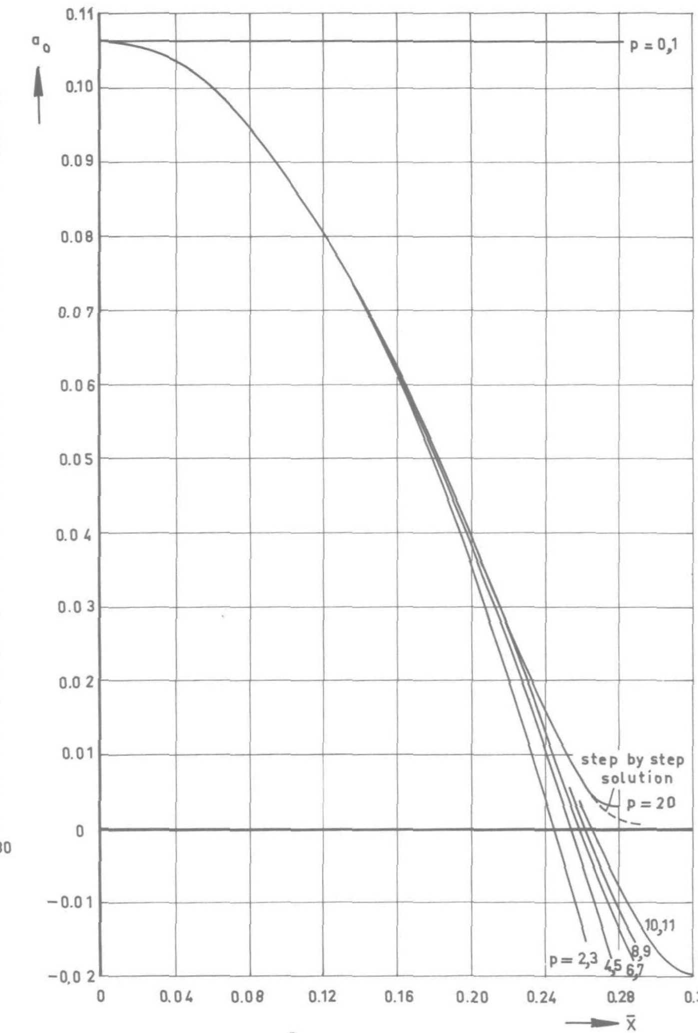

FIG. 8.17: a_o FOR $\bar{U} = 1-\bar{x}^2$; N = 7

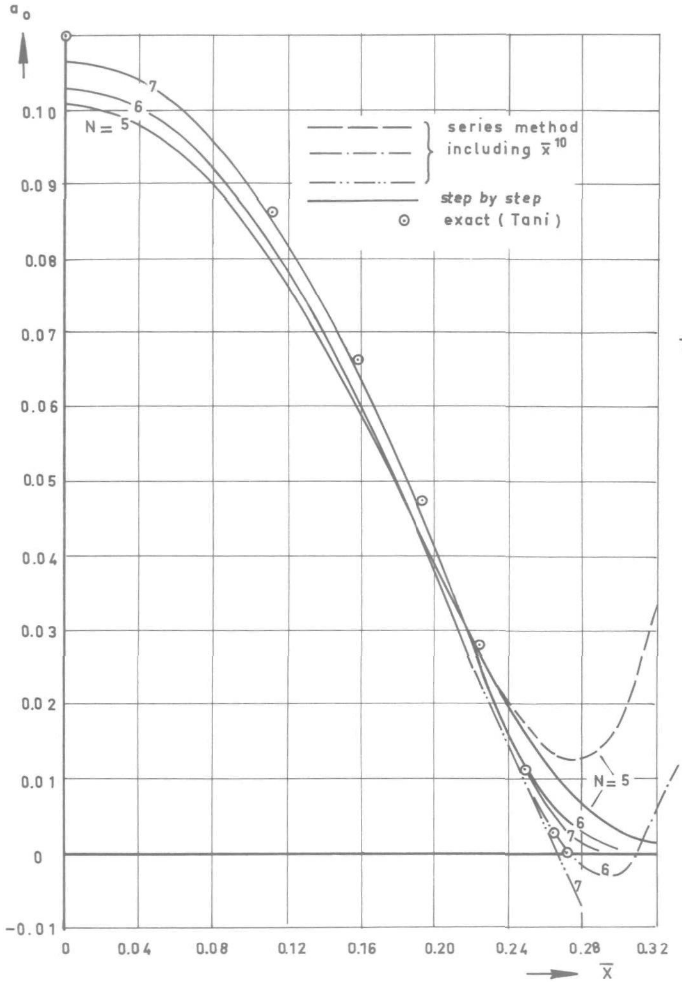

FIG. 8.18 : a_0 FOR $\bar{U} = 1 - \bar{x}^2$; MULTIMOMENT METHOD N = 5,6 AND 7

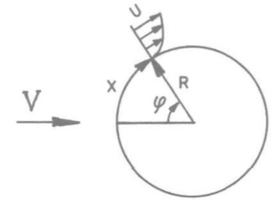

FIG. 8.19 : BOUNDARY LAYER ON A CIRCULAR CYLINDER.

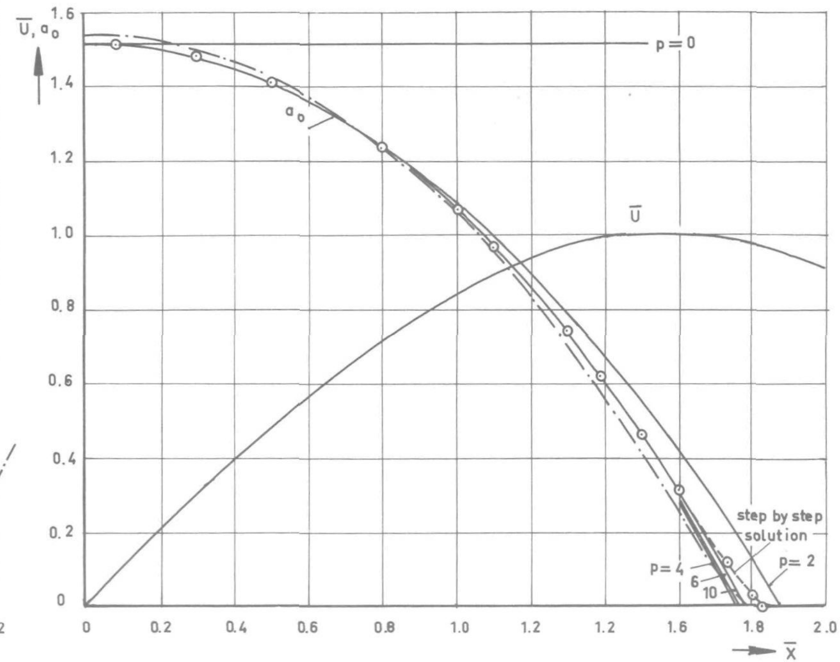

FIG. 8.20 : RESULTS OF DIFFERENT METHODS FOR $\bar{U} = \sin \bar{x}$.

⊙ ⊙ exact (Terrill)
——— multimoment method, N = 7 , series solution of order p .
— — — " " " , step by step solution
—·—·— momentum method

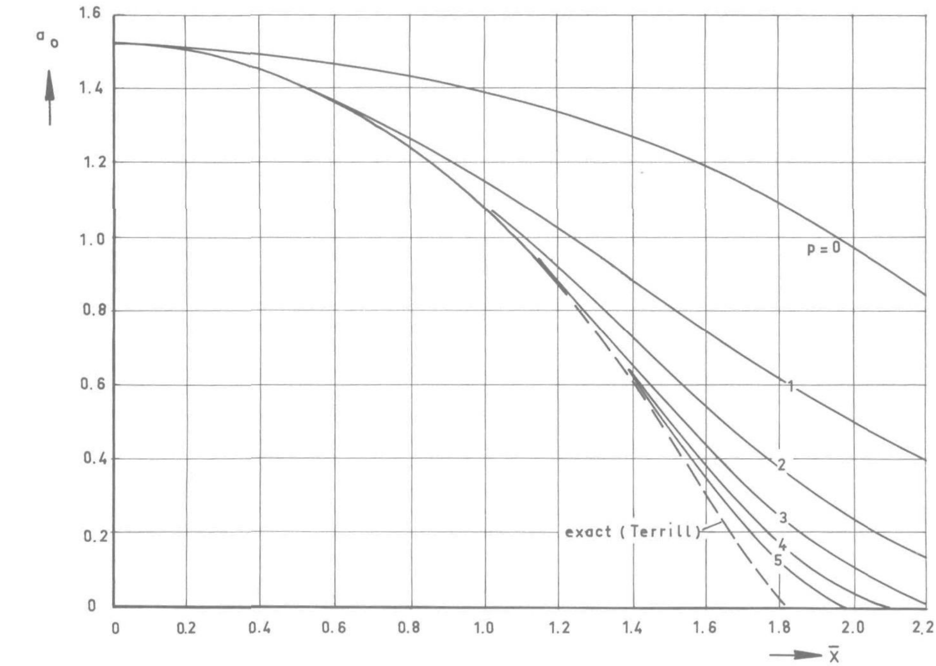

FIG. 8.21: a_0 ACCORDING TO GÖRTLER'S SERIES METHOD FOR $\bar{U} = \sin \bar{x}$

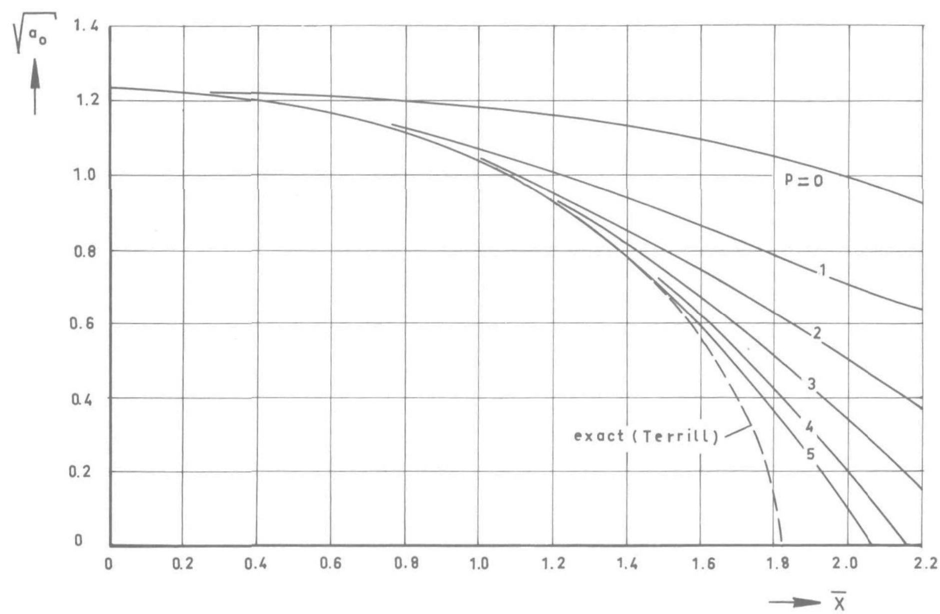

FIG. 8.22: $\sqrt{a_0}$ ACCORDING TO GÖRTLER'S SERIES METHOD FOR $\bar{U} = \sin \bar{x}$

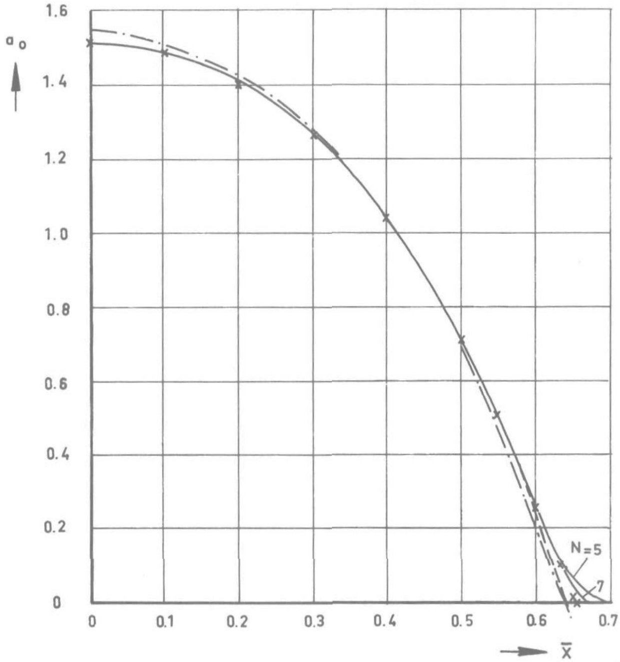

FIG. 8.23: RESULTS OF DIFFERENT METHODS FOR $\bar{U} = \bar{x} - \bar{x}^3$

x x x exact (Curle)

——— multimoment method, step bij step solution

– – – " " , series solution, N = 7, p = 10

—·—·— momentum method

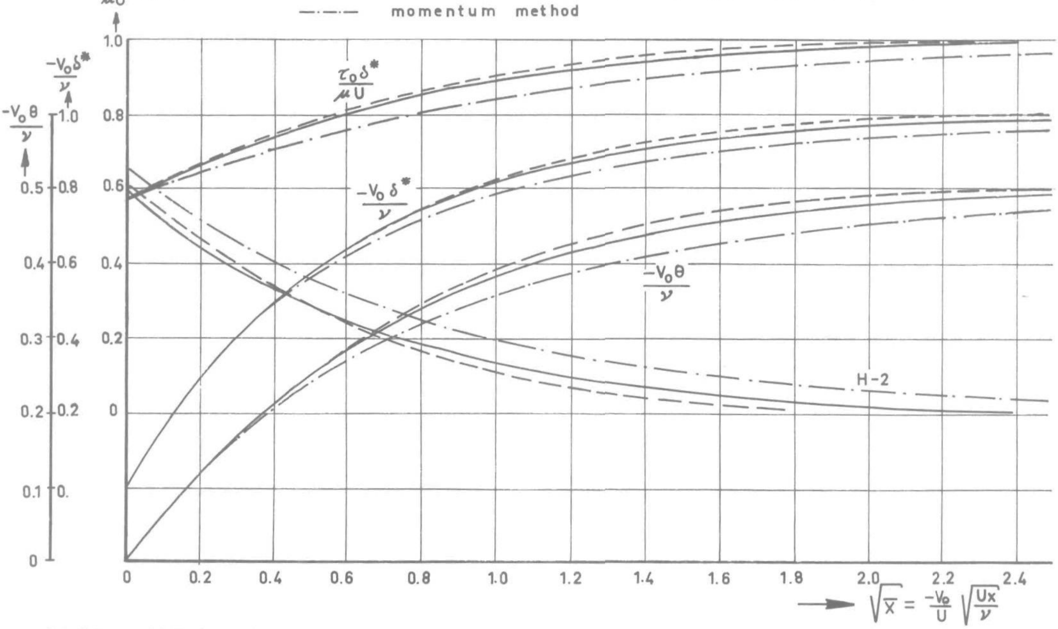

FIG. 8.24: SOME RESULTS FOR THE FLAT PLATE WITH CONSTANT SUCTION VELOCITY

——— exact. Iglisch

—·— Schlichting [55]

– – – – momentum method

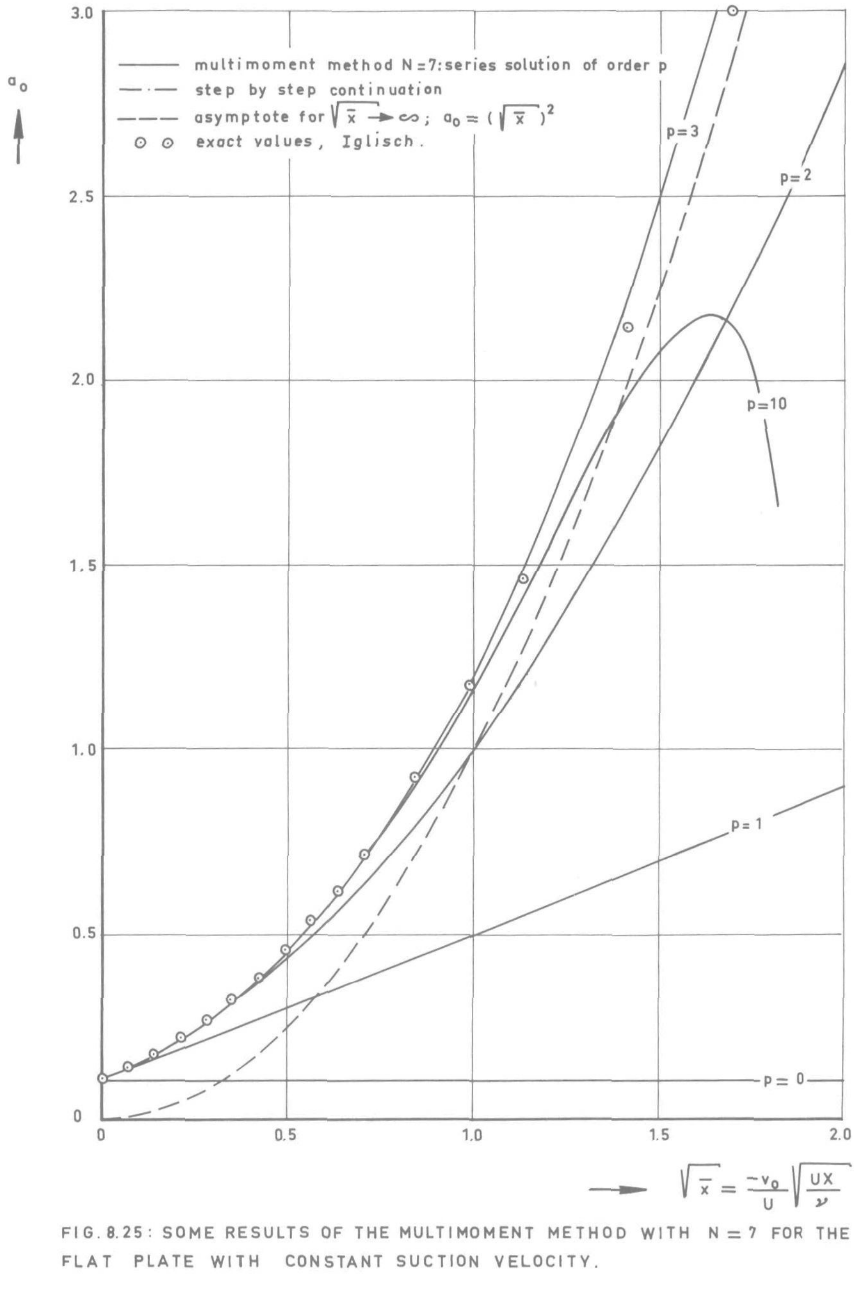

FIG. 8.25: SOME RESULTS OF THE MULTIMOMENT METHOD WITH $N = 7$ FOR THE FLAT PLATE WITH CONSTANT SUCTION VELOCITY.

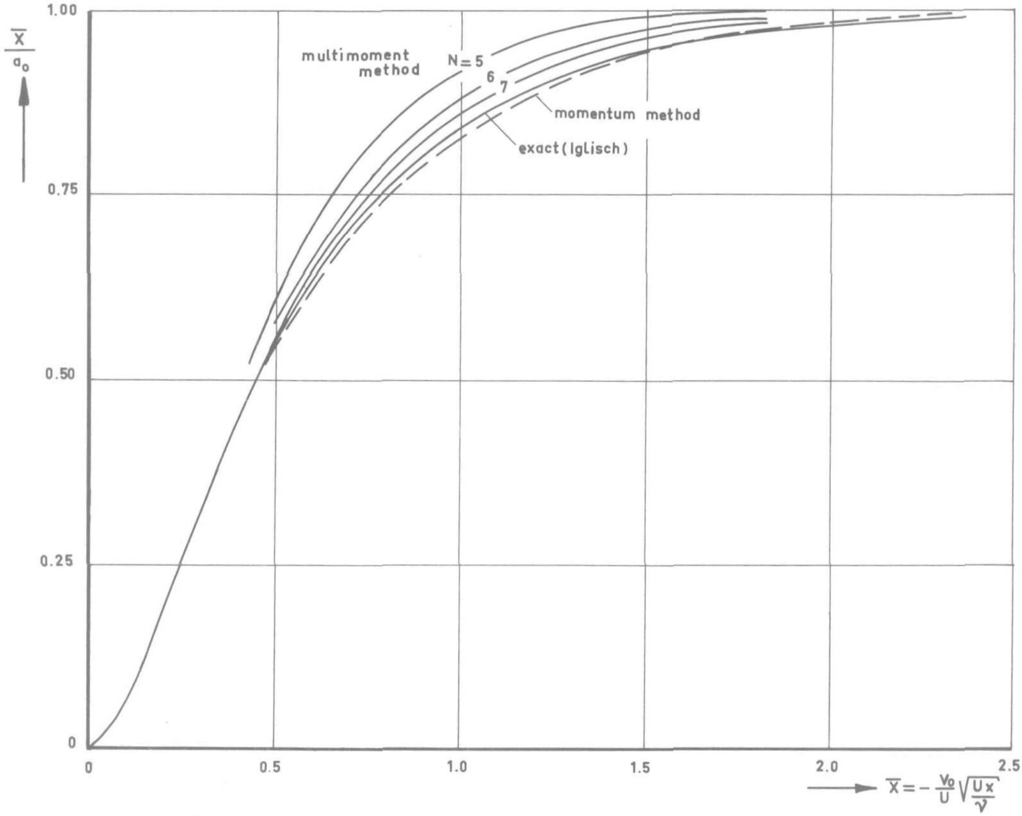

FIG. 8.26 : $\overline{X}/a_o$ FOR THE FLAT PLATE WITH CONSTANT SUCTION VELOCITY.

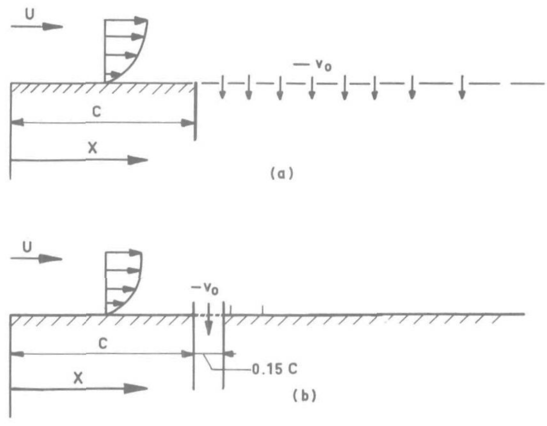

FIG. 8.27: TWO EXAMPLES OF BOUNDARY LAYERS WITH DISCONTINUOUSLY VARYING SUCTION VELOCITY DISCUSSED BY RHEINBOLDT.

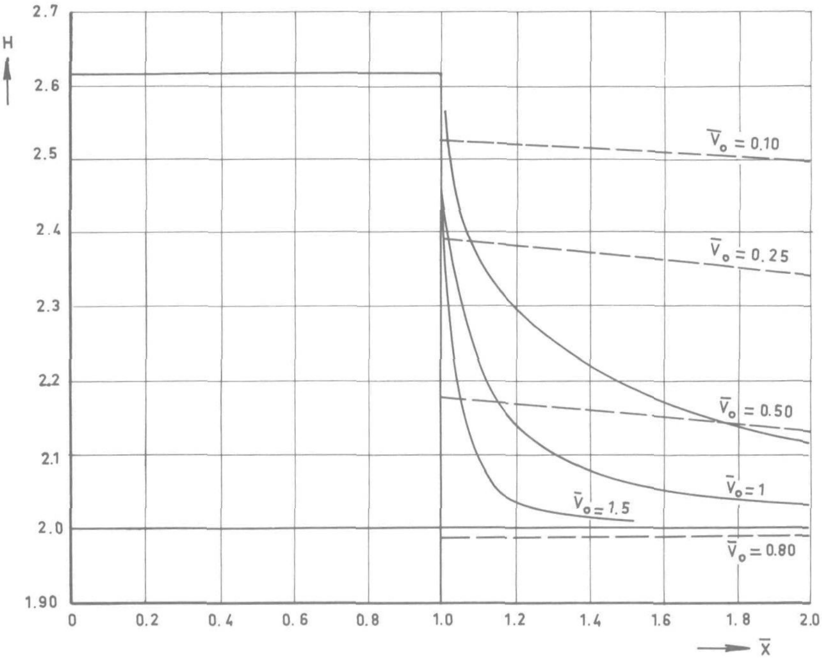

FIG. 8.28 : THE SHAPE FACTOR H FOR RHEINBOLDTS FIRST EXAMPLE ;
——— EXACT ; – – – MULTIMOMENT METHOD.

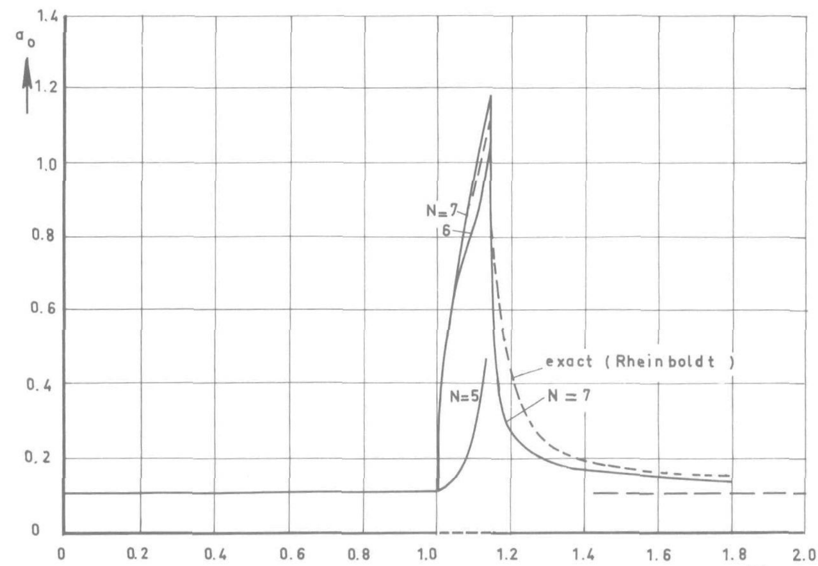

FIG. 8.29: RESULTS OF THE MULTIMOMENT METHOD FOR RHEINBOLDTS SECOND EXAMPLE.

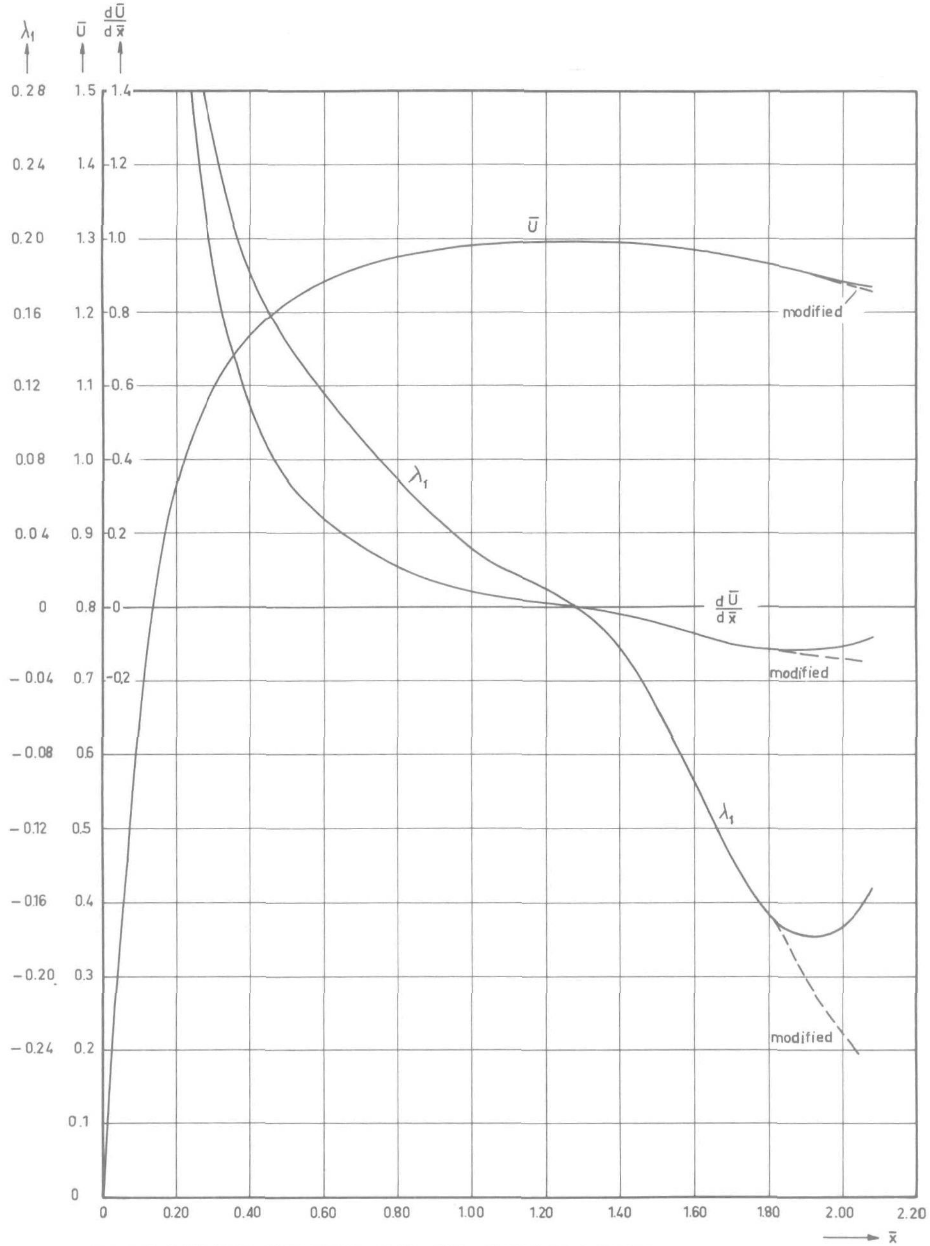

FIG. 8.30: PRESSURE DISTRIBUTION DATA FOR SCHUBAUER'S ELLIPS

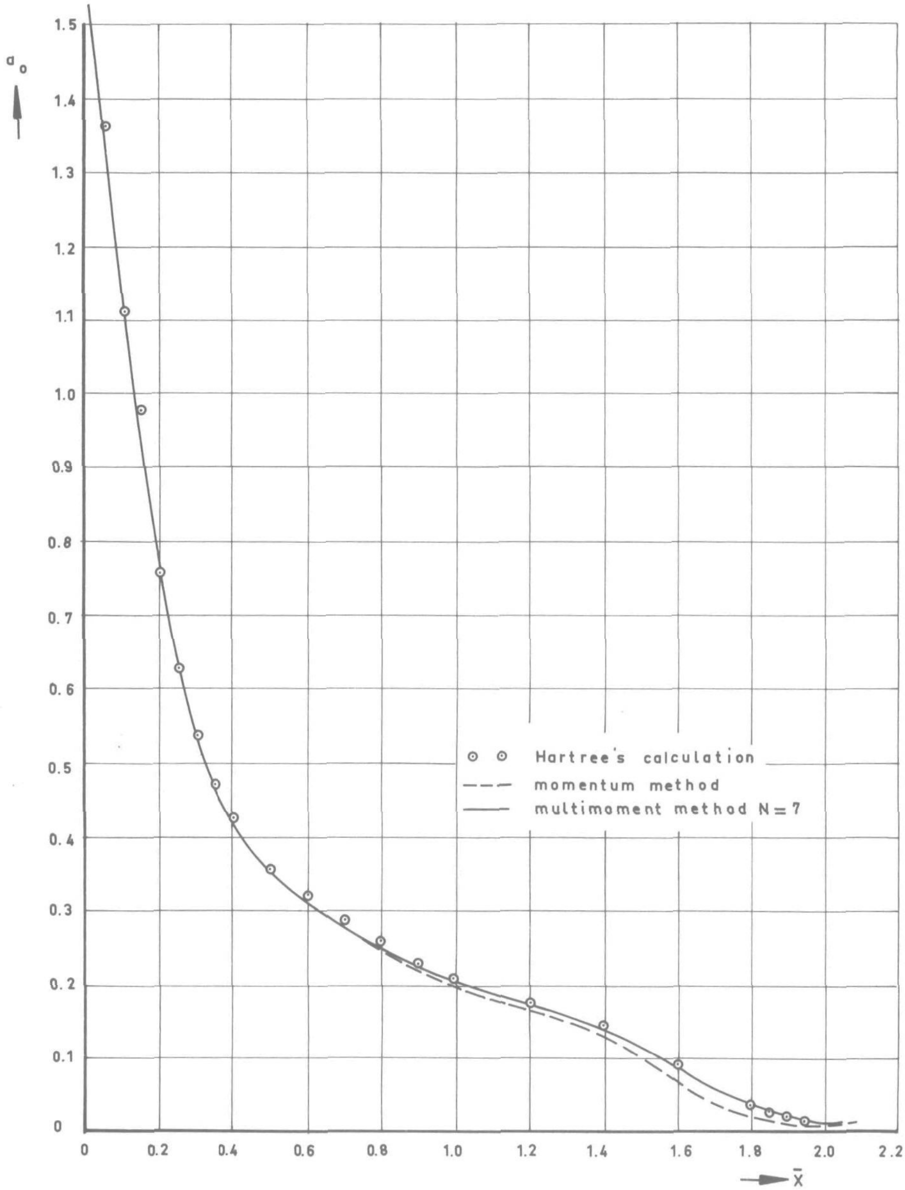

FIG. 8.31: THE WALL SHEAR STRESS PARAMETER a_0 FOR SCHUBAUER'S OBSERVED PRESSURE DISTRIBUTION.

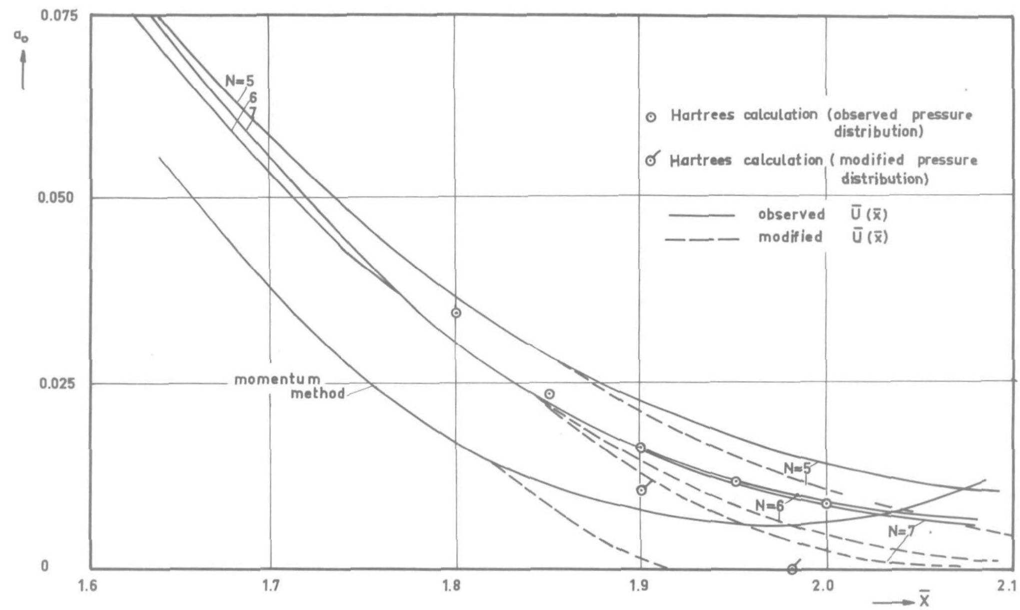

FIG. 8.32: THE SHEAR STRESS PARAMETER a_0 FOR SCHUBAUERS ELLIPTIC CYLINDER; OBSERVED AND MODIFIED PRESSURE DISTRIBUTION

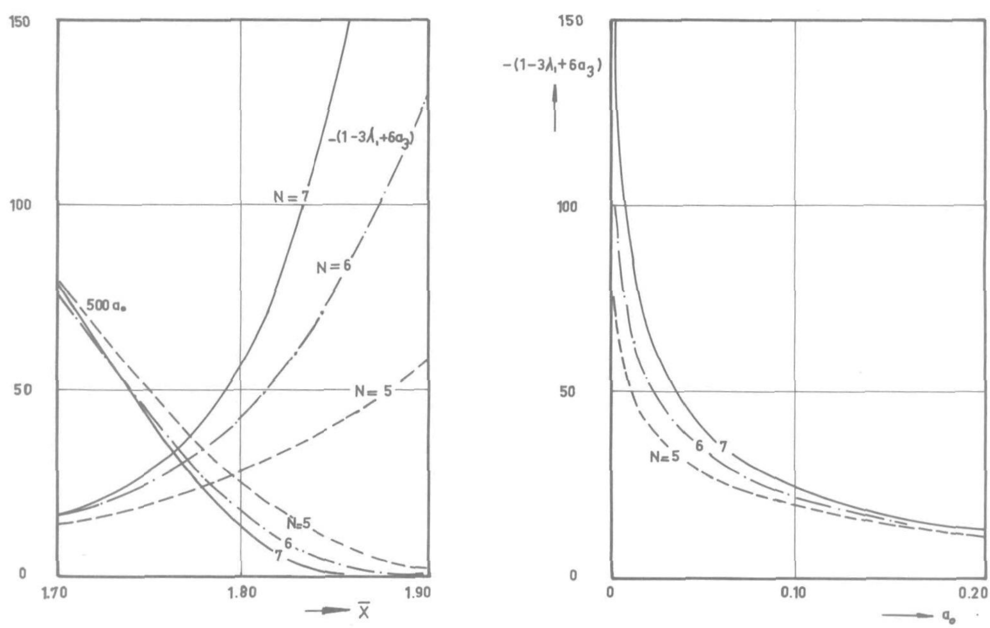

FIG. 8.33: BEHAVIOUR OF THE MULTIMOMENT METHOD NEAR SEPARATION FOR $\bar{U} = \sin \bar{x}$.

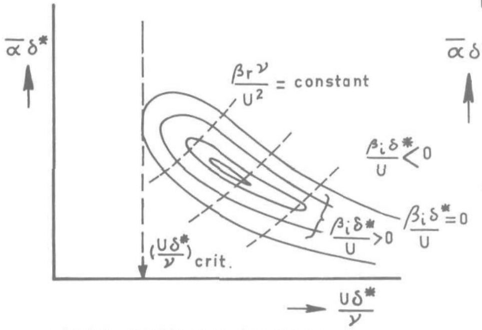

FIG. 9.1: STABILITY DIAGRAM

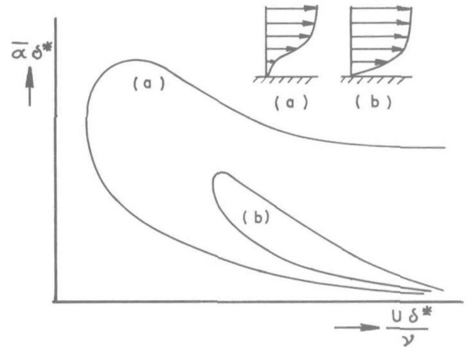

FIG. 9.2: INFLUENCE OF SHAPE OF VELOCITY PROFILE ON STABILITY DIAGRAM

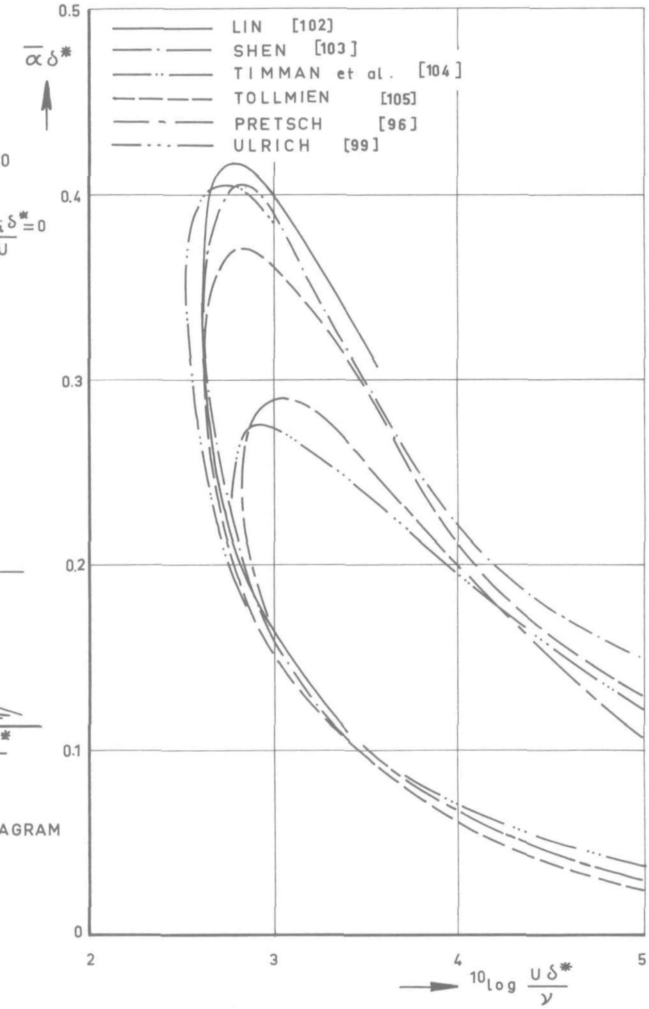

FIG. 9.3: NEUTRAL STABILITY CURVES FOR THE FLAT PLATE WITHOUT SUCTION FROM DIFFERENT SOURCES.

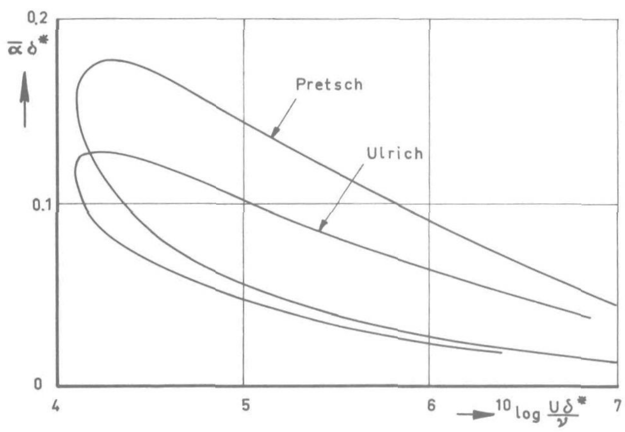

FIG. 9.4: NEUTRAL STABILITY CURVES FOR THE PLANE STAGNATION POINT WITHOUT SUCTION.

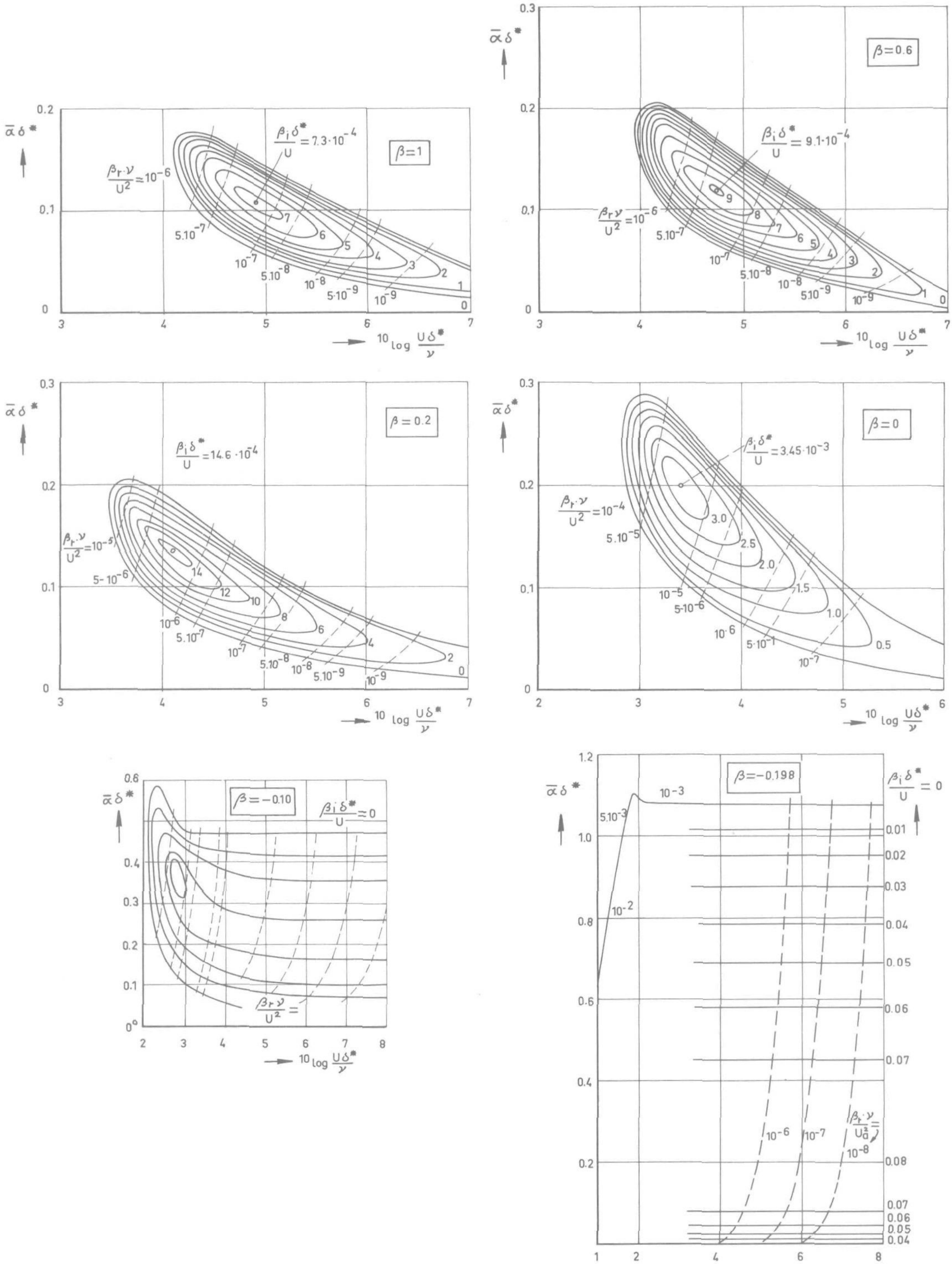

FIG. 9.5: PRETSCH'S DIAGRAMS FOR SOME HARTREE PROFILES.

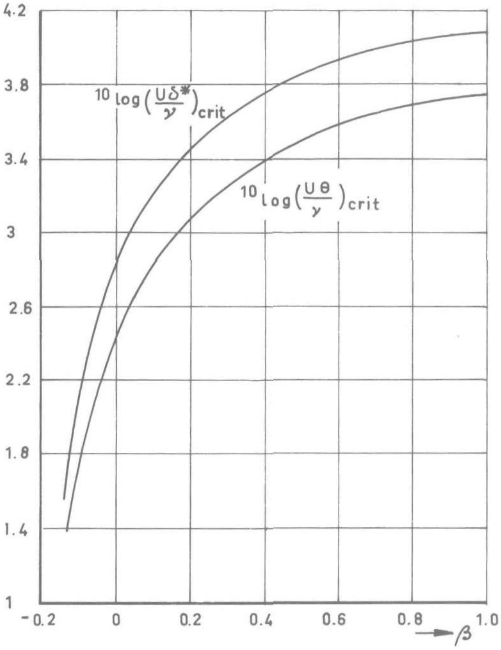

FIG. 9.6: CRITICAL REYNOLDS NUMBERS FOR THE HARTREE PROFILES ACCORDING TO PRETSCH.

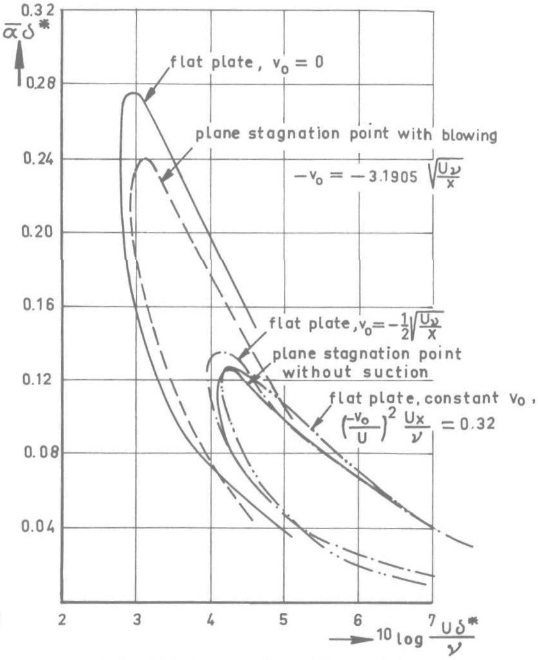

FIG. 9.8: SOME NEUTRAL STABILITY CURVES FOR DIFFERENT BOUNDARY LAYERS ACCORDING TO ULRICH.

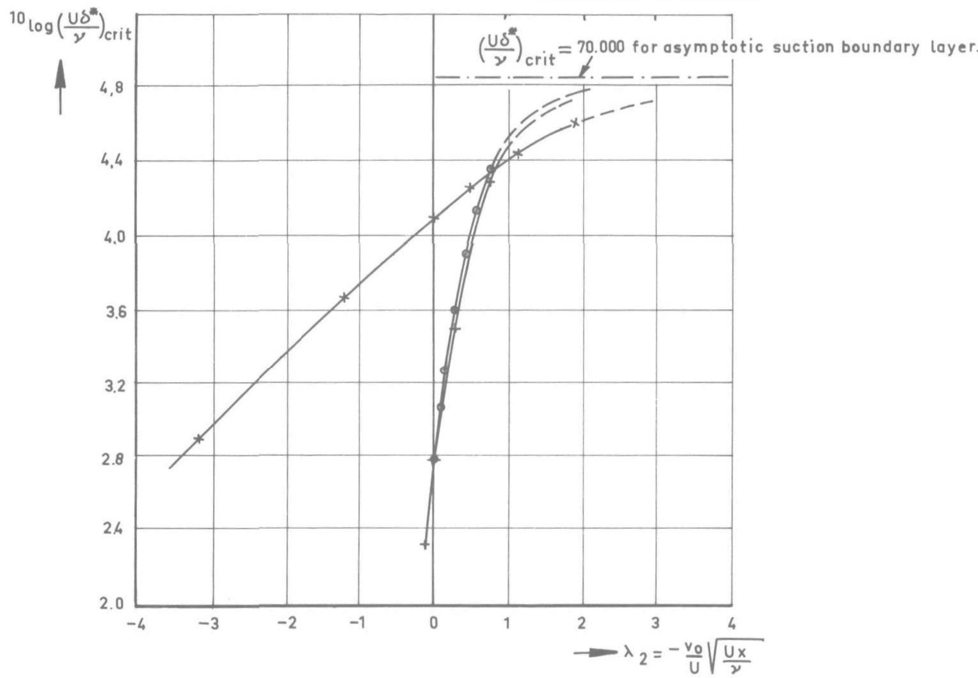

FIG. 9.7: CRITICAL REYNOLDSNUMBERS FOR SOME BOUNDARY LAYER FLOWS WITH SUCTION ACCORDING TO ULRICH

—o— flat plate, v_0 constant

—+— flat plate, $v_0 \sim X^{-1/2}$

—x— plane stagnation point, v_0 constant.

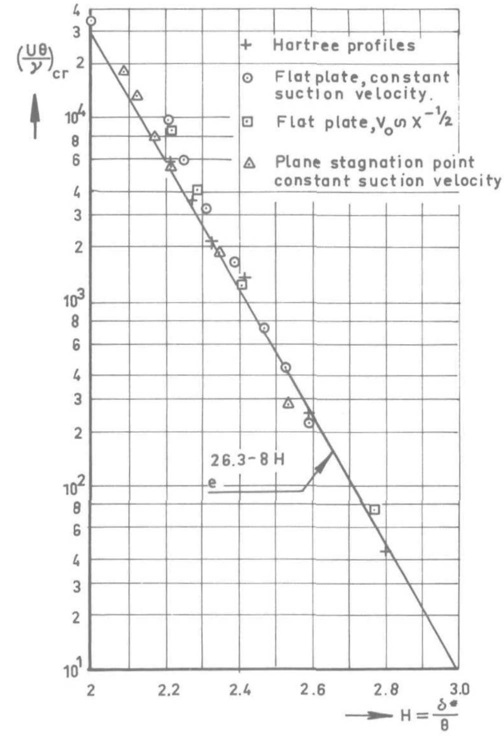

FIG. 9.9 : $\left(\frac{U\theta}{\nu}\right)_{crit}$ FOR SOME BOUNDARY LAYERS WITH AND WITHOUT SUCTION.

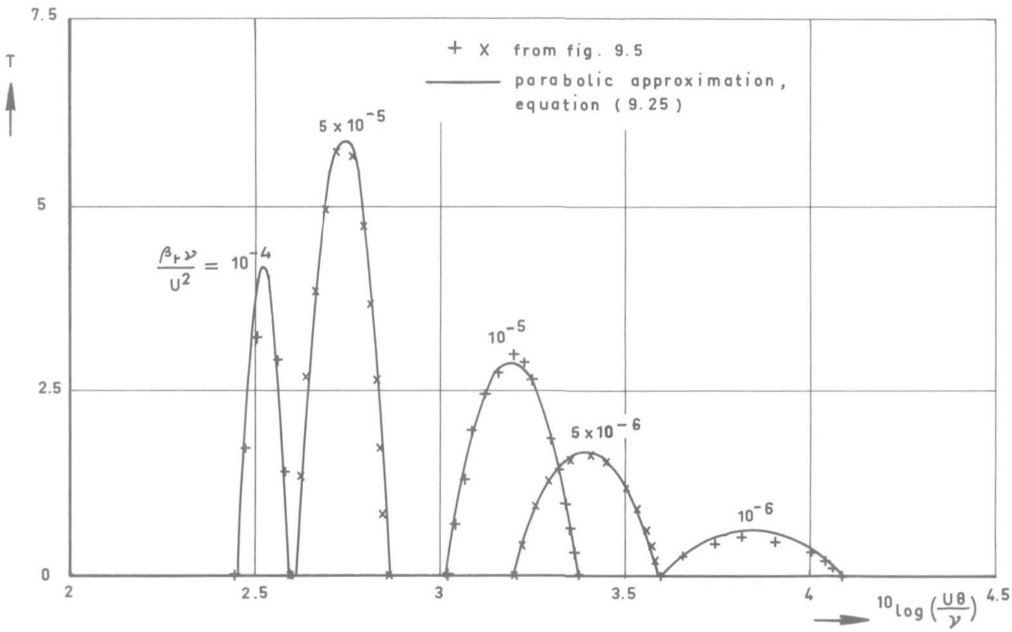

FIG. 9.10: THE FUNCTION T FOR $\beta = 0$ AS DEFINED BY EQUATION (9.17)

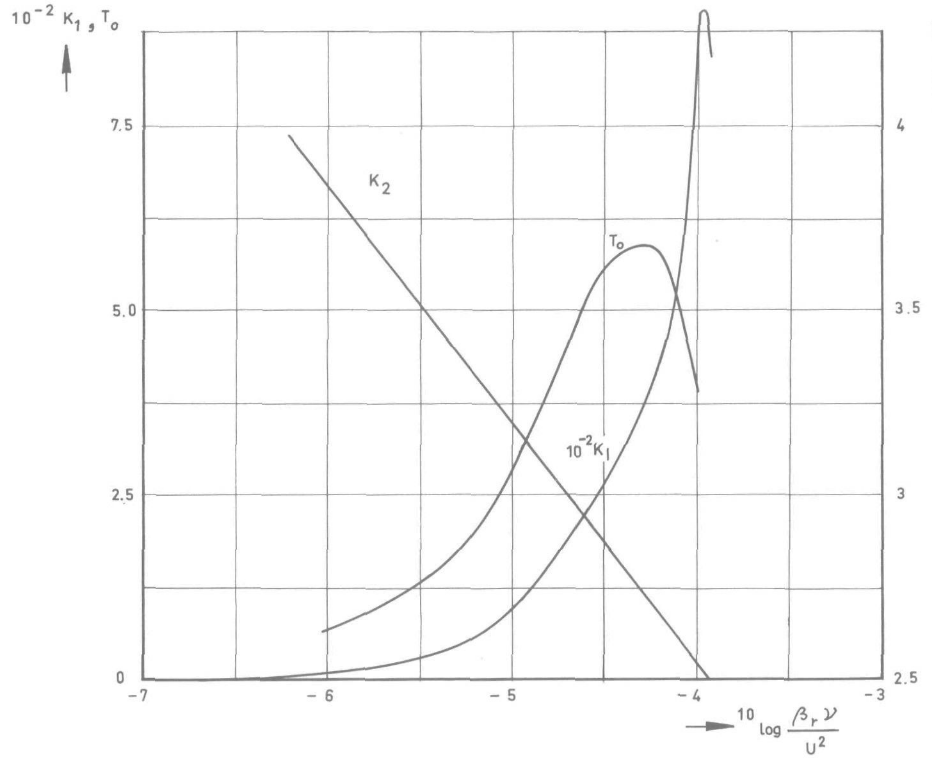

FIG. 9.11: COEFFICIENTS IN EQUATION (9.25) FOR $\beta = 0$.

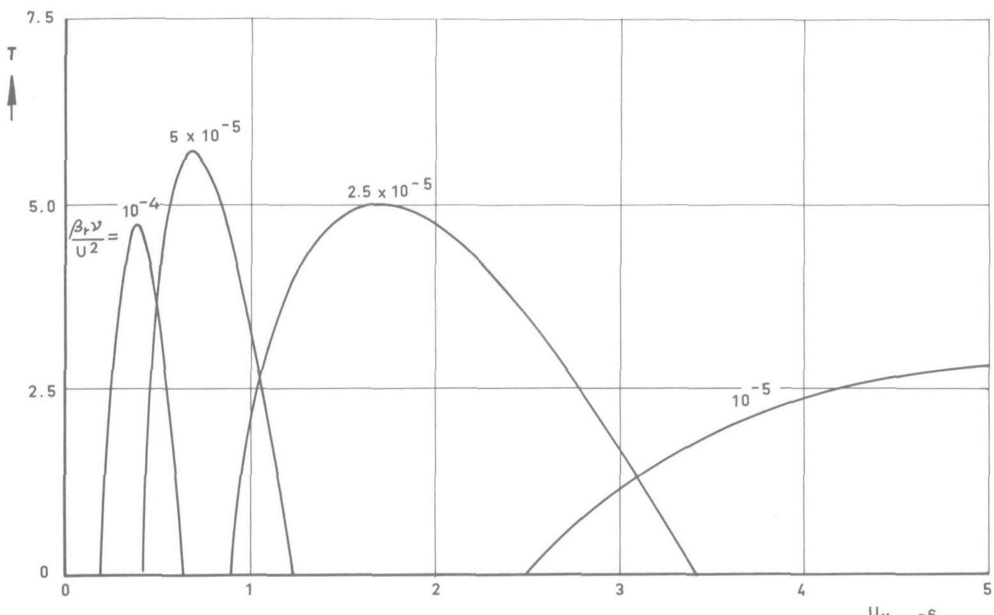

FIG. 9.12 : AMPLIFICATION RATE T FOR THE FLAT PLATE ($\beta = 0$)

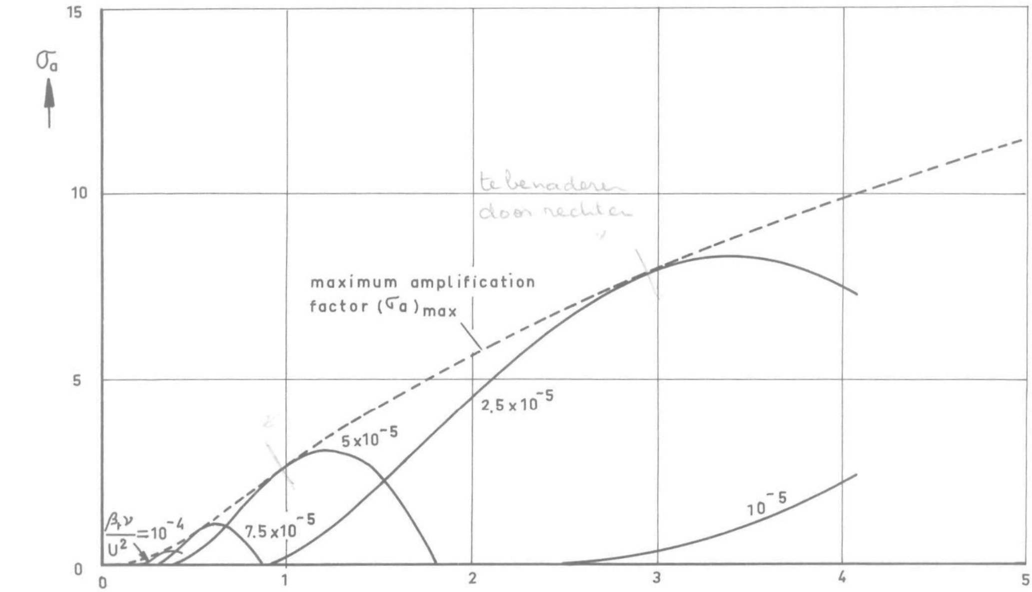

FIG. 9.13: AMPLIFICATION FACTOR σ_a FOR THE FLAT PLATE ($\beta = 0$)

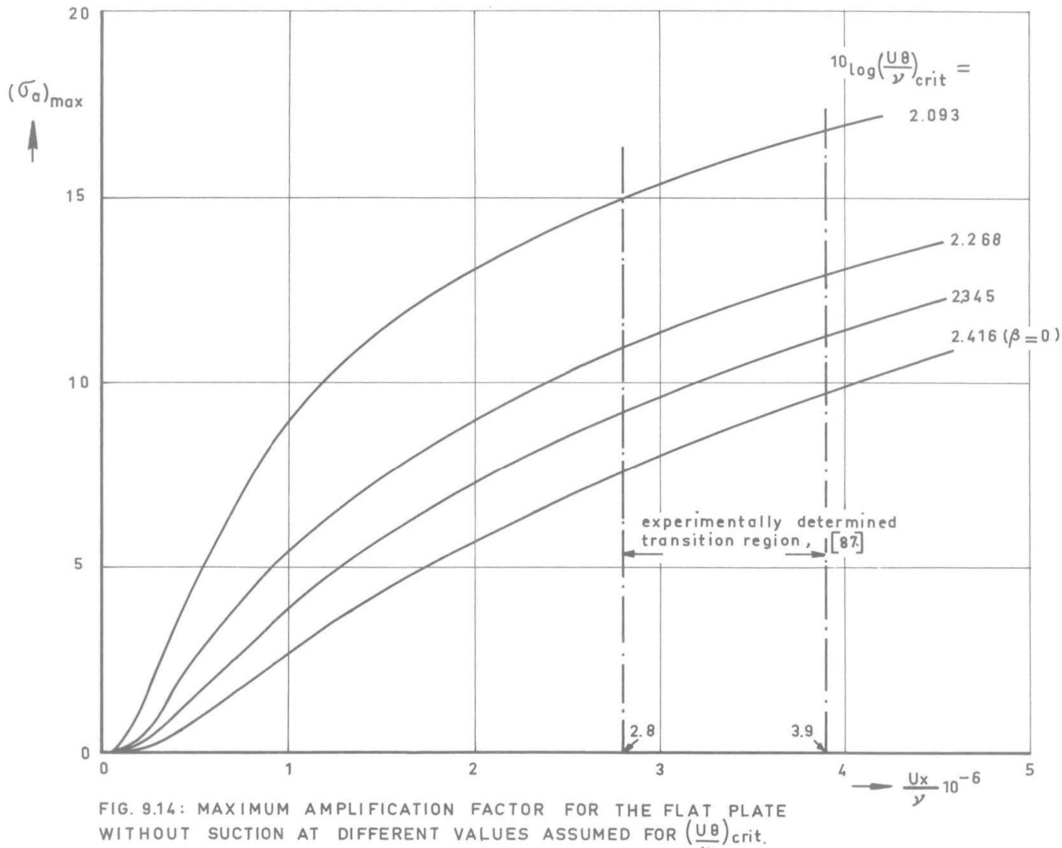

FIG. 9.14: MAXIMUM AMPLIFICATION FACTOR FOR THE FLAT PLATE WITHOUT SUCTION AT DIFFERENT VALUES ASSUMED FOR $\left(\frac{U\theta}{\nu}\right)_{crit}$.

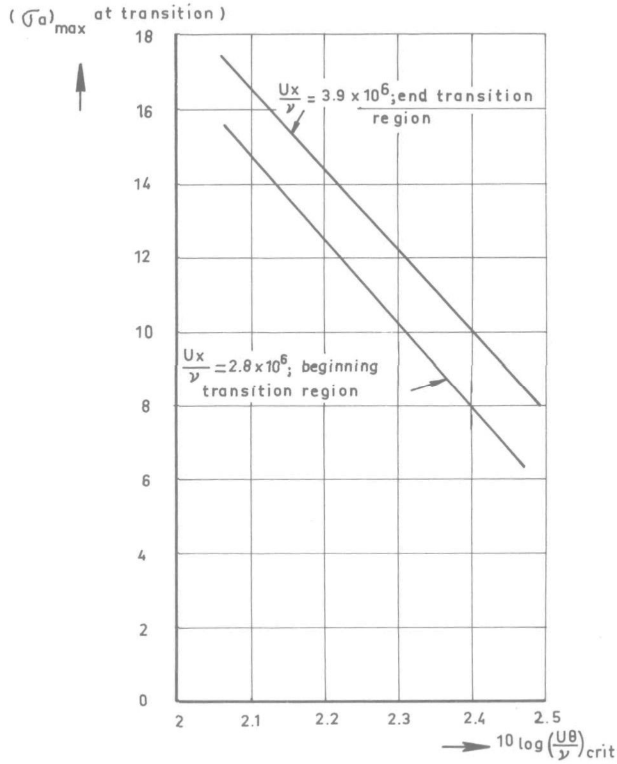

FIG. 9.15 : CROSS PLOT FROM FIG. 9.14.

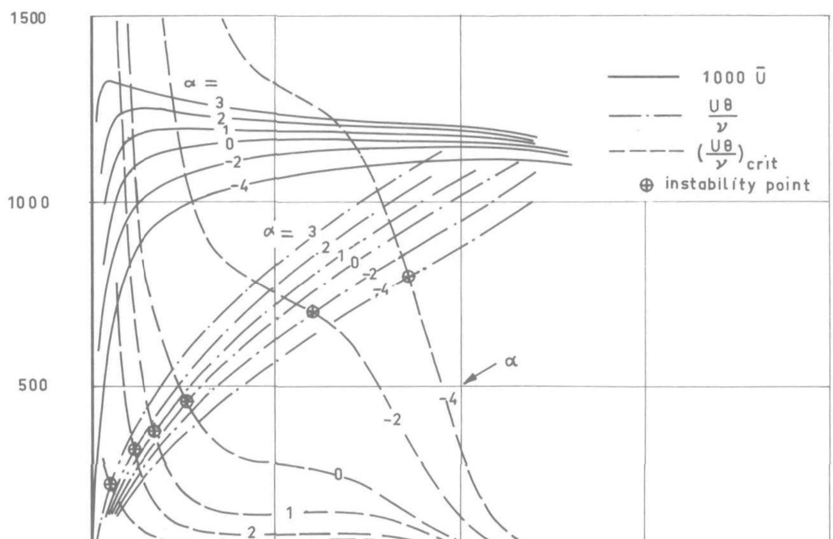

FIG. 9.16 : RESULTS OF THE MOMENTUM METHOD FOR THE EC 1440 AIRFOIL SECTION; $R_c = 4.35 \times 10^6$.

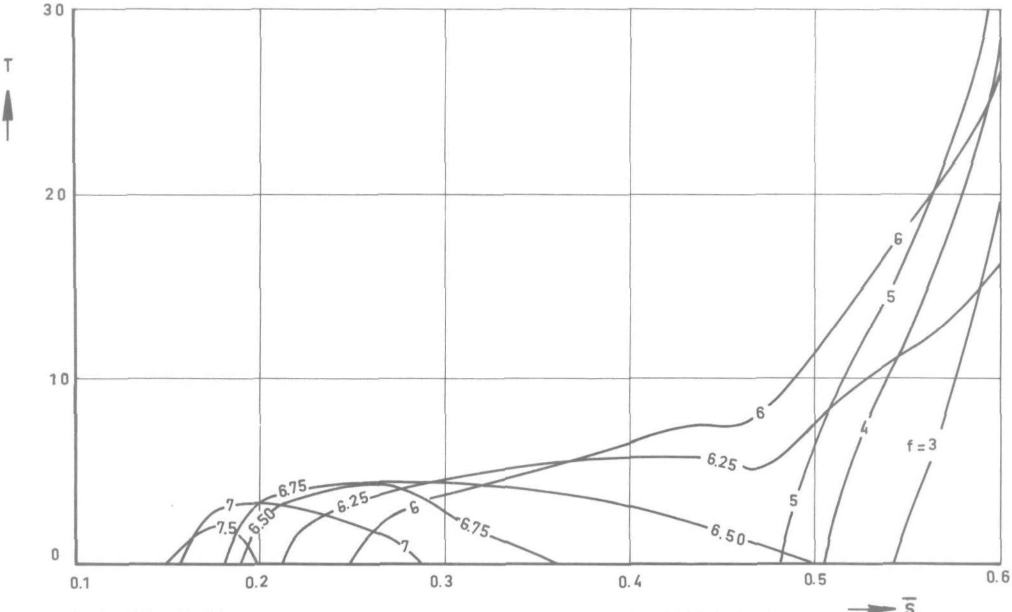

FIG. 9.17: AMPLIFICATION RATE T FOR DIFFERENT FREQUENCES f ;
EC 1440 AIRFOIL SECTION ; $\alpha = 0$, $R_c = 4.35 \times 10^6$.

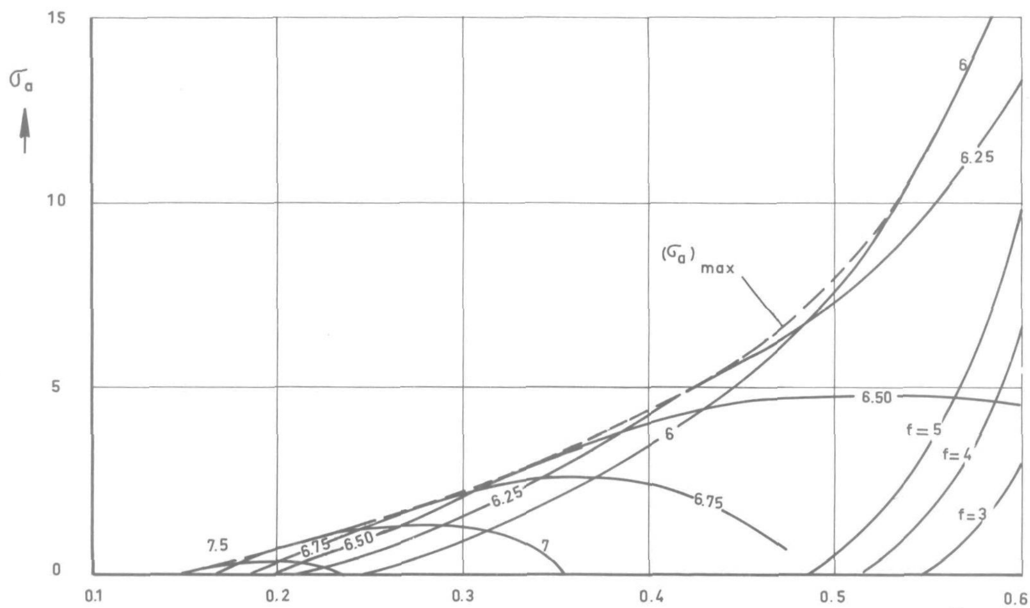

FIG. 9.18: AMPLIFICATION FACTOR FOR DIFFERENT FREQUENCES f;
EC 1440 AIRFOIL SECTION; $\alpha = 0$, $R_c = 4.35 \times 10^6$.

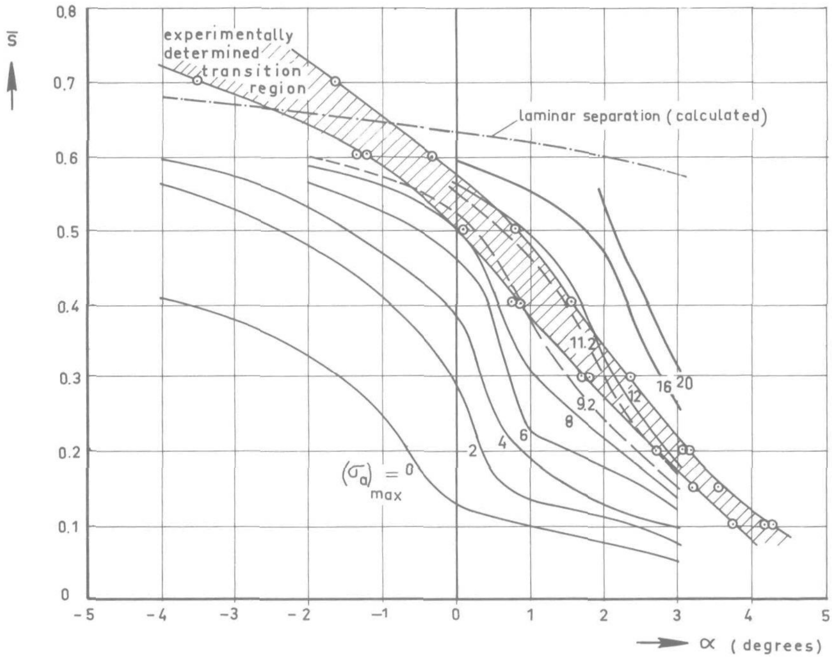

FIG. 9.19: CALCULATED AMPLIFICATION FACTOR AND MEASURED TRANSITION REGION FOR THE EC 1440 AIRFOIL SECTION.

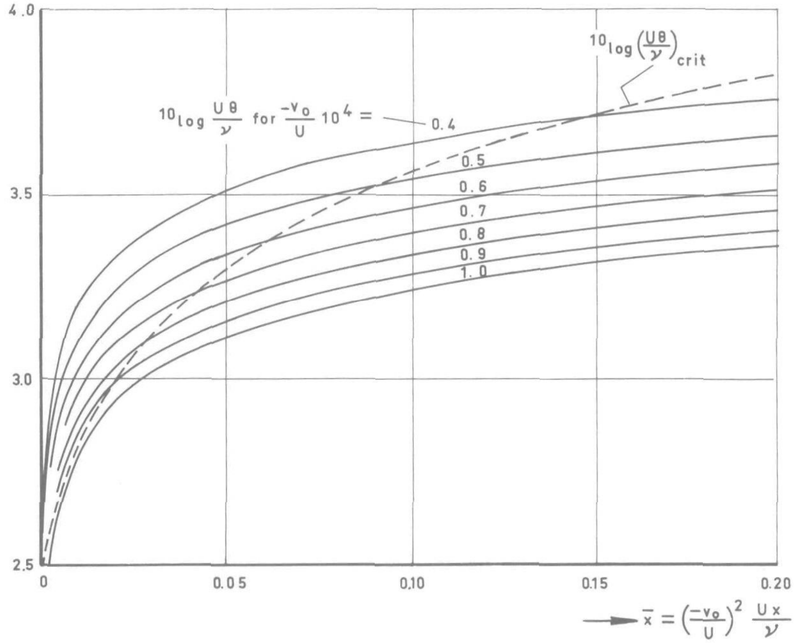

FIG. 9.20: FLAT PLATE WITH CONSTANT SUCTION VELOCITY: $^{10}\log\left(\frac{U\theta}{\nu}\right)_{crit}$ AND $^{10}\log \frac{U\theta}{\nu}$ FOR DIFFERENT SUCTION COEFFICIENTS.

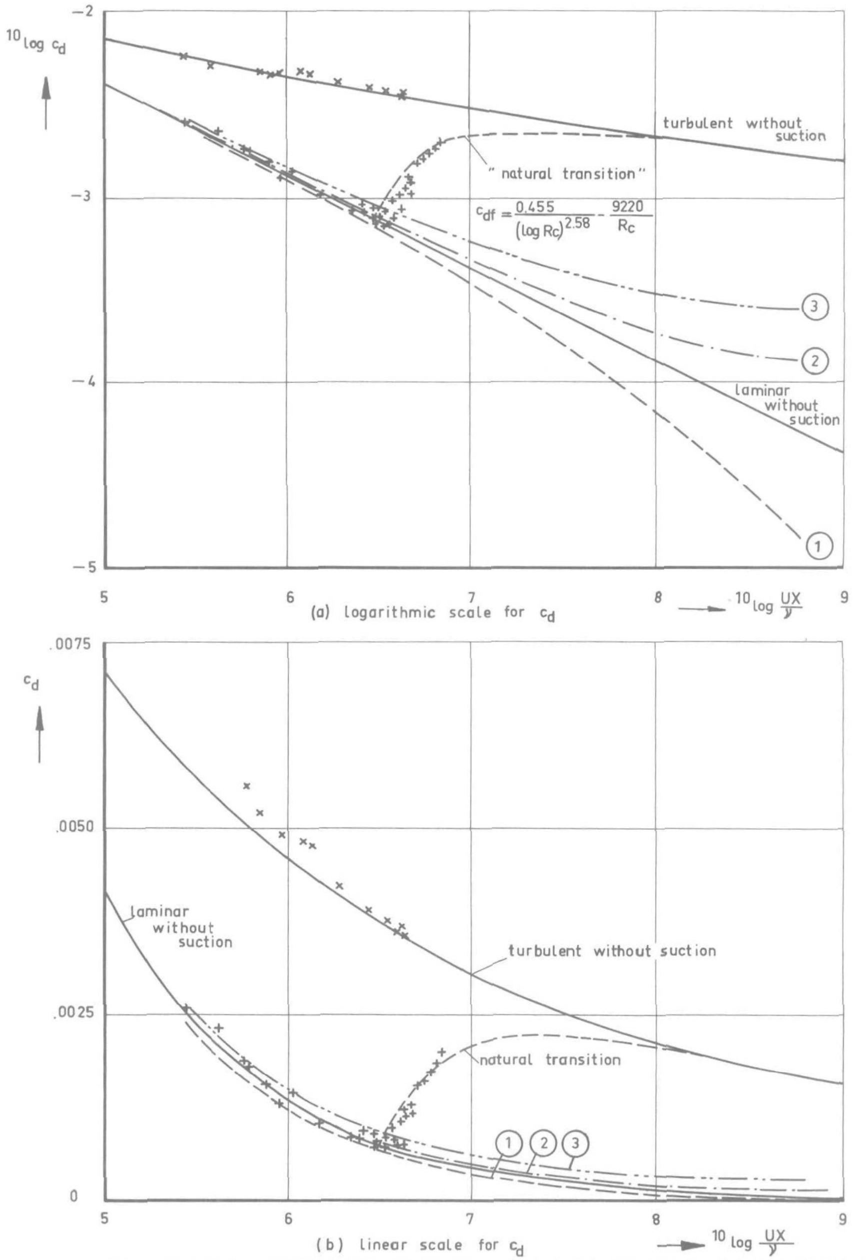

FIG. 9.21: DRAG COEFFICIENT OF FLAT PLATE WITH CONSTANT SUCTION VELOCITY

+	experimental results, smooth plate	no suction
X	" " , trip wire near leading edge	no suction
——	turbulent without suction, Schlichting, $c_{df} = \frac{0.455}{(\log Rc)^{2.58}}$	
——	laminar without suction, Blasius, $c_{df} = 1.328 \left(\frac{UX}{\nu}\right)^{-0.50}$	
1 – – –	laminar, $c_q = \frac{-V_0}{U} = 1.18 \times 10^{-4}$, wake drag only, $c_d = 2\frac{\theta}{X}$	
2 —·—	" " , wake drag + ideal suction drag $c_d = 2\frac{\theta}{X} + c_q$	
3 —··—	" " , friction drag, $c_{df} = 2\frac{\theta}{X} + 2c_q$	

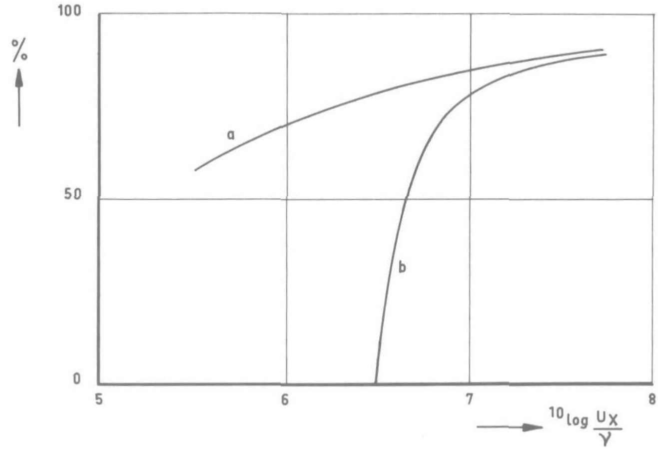

FIG. 9.22: REDUCTION OF TOTAL DRAG FOR THE FLAT PLATE WITH CONSTANT SUCTION VELOCITY ; $\frac{-v_0}{U} = 1.18 \times 10^{-4}$

(a): WITH RESPECT TO THE FULLY TURBULENT BOUNDARY LAYER WITHOUT SUCTION

(b): WITH RESPECT TO THE BOUNDARY LAYER FOR "NATURAL TRANSITION"

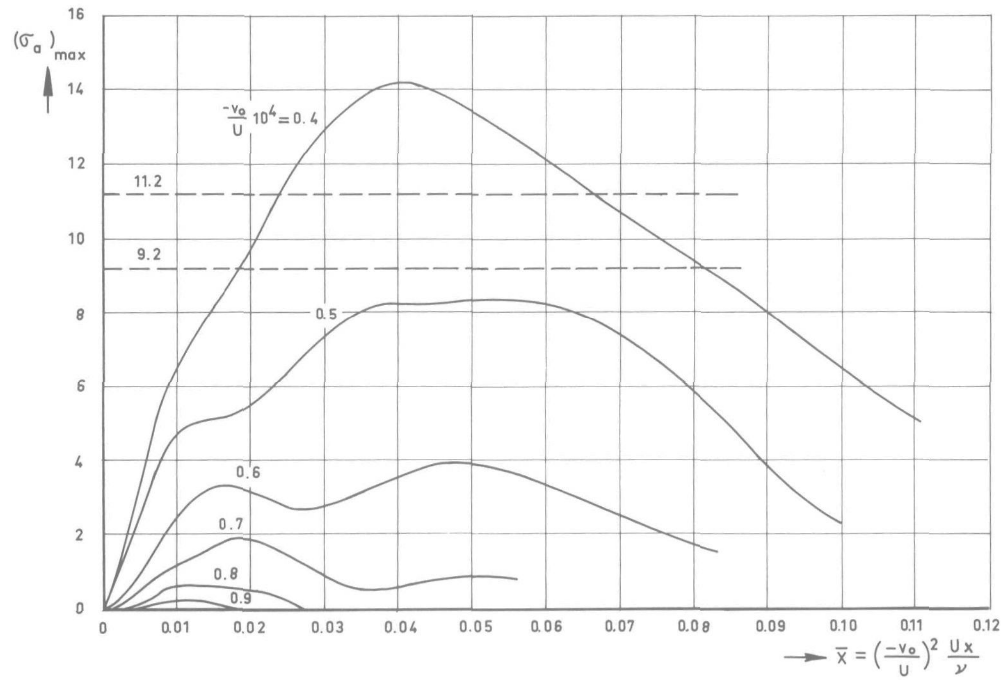

FIG. 9.23: MAXIMUM AMPLIFICATION FACTOR FOR THE FLAT PLATE WITH CONSTANT SUCTION VELOCITY AT DIFFERENT SUCTION FLOW COEFFICIENTS.

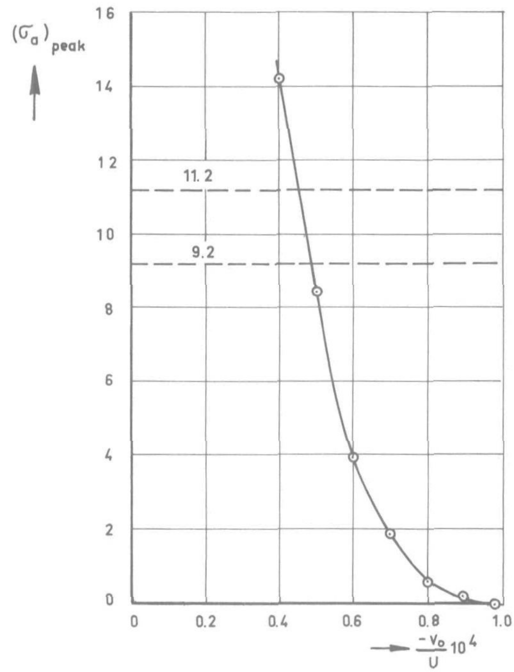

FIG. 9.24 : CROSS PLOT FROM FIG. 9.23; PEAK AMPLIFICATION FACTOR FOR THE FLAT PLATE WITH CONSTANT SUCTION VELOCITY.

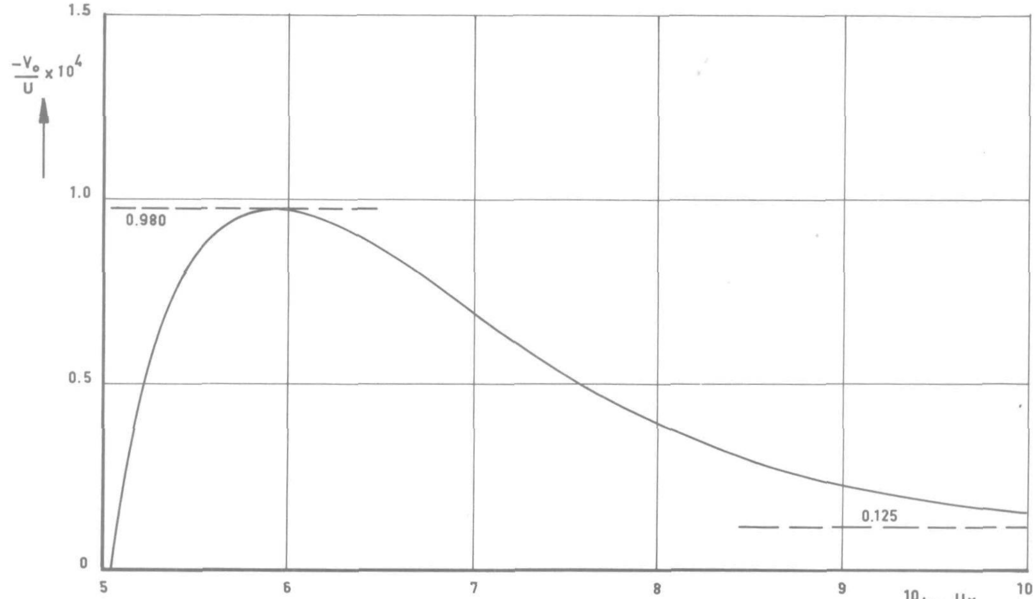

FIG. 9.25 : SUCTION DISTRIBUTION REQUIRED FOR THE FLAT PLATE TO MAINTAIN A NEUTRALLY STABLE BOUNDARY LAYER DOWNSTREAM OF THE INSTABILITY POINT.

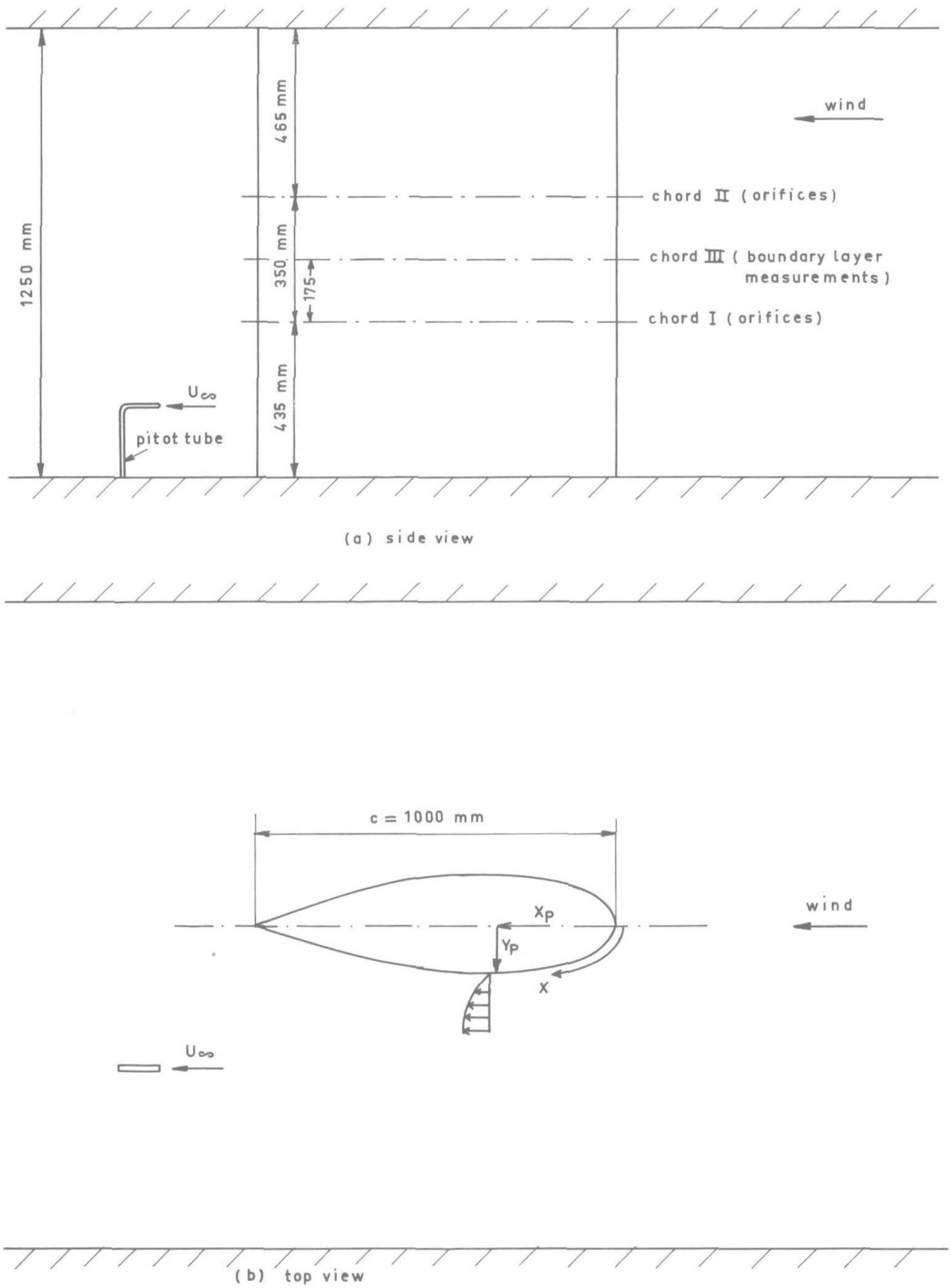

FIG. 10.1 : SET UP OF IMPERVIOUS AIRFOIL SECTION IN WINDTUNNEL

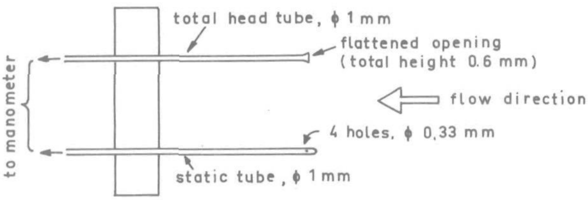

FIG. 10.2: COMBINED TOTAL HEAD- AND STATIC TUBE

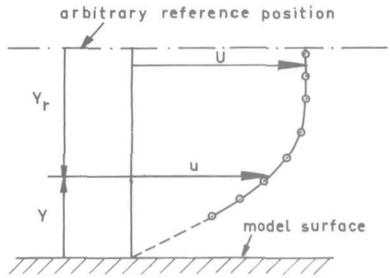

FIG. 10.3: DEFINITIONS USED IN HOT WIRE MEASUREMENTS

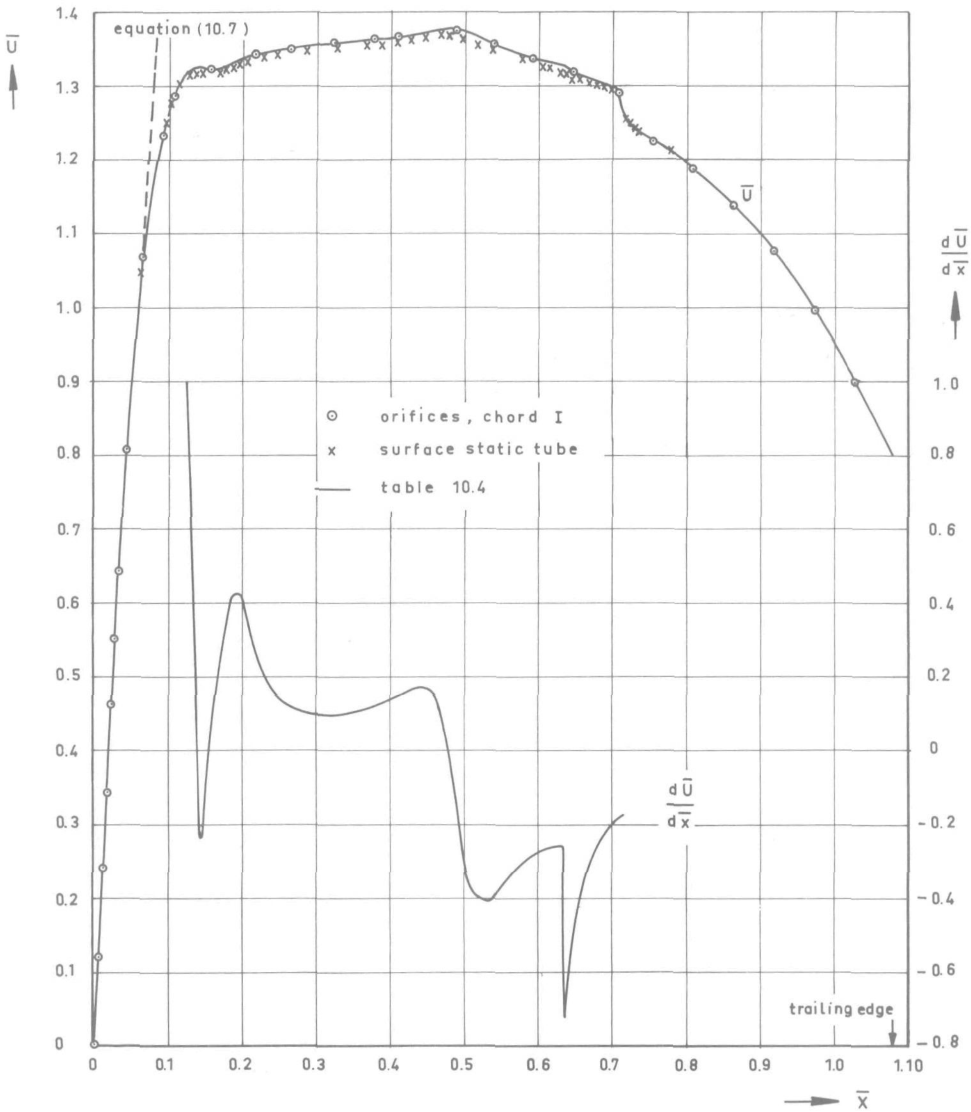

FIG. 10.4: RESULTS OF PRESSURE DISTRUBUTION MEASURUMENTS IN CHORD NUMBER I

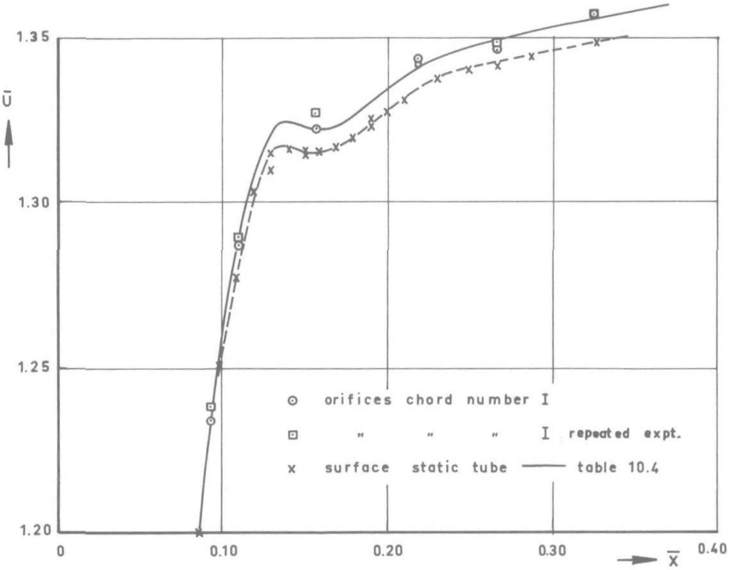

FIG.10.5: $\overline{U}$ ($\overline{x}$) NEAR LEADING EDGE.

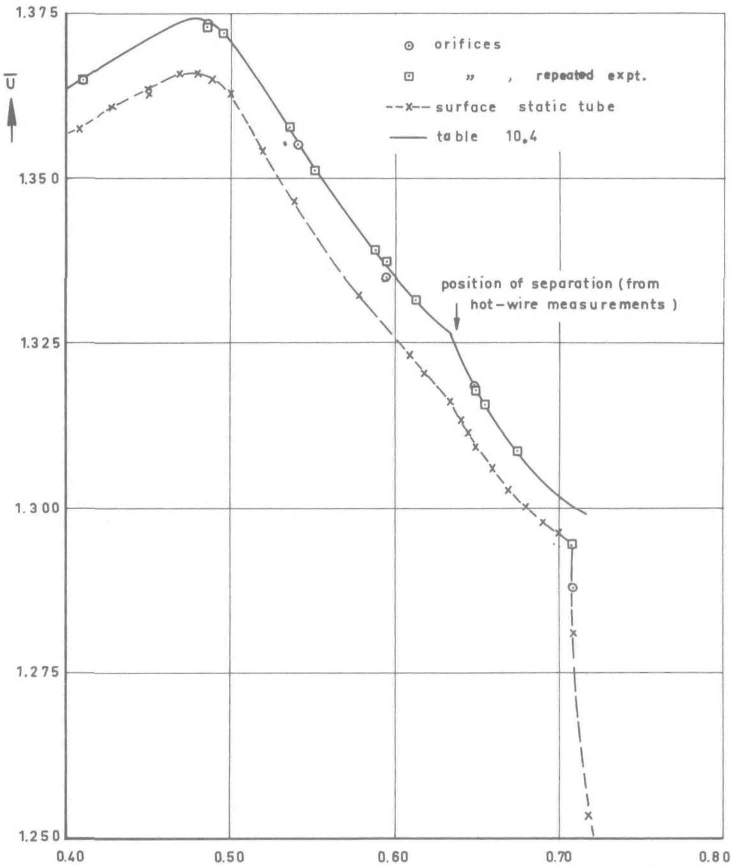

FIG.10.6: $\overline{U}$ ($\overline{x}$) IN REGION OF SEPARATION (CHORD I)

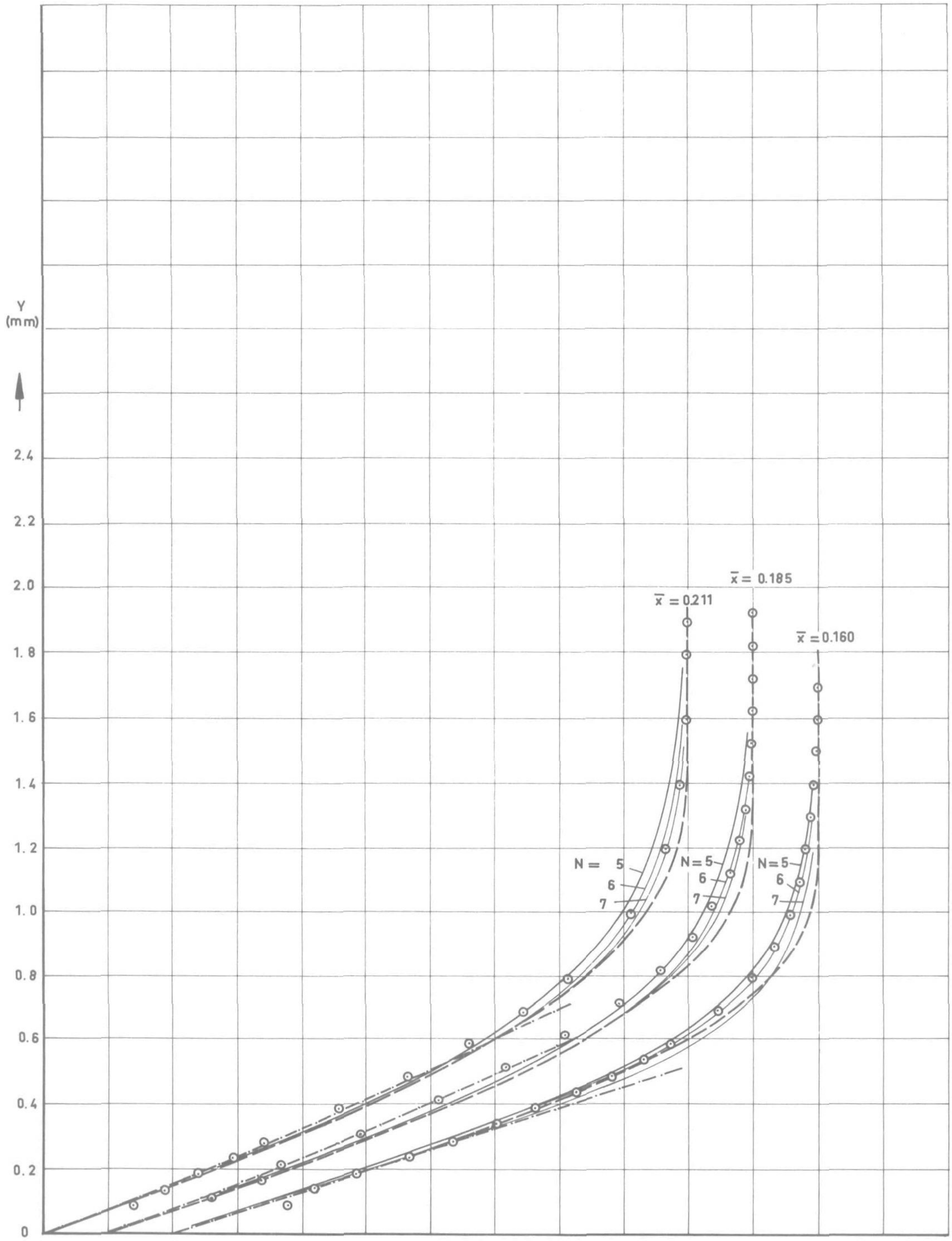

FIG.10.7 A : BOUNDARY LAYER VELOCITY PROFILES FOR THE IMPERVIOUS MODEL ; $\longrightarrow \bar{u}$
(+,⊙ EXPERIMENT, – – – momentum method , ——— multimoment method. , —·—·—·— e.q. (10.4)

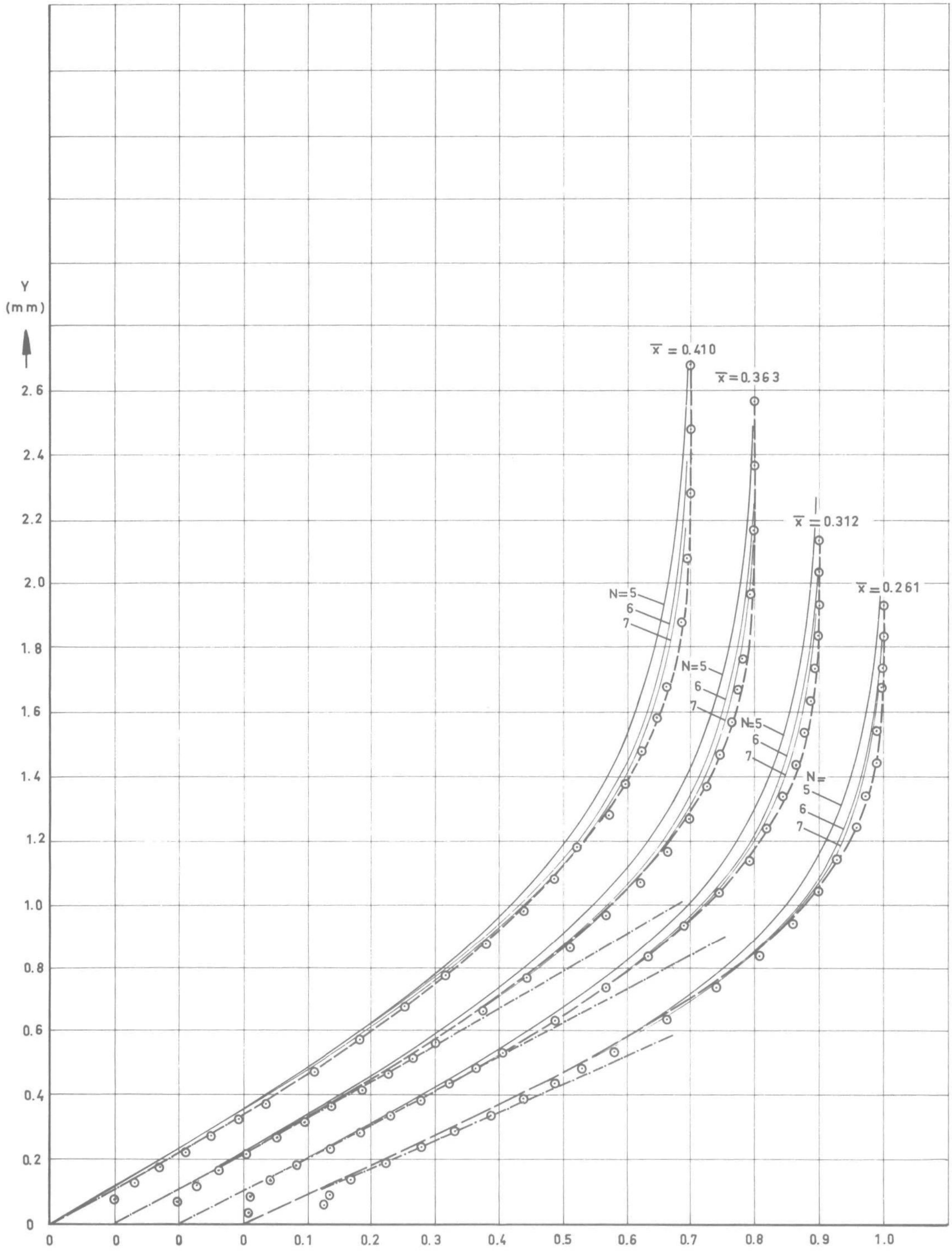

FIG. 10.7 : B CONTINUED

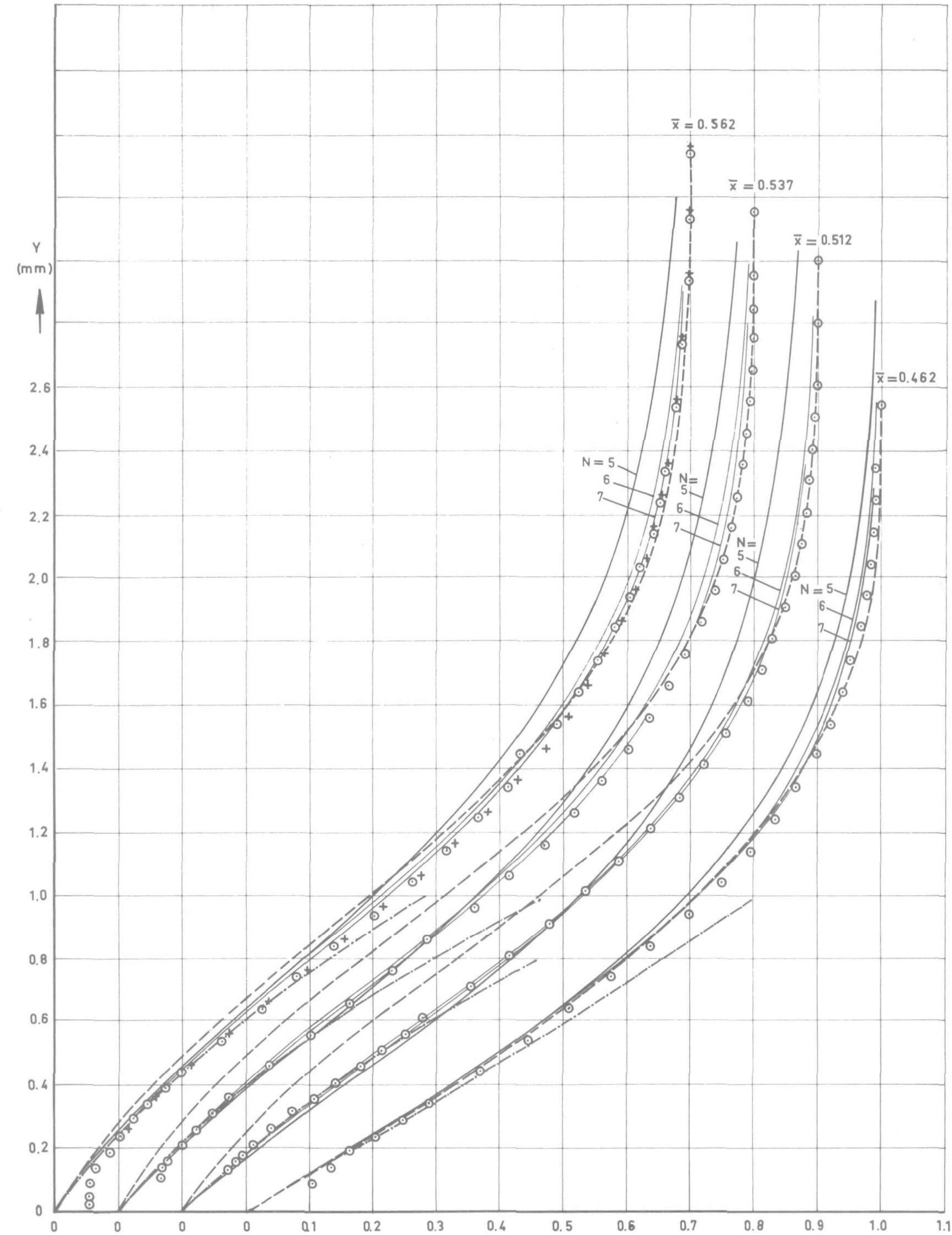

FIG.10.7: C CONTINUED

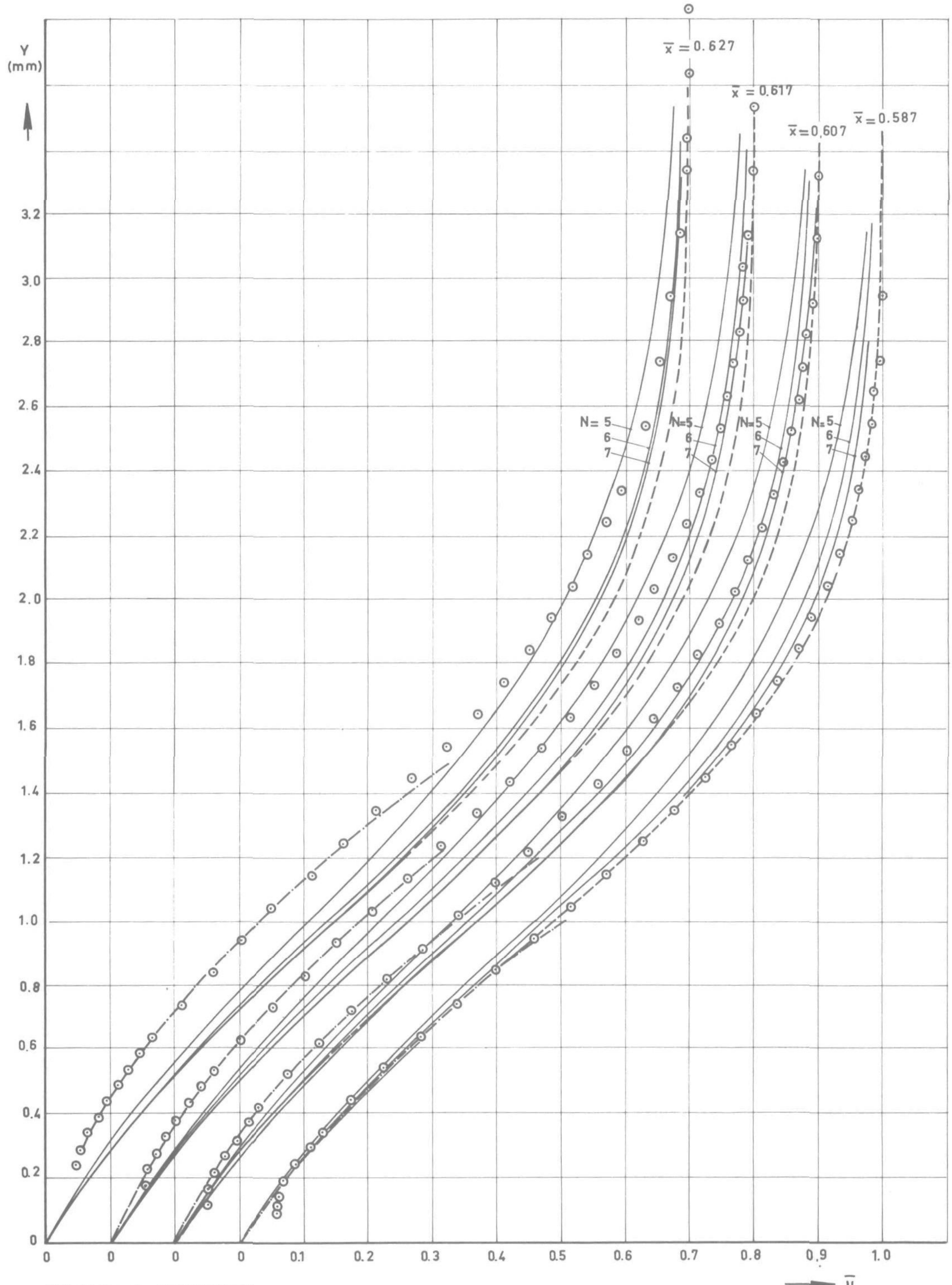

FIG. 10.7 : D CONCLUDED

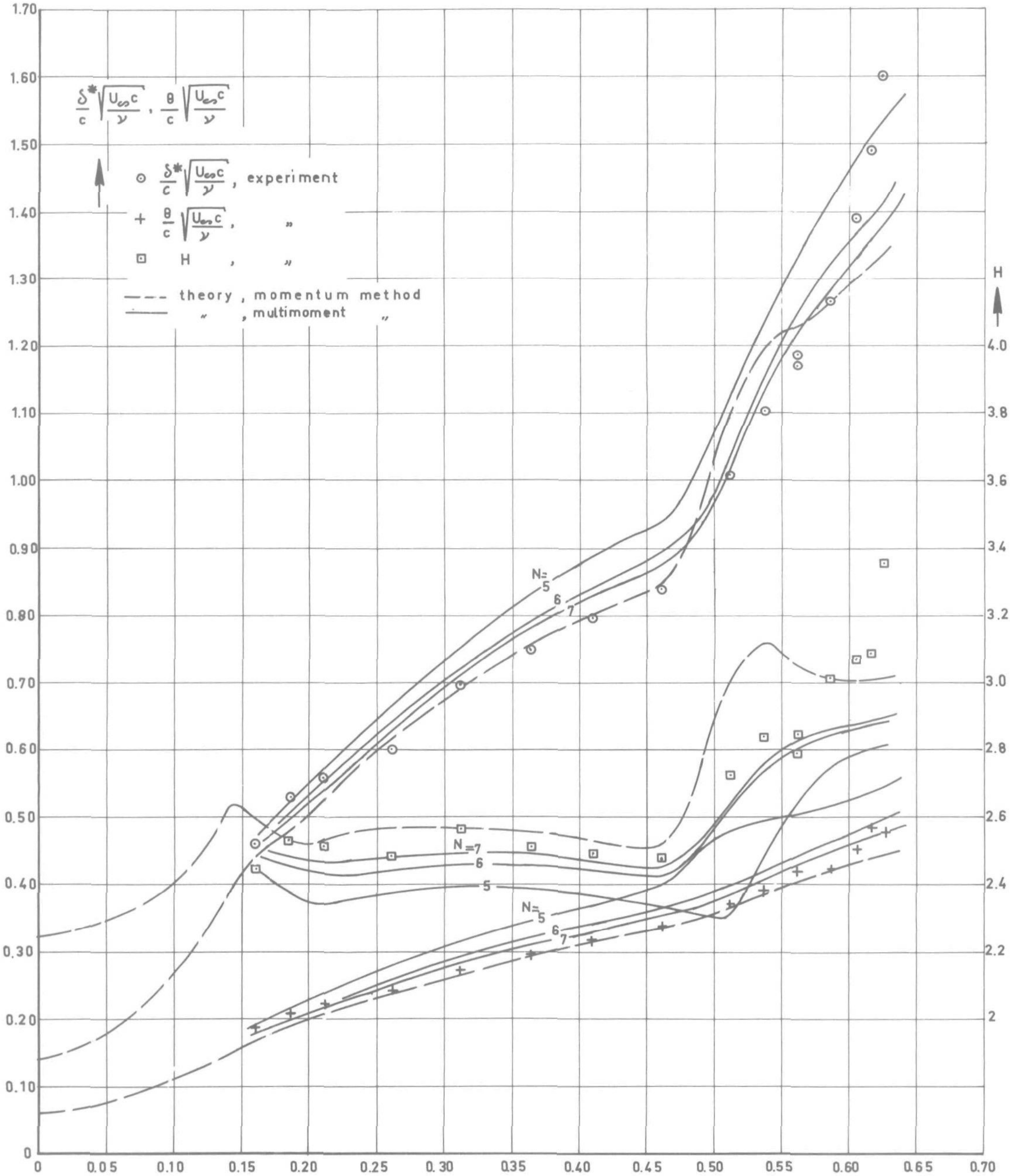

FIG. 10.8: SOME BOUNDARY LAYER PARAMETERS FOR THE IMPERVIOUS AIRFOIL.

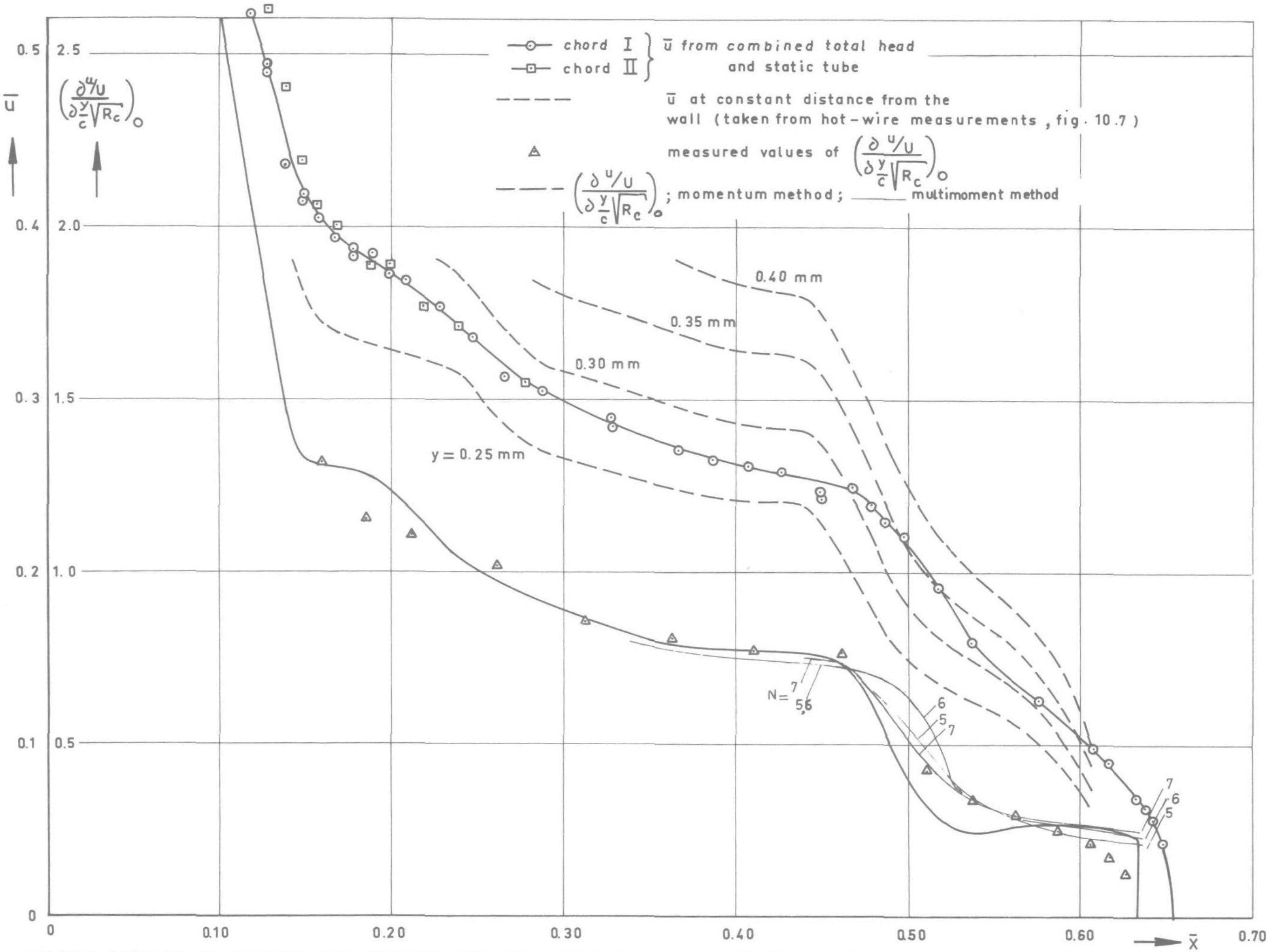

FIG. 10.9: RESULTS OF THEORY AND EXPERIMENT FOR THE WALL SHEAR STRESS; COMPARISON WITH RESULTS OBTAINED FROM THE COMBINED TOTAL HEAD-AND STATIC TUBE.

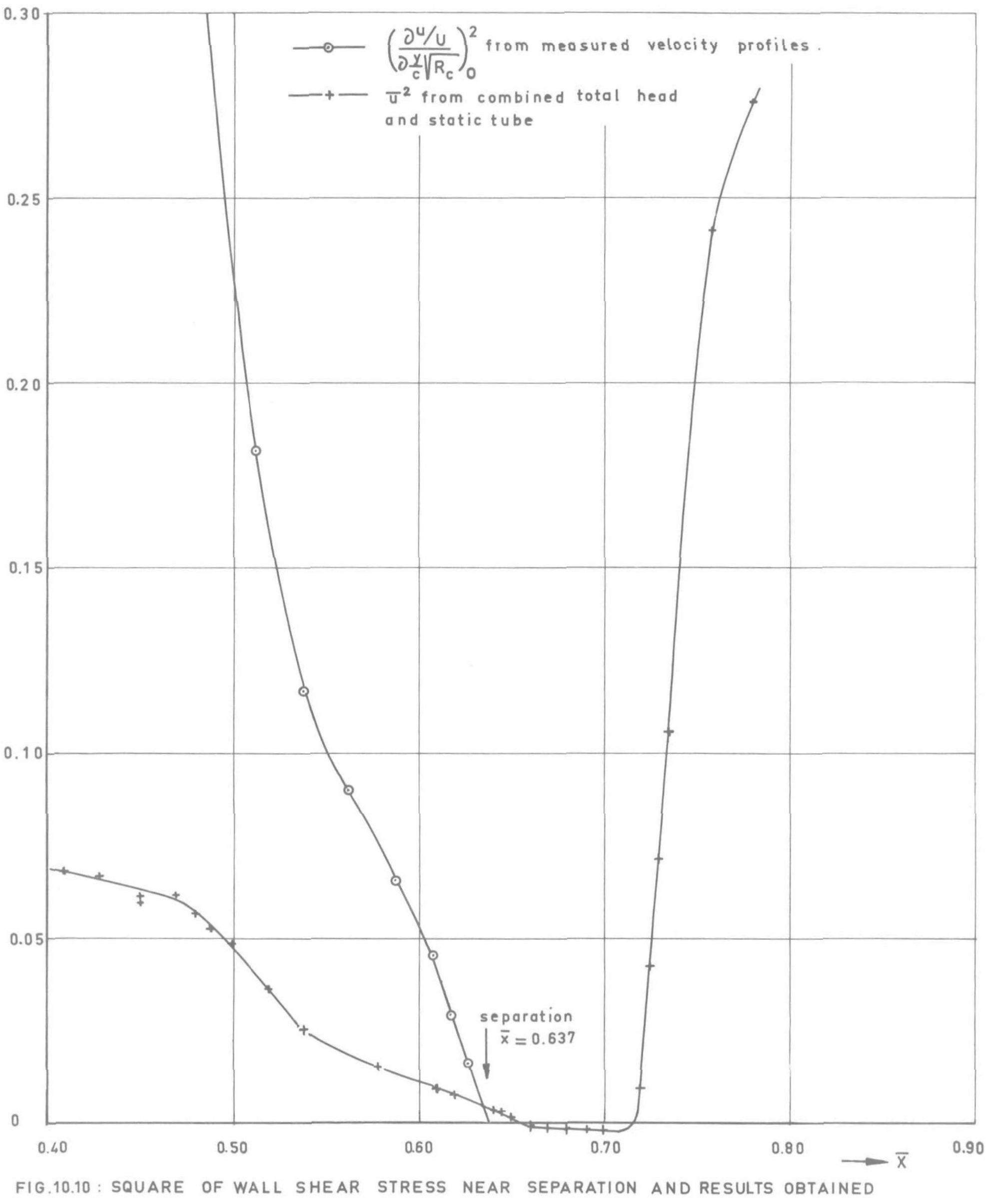

FIG.10.10 : SQUARE OF WALL SHEAR STRESS NEAR SEPARATION AND RESULTS OBTAINED FROM COMBINED TOTAL-HEAD AND STATIC TUBE.

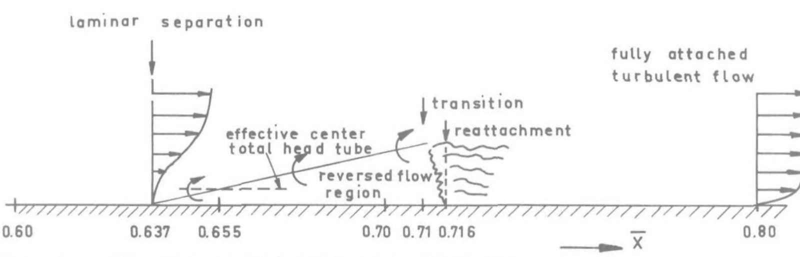

FIG.10.11: SCHEMATIC DESCRIPTION OF FLOW IN SEPARATED REGION.

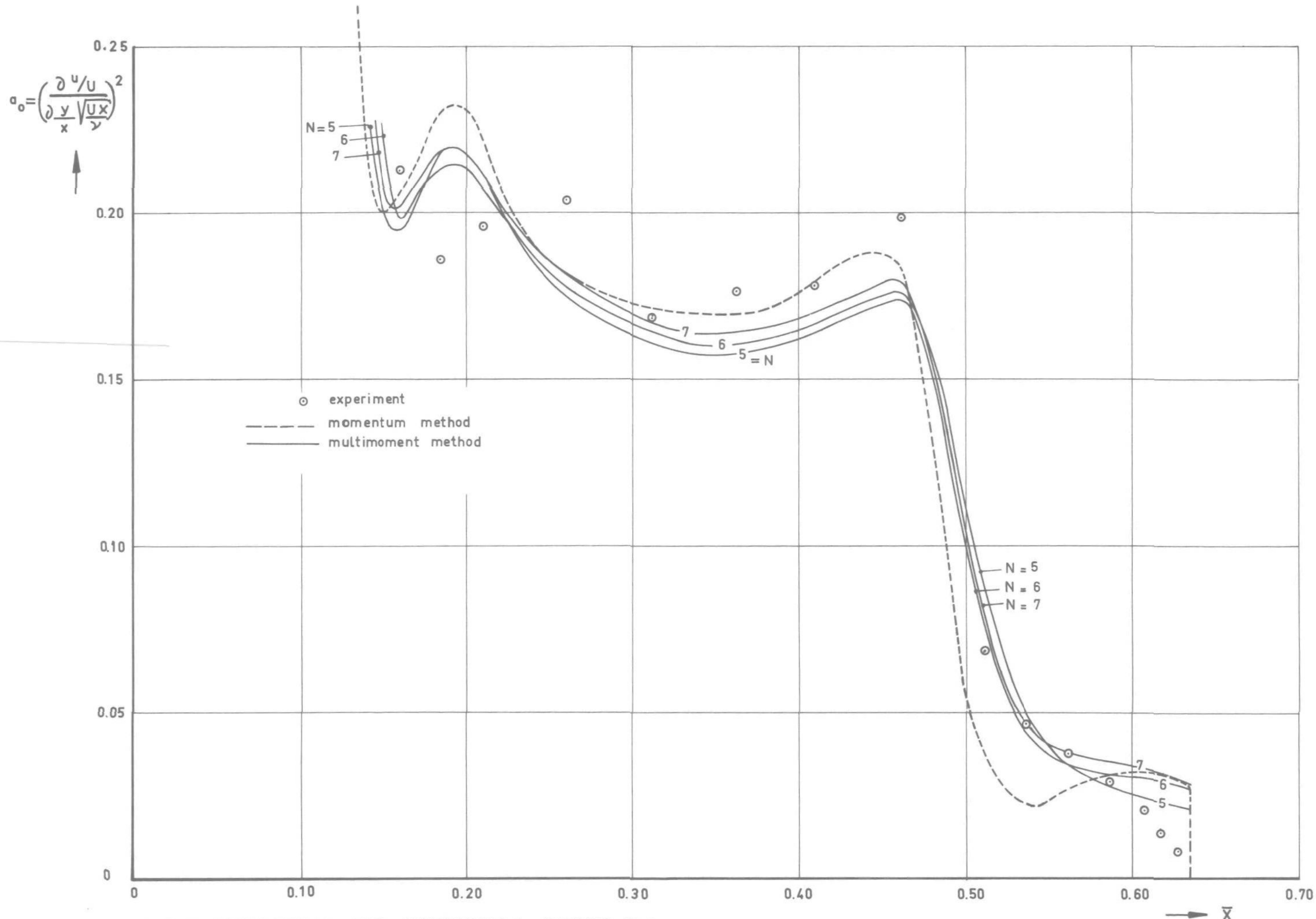

FIG.10.12: THEORETICAL AND EXPERIMENTAL RESULTS FOR a_o

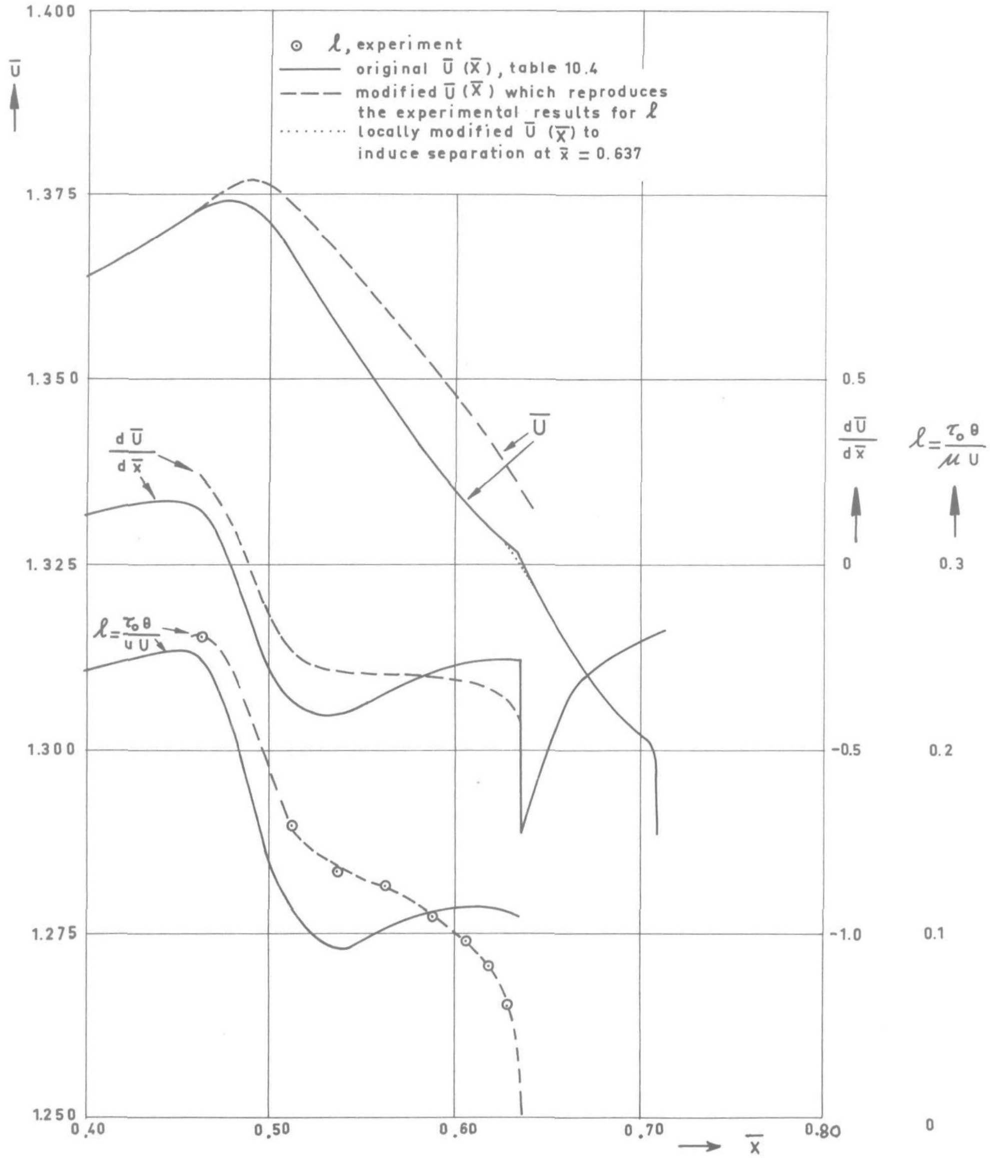

FIG. 10.13: EFFECT OF MODIFICATIONS IN $\overline{U}(\bar{x})$ ON RESULTS OF THE MOMENTUM METHOD.

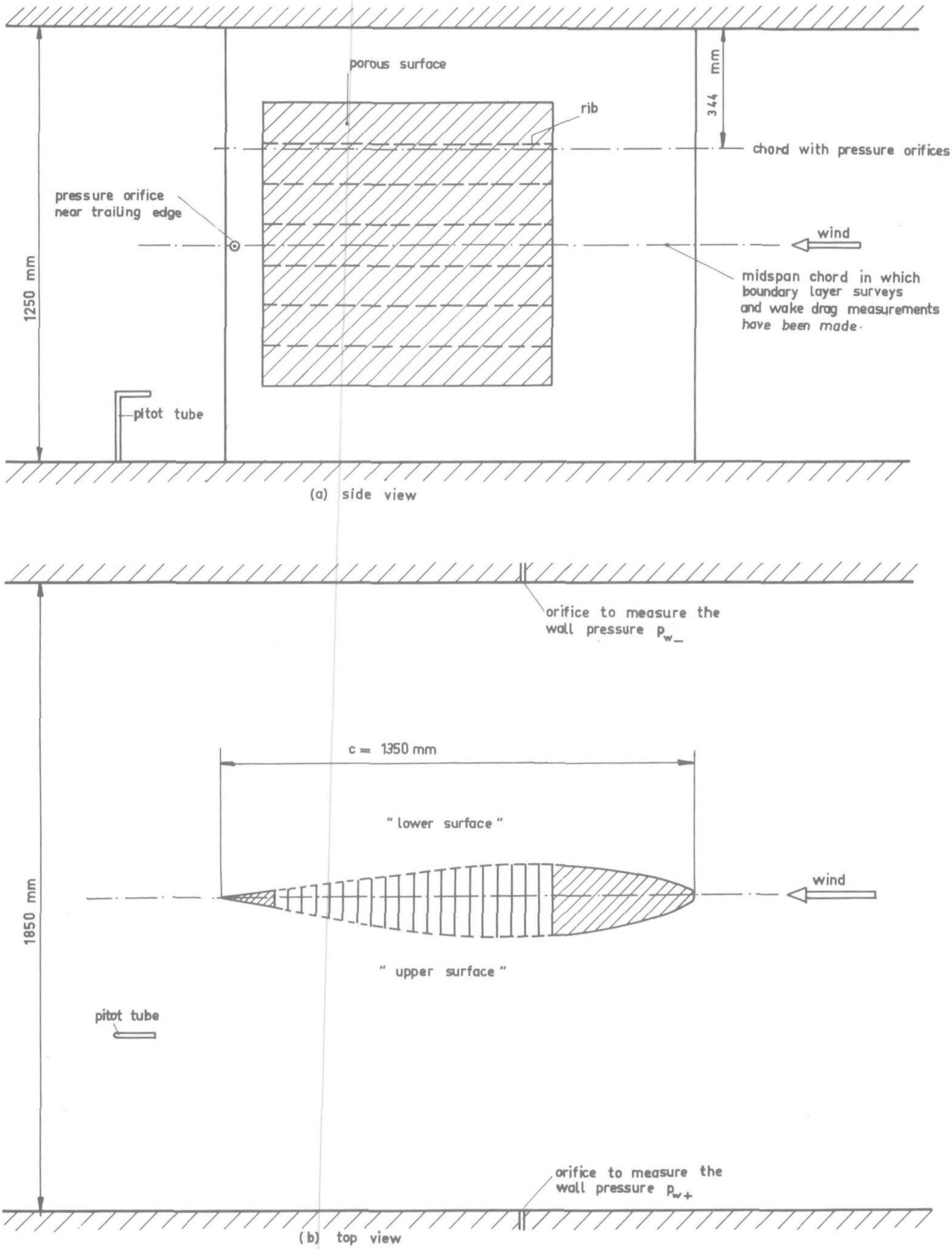

FIG. 11.1: SET UP OF SUCTION MODEL IN WINDTUNNEL

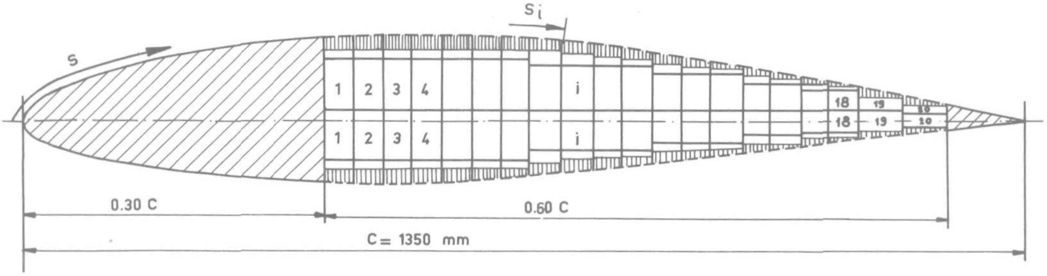

FIG. 11. 2: CROSS SECTION OF MODEL SHOWING SUCTION COMPARTMENTS

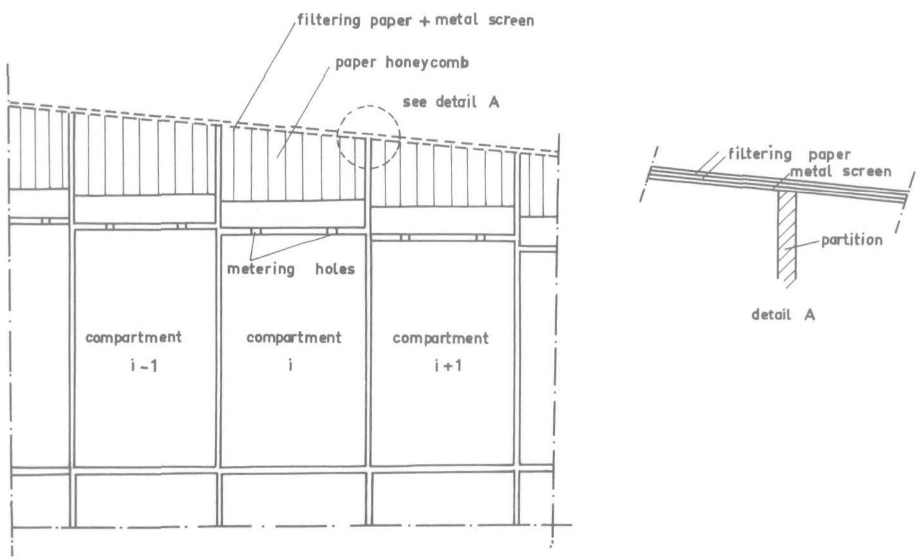

FIG. 11. 3 : CONSTRUCTION OF THE POROUS SURFACE

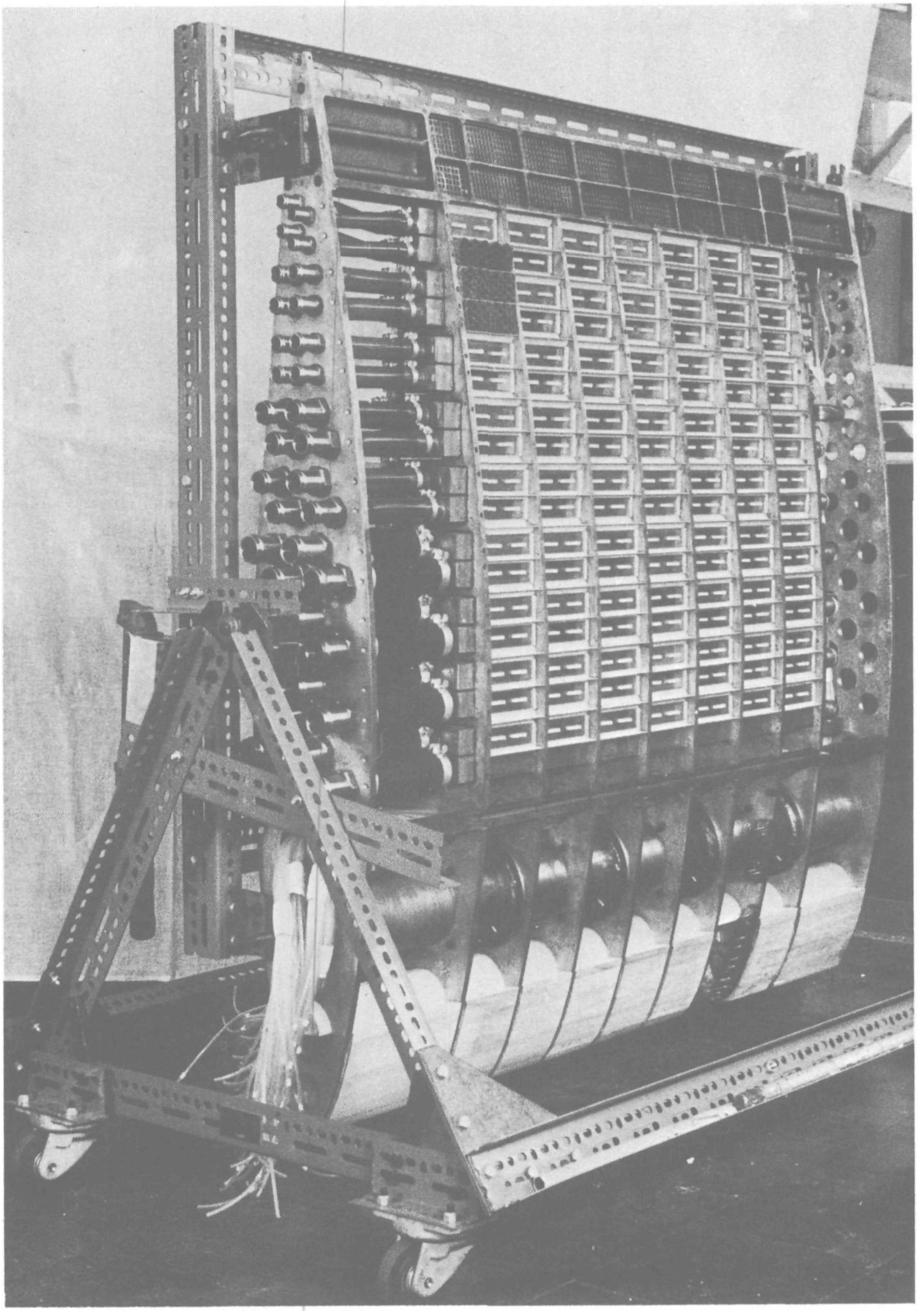

FIG. 11.4: INTERIOR OF MODEL

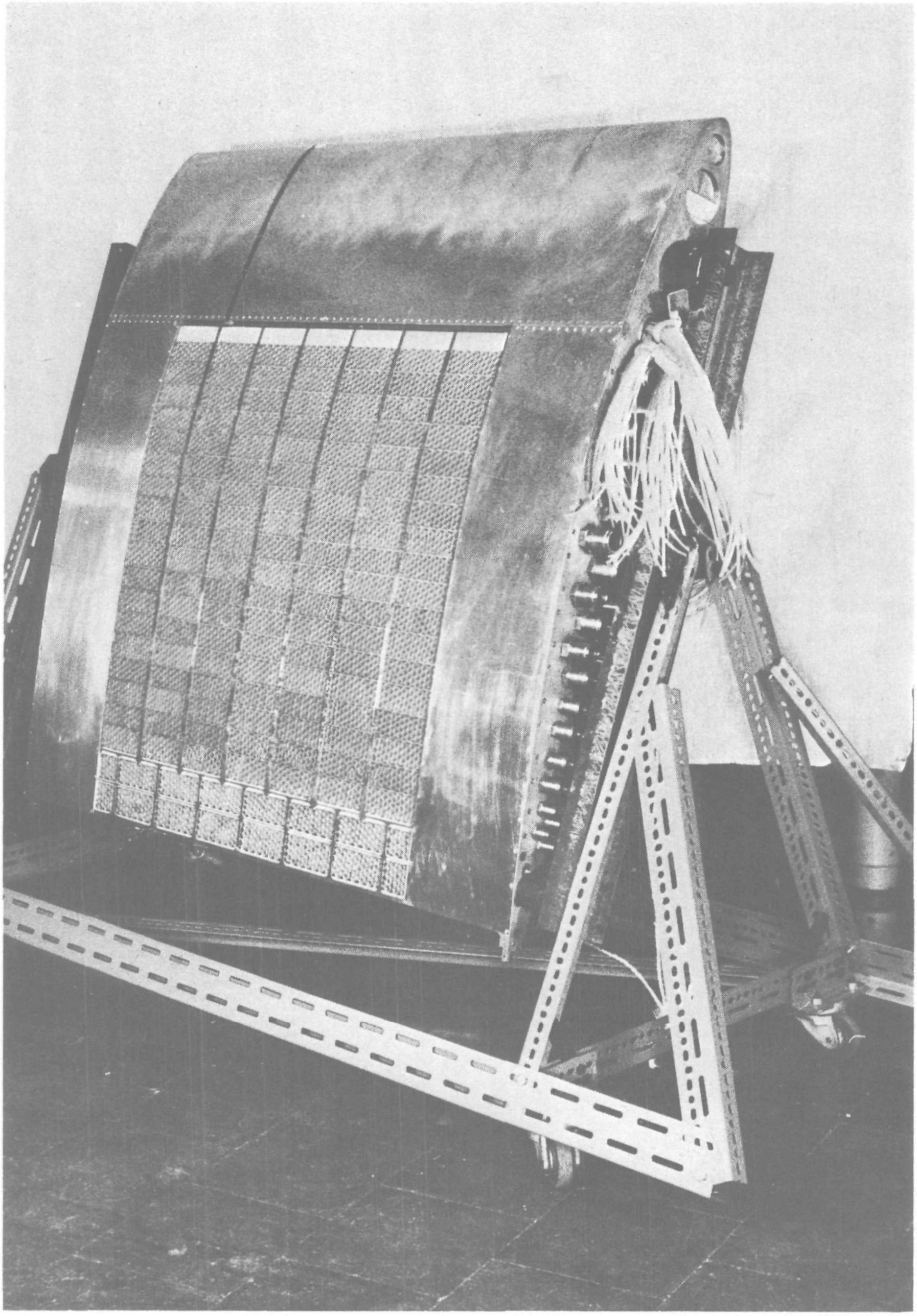

FIG. 11.5: MODEL COMPLETED EXCEPT FOR THE POROUS SURFACE AND TRAILING EDGE

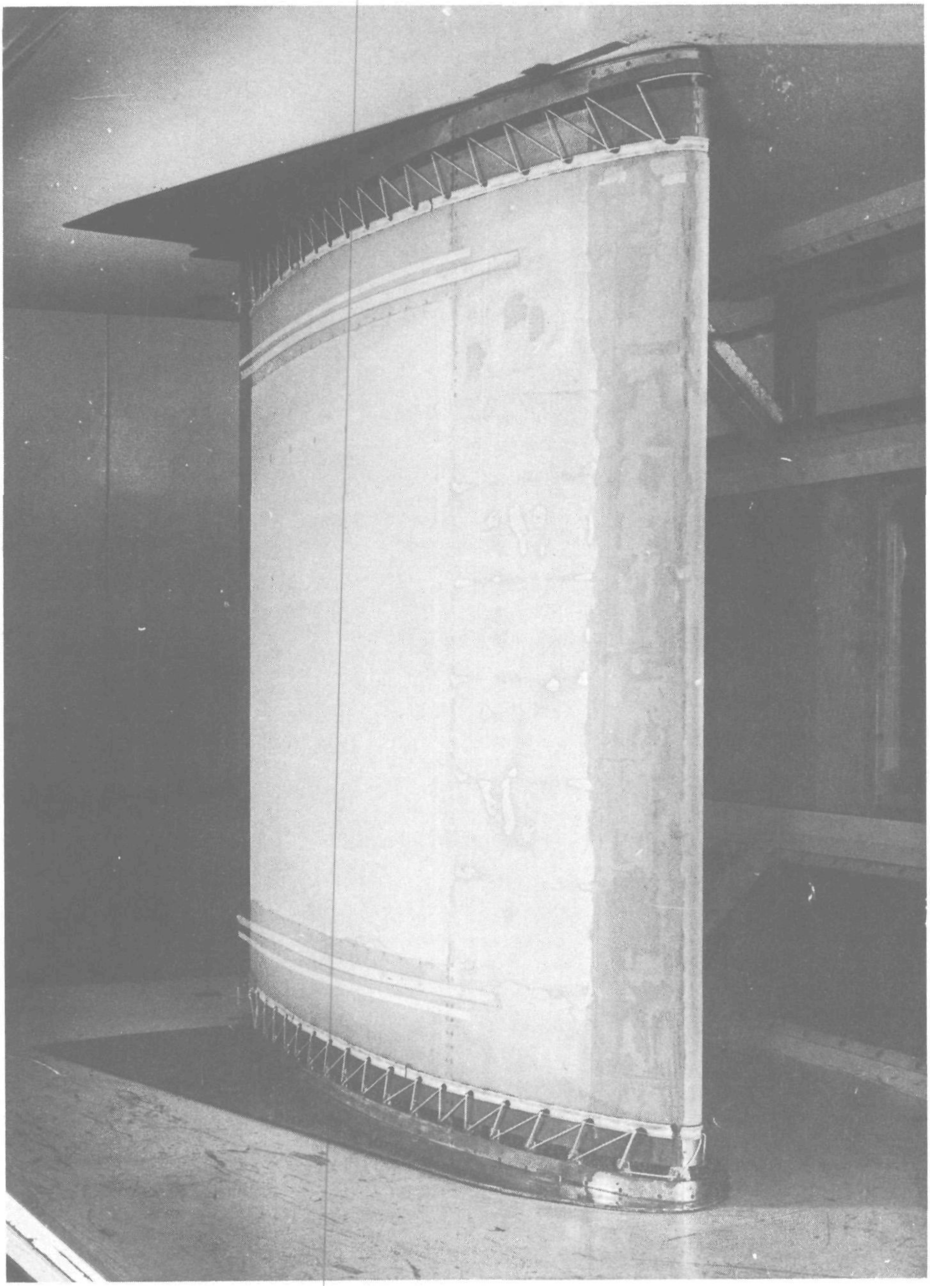

FIG. 11.6: MODEL INSTALLED IN TEST SECTION AND COVERED WITH NYLON

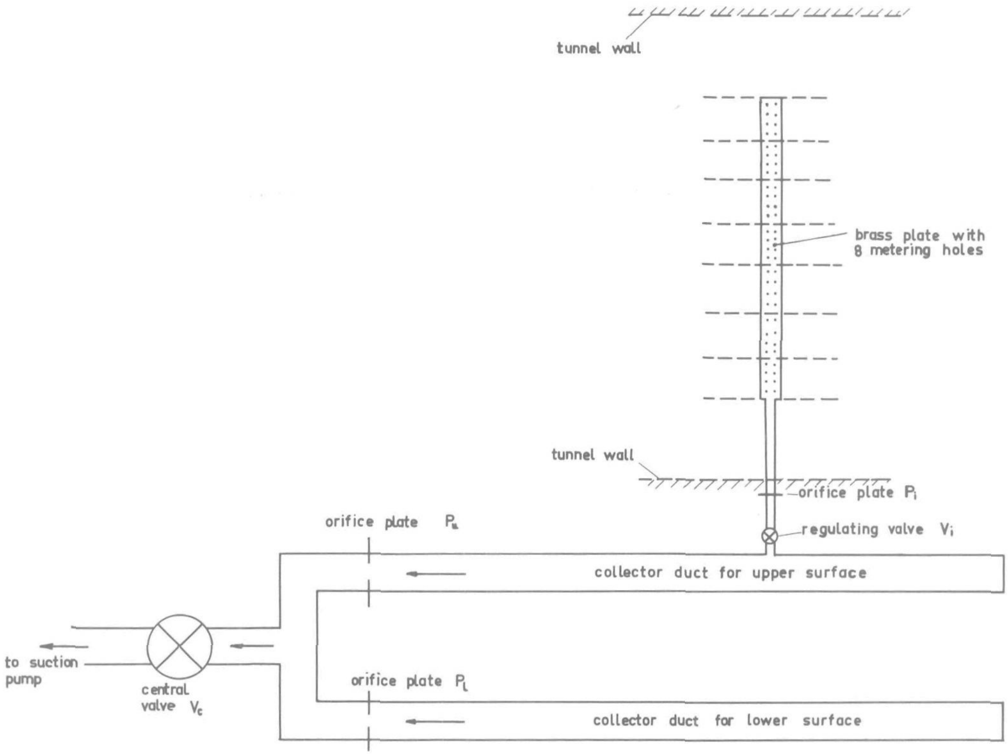

FIG. 11.7: SCHEMATIC REPRESENTATION OF SUCTION INSTALLATION

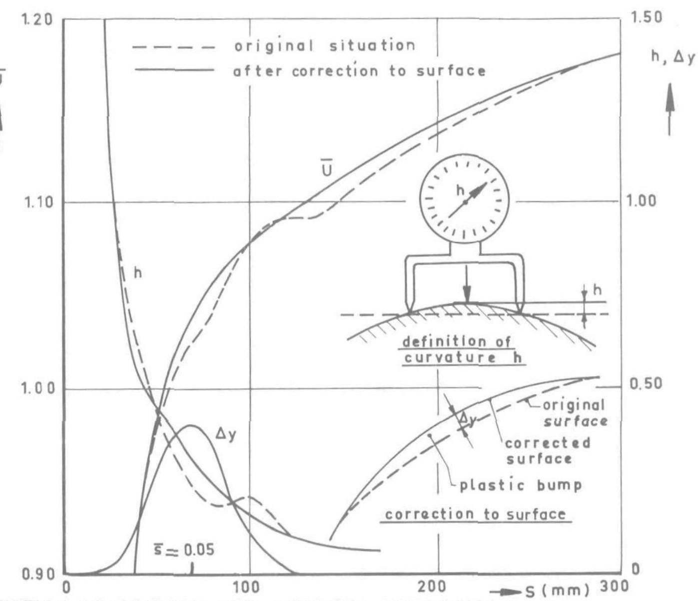

FIG. 11.8 : INFLUENCE OF CHANGES IN THE CURVATURE DISTRIBUTION ON $\overline{U}$(s) FOR THE UPPER SURFACE

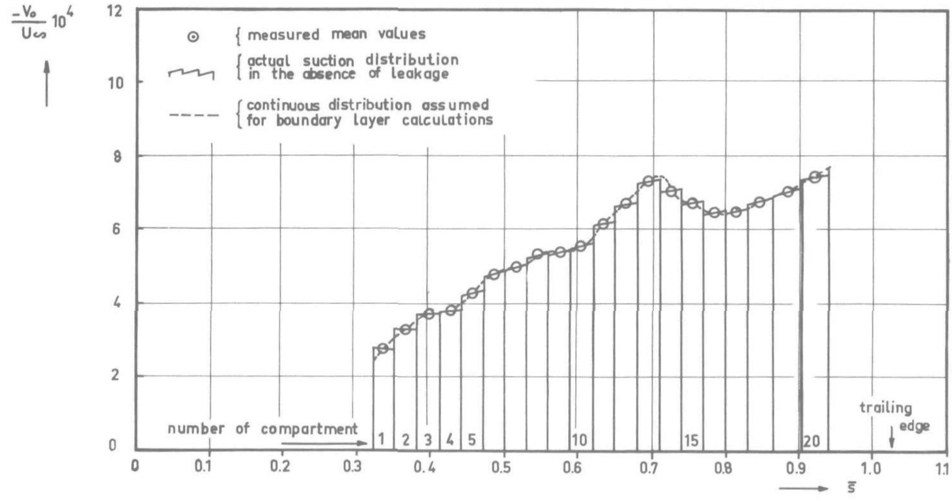

FIG. 11.9 : TYPICAL SUCTION DISTRIBUTION

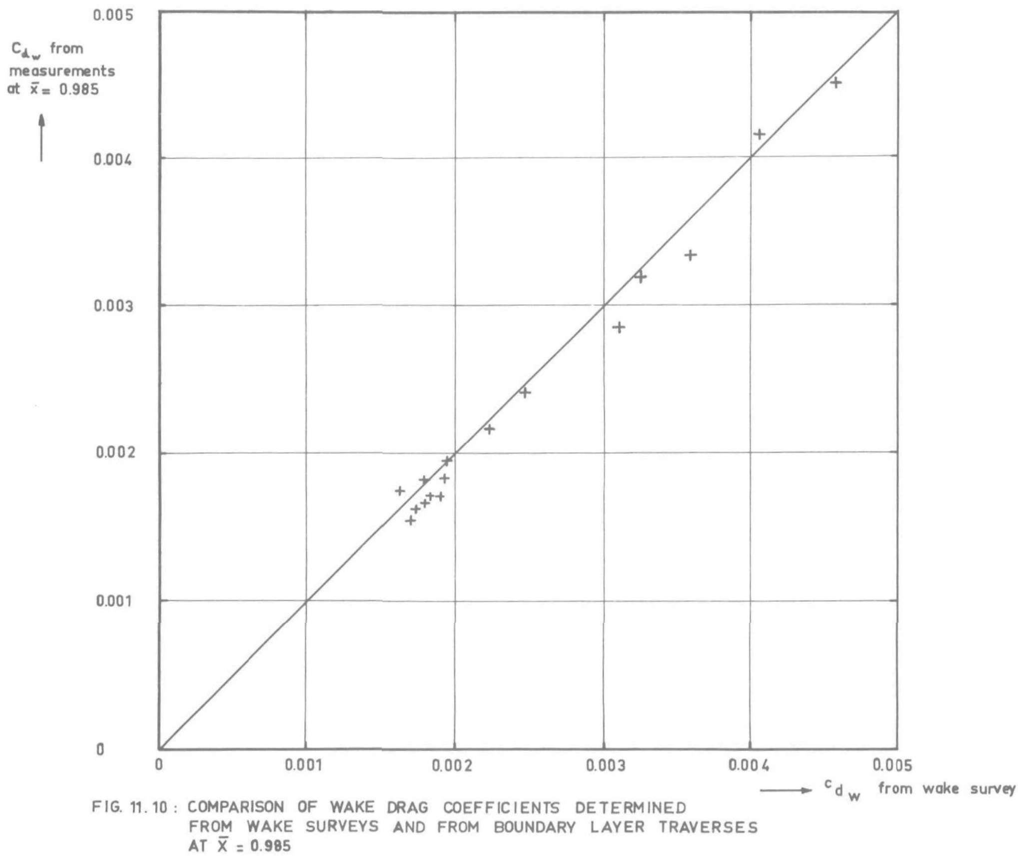

FIG. 11.10 : COMPARISON OF WAKE DRAG COEFFICIENTS DETERMINED FROM WAKE SURVEYS AND FROM BOUNDARY LAYER TRAVERSES AT $\bar{X} = 0.985$

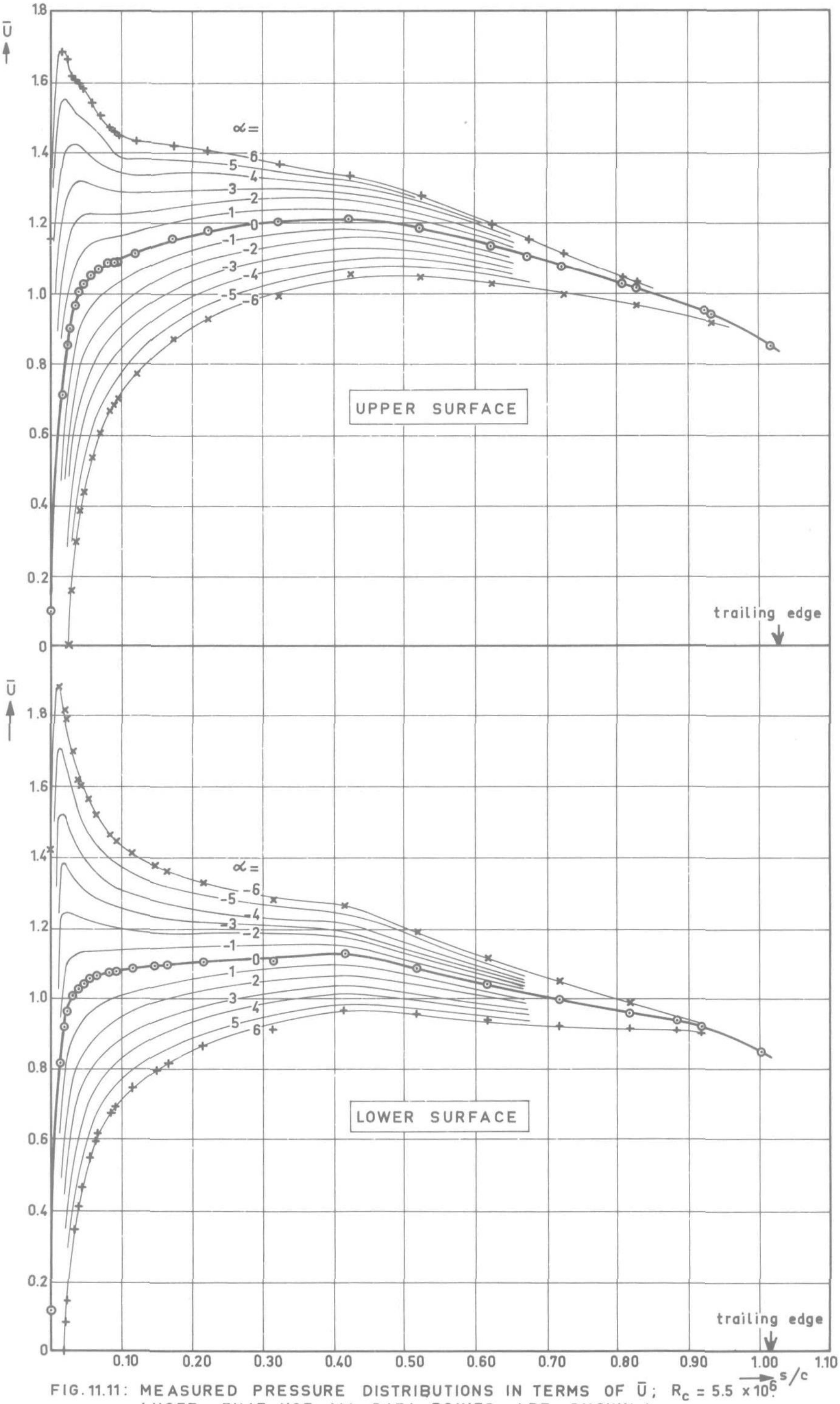

FIG. 11.11: MEASURED PRESSURE DISTRIBUTIONS IN TERMS OF $\bar{U}$; $R_c = 5.5 \times 10^6$.
(NOTE THAT NOT ALL DATA POINTS ARE SHOWN).

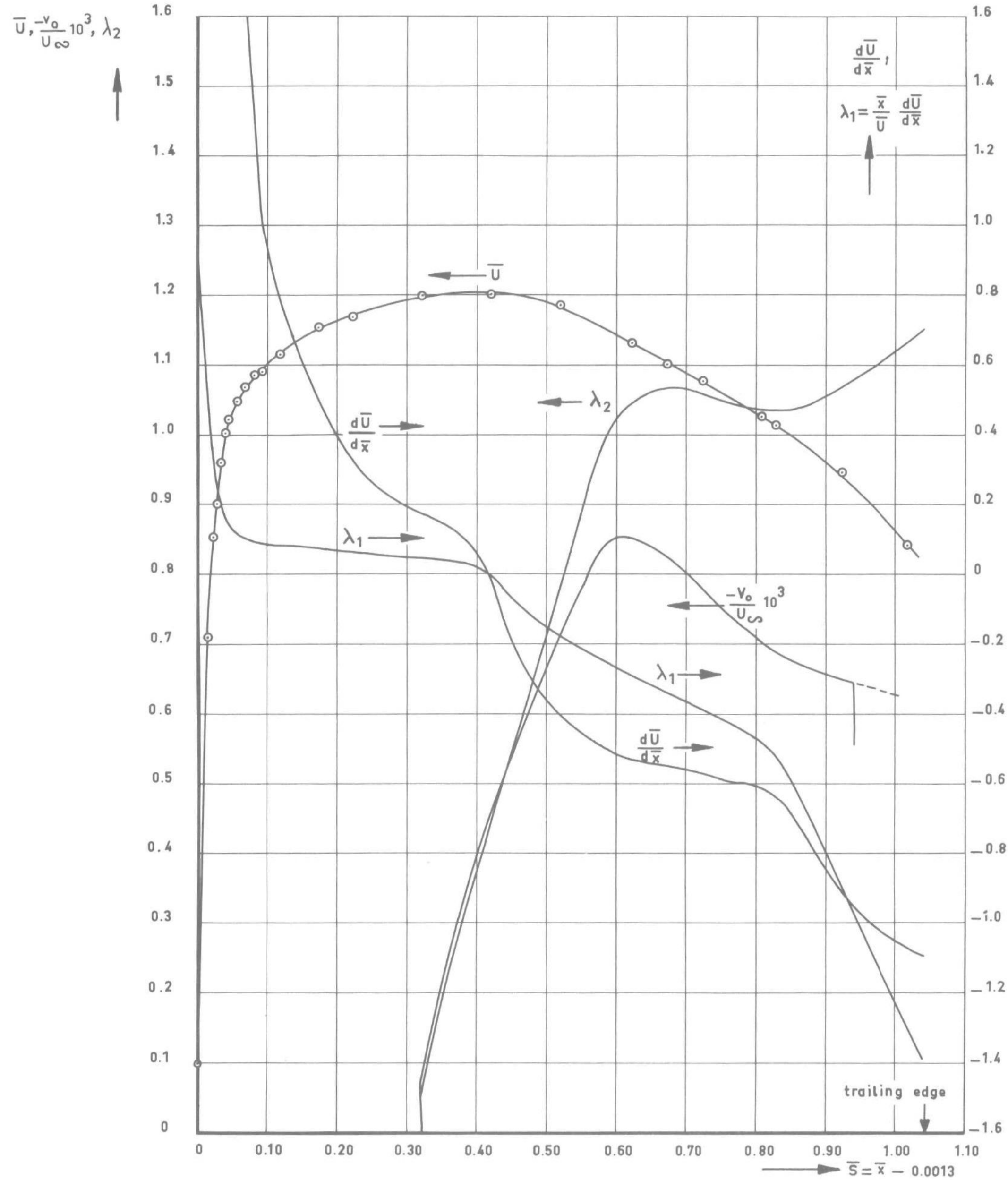

FIG.11.12: DETAILS OF PRESSURE — AND SUCTION DISTRIBUTIONS USED FOR BOUNDARY LAYER CALCULATIONS IN SECTION 11.5 (SEE ALSO TABLE 11.4)

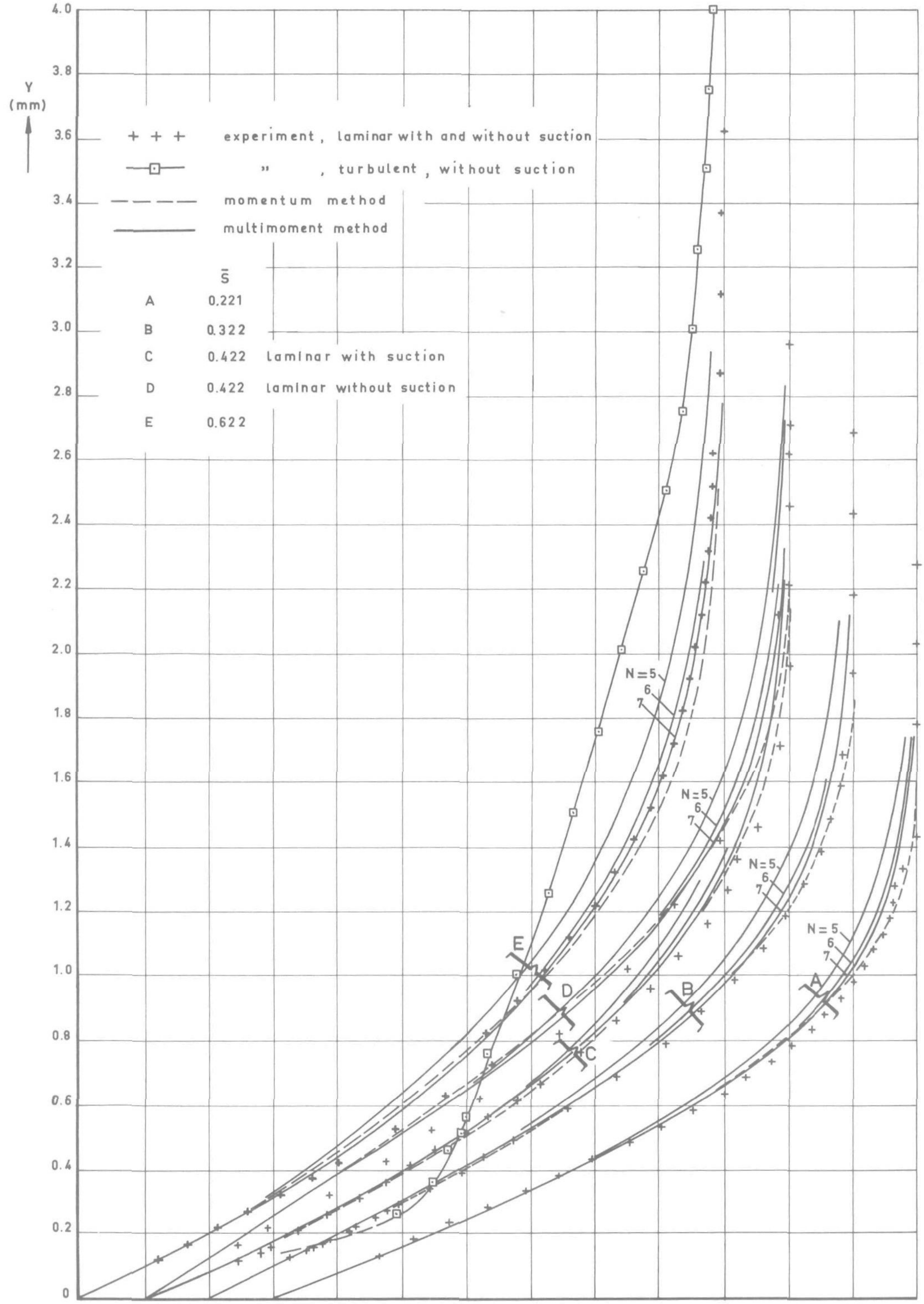

FIG.11.13 A: VELOCITY PROFILES FOR THE BOUNDARY LAYERS DISCUSSED IN SECTION 11.5

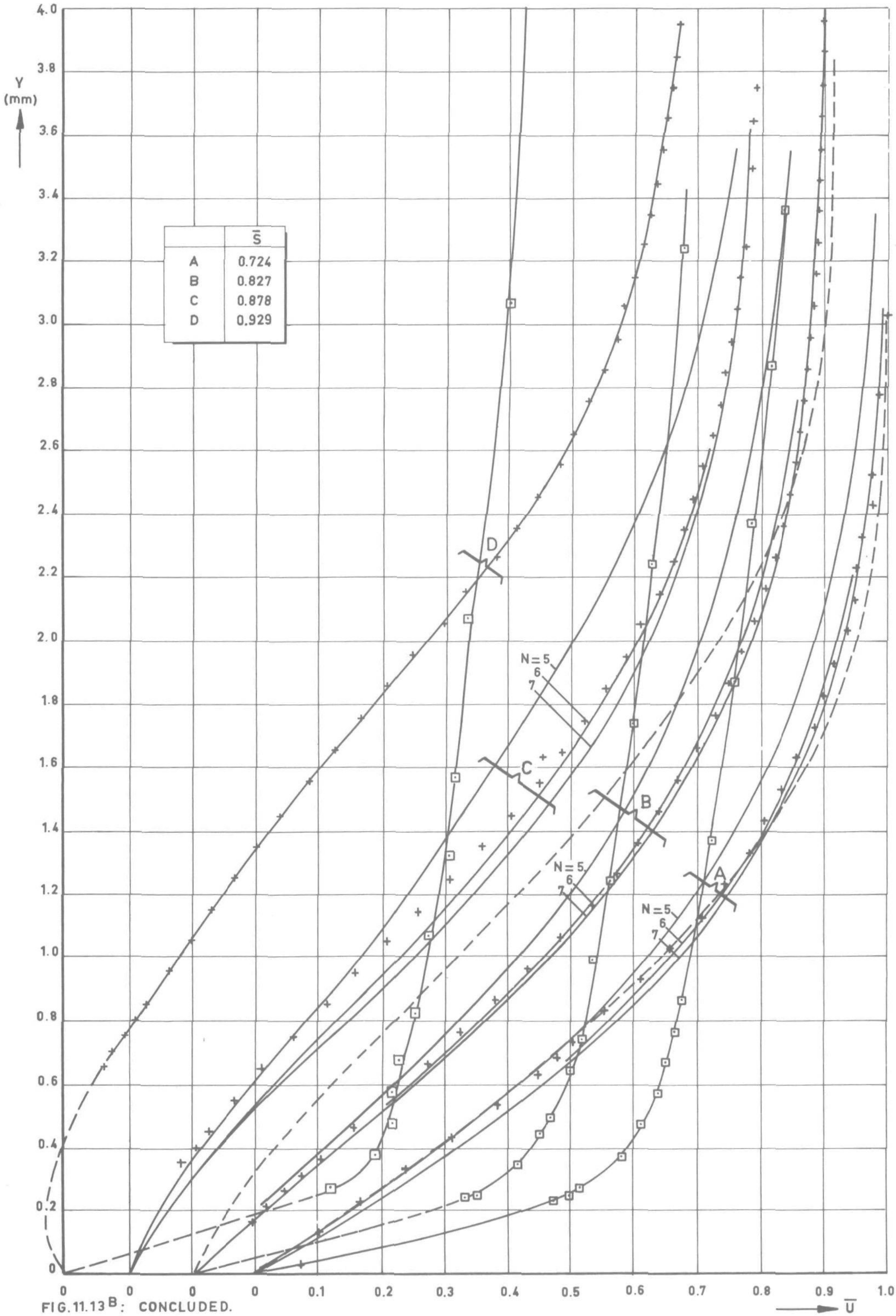

FIG. 11.13 B: CONCLUDED.

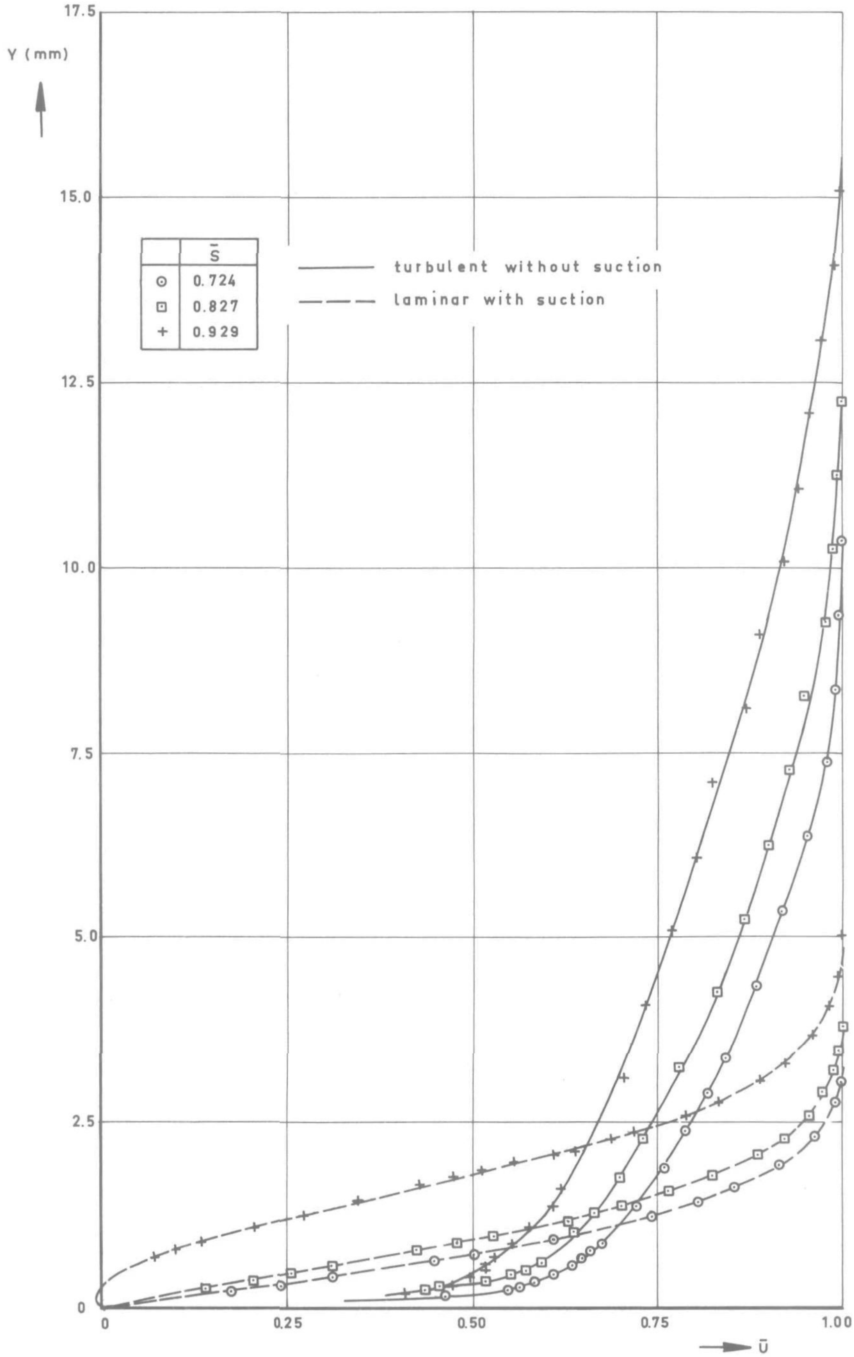

FIG. 11.14 : SOME VELOCITY PROFILES IN THE POROUS REGION WITH AND WITHOUT SUCTION.

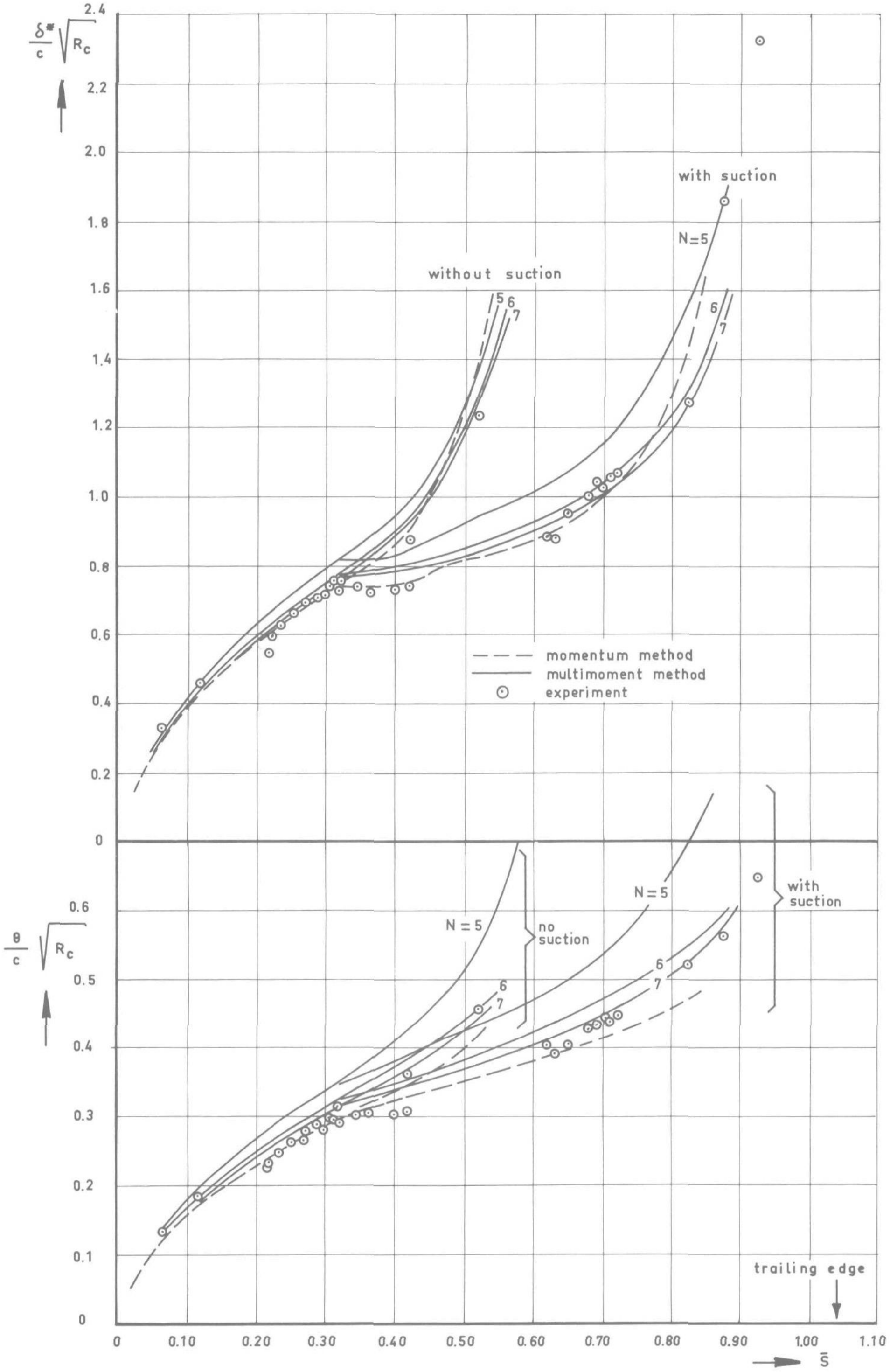

FIG. 11.15: DISPLACEMENT THICKNESS δ^* AND MOMENTUM LOSS THICKNESS θ FOR THE UPPER SURFACE WITH AND WITHOUT SUCTION ; $\alpha = 0$, $R_c = 2.75 \times 10^6$.

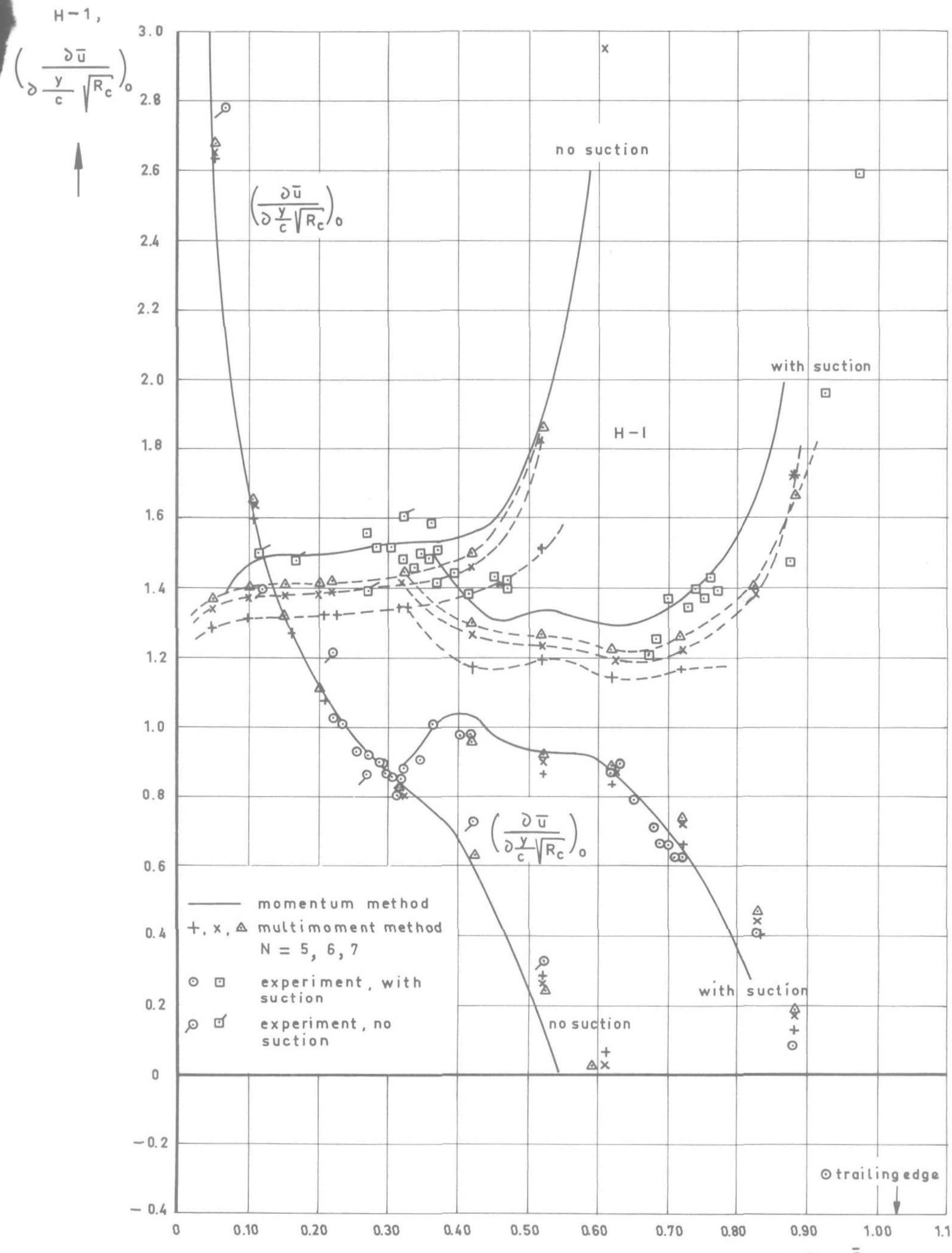

FIG. 11.16 : WALL SHEAR STRESS AND SHAPE FACTOR H FOR THE UPPER SURFACE WITH AND WITHOUT SUCTION ; $\alpha = 0$. $R_c = 2.75 \times 10^6$.

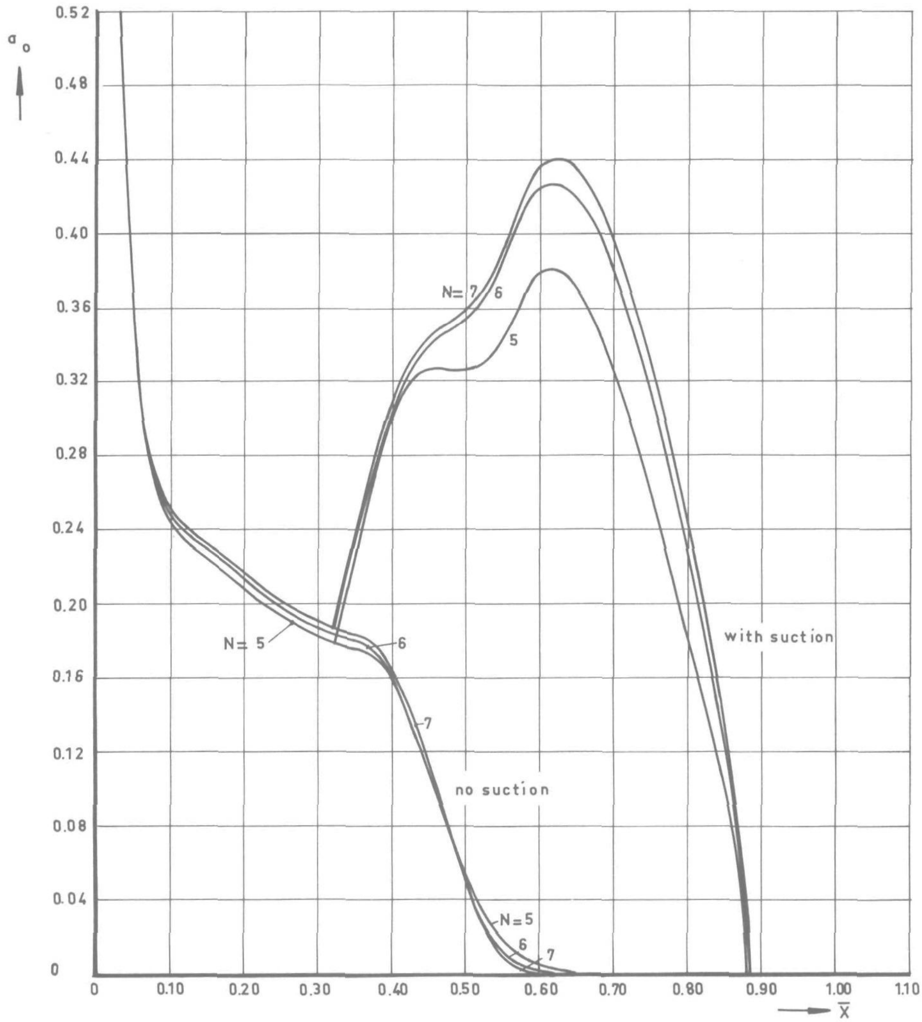

FIG. 11.17: THE SHEAR STRESS PARAMETER a_0 FOR THE TWO BOUNDARY LAYERS DISCUSSED IN SECTION 11.5 ; CALCULATED WITH THE MULTIMOMENT METHOD

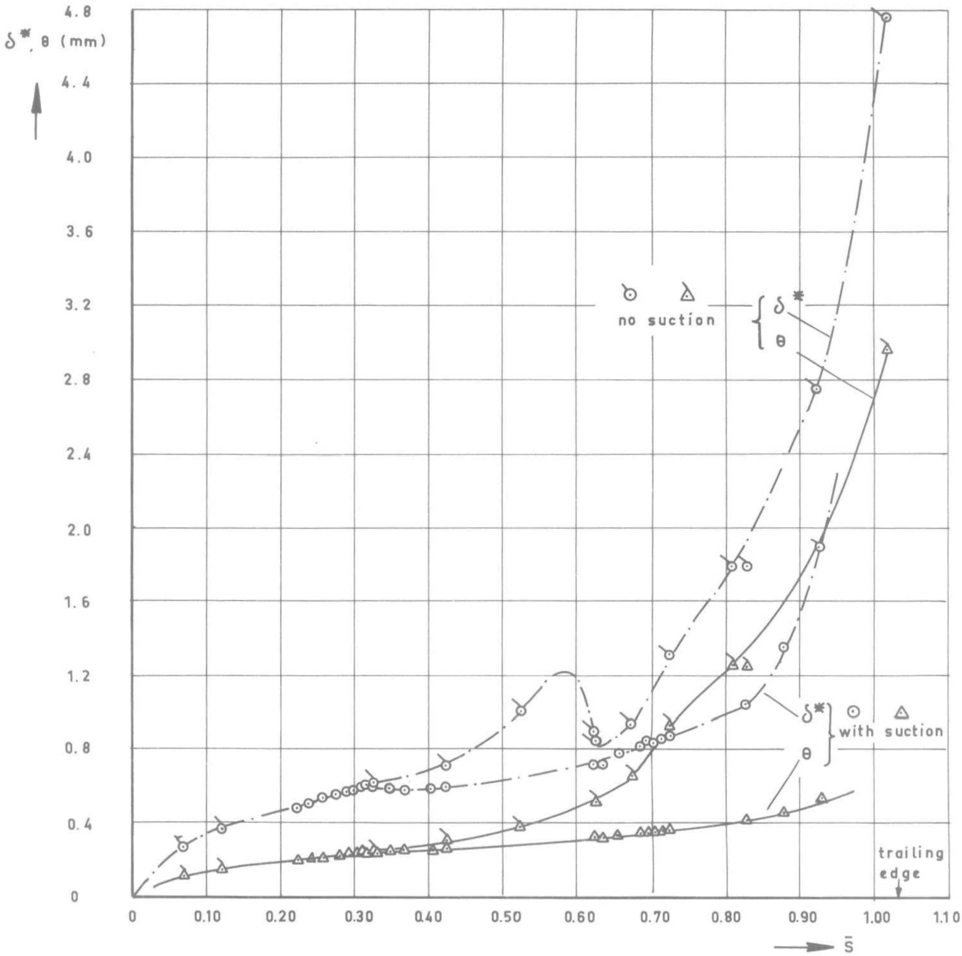

FIG.11.18 : δ^* AND θ FOR THE UPPER SURFACE WITH AND WITHOUT SUCTION ; $\alpha = 0$, $R_c = 2.75 \times 10^6$

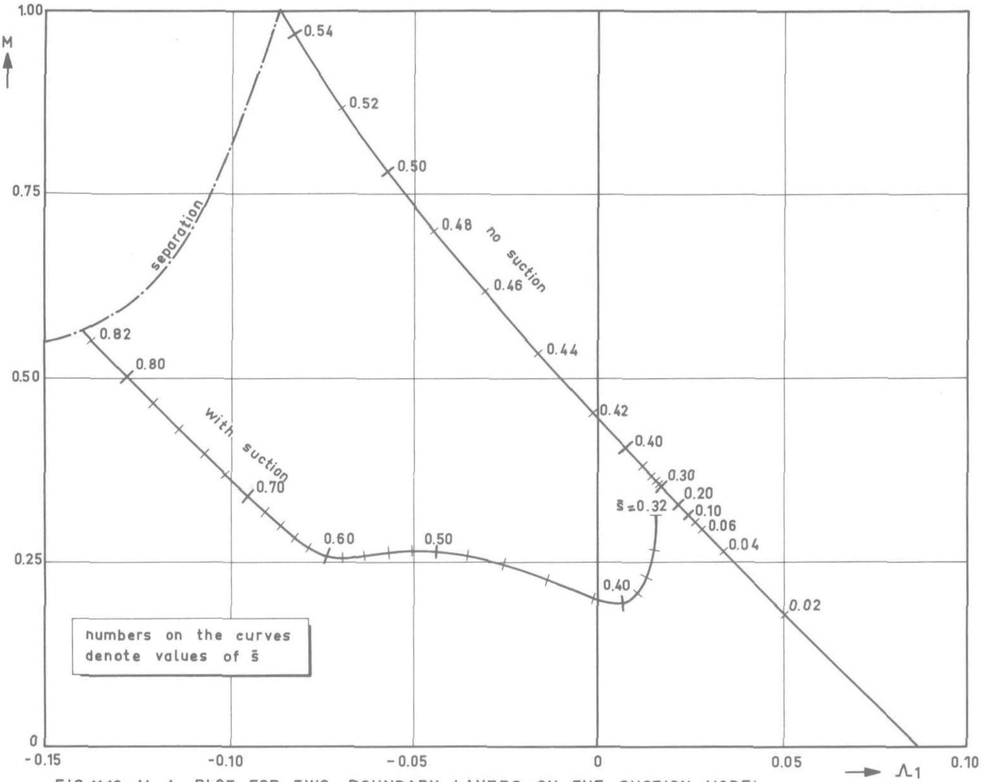

FIG. 11.19: M - Λ_1 PLOT FOR TWO BOUNDARY LAYERS ON THE SUCTION MODEL.

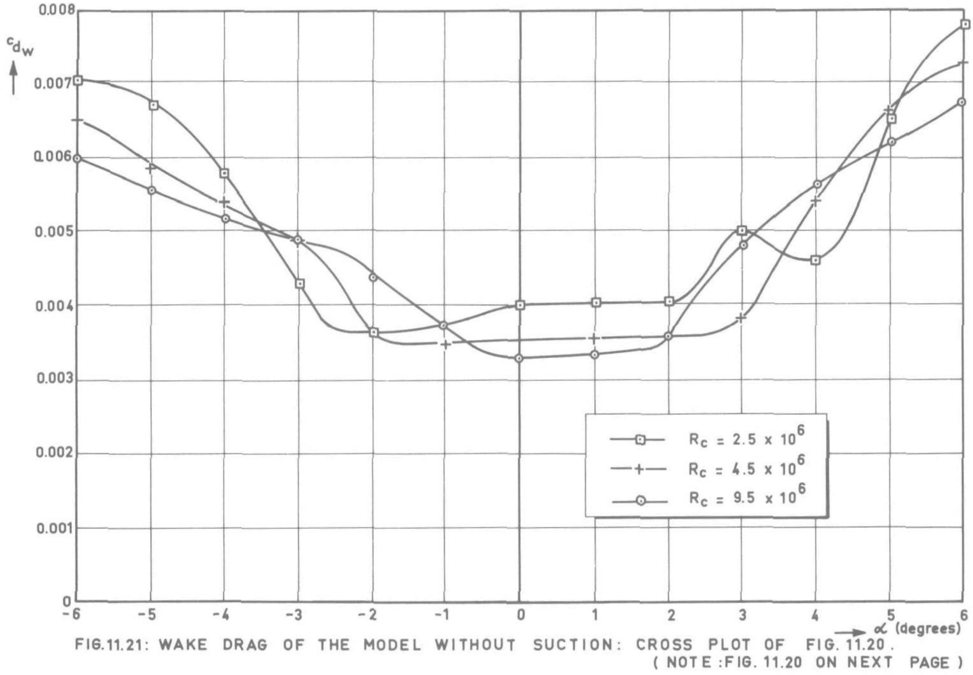

FIG. 11.21: WAKE DRAG OF THE MODEL WITHOUT SUCTION: CROSS PLOT OF FIG. 11.20.
(NOTE : FIG. 11.20 ON NEXT PAGE)

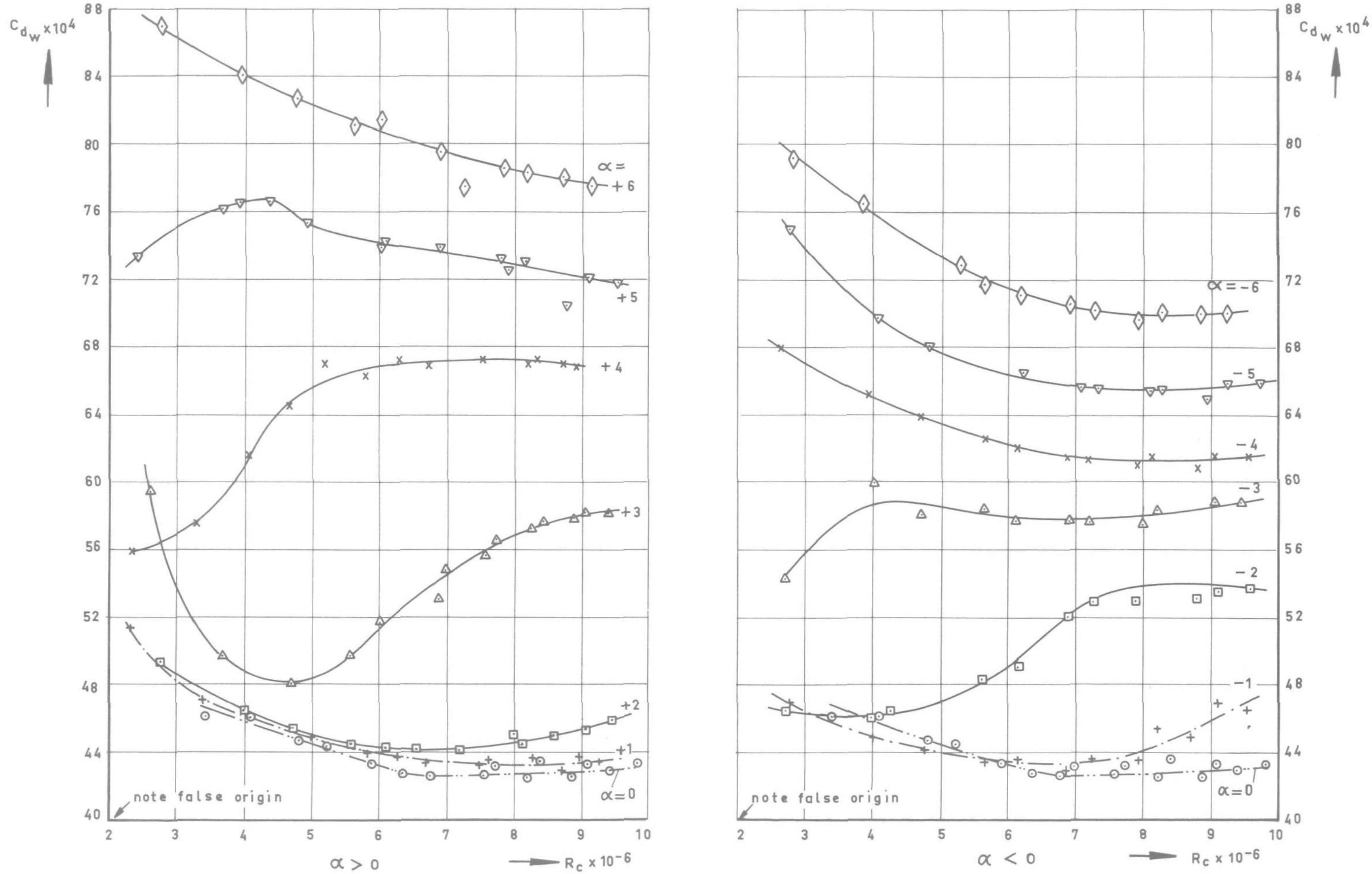

FIG.11.20: WAKE DRAG COEFFICIENTS FOR THE SEALED MODEL DETERMINED FROM WAKE TRAVERSES

(NOTE FIG.11.21 ON PREVIOUS PAGE)

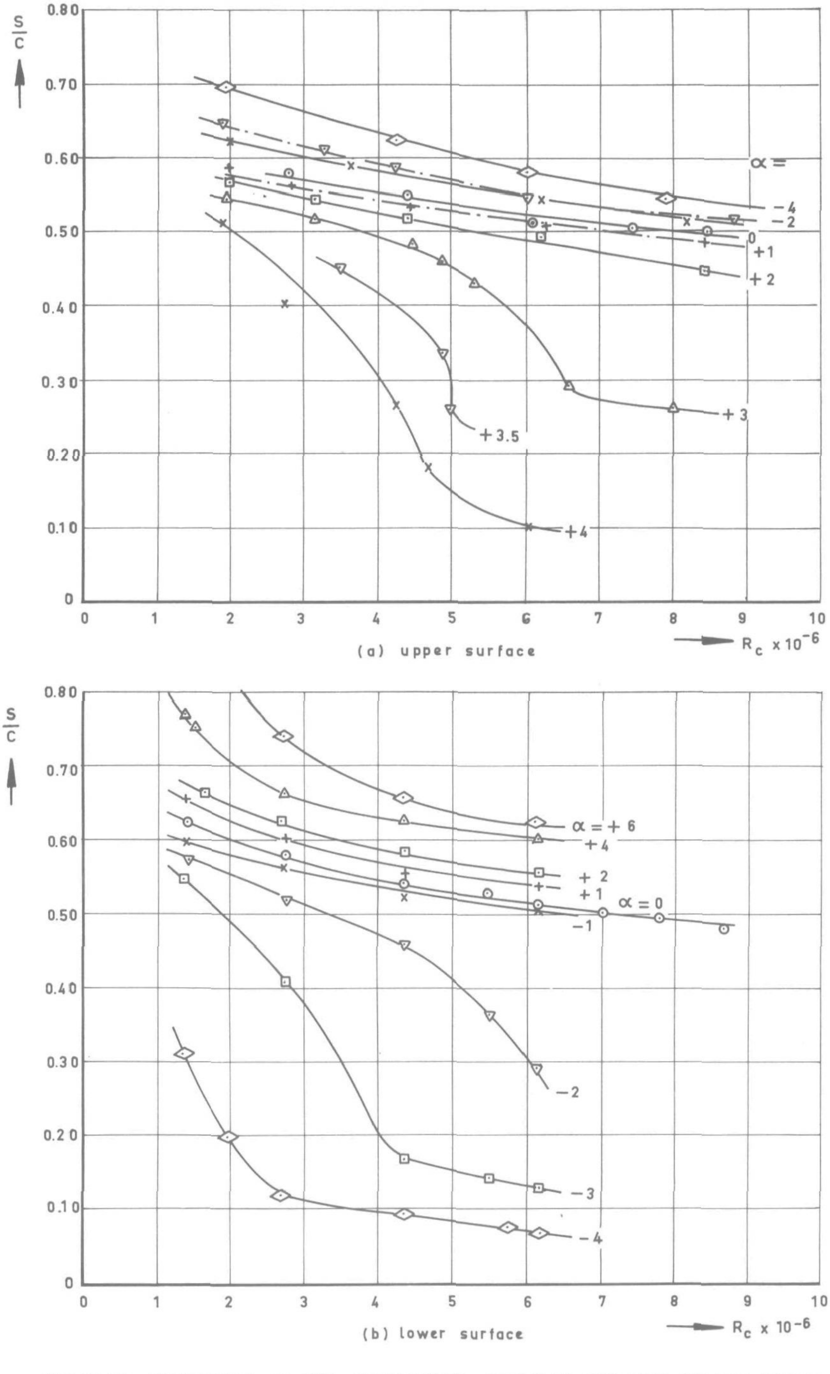

FIG. 11. 22: BEGINNING OF THE TRANSITION POSITION FOR THE SEALED MODEL

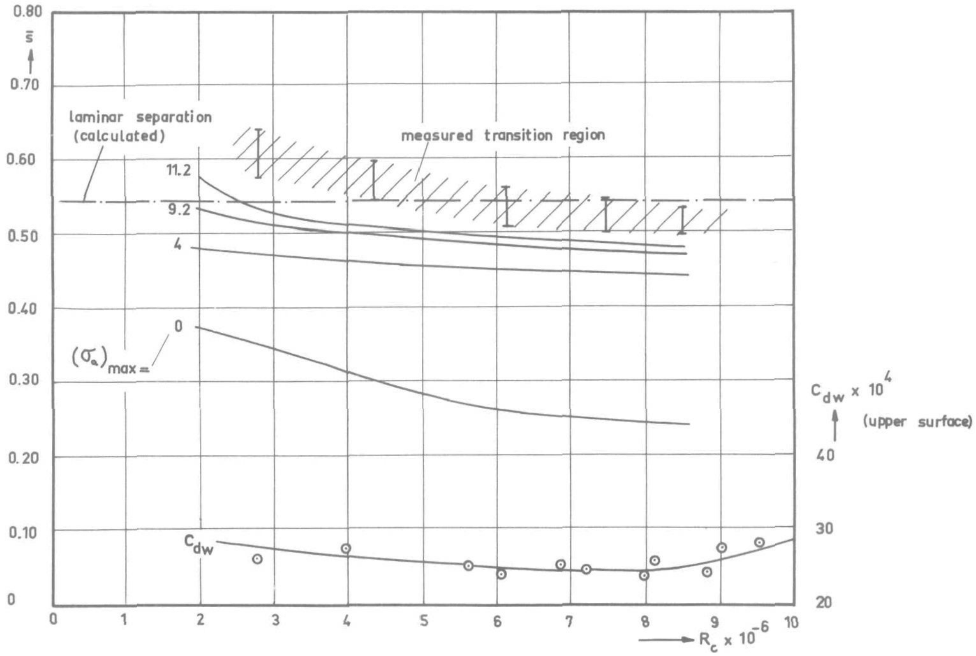

FIG. 11.23. TRANSITION AND DRAG FOR THE UPPER SURFACE
$\alpha = 0^\circ$; NO SUCTION.

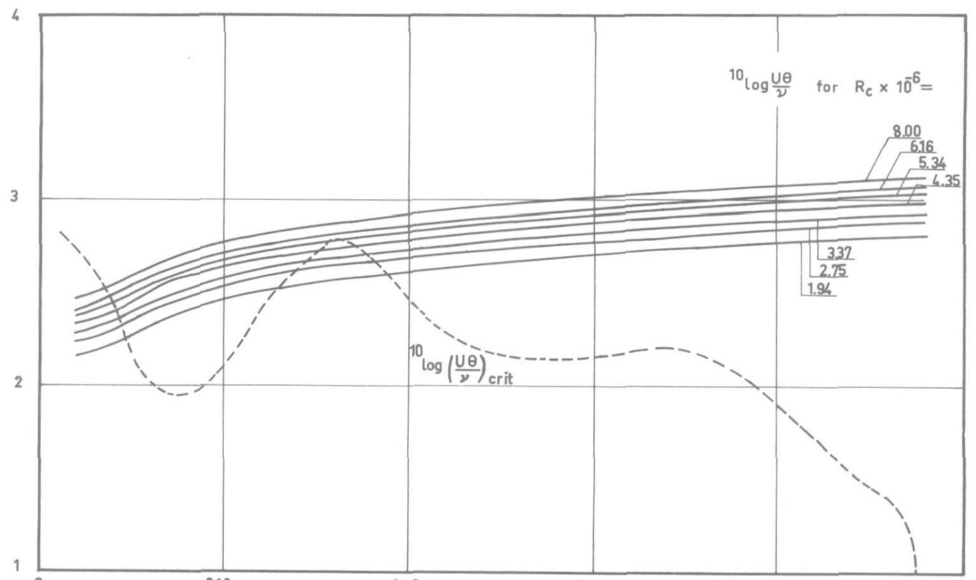

FIG. 11.24. RESULTS OF BOUNDARY LAYER CALCULATIONS WITH THE MOMENTUM METHOD; UPPER SURFACE, $\alpha = +3^\circ$, NO SUCTION.

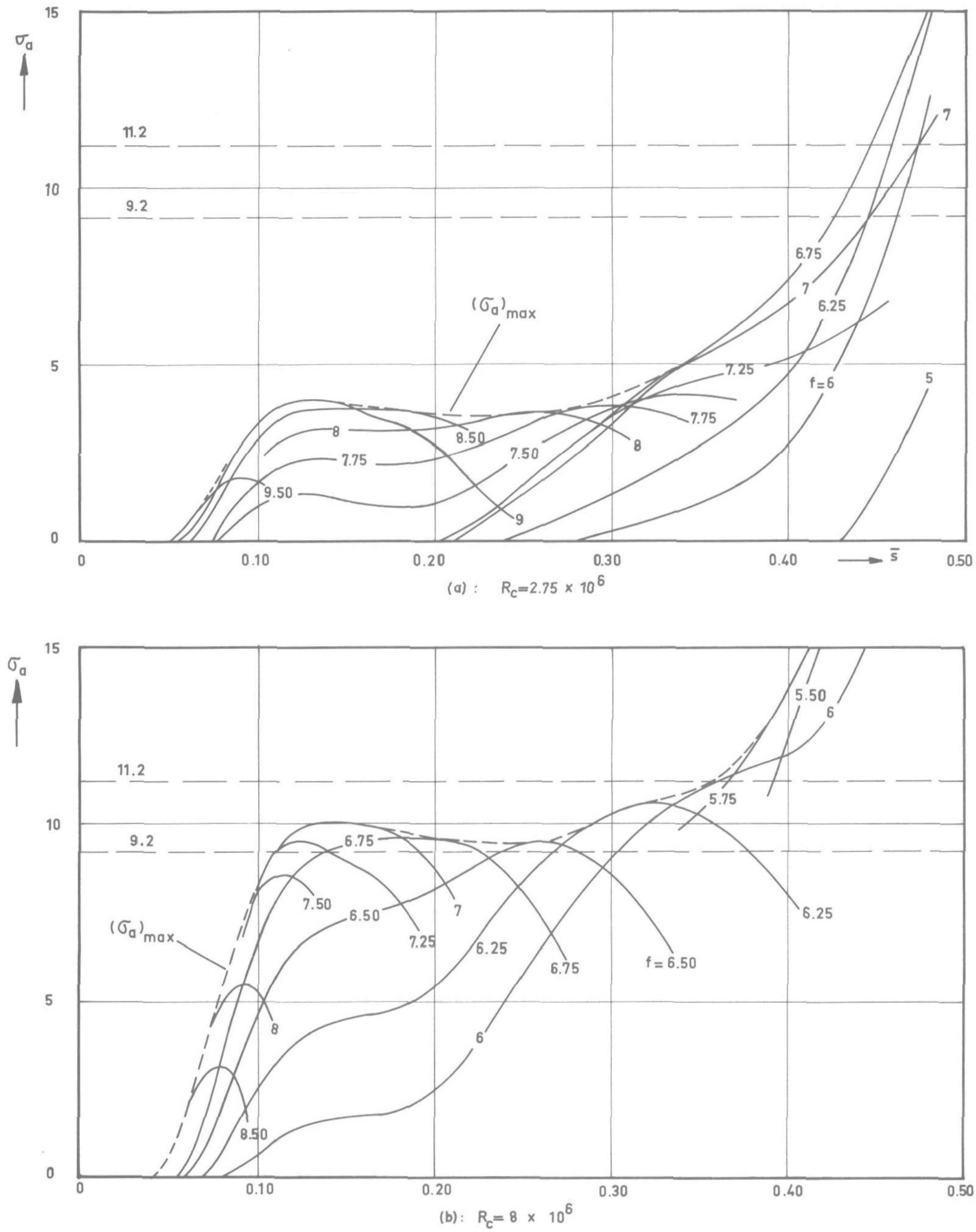

FIG. 11. 25: RESULTS OF AMPLIFICATION CALCULATIONS FOR THE UPPER SURFACE ; $\alpha = 3^{\circ}$; NO SUCTION.
(numbers on the curves denote values of the frequency parameter f)

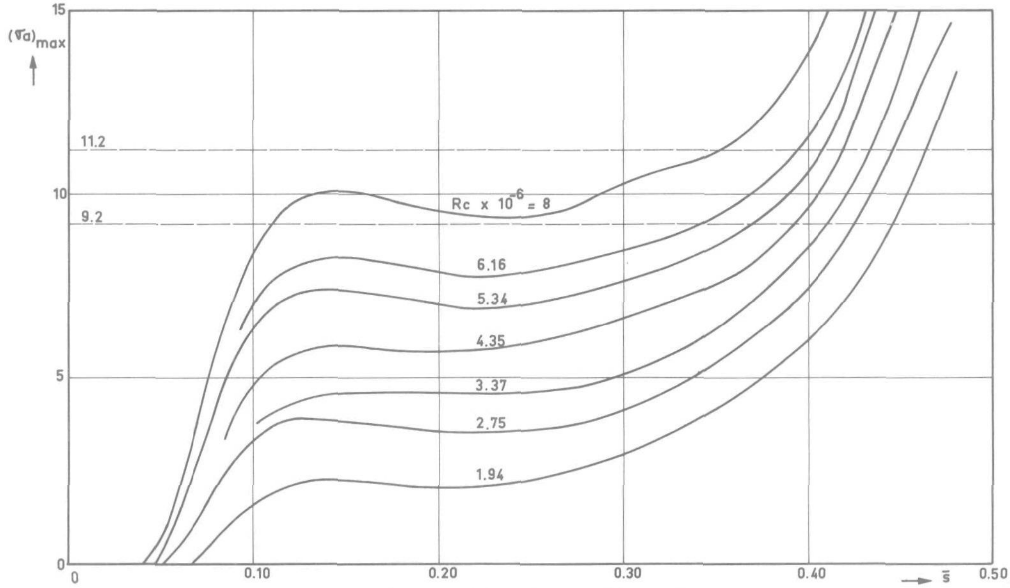

FIG. 11.26: MAXIMUM AMPLIFICATION FACTOR FOR THE UPPER SURFACE AT DIFFERENT VALUES OF R_c; $\alpha = 3°$; NO SUCTION.

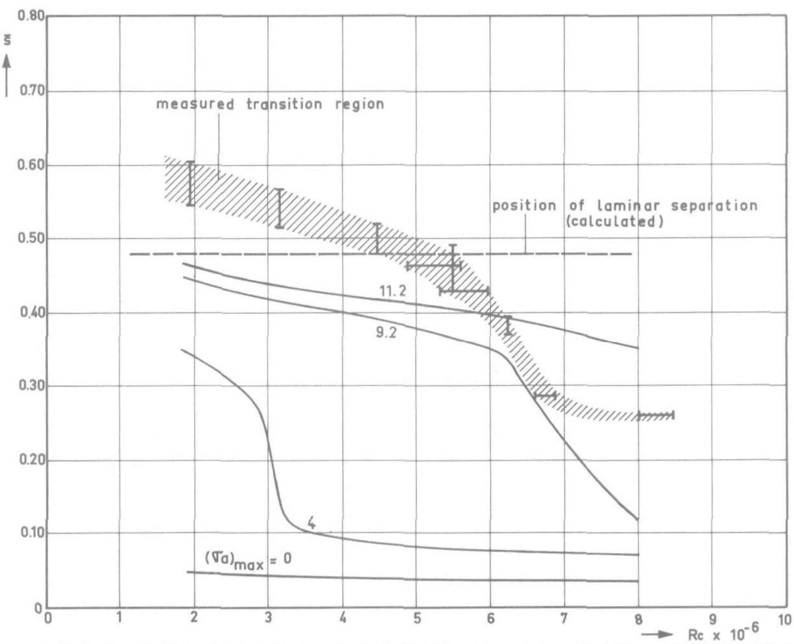

FIG. 11.27: MEASURED TRANSITION REGION AND CALCULATED AMPLIFICATION FACTORS FOR THE UPPER SURFACE WITHOUT SUCTION; $\alpha = 3°$.

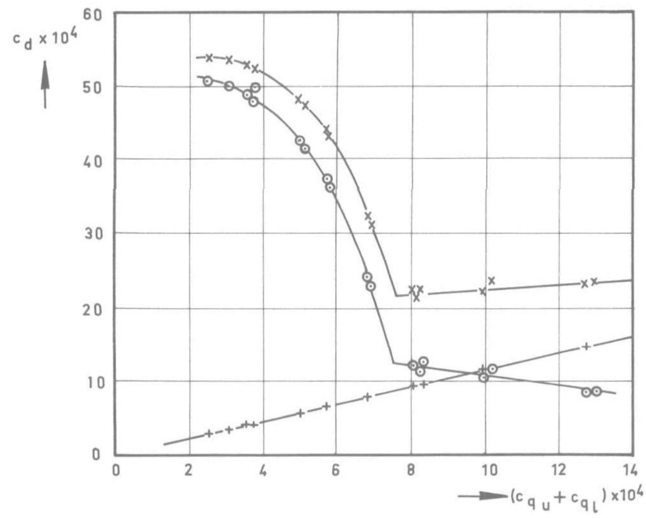

FIG. 11.28: UPPER+LOWER SURFACE

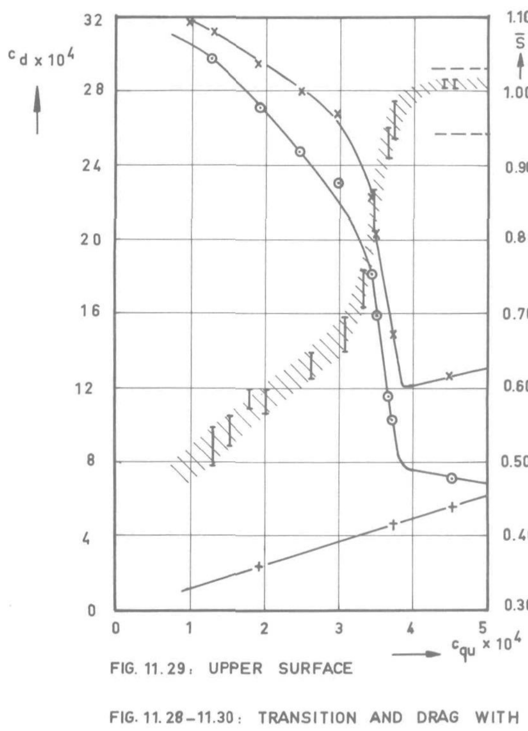

FIG. 11.29: UPPER SURFACE

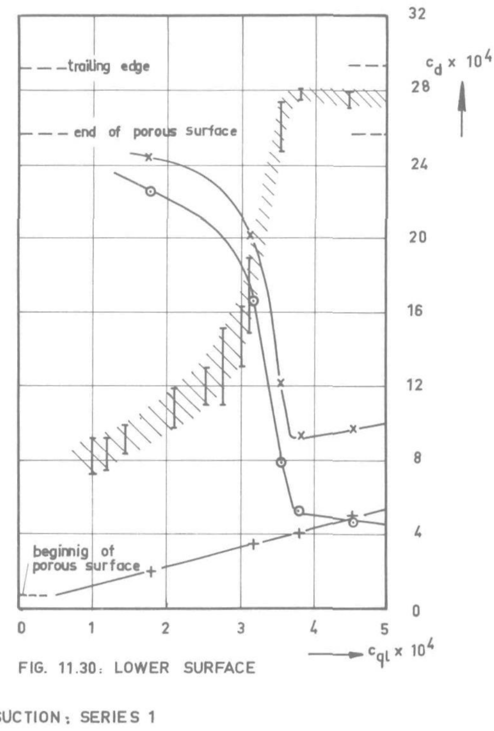

FIG. 11.30: LOWER SURFACE

FIG. 11.28–11.30: TRANSITION AND DRAG WITH SUCTION; SERIES 1

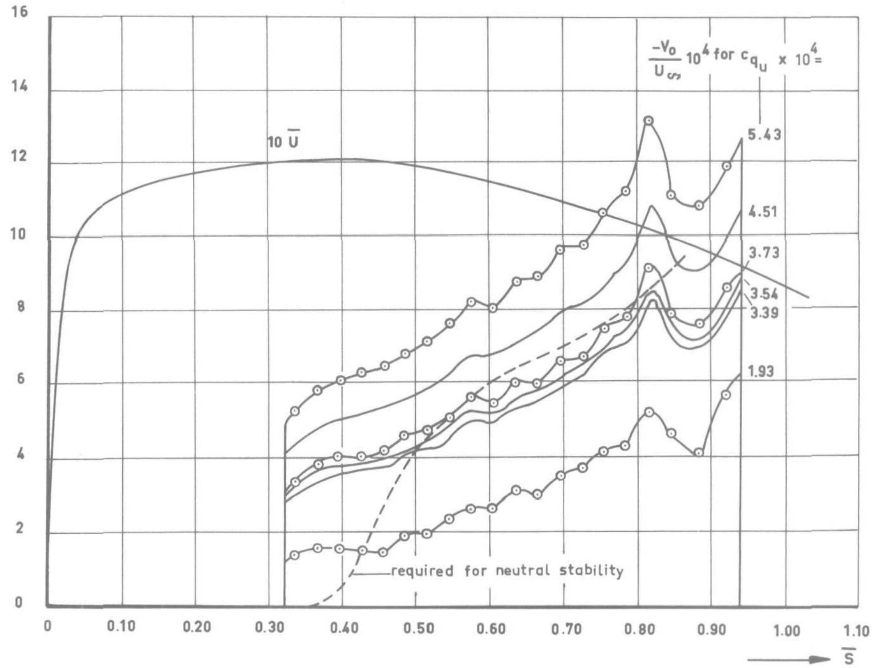

FIG. 11.31: SUCTION VELOCITY DISTRIBUTIONS FOR THE UPPER SURFACE; $\alpha = 0$, SERIES 1.

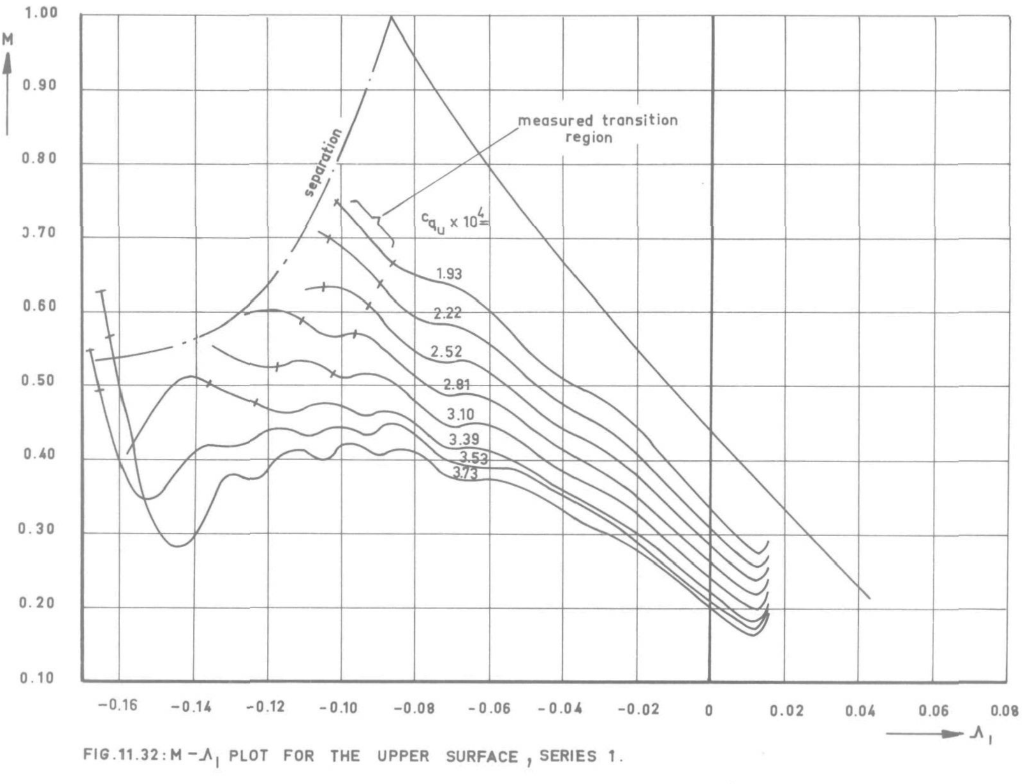

FIG. 11.32: M − Λ_1 PLOT FOR THE UPPER SURFACE, SERIES 1.

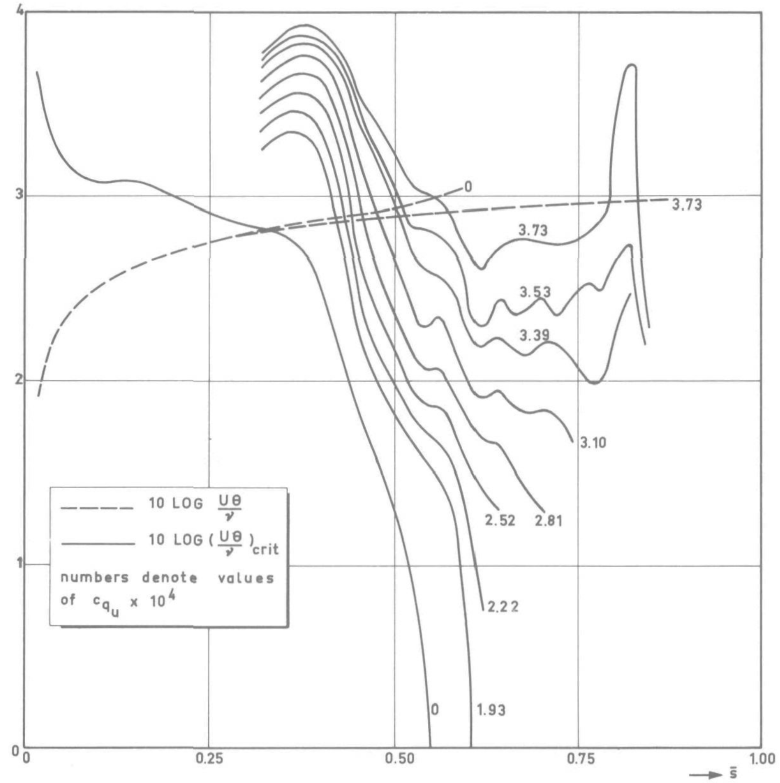

FIG. 11.33: 10 LOG $\frac{U\theta}{\nu}$ AND 10 LOG $(\frac{U\theta}{\nu})_{crit}$ FOR THE UPPER SURFACE; SERIES 1.

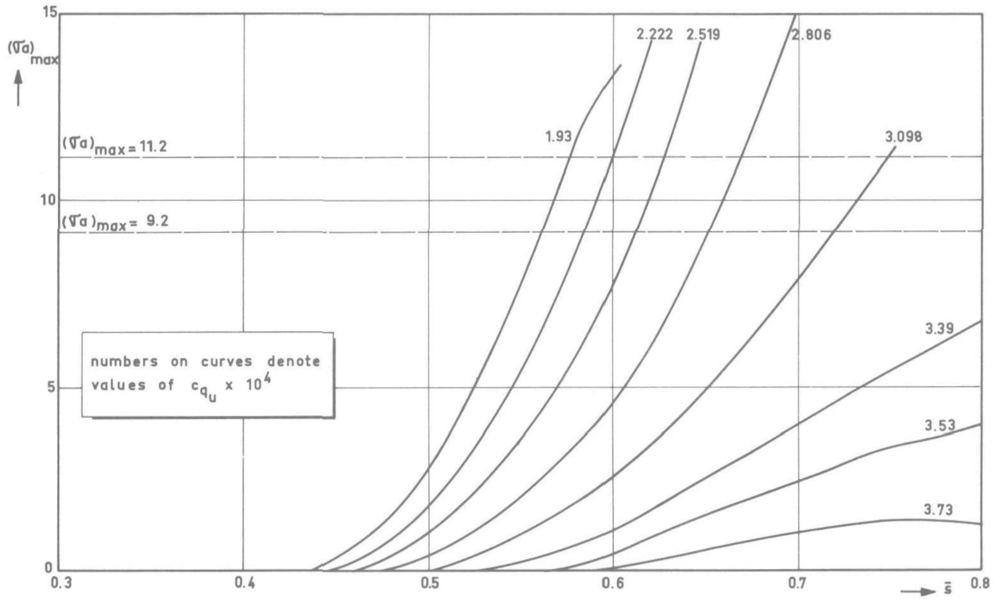

FIG. 11.34: $(\bar{\sigma}a)_{max}$ FOR DIFFERENT VALUES OF $c_{q_u} \times 10^4$; UPPER SURFACE, SERIES 1.

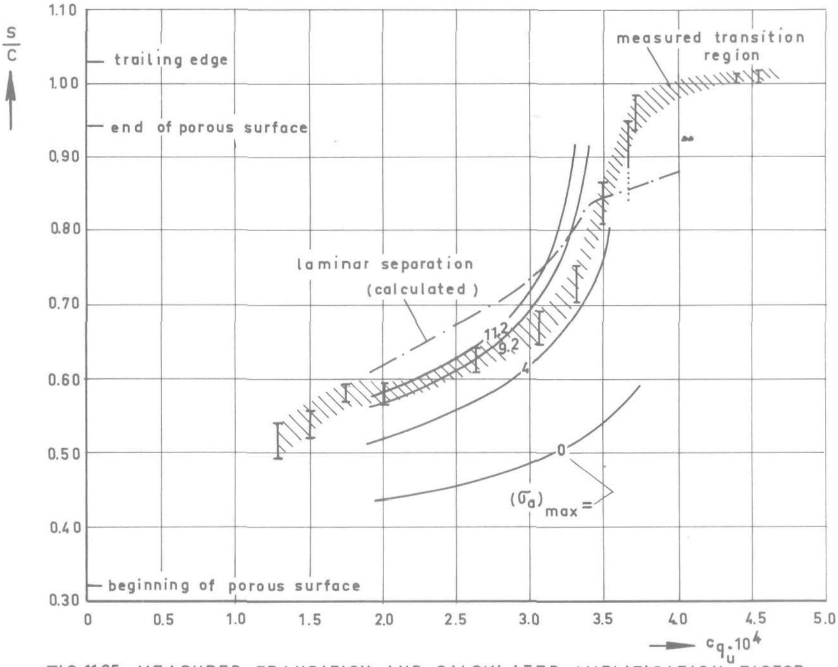

FIG.11.35: MEASURED TRANSITION AND CALCULATED AMPLIFICATION FACTOR FOR THE UPPER SURFACE OF THE SUCTION MODEL, $\alpha = 0°$, $R_c = 3.37 \times 10^6$ SERIES 1.

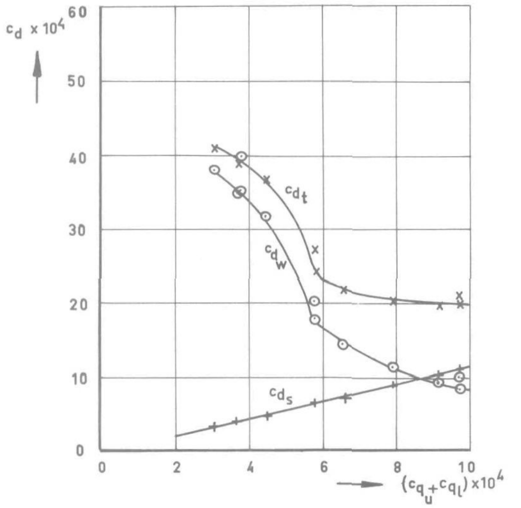

FIG.11.36: TRANSITION AND DRAG UPPER + LOWER SURFACE, SERIES 2.

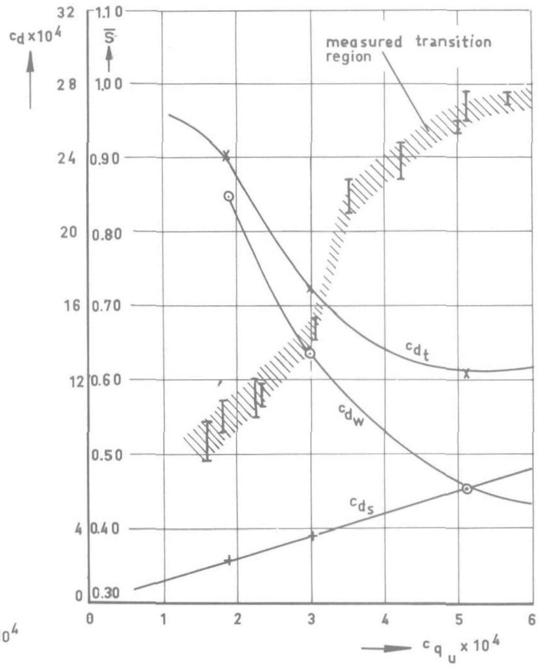

FIG.11.37: TRANSITION AND DRAG; UPPER SURFACE SERIES 2.

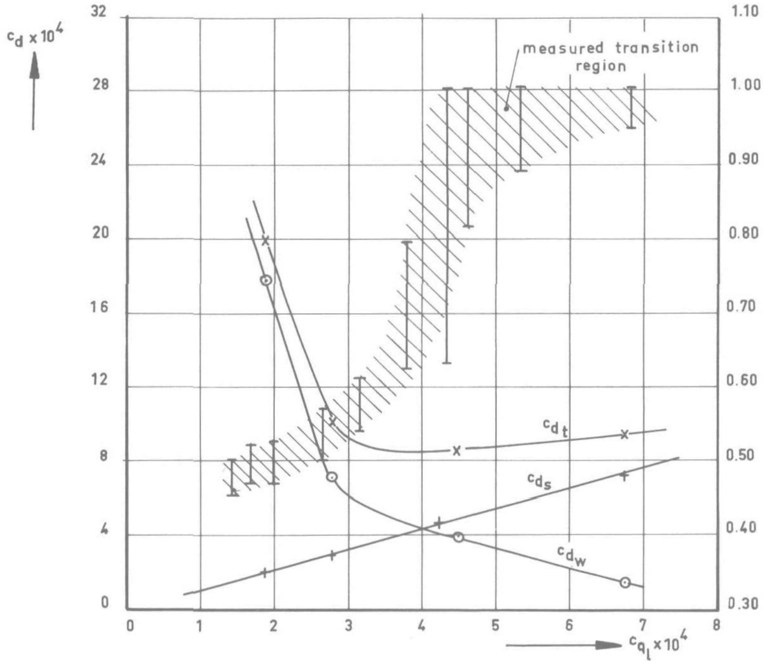

FIG.11.38 : TRANSITION AND DRAG FOR THE LOWER SURFACE ; SERIES 2.

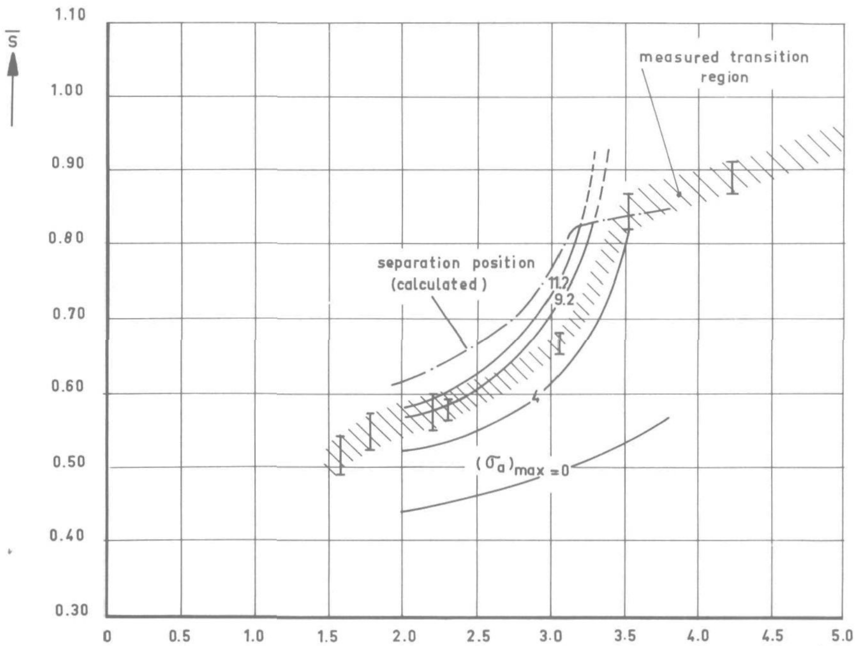

FIG. 11.39 : MEASURED TRANSITION REGION AND CALCULATED AMPLIFICATION FACTOR FOR THE UPPER SURFACE, SERIES 2.

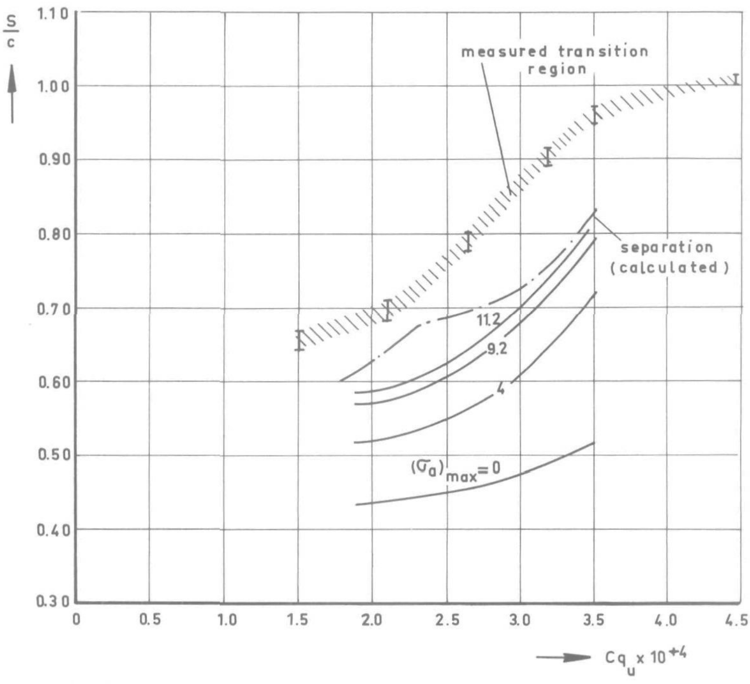

FIG. 11.40 : MEASURED TRANSITION AND CALCULATED AMPLIFICATION FACTOR FOR THE UPPER SURFACE ; $\alpha = 0$; SERIES 3.

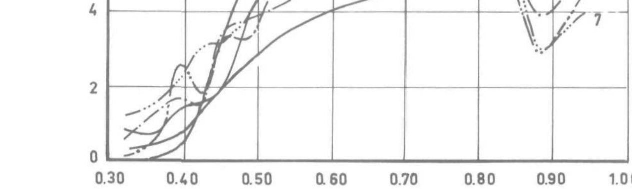

FIG.11.41 : SUCTION DISTRIBUTIONS FOR SERIES 4-7; TRANSITION AT THE END OF THE POROUS SURFACE.

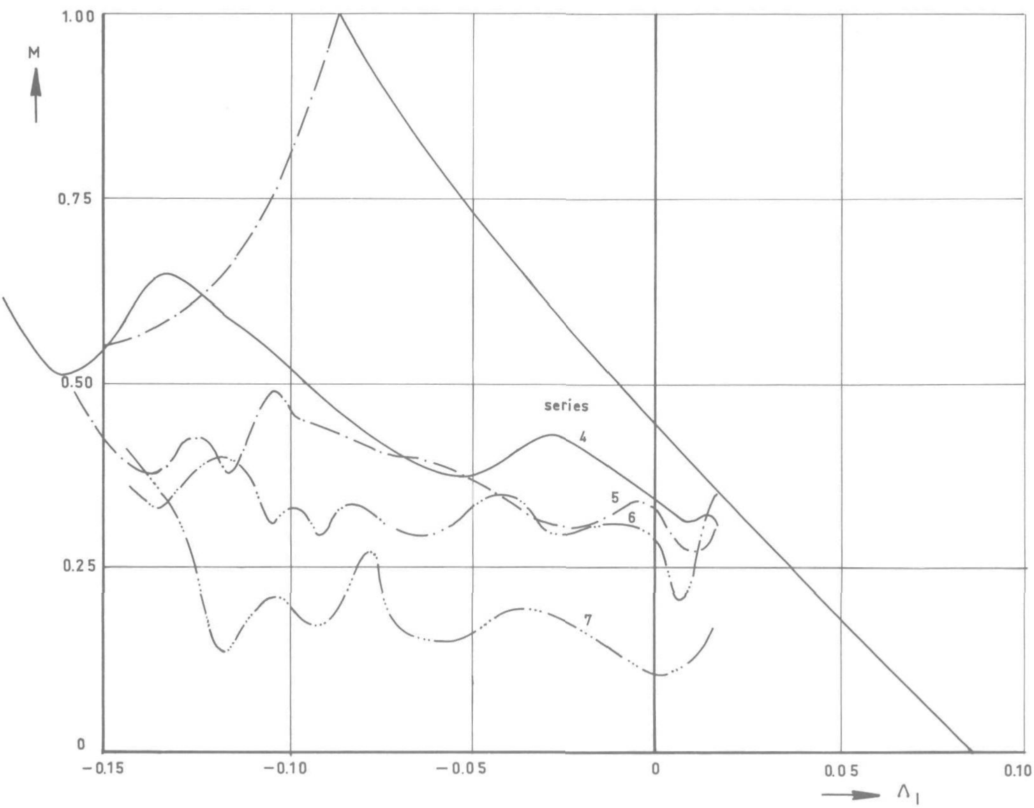

FIG.11.42: M−Λ_1 PLOTS FOR THE SUCTION DISTRUBUTIONS SHOWN IN FIG. 11.41

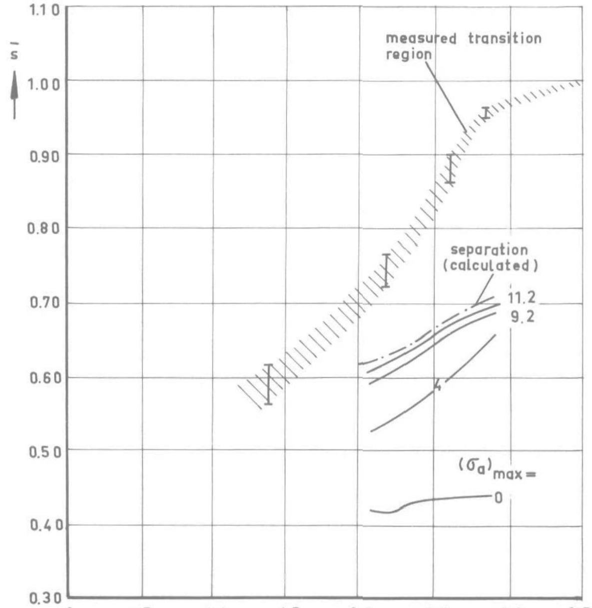

FIG.11.43: MEASURED TRANSITION REGION AND CALCULATED AMPLIFICATION FACTORS FOR THE UPPER SURFACE, SERIES 4.

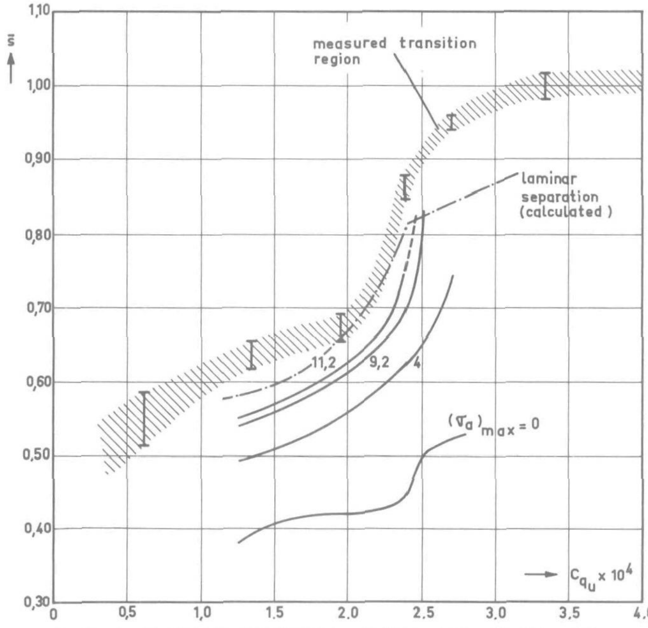

FIG.11.44: MEASURED TRANSITION REGION AND CALCULATED AMPLIFICATION FACTORS FOR THE UPPER SURFACE, SERIES 5.

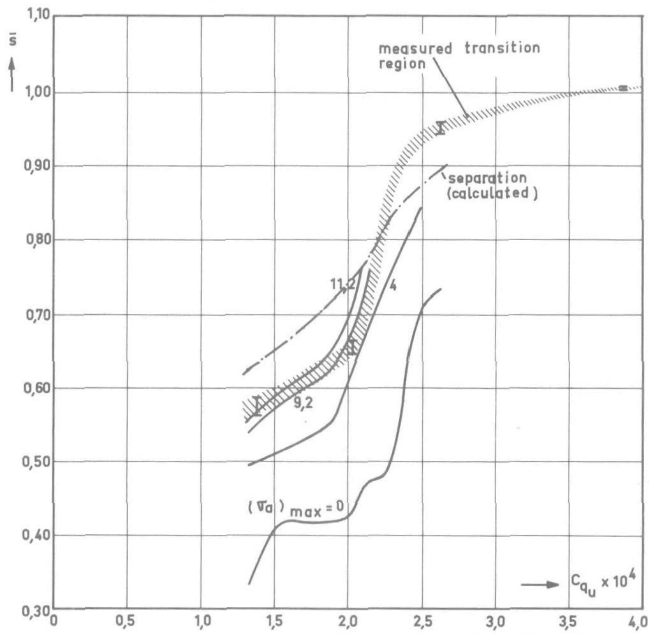

FIG.11.45: MEASURED TRANSITION REGION AND CALCULATED AMPLIFICATION FACTORS FOR THE UPPER SURFACE, SERIES 6.

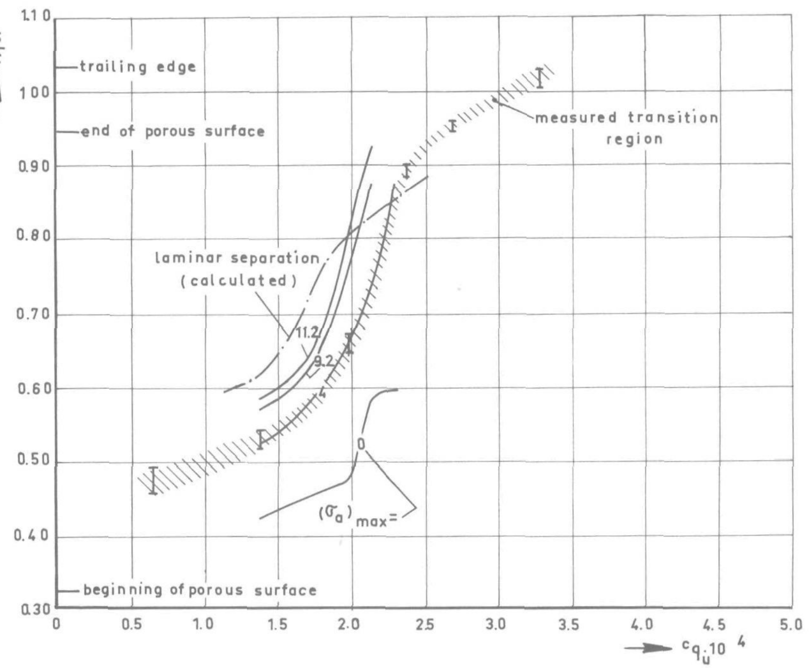

FIG. 11.46: MEASURED TRANSITION AND CALCULATED AMPLIFICATION FACTOR FOR THE UPPER SURFACE OF THE SUCTION MODEL ; $\alpha = 0°$, $R_c = 6.16 \times 10^6$, SERIES 7

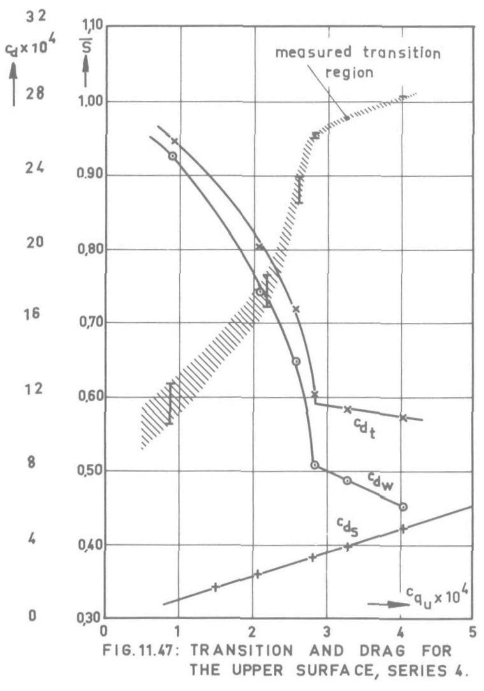

FIG. 11.47: TRANSITION AND DRAG FOR THE UPPER SURFACE, SERIES 4.

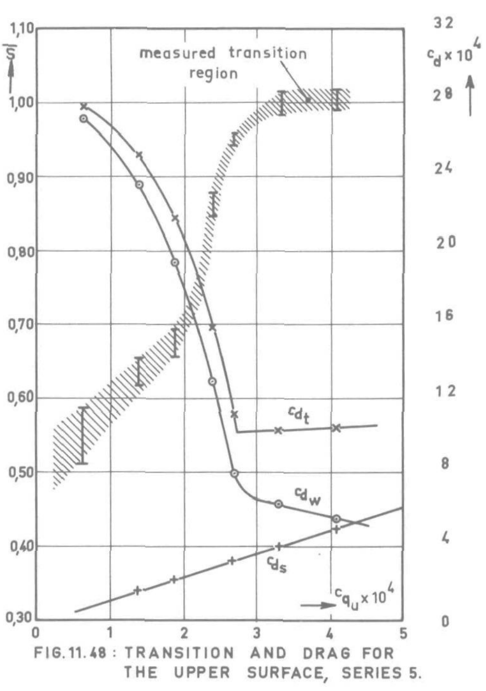

FIG. 11.48: TRANSITION AND DRAG FOR THE UPPER SURFACE, SERIES 5.

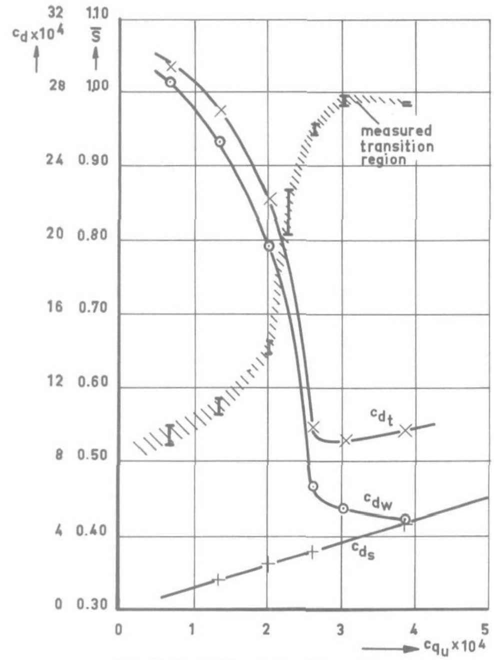

FIG. 11.49: TRANSITION AND DRAG FOR THE UPPER SURFACE, SERIES 6.

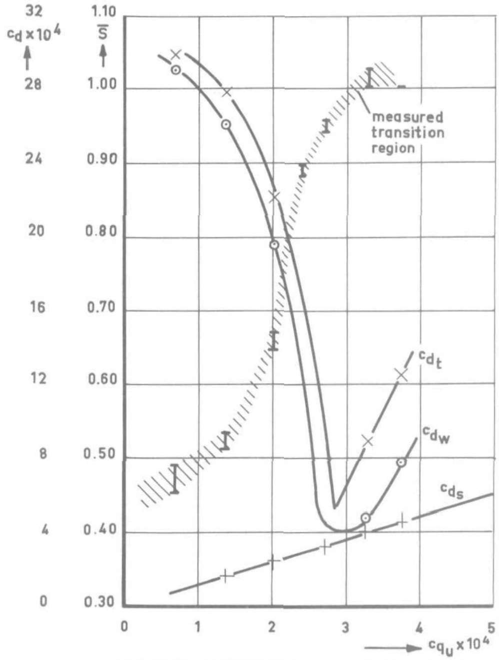

FIG. 11.50: TRANSITION AND DRAG FOR THE UPPER SURFACE, SERIES 7.

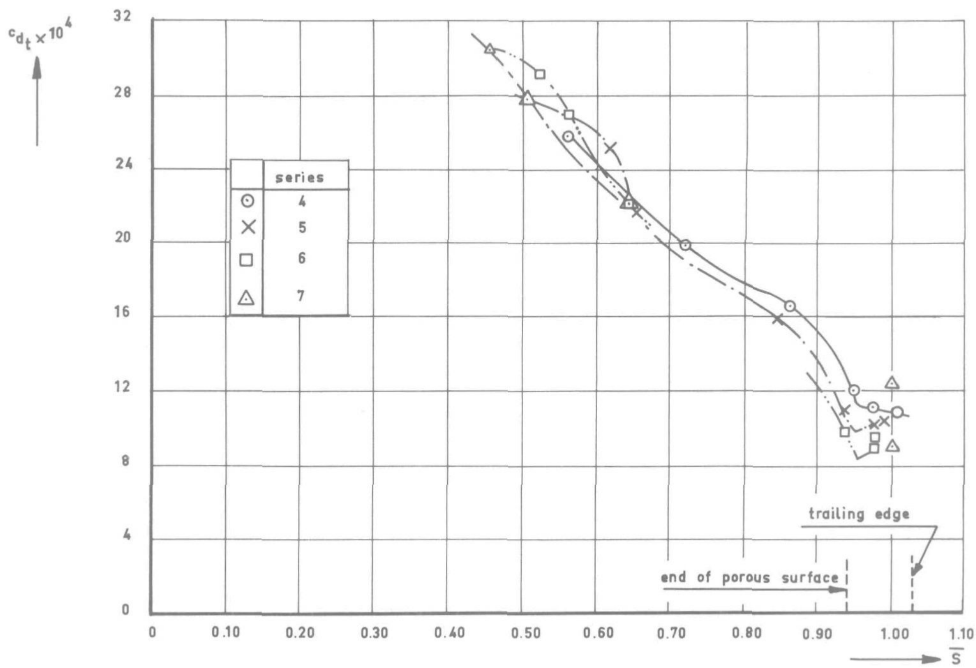

FIG. 11.51: RELATION BETWEEN TOTAL DRAG AND POSITION OF THE BEGINNING OF TRANSITION FOR THE UPPER SURFACE; SERIES 4–7.

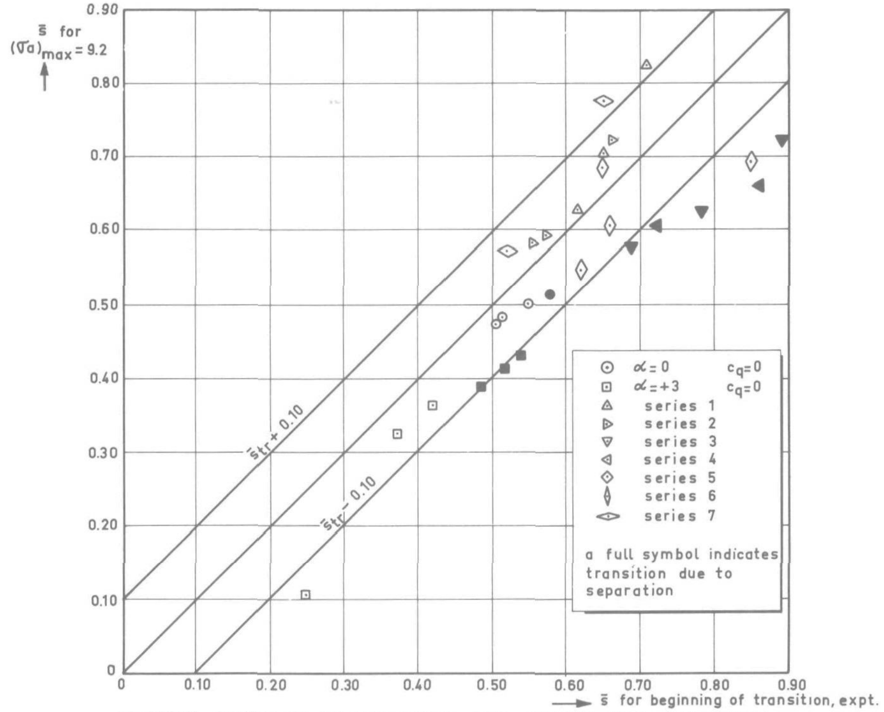

FIG. 11.52: SUMMARY OF MEASURED AND CALCULATED TRANSITION POSITIONS.

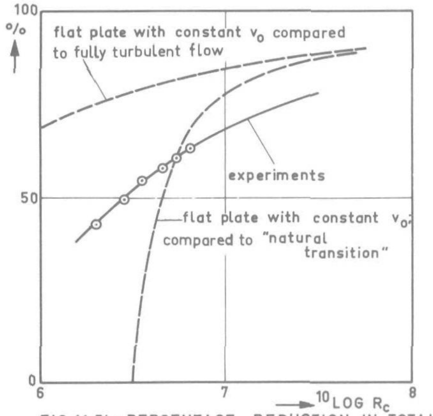

FIG. 11.54: PERCENTAGE REDUCTION IN TOTAL DRAG FOR THE UPPER SURFACE OF THE SUCTION MODEL.

NOTE: FIG. 11.53: ON NEXT PAGE.

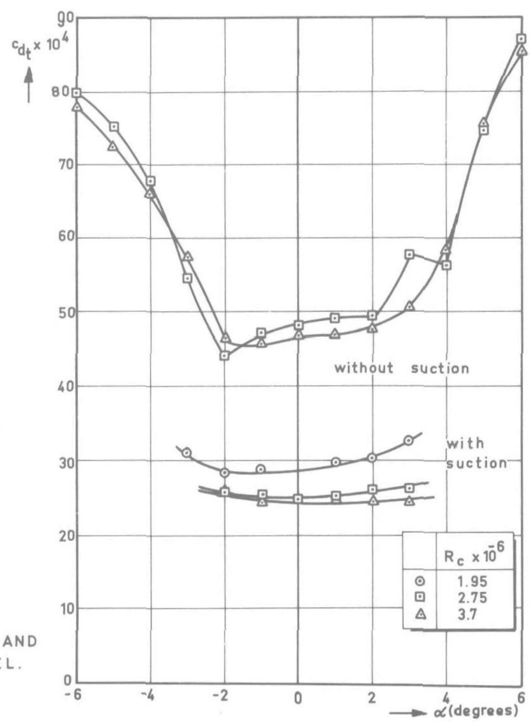

FIG. 11.55: TOTAL DRAG FOR THE UPPER AND LOWER SURFACE OF THE SUCTION MODEL.

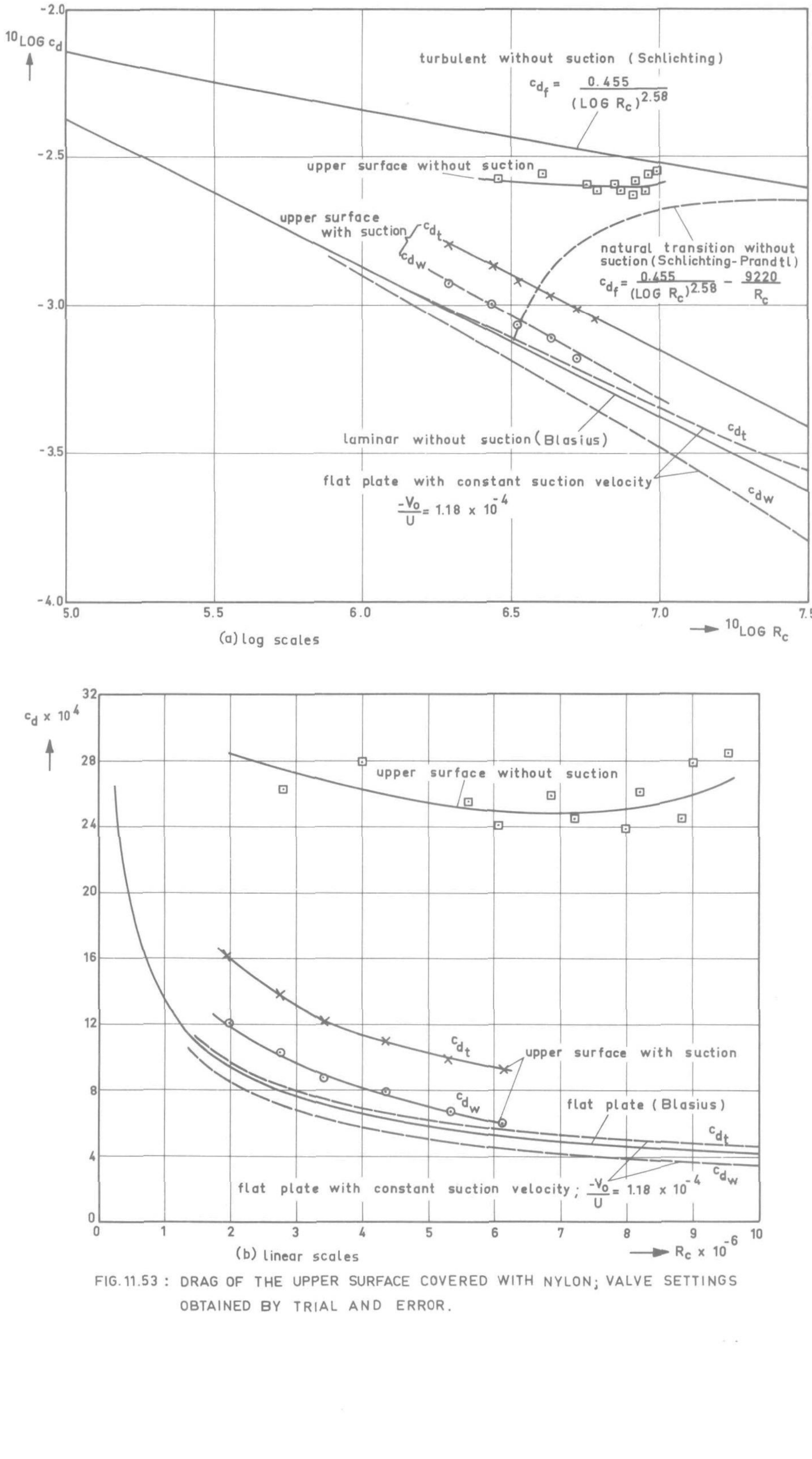

FIG. 11.53 : DRAG OF THE UPPER SURFACE COVERED WITH NYLON; VALVE SETTINGS OBTAINED BY TRIAL AND ERROR.

STELLINGEN.

1. Indien op een vleugelprofiel bij één waarde van de invalshoek de drukverdeling bekend is kan hieruit op eenvoudige wijze de conforme transformatie van het profiel naar een cirkel worden afgeleid. Daarna kan ook de drukverdeling bij willekeurige invalshoeken eenvoudig worden bepaald.

2. Door Raspet is een methode aangegeven waarmee bij benadering kan worden berekend hoe bij een turbulente grenslaag de afzuigintensiteit in koorderichting over een vleugelprofiel moet verlopen om loslating van de grenslaag te voorkomen.
De toepassing van deze methode voor verschillende invalshoeken kan zeer veel worden vereenvoudigd door gebruik te maken van de in stelling 1 bedoelde methode.
Cornish, J.J.: A simplified procedure for calculating boundary layer control systems for unflapped airfoils. Research Rept. 15, Aerophysics Dept., Mississippi State College, 1958.

3. Bij het ontwerpen van een vleugelprofiel met bepaalde gewenste aerodynamische eigenschappen biedt het voordelen de modulus van de conforme transformatie die de cirkel op het profiel afbeeldt voor te schrijven op de cirkelomtrek.

4. Bij vleugelprofielen ontworpen door Wortman komt een "instabilityrange" voor waarin het verloop van de drukgradient zodanig is gekozen dat de laminaire grenslaag niet kan loslaten doch wel omslaat. Het ontwerp van deze "instabilityrange" kan worden verbeterd door toepassing van de methode welke in hoofdstuk 9 van dit proefschrift wordt beschreven.
Wortman, F.X.: Progress in the design of low drag aerofoils. Blz. 748 - 770 in: Boundary layer and flow control, Vol.2, Pergamon Press, 1961.

5. In hoofdstuk 6 van dit proefschrift is een "fasevlak beschrijving" gegeven van de stroming tussen niet-evenwijdige vlakke wanden. Bij deze beschrijving werd uitgegaan van de grenslaagvergelijkingen.

Een analoge beschrijving voor dit geval kan worden gegeven indien wordt uitgegaan van de vergelijkingen van Navier-Stokes. In de gevallen waarin deze vergelijkingen oplossingen van het grenslaagtype toelaten kunnen de vergelijkingen van Navier-Stokes in de grenslaagvergelijkingen worden getransformeerd; de randvoorwaarden blijven echter verschillend. Indien het getal van Reynolds R oneindig groot wordt, naderen ook de randvoorwaarden tot die voor het grenslaagprobleem. Op eenvoudige wijze blijkt dan dat voor dit geval reeds bij vrij kleine waarden van R de grenslaagoplossing dicht wordt benaderd. Dit resultaat werd door Reeves en Kippenhan langs numerieke weg verkregen.

Reeves, B.L. en Kippenhan, C.J.: On a particular class of similar solutions of the equations of motion and energy of a viscous fluid. Journ. Aero-Space Sc. Vol. 29, jan. 1962., blz. 38 - 47.

Ingen, J.L. van: Phaseplane representation of the incompressible viscous flow between non-parallel plane walls. Rept. VTH-118, Onderafdeling der Vliegtuigbouwkunde, Delft, sept. 1964.

6. De oplossingen van de Falkner-Skan vergelijking (zie vergelijking 3.10 van dit proefschrift) vertonen verschillende eigenschappen die op eenvoudige wijze aannemelijk kunnen worden gemaakt door een beschouwing in een driedimensionale faseruimte waar als coordinaten de dimensieloze stroomfunctie f, de snelheid f' en de schuifspanning f'' worden gekozen.

7. De fasevlakbeschouwing van Ku voor de Falkner-Skan vergelijking met $\beta = 1$ is onvolledig.

Ku, Y.K.: Boundary layer problems solved by the method of non-linear mechanics. Proc. 9th. Intern. Congress Appl. Mech., Brussel, 1956, blz. 132 - 144.

8. De methode van Pohlhausen is onbruikbaar voor laminaire grenslagen met afzuiging.

9. Door Görtler wordt gesteld dat zijn reeksmethode voor de berekening van laminaire grenslagen nauwkeurige resultaten levert en even eenvoudig is toe te passen als de "onbetrouwbare methoden van het Pohlhausen type". Deze uitspraak wordt niet gesteund door de resultaten welke met zijn methode worden verkregen.

   Görtler, H.: A new series for the calculation of steady laminar boundary layer flows. Journ. Math. and Mech., Vol. 6, no 1, jan. 1957, blz. 1 - 66.

10. In de bestaande literatuur over oplossingen van de grenslaagvergelijkingen in de omgeving van het loslatingspunt wordt onvoldoende aandacht geschonken aan de invloed van de losgelaten grenslaagstroming op de drukverdeling.

    o.a. Goldstein, S.: On laminar boundary layer flow near a position of separation. Quart. Journ. Mech. 1, 1948, blz. 43 - 69.

11. Het is gewenst dat aan docenten en leden van de wetenschappelijke staven van de Nederlandse universiteiten en hogescholen periodiek een sabbatsjaar wordt verleend.